ABSTRACT

Title of Dissertation: A Study of High Transverse Energy Events in Proton-Proton and Proton-Nucleus Collisions at $\sqrt{s}$ = 27.4 GeV

Richard Scott Holmes, Doctor of Philosophy, 1985

Dissertation directed by: Robert G. Glasser
Professor
Department of Physics and Astronomy

Experiments intended to provide information on the constituents of particles such as protons achieve their probes of very small distances by studying events in which a large momentum transfer takes place. Because partons (quarks and gluons) seem to be confined inside composite particles, it is not possible to observe directly the outcome of a hard parton-parton scatter. Instead, one expects the reaction products to materialize as ordinary particles travelling approximately in the original parton direction, with large momentum components in the plane transverse to the direction of the incoming projectile.

I discuss properties of events in which large amounts of transverse energy ($E_t \approx$ sum of magnitudes of transverse momenta for relativistic secondaries) are produced in five full-azimuth apertures which cover ranges in pseudorapidity (η) of $\Delta\eta = 0.73$ to $\Delta\eta = 1.49$. Data were collected using the Fermilab Multiparticle Spectrometer triggered by a large, segmented calorimeter; 400 GeV/c protons on targets of hydrogen, aluminum, copper, and lead were used.

Cross sections as a function of E_t in each of the five apertures are presented. The cross sections fall exponentially with increasing E_t; the fall-off is more rapid in the narrower apertures. The

dependence on E_t is less steep than is predicted by a quantum chromodynamics-based model. For one of the five apertures, which is centered in the forward hemisphere, the cross sections for the nuclear targets at large E_t are consistent with being proportional to the atomic mass number, A. However, for the other four apertures, the cross sections grow more rapidly than A. A simple phenomenological model is presented which predicts a similar enhancement.

The events selected by requiring high E_t in a large-$\Delta\eta$, full azimuth aperture are predominantly non-jetlike at all values of E_t, but hydrogen target events selected for high E_t in a small-$\Delta\eta$, full azimuth aperture are increasingly planar at increasing E_t. The latter behavior strongly contradicts a longitudinal phase space model but is in general agreement with the QCD-based model, and suggests the onset of jet production. No evidence of a similar increase in jetlike structure is found for events originating in the heavier targets.

A STUDY OF HIGH TRANSVERSE ENERGY EVENTS

IN PROTON-PROTON AND PROTON-NUCLEUS COLLISIONS

AT $\sqrt{s}$ = 27.4 GeV

by
Richard Scott Holmes

Dissertation submitted to the Faculty of the Graduate School
of the University of Maryland in partial fulfillment
of the requirements for the degree of
Doctor of Philosophy
1985

"High p_t Interactions at 400 GeV -- Experimental Method and Cross Sections," with the E557 Collaboration, A. Dzierba _et al_., Bull. Am. Phys. Soc. _27_, 18 (1982).

"High p_t Interactions at 400 GeV -- Comparison of Events from Different Nuclear Targets," with the E557 Collaboration, A. Zieminski _et al_., Bull. Am. Phys. Soc. _27_, 18 (1982).

"High p_t Interactions at 400 GeV -- Search for Event Structure," with the E557 Collaboration, P. Rapp _et al_., Bull. Am. Phys. Soc. _27_, 18 (1982).

"High p_t Interactions at 400 GeV -- Properties of Small Aperture Calorimeter Trigger Events," with the E557 Collaboration, F. Lopez _et al_., Bull. Am. Phys. Soc. _27_, 18 (1982).

"High p_t Interactions at 400 GeV -- Distributions Obtained from the Vertex Detector and Conclusions," with the E557 Collaboration, E. Malamud _et al_., Bull. Am. Phys. Soc. _27_, 18 (1982).

"High Transverse Energy Events in Proton-Nucleus Interactions at 400 GeV/c," with the E557 Collaboration, R. Holmes _et al_., Bull. Am. Phys. Soc. _28_, 747 (1983).

"High p_t Proton-Proton Interactions at 400 GeV/c -- Small Aperture Calorimeter Trigger Cross Sections and Event Structure," with the E557 Collaboration, F. Lopez _et al_., Bull. Am. Phys. Soc. _28_, 747 (1983).

Professional positions held:

1977-78 Graduate Teaching Assistant, University of Maryland.
1978-85 Graduate Research Assistant, University of Maryland.

B. Papers published in proceedings of scientific meetings and conferences.

"Search for Free Muonium in Vacuum Using Thin Foil Targets," W. Beer et al., in Proceedings of the Eighth International Conference on High Energy Physics and Nuclear Structure, Vancouver, Canada, 1979, edited by D. F. Measday and A. W. Thomas (North-Holland, Amsterdam, 1980).

"An Evaluation of Some New Phototubes with High Gain First Dynodes," B. C. Brown et al., IEEE Trans. Nucl. Sci. NS-28, 666 (1981). (1980 Nuclear Science Symposium, Orlando, FL, USA, 5-7 Nov. 1980).

"High Transverse Energy Hadronic Interactions at 400 GeV/c," with the E557 Collaboration, presented by T. L. Watts, J. Phys. Colloq. 43, C3-127 (1982). (XXI Inter. Conf. on High Energy Physics, Paris, France, 1982).

"Properties of High Transverse Energy Hadronic Events," with the E557 Collaboration; presented by C. Halliwell, in Proceedings of the Seventeenth Recontre de Moriond, Moriond, 1982, edited by J. Tran Thanh Van (Editions Frontieres, Gif sur Yvette, France, 1982), p. 95.

C. Technical reports.

"Status Report on the University of Maryland's Transition Radiator-Detector System for Beam Particle Identification," L. C. Myrianthopoulos et al., University of Maryland Department of Physics and Astronomy Technical Report #80-106 (1980).

D. Contributed papers.

"A Transition Radiator-Detector System for Beam Particle Identification," L. C. Myrianthopoulos et al., Bull. Am. Phys. Soc. 25, 490 (1980).

CURRICULUM VITAE

Name: Richard Scott Holmes.

[redacted]

Degree and date to be conferred: Ph.D., 1985.

[redacted]

Collegiate institutions attended	Dates	Degree	Date of Degree
Worcester Polytechnic Institute	1973-77	B.S.	1977.
University of Maryland	1977-85	M.S.	1979.
		Ph.D.	1985.

Major: High Energy Physics.

Professional publications:

A. Papers published in refereed journals.

"Production of High-Transverse-Energy Events in pp Collisions at 400 GeV/c," with the E557 Collaboration, B. Brown et al., Phys. Rev. Lett. 49, 711 (1982).

"Production of High-Transverse-Energy Events in p-Nucleus Collisions at 400 GeV/c," with the E557 Collaboration, B. Brown et al., Phys. Rev. Lett. 50, 11 (1983).

"Study of Jetlike Structure in High-Transverse-Energy Events Produced in pp Collisions at 400 GeV/c," with the E557 Collaboration, B. C. Brown et al., Phys. Rev. D49, 1895 (1984).

APPROVAL SHEET

Title of Dissertation: A Study of High Transverse Energy Events in Proton-Proton and Proton-Nucleus Collisions at $\sqrt{s} = 27.4$ GeV

Name of Candidate: Richard Scott Holmes
Doctor of Philosophy, 1985

Dissertation and Abstract Approved: ______________________________
Robert G. Glasser
Professor
Department of Physics and Astronomy

Date Approved: ______________________________

Now spring bursts
      with warm airs
Now the <u>furor</u> of March skies
      retreats under Zephyrus
And Catullus will forsake
      these Phrygian fields
The sun-drenched farm-lands of Nicaea
& make for the resorts of Asia Minor,
      the famous cities...

-- Catullus

. . .

Are they gaining, Huxley?

-- Gary Larson

DEDICATION

The first person to teach me physics (among other things) was my father.

My mother didn't teach me much about physics -- but there are many other things I learned from her.

This work is dedicated,
with love and gratitude,
to
my parents,
Norma and Kenneth Holmes.

ACKNOWLEDGEMENTS

O for a muse of fire...

One physicist I know (mentioned herein, in fact, not too many lines from now), hates Acknowledgements. "You can't write acknowledgements without sounding obsequious," he says. Well, that's true.

I tried to think of a clever way to do it. (Clever, but not too cute). A conversations between the halves of my brain. Poetry. Gothic. Four part chorus and orchestra? (With cannon).

It can't be done.

There isn't a clever and sincere way to say "thank you" to your karass. All you can do is list the names and say the remarkably unoriginal but heartfelt things graduate students have said since Day One.

Bob Glasser, my advisor. He scowled at me when I let things slide, said nice things when I did good, hauled me in off the ledge once or twice, taught me practically everything I know and about a fiftieth of what he knows about statistics, made me think, gave me ideas, never let me get away with feeling cocky, and never let me get away with feeling stupid. Thank you...

Phil Steinberg, who brought me into this business and laid the groundwork of my training in high energy physics. He directed my Master of Science degree work, and he put me to work on a tiny experiment at Los Alamos that let me learn the basics without being overwhelmed; I won't soon forget Oberon, Titania, Ariel, Umbriel, and Miranda, the five phototubes. Thank you...

The members of the E557 Collaboration, all of whom took their parts in furthering my education as a physicist. Ernie Malamud, our spokesperson, took on a task you'd have to pay me mucho dinero to consider. Andrzej Zieminski got me interested in the nuclear targets and the restricted-rapidity apertures, and he directed me and collaborated with me on some of the early nuclear target analysis. I would have written a completely different dissertation if it weren't for him. Petko Devenski, Bob Ellsworth, Herman Haggerty, Clive Halliwell, Pat Rapp, and Leon Myrianthopoulos were especially helpful, especially good people to work with. Fred Lopez and Seung Ahn, fellow grad students, I owe for favors and friendships. Thank you all...

The MPS support group. Dan Green, Sten Hansen, and Rich Cantal did much to put us on the air and keep us there. They did a magnificent job. Thank you...

Chuck Hagelgans. Not only did he keep the Maryland remote printer and computer terminals functioning, he also took a personal interest in my own welfare. Thank you...

Brenda Dunn and Sheila Godlock, the people who do everything physicists are incapable of. We'd all be out selling shoes without them. Thank you...

People who made a difference in somewhat different ways: David Wolff, Jon Wesick, Jim Volk, Bob Trumble, Tom Swyden, Naomi Ellen Rose, Jan Nobel, Abrey Myers, Louise Halperin, Debby Greene, Hannah Cranor, Donna Bachtell, and probably several other friends I have forgotten and will remember only when it's too late to include them. I hope they'll forgive me. My parents, to whom this work is dedicated, and my sisters, Patricia Wells and Janet Holmes. For everything, thank you all -- profusely...

To all of you: You helped, taught, advised, encouraged, criticized, praised, befriended, commiserated, and celebrated; you gave much and put up with more.

A very fond "Thank you," one and all.

TABLE OF CONTENTS

LIST OF TABLES

LIST OF FIGURES

CHAPTER I

INTRODUCTION

It is now generally accepted that the proton, the neutron, and the rest of the strongly interacting particles collectively known as hadrons are composites: they are made of more fundamental objects, the quarks, bound together by a force mediated by the exchange of particles called gluons. In this dissertation I present results from an experiment designed to provide information on the interactions between quarks and gluons. I begin in this chapter with a discussion of some of the earlier findings in this field and an overview of the rest of this dissertation.

1.1. Historical survey

The first direct experimental evidence of the composite nature of nucleons (protons and neutrons) came from a series of deep inelastic electron-nucleon scattering experiments performed at SLAC in the late 1960's and early 1970's.[1] Figure 1-1 illustrates this process from the viewpoint of the parton model[2,3] in which the process is seen in the infinite-momentum frame of reference as an instantaneous scatter of the electron from a single pointlike constituent of the proton -- a "parton". Various versions of the parton model identified the partons with the quarks (the three valence quarks postulated in the quark model of the hadrons plus a "sea" of quark-antiquark pairs),[3] or with the quarks plus the gluons (the gauge particles of the force binding the quarks together);[4] these models were successful in describing much of the behavior observed in the deep inelastic electron scattering experiments.

In 1971, Berman, Bjorken, and Kogut[5] made predictions about the cross sections for the production of secondary particles in deep inelastic collisions as a function of transverse momentum, p_t. (This quantity is the magnitude of $\vec{p}_t$, the projection of the momentum of the secondary onto the plane transverse to the incoming particle.) They used an extension of the parton model to predict that the cross section should undergo a transition from the exponential form observed at low p_t to a power law at high p_t, and that high-p_t particle production therefore should be readily observable at then-available accelerator energies. Such behavior was found in 1972 at the CERN Intersecting Storage Rings,[6] and was studied in a number of subsequent experiments at CERN and Fermilab.[7] Figure 1-2 shows a typical result, with the cross section breaking away from the exponential form at a p_t of about 1 GeV/c. The cross sections reported for high p_t single particle production had a p_t^{-n} dependence, where n was about 8 (Fig. 1-3).

The Chicago-Princeton collaboration, in an extensive study of high-p_t particle production using proton beams of momenta 200, 300, and 400 GeV/c and targets of beryllium, titanium, and tungsten, made the surprising discovery that for p_t greater than about 3 GeV, the cross section grows as a function of the nucleon number A (the average number of nucleons per nucleus in a given target material) faster than A.[8]

They found that the A dependence of the invariant cross section $E[d\sigma(p_t,A)/dp^3]$ for producing a given type of particle with transverse momentum p_t could be parametrized as

$$E \frac{d\sigma(p_t,A)}{d^3p} = E \frac{d\sigma(p_t,1)}{d^3p} A^{\alpha(p_t)} . \qquad (1-1)$$

It was already known that the total hadronic cross sections increase with A as $A^{2/3}$; due to the large strength of hadronic interactions, the interior of the nucleus is "shadowed" by the nucleons at the surface. Since the volume of the nucleus is approximately proportional to A,[9] the surface area and hence the cross sections for large strength processes such as low p_t production go as $A^{2/3}$. (See Ref. 10). It was assumed that a similar $A^{2/3}$ dependence would apply to high-p_t particle production. For example, this assumption is implicit in the Chicago-Princeton collaboration's early analysis of its tungsten target data.

However, in subsequent studies using several different nuclear targets, Chicago-Princeton found that the value of α increases with p_t through 1.0 as p_t goes from 0 to about 2 GeV/c and reaches about 1.1 for pions at pt ≈ 3 GeV (Fig. 1-4). Up to α = 1.0 this increase could be explained as the disappearance of shadowing. Farrar and (independently) Pumplin and Yen[11] argued that the apparent strength of hadronic interactions is due to multiple interactions of low-momentum partons, while high-p_t processes involve only one or a few low-strength interactions of high-momentum partons. In this regime the nucleus is essentially transparent and one can regard it as a collection of independent nucleons all equally likely to participate in a collision, so that α should be 1.0.

The increase of α beyond 1.0 is more problematical. This "anomalous nuclear enhancement" (ANE), to use Krzywicki's coinage of Ref. 12, has been the subject of much theoretical interest.[11,12,13] The theories can be divided into those based on collective effects and those based on multiple interactions; the latter have had more success, particularly in view of the experimental evidence that high-mass dilepton yields increase as $A^{1.0}$. Large p_t processes may be able to tell us something of the nature of the nucleus, starting with the question of whether it can in fact be treated as a collection of independent nucleons. Viewed another way, nuclear matter can be regarded as a kind of detector capable of providing insight into the space-time development of the hadronization process in which the scattered partons evolve into final state particles.

Some light was shed on the question of what happens to scattered partons by studies of high energy electron-positron collisions beginning at SPEAR[14] and DORIS.[15]. The annihilation of e^+e^- can give rise to a quark-antiquark pair which fly apart back to back and produce hadrons at limited transverse momentum with respect to the original parton directions; the two resulting configurations are termed "jets" (Fig. 1-5). The SPEAR jet studies confirmed quark parton model predictions of jet angular distributions and scaling properties.

Field and Feynman,[16] using information on hadronization and the quark distributions in nucleons obtained from the results of the deep inelastic lepton scattering experiments and e^+e^- data, developed a quark parton model of high p_t production in hadron-hadron collisions. Figure 1-6 illustrates the physics underlying this model: the fundamental process is an elastic quark-quark scattering (gluons were not incorporated), with the subsequent hadronization giving rise to the high p_t hadron h. This is the "leading" (highest p_t) hadron in one of the two jets which arise from the hadronization of the two scattering quarks; two more jets come from the two "spectator" quark or diquark systems. The quark-quark scattering was regarded as a "black box" and the cross section was chosen to give a p_t^{-8} behavior for the high p_t production cross sections, similar to what had been observed.

To produce a hadron at a given high p_t, one must scatter a quark at a higher p_t; since the cross section falls rapidly as p_t increases, the most likely case is that the quark p_t is not very much higher -- about 15%. The quark then must hadronize in such a way as to give an unusually large fraction of its transverse momentum to one hadron. This requirement in combination with the steep p_t dependence of the cross section results in a prediction that the ratio of the cross section for producing a jet at a given p_t to the cross section for producing a single hadron at the same p_t should be large.[17] In an extension of the original Field-Feynman model, Feynman, Field, and Fox computed this ratio, obtaining a value of 370 at $x_t = 0.4$, rising to 1000 at $x_t = 0.7$, where $x_t = 2p_t/\sqrt{s}$.[18]

A further refinement by Feynman, Field, and Fox[19] of this model incorporated gluons and replaced the "black box" parton scattering cross section with quark-quark, quark-gluon, and gluon-gluon cross sections calculated in first-order perturbative quantum chromodynamics (QCD). QCD scale breaking effects also were included.

The latest incarnation of this model, referred to herein as the "QCD/Brem" model, improves on the Feynman-Field-Fox QCD model by incorporating the previously neglected effects of noncollinear gluon bremsstrahlung.[20] I have used a Monte Carlo simulation based on the QCD/Brem model in the present work; it is described more fully in Appendix D.

The promise of a substantial increase in yield at a given p_t prompted a second generation of experiments in which the trigger requirement was "high p_t" in a geometrical aperture large enough to contain the expected jet from a scattered quark, as measured by the response of a segmented ionization calorimeter.[21,22,23] Strictly speaking, these experiments triggered not on high transverse momentum but on what has come to be known as high transverse energy in the trigger aperture. The "particle transverse energy" (E_t) of a group of particles is defined to be $\Sigma\epsilon_i \sin\theta_i$, where ϵ_i is the energy of the i'th particle and θ_i is the polar angle of its direction. For relativistic secondaries, $E_t \approx \Sigma(p_t)_i$, a scalar sum. The transverse momentum of the group of particles, by contrast, is the magnitude of a vector sum, $|\Sigma(\vec{p}_t)_i|$. Transverse energy triggers are discussed further in chapter II.

Experiments E260[21] and E395[22] used two-arm calorimeters, each arm subtending a solid angle of about 1 to 2 sr in the proton-proton center of mass, while E236[23] used a single arm calorimeter subtending about 3 sr. Both E260 and E395 triggered on high p_t single particles and on high transverse energy in a single arm; E395 also used a two-arm transverse energy trigger. Both of these experiments reported yield ratios of jets to single particles larger than 100. E260 published a cross section for jet production which was in qualitative agreement with the predictions of the QCD-based model of Feynman, Field, and Fox.

E260 and E395 both claimed the jets on which they triggered were generally well contained within the acceptances of their calorimeters. However, Dris has shown[24] that a limited solid angle calorimeter is in fact biased in favor of well-contained jets. Briefly, the argument is as follows: Suppose we are triggering on 5 GeV transverse energy in a calorimeter whose size is comparable to an average jet's size. The trigger requirement can be satisfied by, say, a typical 6 GeV jet that leaves 5/6 of its energy in the calorimeter, or by a 5 GeV jet that is smaller than average and leaves all its energy in the calorimeter. While only a small fraction of 5 GeV jets will be so well contained, they still are much more likely than the average 6 GeV jet owing to the steep energy dependence of the jet cross section. Therefore the trigger will select predominantly well-contained, 5 GeV jets.

As a corollary, if one reduces the size of one's trigger sector, one will collect well-contained, <u>smaller</u> jets. It follows that unless one uses a calorimeter larger than the largest jets, one will observe a "jet cross section" that depends on the size of the trigger sector. E395 and E236 verified this prediction experimentally, and E236 declined to extract a "jet cross section" for this reason. However, features of the event structure in the E236 data were reported to agree well with the Feynman-Field-Fox QCD model.

E260 studied the A dependence of the "jet cross section," comparing production from aluminum and hydrogen targets. An $A^{\alpha(p_t)}$ dependence was found, with α exceeding 1.0 for p_t larger than about 1 GeV/c. This behavior was qualitatively very similar to the ANE observed with high p_t single particles.

The confusion brought about by the solid angle dependence of the "jet cross section," as well as lingering doubts as to whether the jetlike structure observed in these experiments might have been an artifact of the trigger requirement, led to the proposal of Fermilab experiment E557,[25] which would use a calorimeter much larger than those in the experiments discussed above. Such a calorimeter would be much larger than a jet, thereby circumventing the Dris effect; it would permit triggers which would not be inherently biased in favor of jetlike structure; and it would enable study of the event structure at all azimuthal angles, not just in the regions near and opposite the jets.

1.2. Dissertation contents

This dissertation presents results from E557, using events satisfying a large, full-azimuth calorimeter trigger or a minimum bias trigger, with 400 GeV/c protons incident on targets of hydrogen, aluminum, copper, and lead.

Chapter II describes the design of E557, including an overview of the apparatus and a discussion of the triggers. The data set for this analysis is described. Chapter III is a discussion of the calorimeter resolution function. In Chapter IV I discuss cross sections for production of transverse energy into various geometrical acceptances, and I compare the results for the four targets. Chapter V contains an analysis of the event structure in hydrogen and nuclear targets. In Chapter VI I compare my results to some models and to results from other experiments. Details of the apparatus, trigger logic, and data acquisition; procedures for calorimeter phototube voltage setting; a discussion of offline calibration, pedestal finding, and vertex finding; a description of two Monte Carlo simulations; and a discussion of the statistics of weighted events are to be found in the appendices.

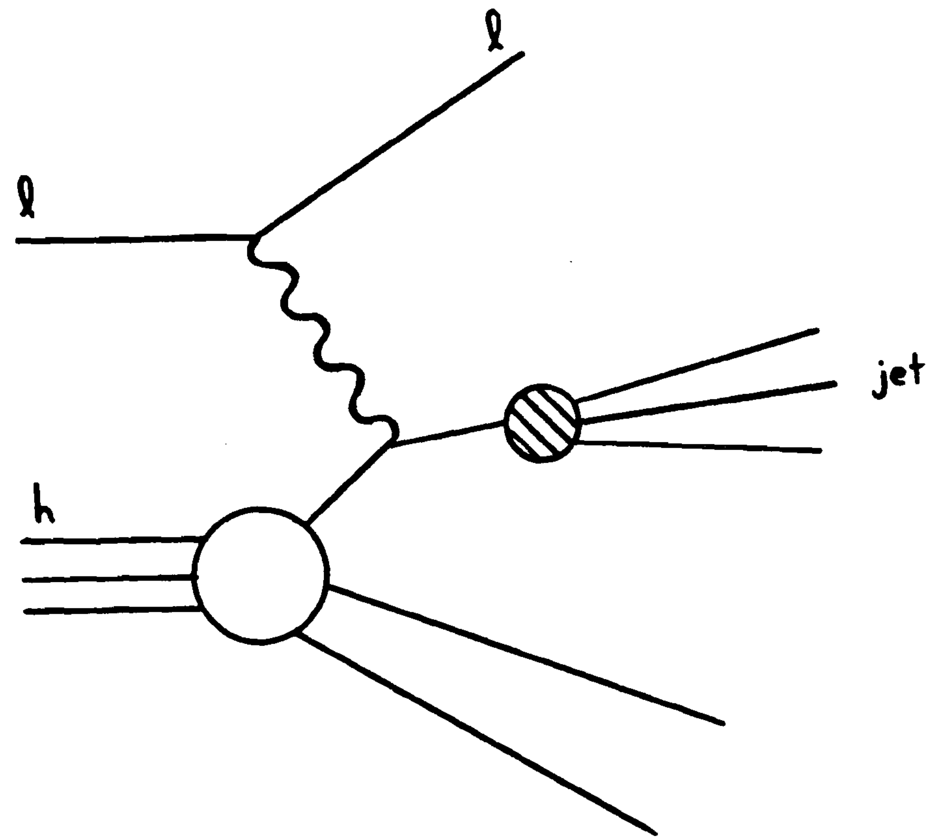

FIG. 1-1. Parton model view of deep inelastic lepton scattering: lepton (ℓ) scatters from parton in hadron (h), giving rise to a jet.

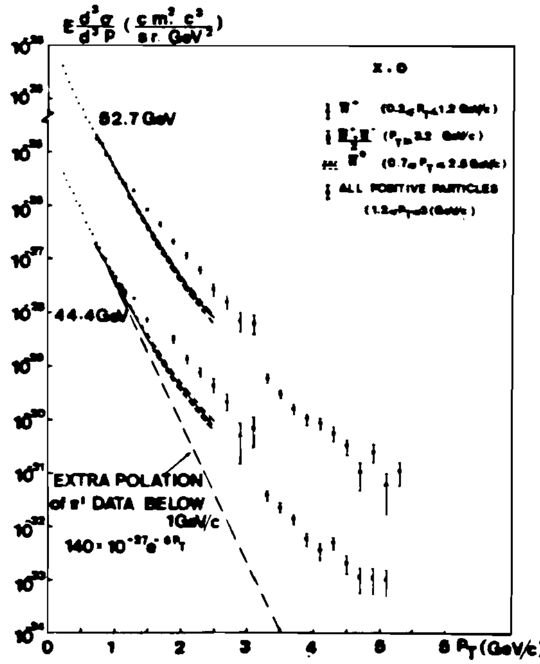

FIG. 1-2. Pion invariant cross section versus p_t. Source: Ref. 26.

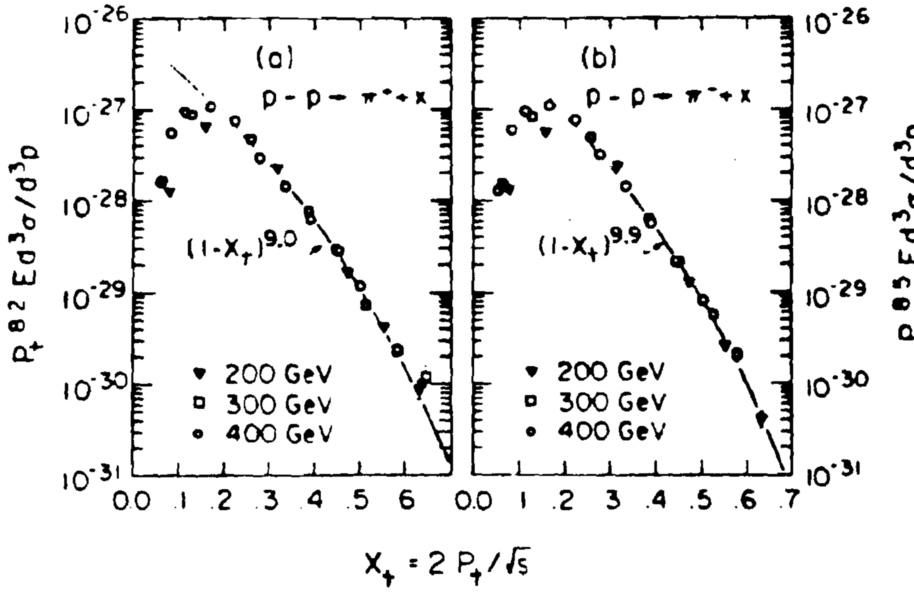

FIG. 1-3. Scaling properties of the π^+ and π^- cross sections versus $x_t = 2p_t/\sqrt{s}$. Source: Ref. 27.

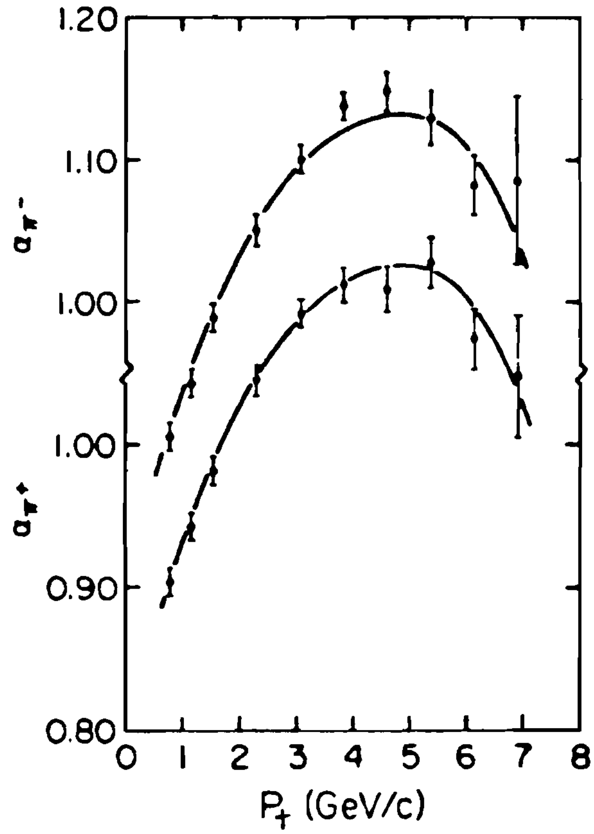

FIG. 1-4. Value of the power α in the parametrization $d\sigma/dp_t \propto A^{\alpha}$ versus p_t for π^+ and π^- production. Source: Ref. 27.

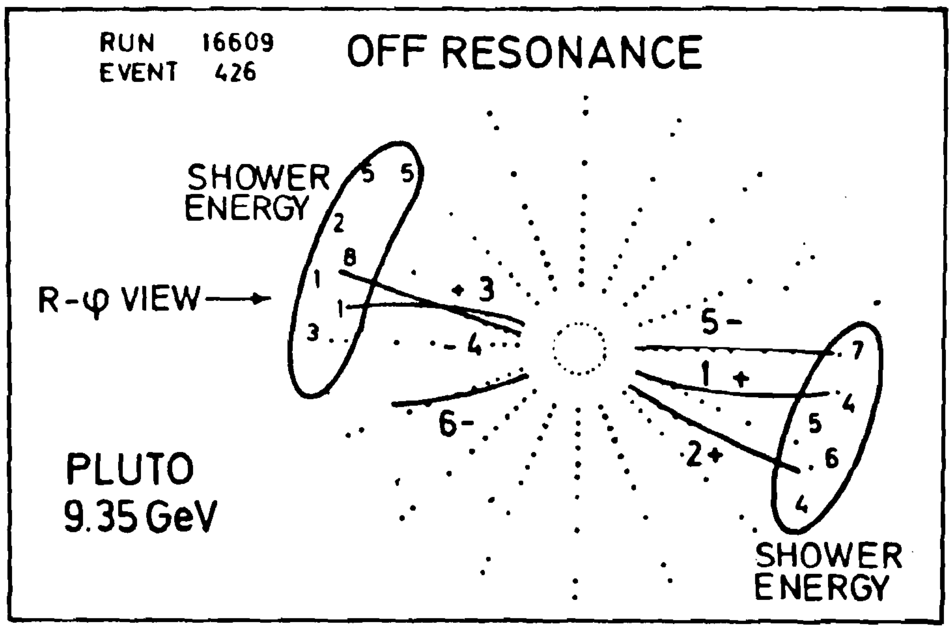

FIG. 1-5. A "nontypical nice jetlike event" from e^+e^- data at $\sqrt{s}$ = 9.35 GeV. Source: Ref. 15.

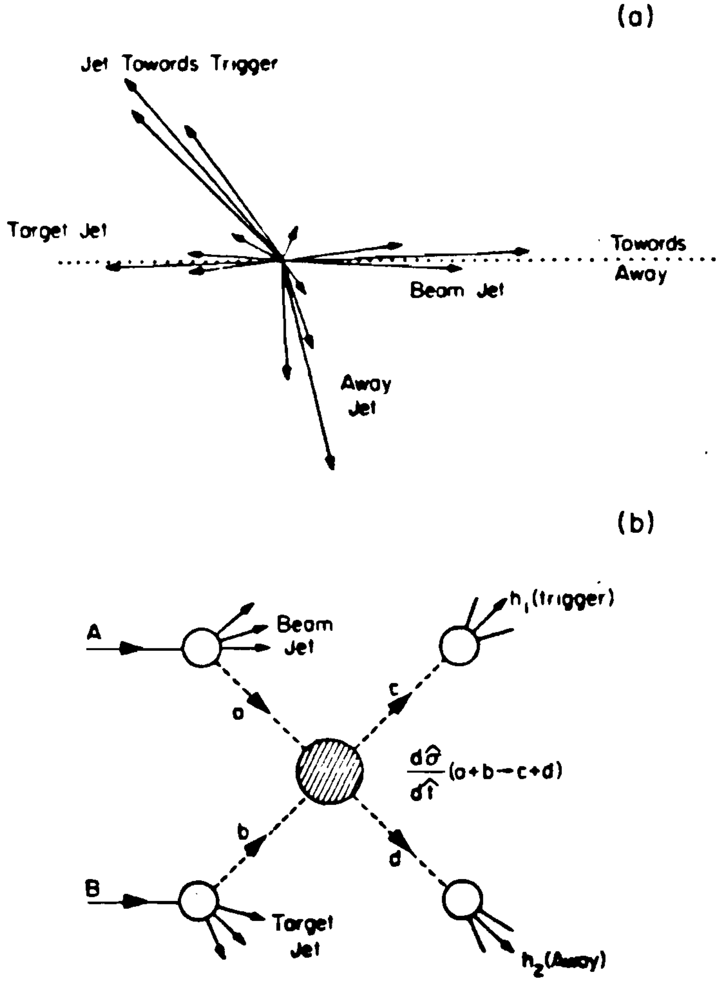

FIG. 1-6. (a) Four-jet structure resulting from a hard hadron-hadron scatter in the Field-Feynman model, seen in the center of mass frame. (b) Diagram of hard scattering between two hadrons, A and B. Partons a and b scatter, producing partons c and d which give rise to high-p_t hadrons h_1 and h_2, with accompanying jets.

References for Chapter I

1. E. D. Bloom *et al.*, Phys. Rev. Lett. 23, 930 (1969); M. Breidenbach *et al.*, Phys. Rev. Lett. 23, 935 (1969); G. Miller *et al.*, Phys. Rev. D 5, 528 (1972).
2. R. P. Feynman, Phys. Rev. Lett. 23, 1415 (1969).
3. J. D. Bjorken and E. A. Paschos, Phys. Rev. 185, 1975 (1969).
4. J. Kuti and V. F. Weiskopf, Phys. Rev. D 4, 3418 (1971).
5. S. M. Berman, J. D. Bjorken, and J. B. Kogut, Phys. Rev. D 4, 3388 (1971).
6. F. W. Büsser *et al.*, Phys. Lett. 46B, 471 (1973); 51B, 306 (1974); 55B, 232 (1975).
7. An extensive list of references on early high-p_t and jet experiments is given in M. Jacob and P. V. Landshoff, Phys. Rep. 48, 285 (1978).
8. J. W. Cronin *et al.*, Phys. Rev. D 11, 3105 (1975).
9. M. A. Preston and R. K. Bhaduri, *Structure of the Nucleus* (Addison-Wesley, Reading, Massachusetts, 1975).
10. R. L. Glauber, in *Lectures in Theoretical Physics*, edited by W. E. Brittin and L. E. Dunham (Interscience, N. Y., 1959).
11. J. Pumplin and E. Yen, Phys. Rev. D 11, 1812 (1975); G. Farrar, Phys. Lett. 56B, 185 (1975).
12. A. Krzywicki, Phys. Rev. D 14, 152 (1976).
13. P. M. Fishbane and J. S. Trefil, Phys. Rev. D 12, 2113 (1976); P. M.

Fishbane, J. K. Kotsonis, and J. S. Trefil, Phys. Rev. D 16, 122 (1977); J. H. Kühn, Phys. Rev. D 13, 2948 (1976); F. Takagi, Phys. Rev. Lett. 43, 1296 (1979); V. V. Zmushko, Sov. J. Nucl. Phys. 32, 231 (1980); D. Treleani and G. Wilk, Nuovo Cimento A 60A, 201 (1980); U. Sukhatme and G. Wilk, Phys. Rev D 25, 1978 (1982).

14. G. Hanson et al., Phys. Rev. Lett. 35, 1609 (1975).
15. G. Flügge, Act. Phys. Austr., Suppl. XXI, 81 (1979)
16. R. D. Field and R. P. Feynman, Phys. Rev. D 15, 2590 (1977).
17. S. D. Ellis, M. Jacob, and P. V. Landshoff, Nucl. Phys. B108, 93 (1976).
18. R. P. Feynman, R. D. Field, and G. C. Fox, Nucl. Phys. B128, 1 (1977).
19. R. P. Feynman, R. D. Field, and G. C. Fox, Phys. Rev. D 18, 3320 (1978).
20. G. C. Fox and R. L. Kelly, in Workshop on Proton-Antiproton Collider Physics, Madison, Wisconsin (AIP Conference Proceedings 85), edited by V. Barger, D. Cline, and F. Halzen (AIP, New York, 1982), p. 435; R. D. Field, G. C. Fox, and R. L. Kelly, Phys. Lett. 119B, 439 (1982).
21. C. Bromberg et al., Phys. Rev. Lett. 38, 1447 (1977); Nucl. Phys. B134, 189 (1978); Phys. Rev. Lett. 42, 1202 (1979); Phys. Rev. Lett. 43, 561 (1979); Phys. Rev. Lett. 43, 565 (1979); Nucl. Phys. B171, 1 (1980); B171, 38 (1980).
22. M. D. Corcoran et al., Phys. Rev. Lett. 41, 9 (1978); Physica Scripta 19, 95 (1979); Phys. Rev. D 21, 641 (1980); Phys. Rev. Lett. 44, 514 (1980).
23. V. Cook et al., Nucl. Phys. B186, 219 (1981).

24. M. Dris, Nucl. Inst. Meth. 158, 89 (1979).

25. V. Ashford et al., Fermilab Proposal No. E557, 1977 (unpublished).

26. M. Banner et al., Phys. Lett 44B, 537 (1973).

27. D. Antreasyan et al., Phys. Rev. D 19, 764 (1979).

CHAPTER II

EXPERIMENT E557

A "Proposal to Study Hadron Jets with the Calorimeter Triggered Multiparticle Spectrometer" was submitted to the Fermi National Accelerator Laboratory (Fermilab) in May, 1977.[1] The experiment was approved and designated E557. Our first data-taking running period was in the Spring of 1981; we logged 194 hours of beam time, most of it for testing and calibration, and recorded 537,000 events on tape. As of April, 1985 results from E557 have been reported in three published articles,[2,3,4] and two PhD dissertations in addition to this one have been or will soon be written.[5,6] In this chapter I discuss the design of E557, the apparatus, the triggers, and the data set on which my analysis is based.

2.1. Design and goals of E557

E557 was designed as an extension and improvement of the earlier Fermilab experiment E260. As in the predecessor experiment, the intent was to explore parton-parton interactions by studying events in which the collision of two hadrons gave rise to jets, and the method was to use a large particle-detection system triggered by a calorimeter on events with high transverse energy. It was envisioned that both negative ($\bar{p}$, K^-, and π^-) and positive (p, K^+, and π^+) beams with momenta of 200, 300, and 400 GeV/c would be used in combination with both a liquid hydrogen target and several "nuclear targets" in the form of metal foils.

The chief differences between E557 and E260 were a higher beam energy, a larger calorimeter with improved angular resolution and more flexibility for triggering, an additional Cherenkov counter for improved identification of final state particles, and the capability of tagging different species of beam particles using Cherenkov counters and a transition radiator-detector system.

2.2. Coordinate systems

The Cartesian coordinate system used herein, except where noted, to refer to positions of apparatus and the like has its origin at the intersection of the nominal beam line with the plane defined by the upstream face of the spectrometer magnet. The x direction is horizontal, to the left as one faces downstream. The y direction is upward and the z direction is downstream along the nominal beam line.

In discussing acceptances and particle trajectories it is more convenient to use a spherical polar coordinate system with origin either at the point of an interaction or in the center of the hydrogen target. The longitudinal coordinate, z, is parallel to the nominal beam line; the polar angle, θ^*, is measured from the z axis in the proton-proton center-of-mass frame (θ denotes the equivalent angle in the laboratory frame), and ϕ, the azimuthal angle, is measured such that $\phi = 0°$ is horizontal to the left when looking downstream and $\phi = 90°$ is up. Unless otherwise stated, in this dissertation "center of mass" refers to that of a system which in the laboratory frame consists of a 400 GeV/c proton and a stationary proton in the hydrogen target.

2.3. Apparatus

E557 made use of the Multiparticle Spectrometer facility (MPS), a facility designed for the analysis of large-multiplicity events, located in the west branch of the M6 beam line at Fermilab (M6W). The following is an overview of the apparatus; details may be found in Appendix A and in the cited references.

The MPS, shown schematically in Fig. 2-1, was built in 1975 by a collaboration of the California Institute of Technology, Fermilab, Indiana University, the University of California at Los Angeles, and the University of Illinois at Chicago Circle. To the existing analysis magnet and particle tracking system the E557 collaboration added a large-acceptance, full-azimuth, highly segmented calorimeter system for measurement of energy carried by both neutral and charged particles, as well as a system for beam particle mass identification; the original segmented Cherenkov counter, used to identify particles in the final state, was upgraded to a two component segmented Cherenkov counter system. The other major components of the MPS are the target station, redesigned for E557; the superconducting analysis magnet; and a charged particle tracking system consisting of proportional wire chambers and spark chambers.

The calorimeter played a major role in E557; it enabled us to trigger on high transverse energy events, and was used to measure the energy flow in the final state as a function of θ^* and ϕ. It covered the full azimuth over a wide range of polar angles approximately centered on 90° in the proton-proton center of mass. The calorimeter was divided longitudinally into three sections, denoted Electromagnetic (EM), Front Hadron (FH), and Back Hadron (BH). Laterally it was divided into small modules; EM had 126 modules, each of which had a FH module of the same height and width immediately behind it, while BH had 28 modules, larger than those in EM and FH. The division of EM and FH is shown in Fig. 2-2 and that of BH in Fig. 2-3. Each EM module was a sandwich of 14 half-inch thick sheets of lead alternating with half-inch sheets of plastic scintillator. The FH modules consisted of a 40-layer sandwich of scintillator and half-inch steel, while the BH modules contained 22 layers of scintillator and one-inch steel (Fig. 2-4). An electron or photon striking an EM module would dissipate its energy, mainly in the lead, by producing a shower of secondary particles and generally would lose nearly all of its energy by the end of the EM module, 30 cm in depth (total of 16 radiation lengths). The shower energy was sampled by the scintillator sheets, whose total light output was then proportional to the ionization in the module, which in turn was proportional to the energy deposited in the module. A hadron would generally start to shower in either the EM section or the FH section; energy would be deposited mainly in the FH section (3.8 nuclear absorption lengths) and shower leakage from FH would be absorbed in BH (3.7 absorption lengths). Light from all of the scintillators in each module was sampled by a waveshifter bar, whose light output travelled through an acrylic light pipe to a photomultiplier tube, where it produced an electrical signal. Analysis of the phototube pulse heights therefore permitted measurement of the energy carried by the final state photons, electrons, and charged and neutral hadrons striking the calorimeter.

The front face of the calorimeter was located 9.4 m downstream of the center of the hydrogen target and was 3.09 m × 2.29 m in size with a 0.65 m × 0.42 m rectangular hole in the center. The shape was chosen to match the acceptance of the spectrometer and to compensate for the magnet's horizontal smearing of charged particles.

The charged particle spectrometer was used in this analysis only to find the vertex. It consisted of thirty-four planes of proportional wire chambers (8500 wires), twenty-four planes of magnetostrictive spark chambers, and a superconducting analysis magnet. The magnet was used to distinguish positively and negatively charged particles and to measure their momenta by bending their paths horizontally. For this experiment, to limit smearing of our transverse momentum trigger, the magnet was operated at a reduced field; we used a current of 50 amps, corresponding to a change in p_x for each fast charged particle of about 0.2 GeV/c. The intent was to minimize both the number of particles bent into or out of the trigger aperture and the distortion of the paths of the triggering particles.

The hydrogen target was 45 cm long and was centered 1.4 m upstream of the magnet face. Two nuclear target foils were located at about $z = -1.19$ m and $z = -1.14$ m.

The geometrical acceptance of the apparatus -- the angular region defined by the initial trajectories of very high momentum secondaries that hit the calorimeter -- covered all azumuthal angles when the center-of-mass polar angle lay in the range $59° < \theta^* < 114°$, measured from the center of the hydrogen target. (The acceptance of the spectrometer alone was complete for $0° < \theta^* < 114°$). An overall acceptance equivalent to 2π azimuthal acceptance for $47° < \theta^* < 125°$ has been estimated, corresponding to $-0.65 < \eta^* < 0.84$, where η^* is the center-of-mass pseudorapidity, $\eta^* = 1/2 \ln((1+\cos\theta^*)/(1-\cos\theta^*))$. Acceptances measured from the nuclear target positions were smaller by about 2%. Figure 2-2 shows the positions at the front face of the calorimeter corresponding to $\theta^* = 45°$, $90°$, and $135°$.

2.4. Triggers

The calorimeter was used to trigger the MPS on events with high transverse energy. The trigger logic and the data acquisition system are described in Appendix A. The following is a less detailed look at the trigger, with some calorimeter design considerations.

In Chapter I, "particle transverse energy" (E_t) was defined as the sum, over all final state particles entering some aperture, of the particle energy times the sine of the angle the particle's path makes with the path of the beam particle. To compute this quantity accurately one must have good knowledge of the trajectories of all the particles in the aperture, neutral as well as charged. Accurately measuring the trajectory of one charged particle in time to trigger a detector is a challenge; accurately measuring the trajectory of a neutral particle at all is difficult; accurately measuring the trajectories of all charged and neutral particles of a high-multiplicity event to make a trigger is far beyond present feasibility.

What can be done for triggering purposes is to measure a quantity that approximates the particle transverse energy. For E557, each calorimeter module was set up to give a signal proportional to the total energy deposited in it multiplied by the sine of the angle between the center of the module and the incoming beam in the laboratory frame (a process described in Appendix B). The summed outputs of all the modules in some aperture is the "calorimeter transverse energy" (E_t^C) for that aperture.

The calorimeter transverse energy is a good approximation to the particle transverse energy if (1) all the particles in the aperture of interest enter the calorimeter, (2) the particles hit near the centers of the modules, (3) the particles leave nearly all their energy in the struck modules, and (4) the calorimeter accurately measures the energies deposited in it. Additionally, in order to be able to understand the event structure, one would like the probability that more than one particle will hit any module to be small. Obviously these conditions will never be fulfilled perfectly, but they suggest design criteria for the calorimeter and associated apparatus which will allow these conditions to be approximately fulfilled.

For example, there are two advantages to making each module as small as possible: the chance that two uncorrelated particles will strike the same module will be negligible, and the error in computing transverse energy due to assigning the angle of the center of the module rather than the actual particle angle will be small. On the other hand, if the modules are too small, a large fraction of the energy lost by a particle will leak into neighboring modules to be included in the E_t^C sum as separate "particles" at the centers of those modules. A balance of these considerations led to the division into modules of the EM and FH sections shown in Fig. 2-2. The smallest modules, 4" by 8" in size, are nearest the center where the particle flux is largest. (Note, however, that these central modules are the <u>largest</u> in terms of width in ϕ. In cos θ^* they are about as large as many other modules as well). Most of the modules are 8" by 8"; the outermost are 8" by 12".

Figure 2-3 shows the division of the BH section. It was more coarsely divided than EM and FH because it was intended only to measure the leakage from the back of FH, not individual final state particles. The large outer modules did not function properly in the Spring 1981 running period due to problems with the optical couplings to the phototubes, and were not used for triggering or analysis.

An interaction in the target region was detected by the coincidence of a beam particle traversing the target with either the absence of a charged particle in the beam path 8 meters downstream of the target, or the presence of several charged particles immediately downstream of the targets. The high-E_t triggers used in E557 required E_t^C to be above a threshold in some region of the calorimeter in coincidence with an interaction in the target region. Several trigger apertures in the calorimeter were used, but this analysis uses only "Global trigger" data, in which the threshold requirement was imposed on the E_t^C computed by summing over all the modules in the EM and FH sections and the smaller modules in the BH section. Thesholds from 6 to 17 GeV were used.

To obtain data at all available values of E_t^C the Global data were supplemented by data from runs in which there was no E_t^C threshold requirement, but only the target region interaction requirement; this was the "Interacting Beam" trigger.

2.5. Beam and targets

Due to the limited amount of beam time available in the Spring 1981 running period, only a 400 GeV/c diffractive proton beam was used. This gave a proton-proton center-of-mass energy of $\sqrt{s} = 27.4$ GeV. Flux at the MPS was 5×10^5 to 1×10^6 protons per pulse with four to six pulses per minute.

In each run there were three targets: liquid hydrogen and two nuclear targets. During the course of the running period five nuclear targets were used: two thicknesses of aluminum, two of copper, and one of lead.

2.6. Data set

Data were taken in a series of runs, with usually one thousand to five thousand events written to tape in each run. Global and Interacting Beam triggers were taken in separate runs, and the Global trigger threshold was changed only between runs. This analysis made use of all Global and Interacting Beam trigger runs from the Spring 1981 running period for which there were no known hardware problems capable of significantly affecting the results.

The data runs have been divided into four "run groups" corresponding to the four different configurations of nuclear targets that were used. These run groups are designated O, A, B, and P. (There were no Global trigger runs in group P). The materials, thicknesses, and positions of the nuclear targets for each run group are listed in Table 2-1.

Vertices were found and calorimeter energies computed in offline data processing (Appendix C). Any events for which the vertex-finding algorithm failed were discarded, as were events whose vertices lay outside the target region, $-1.75 < z < -1.05$. (Biases were thereby introduced which had to be corrected for in the analysis). Table 2-2 summarizes the data set for this analysis; shown for each run used are the run identification number, the number of events written to tape, and the number of events with vertices found in the "fiducial hydrogen target region" and the "nuclear target region". These two regions are defined to be -1.65 m $< z < -1.25$ m and $(z_1-2.6$ cm$) < z < (z_1+13.4$ cm$)$, respectively, where z_1 is the position in z of the upstream nuclear target, given in Table 2-1. The vertices were used in computing calorimeter energies from the phototube pulse heights (Appendix C).

In addition to the experimental data, I have used data from two Monte Carlo simulations: a Longitudinal Phase Space model (LPS), and a Quantum Chromodynamics/Gluon Bremsstrahlung model (QCD/Brem); these are described in Appendix D. Only proton-proton events were modelled in the simulations, and the vertices were distributed only in the fiducial hydrogen target region. There were 26,155 events in the LPS data and 75,925 events in the QCD/brem data.

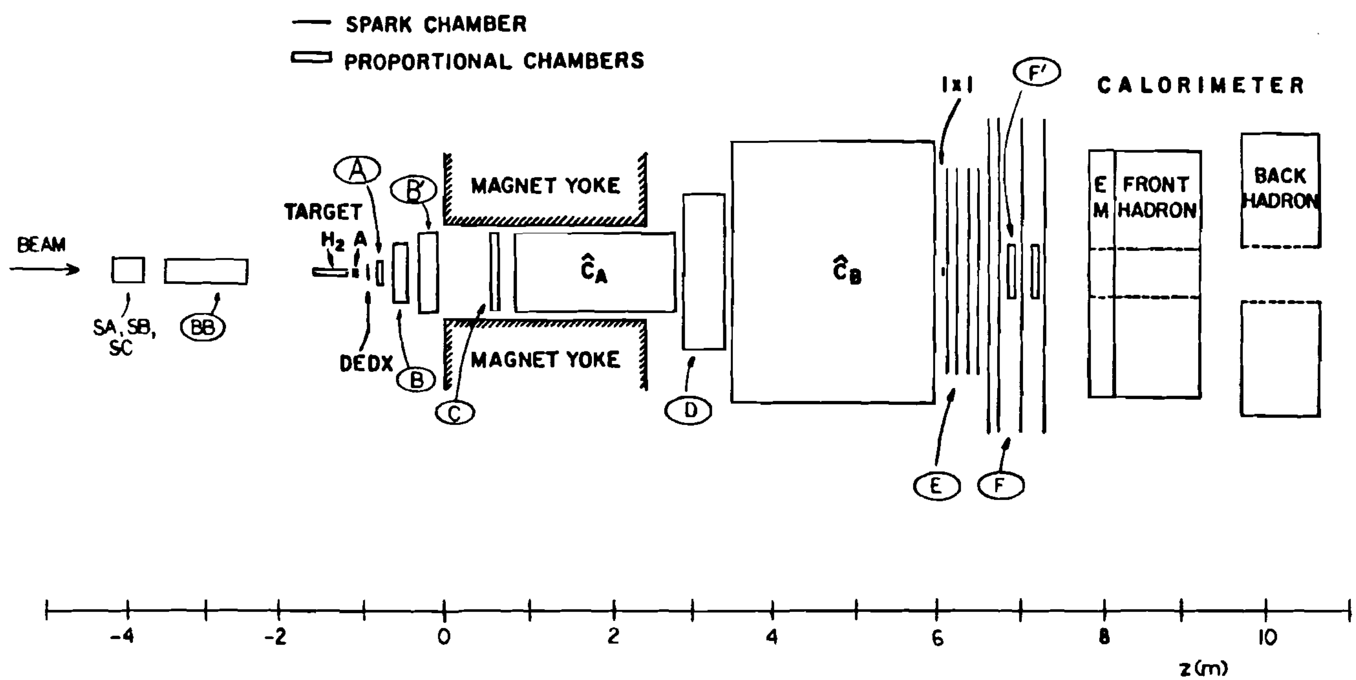

FIG. 2-1. Fermilab Multiparticle Spectrometer (plan view).

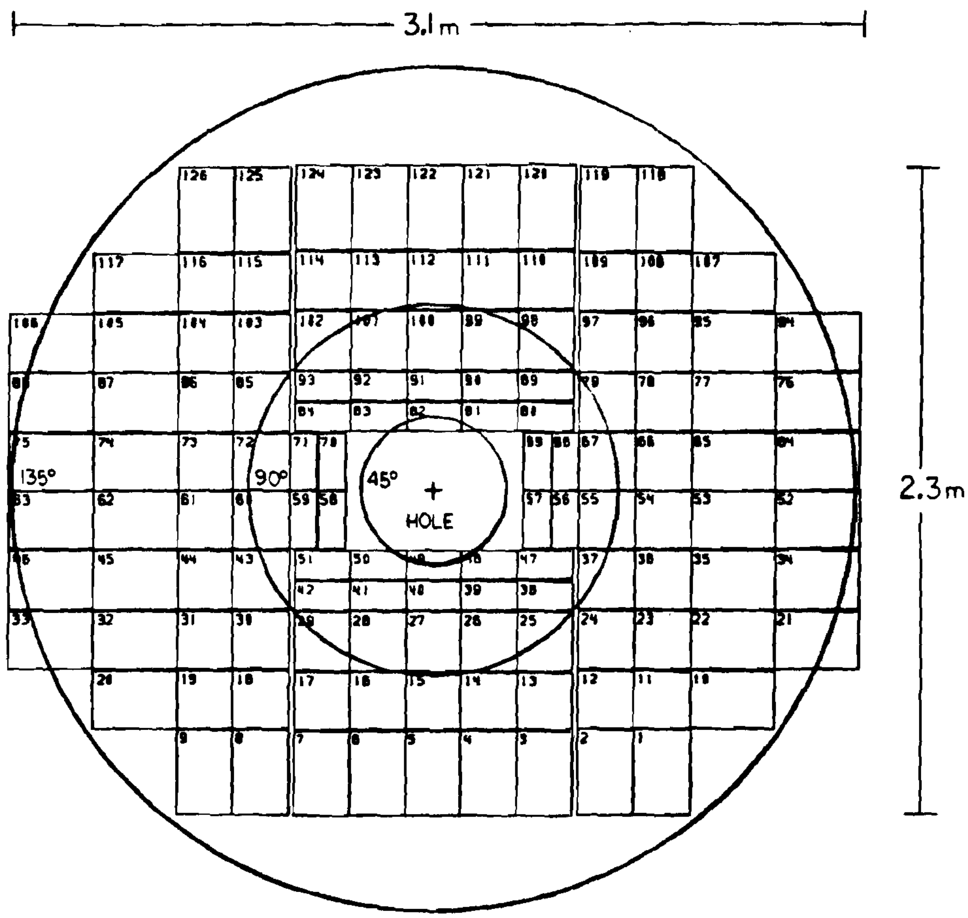

FIG. 2-2. Division of EM and FH calorimeter sections. The numbers shown identify the 126 modules in the EM section; each of the 126 FH modules was located directly behind an EM module with the same height and width, and was identified with the same number plus 130. Circles show the positions of center-of-mass polar angles $\theta^{*} = 45°$, $90°$, and $135°$ at the front face of the EM section.

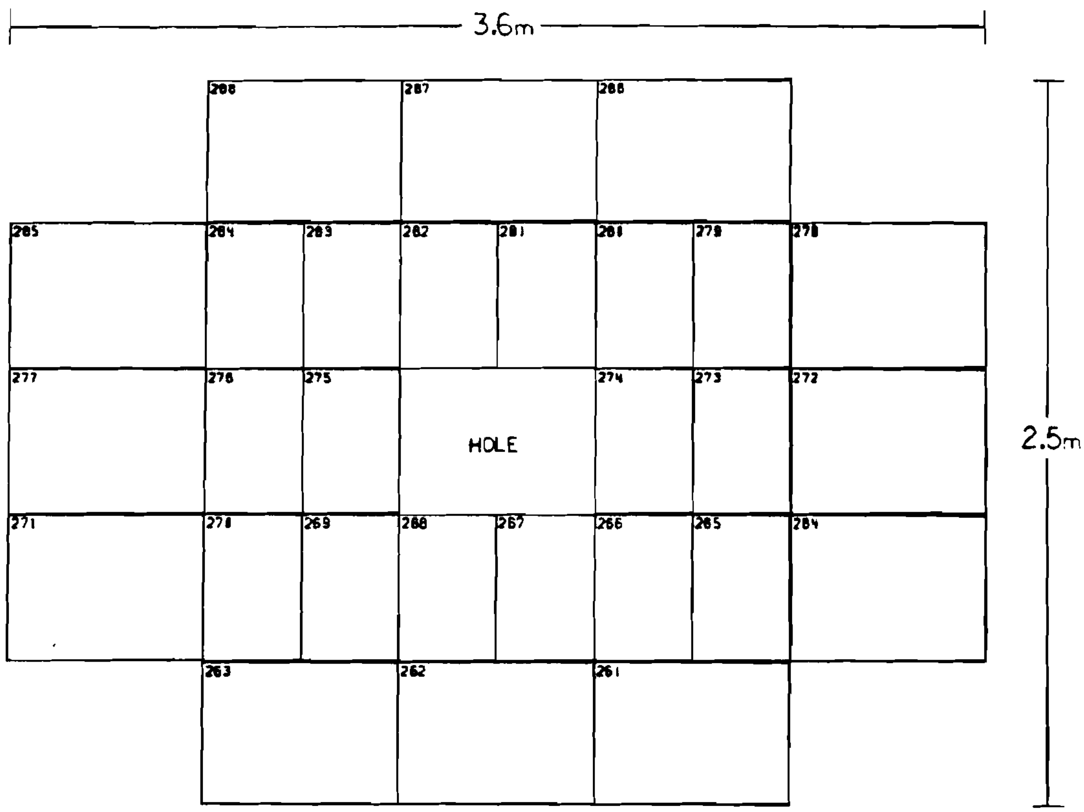

FIG. 2-3. Division of the BH calorimeter section. The 28 modules are identified by the numbers 261 to 288.

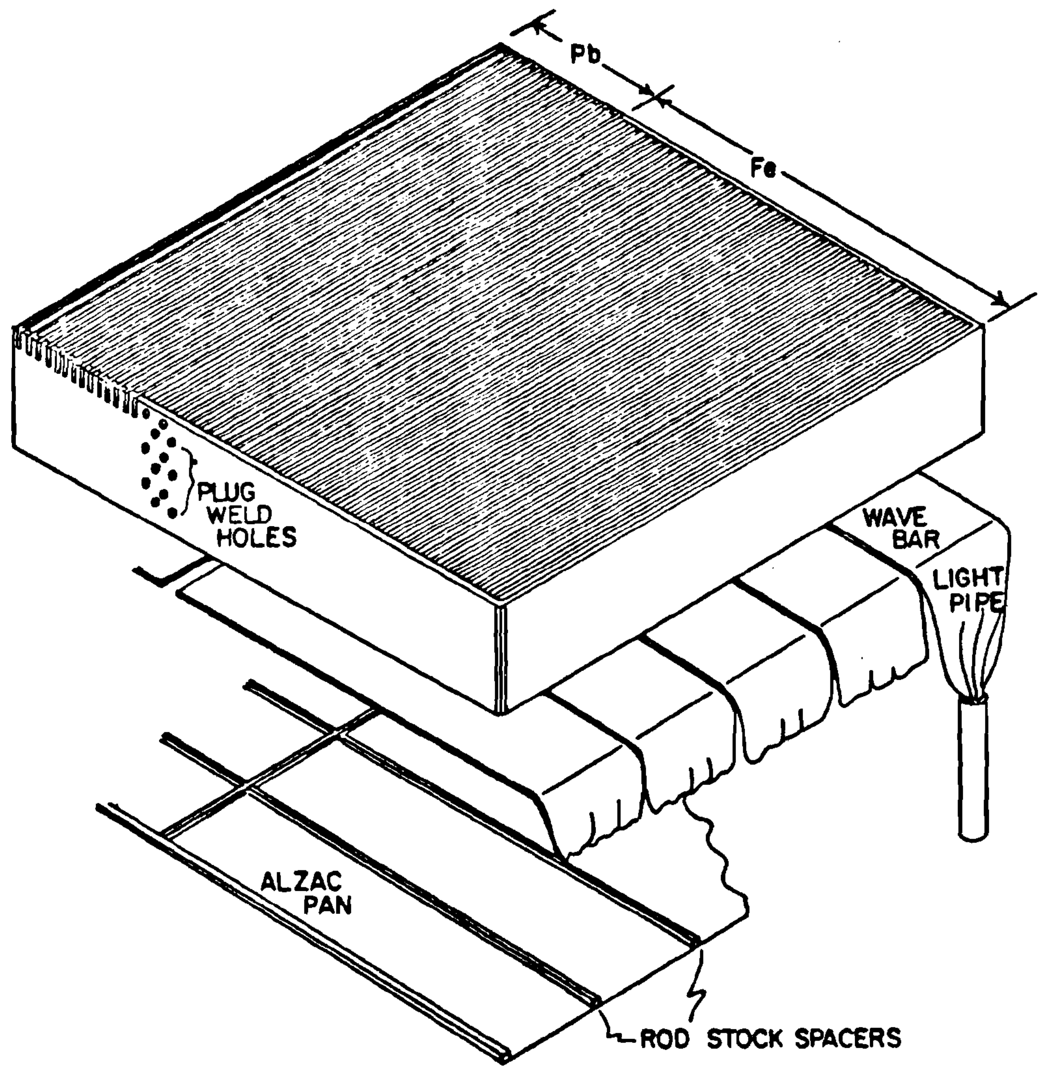

FIG. 2-4. Exploded view of a portion of the calorimeter, showing parts of five EM and five FH modules.

TABLE 2-1. Nuclear targets.

Run group	Material	Position (m from magnet face)	Thickness (m)
0	Pb	-1.194	1.53×10^{-4}
	Al	-1.144	7.94×10^{-4}
A	Cu	-1.189	3.97×10^{-4}
	Al	-1.139	7.94×10^{-4}
B	Pb	-1.188	1.53×10^{-4}
	Al	-1.138	2.56×10^{-4}
P	Cu	-1.186	0.74×10^{-4}
	Al	-1.136	7.94×10^{-4}

TABLE 2-2. Raw data set.

		Number of triggers		
Run Group	Run Number	Raw	Fiducial H_2 target region	Nuclear target region
		Interacting beam trigger		
0	589	6556	2710	233
	611	2077	1064	75
	613	1138	610	57
	614	1757	964	75
	Total	11528	5348	440
A	654	3509	1684	202
	670	1328	660	92
	679	1828	860	116
	693	1045	443	66
	696	2784	1438	209
	Total	10494	5085	685
B	744	4150	1982	137
	754	2843	1226	72
	761	4421	1959	131
	768	2292	981	68
	775	3258	1461	98
	780	5102	2302	155
	792	5142	1712	145
	Total	27208	11623	806

TABLE 2-2. (Continued)

Run Group	Run Number	Raw	Number of triggers: Fiducial H_2 target region	Nuclear target region
P	972	6075	2142	186
	979	8735	4455	380
	998	3055	645	168
	1003	4873	2280	177
	Total	22738	9522	911
Total		71968	31578	2842
		Global trigger		
0	591	1833	266	254
	592	1629	313	259
	593	12753	3130	1823
	619	2489	1304	201
	620	2015	966	181
	621	659	233	104
	622	1503	533	244
	625	638	146	183
	626	6156	1256	1439
	627	6890	1371	1658
	628	2689	375	618
	629	6455	1004	1519
	631	4952	792	1169
	632	1849	297	399
	Total	52510	11986	10051

TABLE 2-2. (Continued)

Run Group	Run Number	Raw	Fiducial H_2 target region	Nuclear target region
		Number of triggers		
A	663	3470	435	1289
	672	1354	127	420
	685	5451	775	2032
	686	2135	272	826
	688	18203	2491	5873
	Total	30613	4100	10440
B	772	2924	317	718
	783	1317	183	362
	784	4038	572	1159
	789	3841	588	1127
	794	5699	850	1330
	Total	17819	2510	4696
Total		100942	18596	25187
Grand total		172910	50174	28029

References for Chapter II

1. V. Ashford et al., Fermilab Proposal No. E557, 1977 (unpublished).
2. B. Brown, P. Devenski, S. Gronemeyer, H. Haggerty, E. Malamud, P. Rapp, R. Abrams, H. Goldberg, C. Halliwell, F. Lopez, S. Margulies, D. McLeod, J. Solomon, A. Dzierba, J. Florian, R. Heinz, J. Krider, J. Martin, D. Petersen, P. Smith, S. Teige, R. Ellsworth, R. Glasser, R. Holmes, L. Myrianthopoulos, H. Strobele, G. Yodh, A. Zieminski, S. Ahn, and T. Watts, Phys. Rev. Lett. 49, 711 (1982).
3. B. Brown et al., Phys. Rev. Lett. 50, 11 (1983).
4. B. C. Brown et al., Phys. Rev. D 29, 1895 (1984).
5. F. Lopez, Ph.D. dissertation, University of Illinois at Chicago, 1983.
6. S. Ahn, Ph.D. dissertation, Rutgers University (in preparation).

CHAPTER III

APERTURES AND RESOLUTION FUNCTIONS

To learn about the energy entering the calorimeter from a study of its outputs, one must understand the how the former is transformed into the latter in the calorimeter. If a given signal coming from a given module always corresponded to a particular energy entering the front of that module, life would be somewhat simpler. The real world is not so accommodating, and the following chapter is a description of my study of the E557 calorimeter and a discussion of the limitations imposed on my analysis of the E557 data due to complexities of the calorimeter response. I begin with a description of the five full-azimuth apertures I chose to work with in the physics analysis presented in Chapters IV and V. The remainder of this chapter documents a search for suitable calorimeter resolution functions.

3.1. Calorimeter apertures

Early results from E557[1] confirmed the finding of DeMarzo _et al._[2] that in the energy range of present fixed-target accelerators, proton-proton collisions selected with a full-azimuth, large-$\Delta\eta$ transverse energy trigger, such as the E557 Global trigger, are predominantly non-jetlike. Subsequently it was shown[3] that a small-$\Delta\phi$, large-$\Delta\eta$

transverse energy trigger selects events with short-range correlations stronger than those forced by the trigger or by kinematics; this has been interpreted as evidence of jet production.

This is in qualitative agreement with some theoretical speculations[4] suggesting that in events selected by a calorimeter trigger, the fraction which are jetlike should increase as the solid angle of the trigger aperture decreases. It therefore is of interest to study events in which large amounts of E_t^C are produced in apertures which are small in η rather than in ϕ.

A map of the front face of the E557 calorimeter in a projection where curves of constant ϕ and curves of constant cos θ^* are straight lines (Fig. 3-1) quickly convinces one that this piece of apparatus was not designed to be divided into bands in pseudorapidity. I have, nevertheless, divided the calorimeter into approximations of such bands. In deciding on boundaries, I used two main criteria:

- The bands should have reasonable shapes in cos θ^*-ϕ space. One cannot draw boundaries that do not deviate substantially from lines of constant cos θ^*, but I have attempted to minimize their jaggedness.
- The division should be approximately symmetric under rotations in ϕ and reflections in cos θ^*.

The divisions selected are shown in Fig. 3-2 (x-y space) and Fig. 3-3 (cos θ^*-ϕ space). Figures 3-2a and 3-3a show the calorimeter divided into three large bands, labelled 1, 2, and 3 from the innermost to outermost. Note that the two EM modules closest to the center, and the FH modules behind them, are excluded from band 1, in order to make bands 1 and 3 nearly equal in acceptance and symmetric in position.

Figures 3-2b and 3-3b show a band approximately centered on $\theta^* = 90°$, labelled 4, which is wider than band 2.

The five apertures selected for this analysis are:

- Global -- All modules in EM, FH, and BH calorimeters
- A-Global -- (A for "Almost") All EM and FH modules in bands 1, 2, and 3.
- B2/3 -- All modules in a region corresponding approximately to the backward two-thirds of the calorimeter, bands 2 and 3.
- F2/3 -- All modules in a region corresponding approximately to the forward two-thirds of the calorimeter, bands 1 and 2.
- M1/2 -- All modules in a region corresponding approximately to the middle one-half of the calorimeter, band 4.

Note that BH is used only for Global, since its larger modules cannot be matched to these apertures. Acceptances for the five apertures and their regions of overlap are given in Table 3-1. These acceptances are for particles entering the EM modules only; slant entries into FH through the hole and entries into the BH calorimeter will very slightly increase the effective acceptances of all but B2/3 and M1/2. Computation of acceptances does take into account shadowing by the magnet aperture. In terms of widths in pseudorapidity the acceptances are: Global, $\Delta\eta = 1.49$; A-global, $\Delta\eta = 1.35$; B 2/3, $\Delta\eta = 0.84$; F 2/3, $\Delta\eta = 0.88$; and M 1/2, $\Delta\eta = 0.73$.

The F2/3 and B2/3 apertures cover nearly symmetric regions of acceptance with respect to front-back reflection (Fig. 3-4).

3.2. Necessity of understanding the resolution function

In principle, the response of the calorimeter to an isolated incoming particle depends on (1) the energy of the particle (2) its identity (hadron, muon, electron, or gamma) (3) the entry point and (4) the entry angle. Whether the particle came from a high-p_t quark-quark scatter or a low-p_t interaction or, for that matter, a secondary interaction in the Cerenkov counters is unimportant.

A major difficulty arises, however, when one tries to understand events as opposed to particles. In an event, particles are in general not isolated and one cannot disentangle individual particle signals in the calorimeter with any great reliability on an event-by-event basis. One therefore tries to use the entire set of calorimeter signals to characterize events as a whole. To do so, one wants to construct a resolution function, $R(E_t^C;\alpha)$, which is the probability function for a calorimeter transverse energy E_t^C given an input event described by a set of parameters denoted by α.

For an imaginary perfect-resolution calorimeter, one whose output voltages are proportional to E_t with perfect accuracy, $R(E_t^C;\alpha)$ would be a Dirac delta function, $\delta(E_t^C-E_t)$. A slightly less imaginary device, a "perfectly uniform E_t calorimeter," would be one with granularity much finer than the scale of the event structure, whose outputs are subject to fluctuations, but whose response function is exactly the same for all particle entry points and angles and which literally samples E_t, not E weighted by the sine of the angle to the modules' centers. Such a calorimeter would give a resolution function with nonzero mean and width, but the shape of this resolution function would depend only on

E_t. For such a calorimeter, the set of parameters α used to define R would consist solely of E_t. One could not determine, given the observed E_t^C for an event, what the true E_t was on an event by event basis, but it could be done statistically. That is, given only output E_t^C spectra, one could estimate E_t spectra. If the resolution function $R(E_t^C;E_t)$ were the same regardless of the nature of the mechanism which produced the events measured by the calorimeter -- if, as one would hope, R really told us only about properties of the calorimeter -- then one would have

$$\frac{d\sigma}{dE_t^C} = \int_0^\infty \frac{d\sigma}{dE_t} R(E_t^C;E_t)\, dE_t \tag{3-1}$$

and by inverting this equation one could estimate $d\sigma/dE_t$ from $d\sigma/E_t^C$.

Real-world calorimeters -- and their simulations -- are more difficult to deal with. The E557 calorimeter did not have ultrafine granularity; its response was not identical for all entry points and angles; energy could leak through the central hole, the sides, and the back; several modules were defective during the run. Moreover, like all real calorimeters, it responded to energy, not transverse energy. Therefore the response of the calorimeter in general depended on the energies, identities, entry points, and entry angles of all the particles, and one may not be able to make a reliable determination -- even in a statistical sense -- of, for example, transverse energies of the incoming particles summed over the global aperture knowing only the global sum of the calorimeter output signals. In fact, 5 GeV E_t (global sum for actual particles) events arising from hard quark-quark scatters in general cannot be expected to look like 5 GeV E_t events arising from soft collisions -- there may be more, or fewer, particles in the final state striking the face of the calorimeter; more, or fewer, cases of two or more particles in a single module; more, or fewer, particles near 90° in the center of mass as compared to those at smaller angles; more, or fewer, 'slant' entries into the sides of the central hole; and so on. Thus, for a real, nonuniform calorimeter, there is no reason to expect 5 GeV E_t events of one class to give rise to the same global sum of calorimeter signals as that from 5 GeV E_t events of the other class. $R(E_t^C,E_t)$ will be "production mechanism dependent." To get a resolution function which is production mechanism independent one must deal with additional parameters of the event. One may be able to use, for example, the outputs of a subset of the calorimeter modules to subdivide the data into groups within which R might, to good accuracy, be a function only of E_t. In such a case, a good estimate of the true E_t spectrum can still be extracted. Failing that, one procedure would be to devise a resolution function that depends on additional parameters describing the particles entering the calorimeter, and then to measure these parameters for the experimental data using the apparatus upstream of the calorimeter.

3.3. Production mechanism dependence

I have studied the calorimeter response by using the results of two Monte Carlo simulations: the QCD/Bremsstrahlung model and the Longitudinal Phase Space (LPS) model (described in Appendix D). The function $R(E_t^C;E_t)$ is computed from the Monte Carlo data as follows: a scatterplot (that is, a two-dimensional histogram) is made of E_t^C versus E_t. Each bin of such a plot represents a measurement of the double differential $d^2\sigma/dE_t^C dE_t$, integrated over the bin. $R(E_t^C;E_t)$ is just

$(d^2\sigma/dE^C_t dE_t)/(d\sigma/dE_t)$. So

$$\int_0^\infty R(E^C_t;E_t)\, dE^C_t = \frac{\int_0^\infty (d^2\sigma/dE_t dE^C_t)\, dE^C_t}{d\sigma/dE_t} = 1 \tag{3-2}$$

and

$$\int_0^\infty \frac{d\sigma}{dE_t} R(E^C_t;E_t)\, dE_t = \int_0^\infty (d^2\sigma/dE_t dE^C_t)\, dE_t = \frac{d\sigma}{dE^C_t} \tag{3-3}$$

as required. If the scatterplot bins are narrow enough in both E_t and E^C_t, then C_{ij}, the content of the bin in the neighborhood of (E_{ti}, E^C_{tj}) is approximately $R(E^C_{tj},E_{ti})\Delta E_{ti}\Delta E^C_{tj}$, and one can take appropriately normalized values of the scatterplot as approximate measurements of $R(E^C_t,E_t)$. One can then check $R(E^C_t;E_t)$ for production mechanism dependence.

The expected dependence is observed and is significant (Fig. 3-5). In fact, resolution functions obtained from scatterplots made with event weights differ from those obtained using the same data but without weights. The calorimeter's response to a class of events should not depend on the weights attached to those events; this is just another instance of production mechanism dependence (or more accurately, production spectrum dependence), and again it arises because the calorimeter response is not simply a function of E_t.

3.4. Additional parameters

A production mechanism independent parametrization of the calorimeter resolution therefore requires that one use other parameters in addition to, and perhaps in place of, E_t.

At this point it is useful to consider the various causes for the differences between E_t and E_t^C. The most important ones are:

- Calorimeter response fluctuations.
- Granularity.
- 'Bad' (malfunctioning) modules.
- Leakage of various sorts: transverse and longitudinal; module-to-module, module-to-air, and air-to-module.

The first of these is really a major component of the production mechanism independent behavior of the calorimeter being studied. The same simulation of the calorimeter is used in both Monte Carlos, so the behavior of the fluctuations is the same for both.

'Granularity' refers to the fact that I multiply the calorimeter energy from a module by the angle subtended at the vertex between the beam and the center of the module in computing transverse energy, whereas the actual angles of the secondaries are distributed over the module and its neighbors; in fact the average actual angle is generally not the same as the central angle. Monte Carlo studies indicate that granularity is not a dominant cause of transverse energy shifts.

The Monte Carlo computes responses for all modules, but to simulate our experiment some modules can be turned off in the analysis -- notably the large BH modules, but also some five EM and FH modules. Therefore Monte Carlo studies of bad module effects are straightforward.

The most difficult item in this list is leakage. The Monte Carlo data tapes I used contain information on particle energies and module energies, but no direct indication of how much energy in each module was deposited by each particle. Thus there is no direct measure of leakage. (A definition of "leakage" is in order. It turns out to be simplest for my Monte Carlo studies to define the "track (transverse) energy" for a given aperture as the sum of (transverse) energies of the tracks entering the EM modules in that aperture, regardless of whether they entered through the front face or through the sides of modules bordering on the hole. Tracks entering FH modules via the hole, or BH modules, are not counted in the track (transverse) energy sums. Therefore, by "leakage" I mean any energy entering or leaving a module other than in the form of particles from the upstream of the calorimeter entering the EM modules. This includes shower energy leaving one module and entering another (transversely or longitudinally), shower energy leaving a module and escaping from the calorimeter (again, transversely or longitudinally), and particles entering the FH or BH calorimeters directly).

Note the following: (1) Leakage between two good modules both in a given aperture will not contribute to an energy shift in that aperture. It will, however, contribute to a transverse energy shift, because energy belonging to one module will be assigned the angle of the other. (2) Because the Global aperture includes the BH calorimeter, longitudinal leakage for this aperture should be small. (3) Because the Global aperture involves all modules, the types of transverse leakage corresponding to an energy shift are: between good and bad modules; into the modules in the ring bordering the hole (so-called 'ring modules'); and out of ring modules. Energy leakage out of modules bordering the outer edge of the calorimeter is small because the energy deposited there in the first place is small. Of course, at the outer boundary $\sin\theta$ is large, so there could in principle be significant transverse energy leakage at the outer boundary.

In order to isolate effects of leakage, in and out, at the ring and the outer boundary, I have studied the quantity $\Delta E = E - E^G$, where E^G is the same as E^C but with all modules considered 'good'; that is, no module responses were set to zero to simulate bad modules. Figure 3-6 shows the distribution of ΔE in the LPS and QCD/brem Monte Carlo data. I divided the events into three classes according to whether ΔE was large and negative (< -15 GeV), large and positive (> 15 GeV) or small (-15 GeV < ΔE < 15 GeV). For each class of events and each EM and FH module I computed the average energy measurement for the module, divided by the global calorimeter energy. Figures 3-7a to 3-7c show the results for the LPS Monte Carlo data; QCD/brem results are in Fig. 3-8. The figures represent the lower right quadrant of the calorimeter; the other three quadrants give the same results. The number displayed in each module just below the EM module number is the average percentage of the Global energy that was contributed by that module. For example, if E_i^C is the energy measured in module number i, then the number underneath the '49' in module 49 is 100 times $r_{49} = \langle E_{49}^C/(\sum_i E_i^C)\rangle$, where the sum is over the Global aperture modules in the EM section. The next number is the corresponding quantity for the corresponding FH module (100 r_{179}), and the final number is the corresponding quantity for dualmods (summed pair of EM and FH modules; 100 r_{49+179}).

The results for both Monte Carlos are similar. For the modules which have a surface on the inside of the hole, the average energy response of the module as a fraction of the global sum varies significantly with ΔE. Compensating differences are spread among the rest of the modules and are relatively small on a per-module basis.

(Similar results are seen when percentages of transverse energy are computed, or when events are classified by transverse energy shift. The latter studies indicate that transverse energy leakage at the outer boundary is relatively small).

The twenty 'ring' modules -- EM modules 48, 49, 50, 57, 58, 69, 70, 81, 82, and 83, and the corresponding FH modules -- may be subdivided into two types, EM and FH, and two positions, 'x' (left and right of the hole) and 'y' (above and below), making in total four subdivisions. The following correspondence between energy shift and the ratios r_i for these modules may then be noted:

- For $\Delta E < -15$ GeV, compared to -15 GeV $< \Delta E <$ 15 GeV, r_i is:
  - about the same for EM ring modules
  - substantially larger (by 50%-100%) for FH ring modules.
- For $\Delta E >$ 15 GeV, compared to -15 GeV $< \Delta E <$ 15 GeV, r_i is:
  - larger for EM ring modules, more so for 'y' modules than for 'x' modules
  - substantially larger for FH ring 'y' modules, slightly larger for FH ring 'x' modules.

Apparently a major component of ΔE is leakage at the hole. Large positive ΔE means a large amount of energy has leaked out; this tends to occur in events where large amounts of energy entered the front face of the ring modules. The energy that did not leak contributes to higher than average responses in EM and FH ring modules. Large negative ΔE means a large amount of energy has leaked in; that is, particles have entered FH and BH modules through the hole, contributing to larger than usual responses in FH, but not EM, ring modules.

These data suggest that the energy measurements in the ring modules might make a suitable set of parameters for a subdivision of the data into groups within which the resolution function depends only on E_t. I studied the dependence of the behavior of the calorimeter on quantities which are sums of the above r_i's over the four subdivisions of the ring, denoted by $r_{x/EM}$, $r_{y/EM}$, $r_{x/FH}$, and $r_{y/FH}$. Figures 3-9a to 3-9d show mean values of these quantities as functions of ΔE for the QCD/brem Monte Carlo. $\langle r_{x/EM} \rangle$ and $\langle r_{y/EM} \rangle$ rise approximately linearly with ΔE; $\langle r_{x/FH} \rangle$ and $\langle r_{y/FH} \rangle$ both fall as ΔE increases to zero, but for $\Delta E > 0$, $\langle r_{x/FH} \rangle$ stays nearly constant while $\langle r_{y/FH} \rangle$ increases.

These differences in the behavior of these quantities suggest that at least three of the four need to be considered separately -- that to separate events into groups for which $R(E_t^C, E_t)$ is production mechanism independent, slicing on a single quantity derived from the responses of the ring modules will be insufficient. I have compared ΔE in the two Monte Carlos with and without cuts on the four r's. As shown in Figs. 3-10a to 3-10d, the distribution of each of the four r's falls approximately exponentially, which implies that fairly stringent cuts are needed. Figures 3-11a and 3-11b show the distribution of ΔE in the LPS and QCD/brem models, respectively, for events where the global energy sum is between 120 GeV and 240 GeV. The following cuts then were applied:

$$0.04 < r_{x/EM} < 0.08$$

$$0.14 < r_{y/EM} < 0.18$$

$$0.00 < r_{x/FH} < 0.04$$

$$0.04 < r_{y/FH} < 0.08.$$

The distributions of ΔE after these cuts are shown in Figs. 3-12a and 3-

12b. The two Monte Carlos now give the same results, within the error bars -- which are enormous because of the severe degradation of the statistics: after the cuts only 25 QCD/brem events and 14 LPS events remain, out of 31,908 and 11,007, respectively. The cuts on r were chosen to be near the peaks of their distributions; most other slices would contain even fewer events.

This illustrates the problem with the proposed procedure: it is infeasible with the available statistics. As an example, if one must separate events according to three different variables -- say, $r_{x/FH}$, $r_{y/FH}$, and a linear combination of $r_{x/EM}$ and $r_{y/EM}$, and if one takes n slices in each variable, one must deal with n^3 separate sets of distributions to be corrected separately and recombined. Five slices for each variable means a total of 125 subdivisions of the data. Not only is this a great complication, but the meager statistics of the E557 Spring 1981 data set would be so much further reduced in each subdivision as to make meaningful analysis virtually impossible. Even the Monte Carlo data, as we have seen, cannot survive narrow slicing on several variables.

3.5. Compromise: $R(E_t^C;E_t)$

I was unable to find a way to construct a production mechanism independent resolution function given the data available. The function $R(E_t^C;E_t)$, while production mechanism dependent, is better than nothing. I decided to use $R(E_t^C;E_t)$ as computed from Monte Carlo data that, in some sense, are the best available simulation of the experimental data.

As will be seen in the following chapters, neither of the Monte

Carlos described in Appendix D represent the experimental data very well: the event structure in the experimental data falls between the LPS and QCD/brem extremes. I therefore have constructed a "Hybrid Monte Carlo" data set, consisting of the combined LPS and QCD/brem events. Operationally, a Hybrid Monte Carlo histogram is generated by summing the corresponding LPS and QCD/brem histograms, each of which is scaled by a weighting factor chosen to minimize the mean square difference between the Hybrid and experimental global $d\sigma/dE_t^C$. The scaling factors for the LPS and QCD/brem events were 0.43 and 1.30, respectively.

The Hybrid data are dominated by QCD/brem events at high E_t^C. Because the spectral slope of the QCD/brem global E_t^C spectrum is quite different from that seen in the experimental data, the Hybrid global E_t^C spectrum fits the latter very badly at high E_t^C. It should not be taken seriously as a physics model of the real events.

3.6. Parametrization of the resolution functions

Separate resolution functions were used for each of the five apertures. Rather than using normalized contents of E_t^C versus E_t scatterplots directly as measurements of the resolution functions, I chose to use parametrizations of these data. Clearly, since E_t^C must be non-negative, $R(E_t^C;E_t)$ must have an endpoint at $E_t^C = 0$. However, for fixed E_t larger than about 1 GeV, $R(E_t^C;E_t)$ is found to be nearly Gaussian, within the errors dictated by the weights and statistics of the Monte Carlo data. I therefore have used the parametrization

$$R(E_t^C;E_t) = \frac{N(E_t)}{\sqrt{2\pi\sigma^2(E_t)}} \exp\left[-(E_t^C-\mu(E_t))^2/2\sigma^2(E_t)\right], \quad E_t^C \geq 0$$

$$= 0, \qquad E_t^C < 0 \tag{3-4}$$

where $N(E_t)$ is given by the normalization condition (3-2), and $\mu(E_t)$ and $\sigma^2(E_t)$ are quadratics in E_t:

$$\begin{aligned} \mu(E_t) &= M_1E_t^2 + M_2E_t + M_3 \\ \sigma^2(E_t) &= S_1E_t^2 + S_2E_t + S_3 \end{aligned} \tag{3-5}$$

The M_i's and the S_i's were determined by separate fits to the mean and variance of E_t^C as functions of E_t from the Hybrid Monte Carlo data. To do these fits required knowledge not only of the means and variances of E_t^C, but also of the variances of these means and variances. These were computed from the Monto Carlo data, wherein different events enter with different weights. A discussion of the statistics of weighted events, and derivations of the appropriate formulas, may be found in Appendix E. The results of the parametrizations are given in Table 3-2.

3.7. Limitations

Clearly, the resolution functions I have constructed are far from perfect. The production mechanism dependence is only one problem. Another is with the simulation of the apparatus. There is no simulation of secondary interactions between the vertex and the calorimeter. The calorimeter modules are modelled, not as sandwiches of scintillator and steel or lead, but as uniform blocks of the same total number of interaction and radiation lengths. Showers are not modelled at a microscopic level, but as average showers corresponding to the energies and types of the initiating particles. Fluctuations in the shower development are not modelled.

Most of these deficiencies affect low-energy tracks most. A low-energy hadron in the real calorimeter, for example, whose energy is entirely absorbed in the first layer of absorber and is therefore lost would in the model give rise to a shower and be detected. Another shortcoming of the simulation is that shower widths are assumed to be independent of energy whereas in fact they decrease as energy increases; again, low-energy tracks are treated less correctly than high energy ones.

We therefore can expect the simulation to be least accurate for low-E_t events -- as is the Gaussian parametrization of the resolution functions. The implication is that Monte Carlo data at low E_t^C, resolution functions at low E_t, and the low ends of the corrected transverse energy scales are the least reliable. The resolution functions and corrected transverse energies at high E_t are more trustworthy, but, due to the production mechanism dependence of the resolution functions, only to the extent that the Hybrid events simulate real events closely enough.

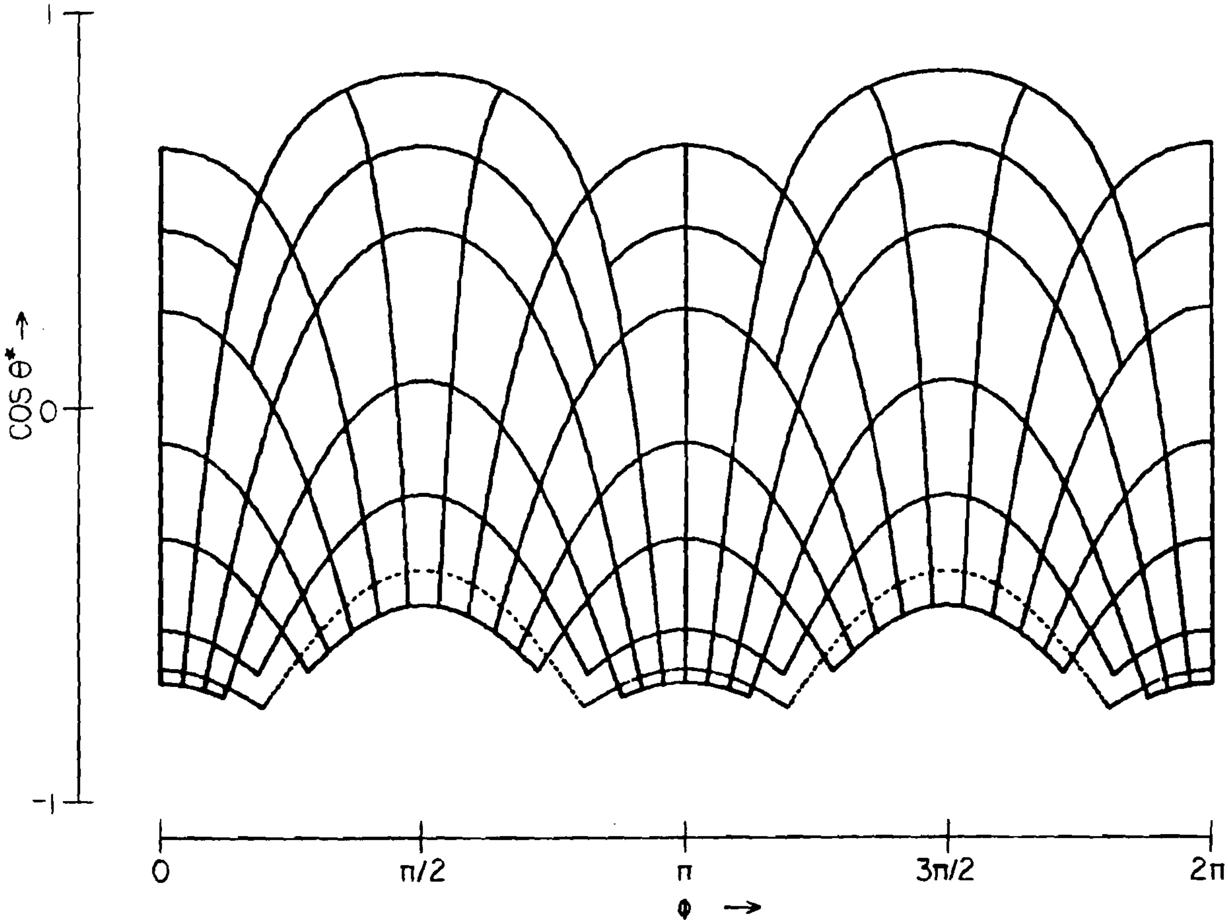

FIG. 3-1. Front face of E557 calorimeter, drawn in cos θ^* - ϕ space: curves of constant cos θ^* are straight horizontal lines; curves of constant ϕ are straight vertical lines. Modules adjacent to center hole are at top. Modules on outer boundary are at bottom. Dotted line indicates magnet aperture.

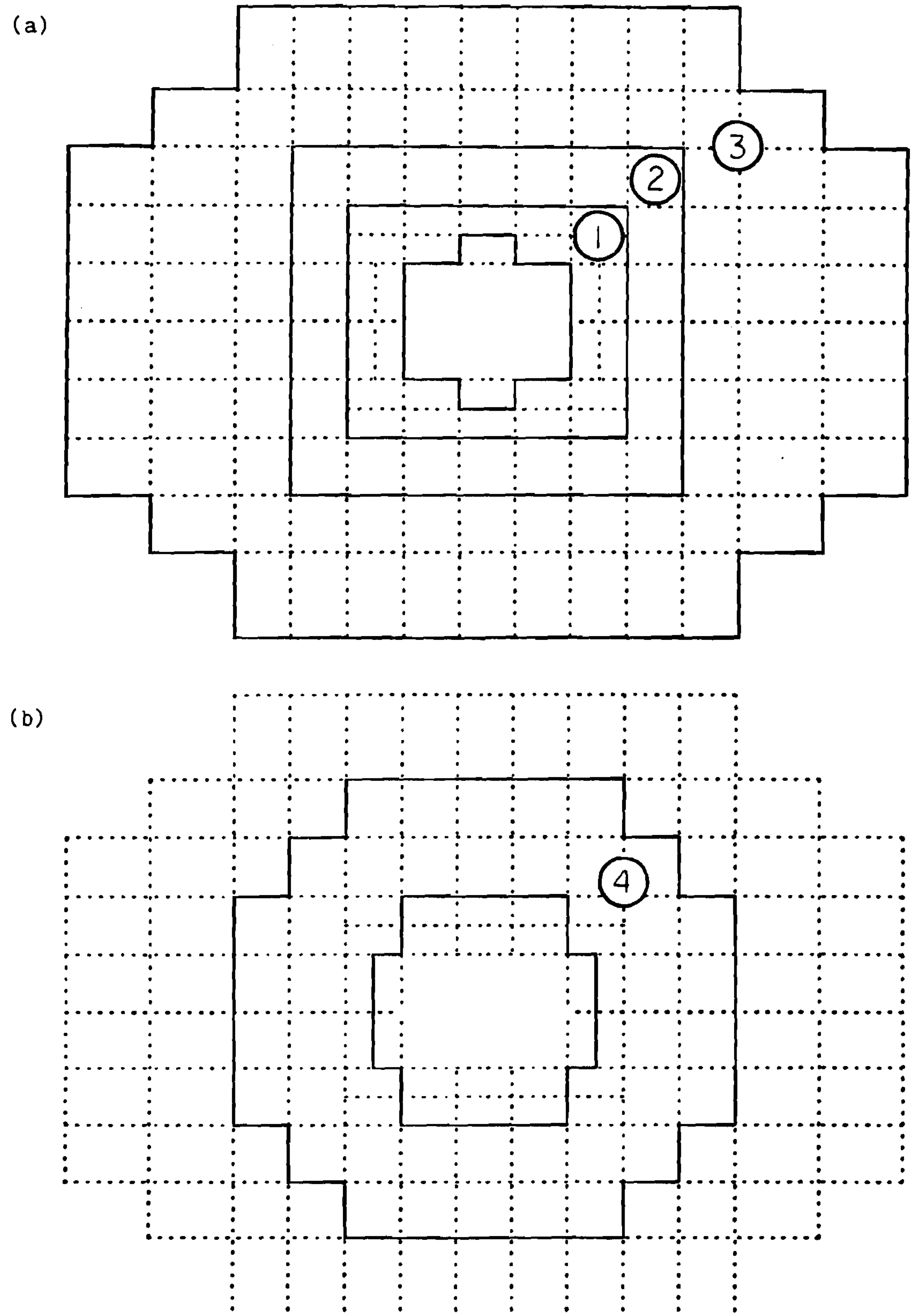

FIG. 3-2. Subdivisions of the calorimeter, in x - y space.

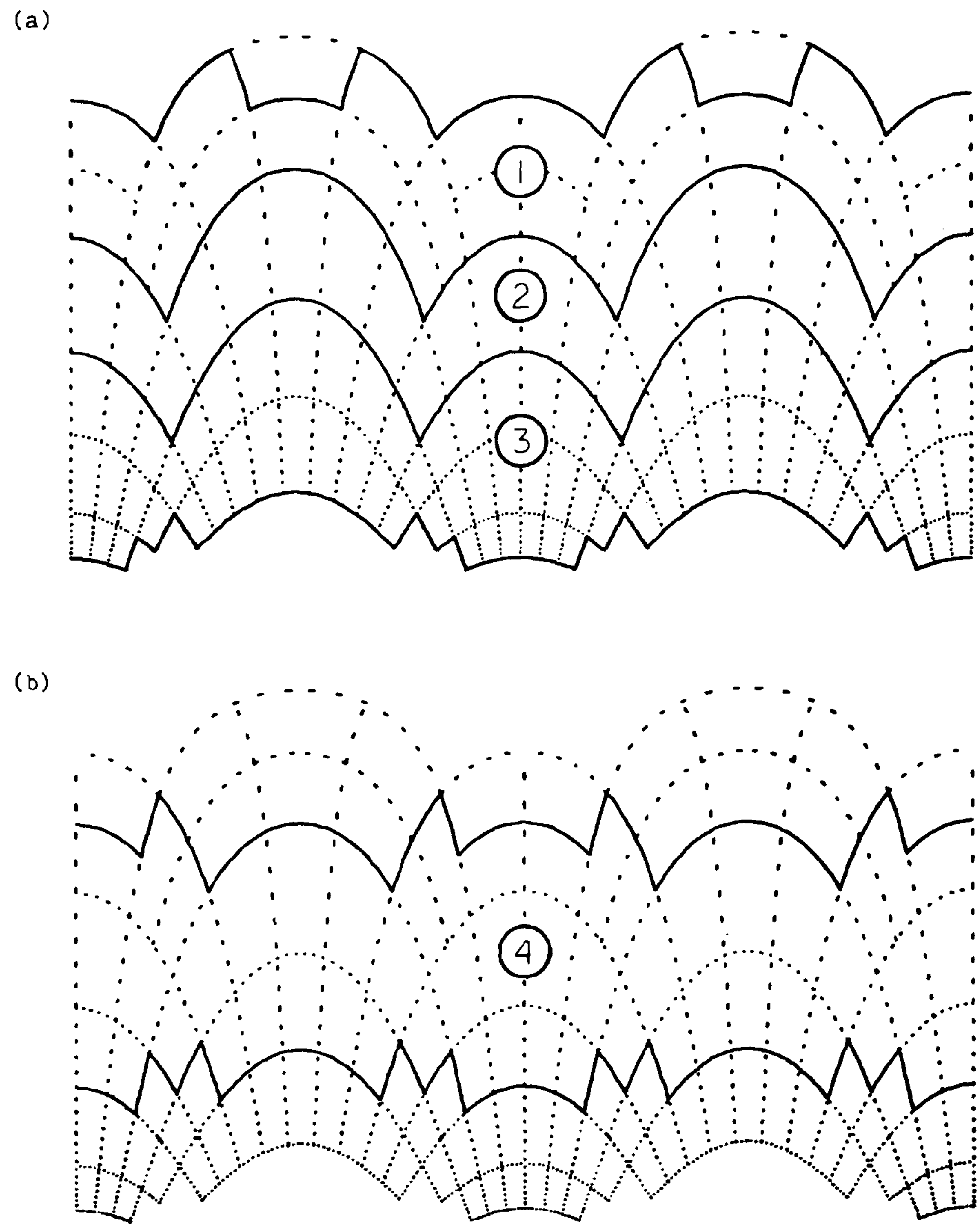

FIG. 3-3. Subdivisions of the calorimeter, in cos θ^* - ϕ space.

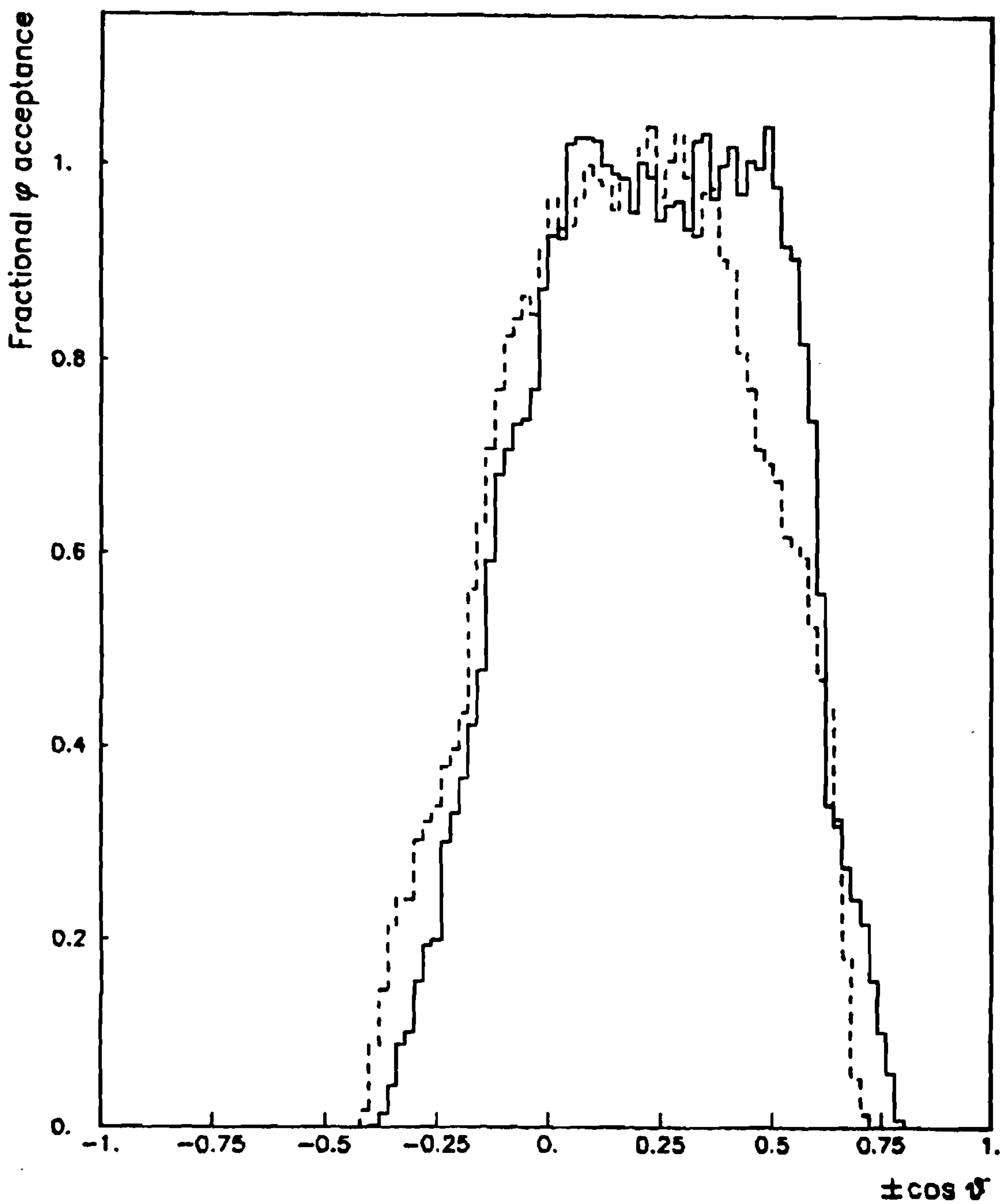

FIG. 3-4. Fraction of full 2π acceptance in ϕ as function of: $\cos\theta^*$, for F 2/3 aperture (solid line); $-\cos\theta^*$, for B 2/3 aperture (dashed line).

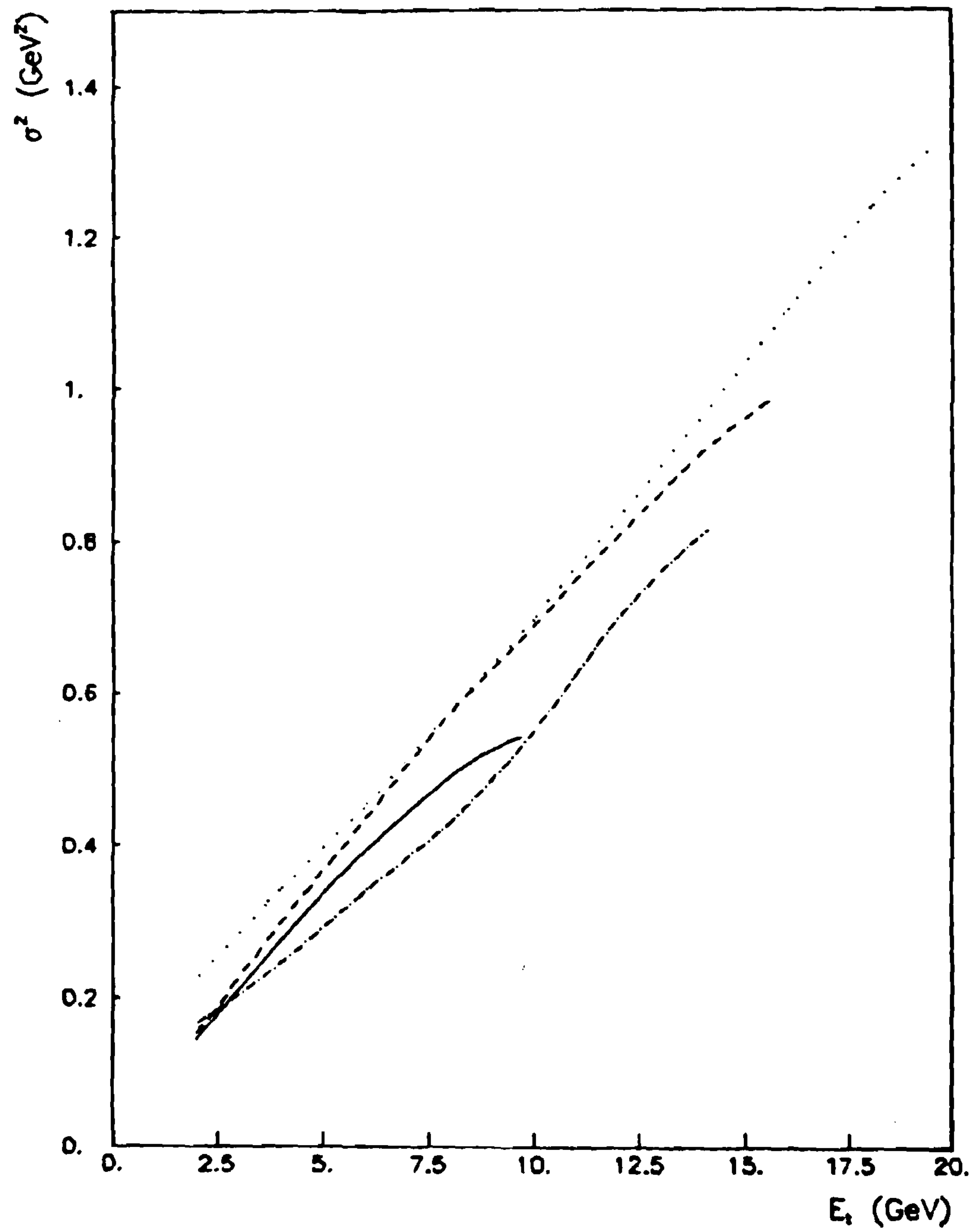

FIG. 3-5. Variance of $R(E_t^C;E_t)$ versus E_t, Global aperture, for four models: LPS with event weights (solid line), LPS without event weights (dashed line), QCD/brem with event weights (dot-dashed line), and QCD/brem without event weights (dotted line).

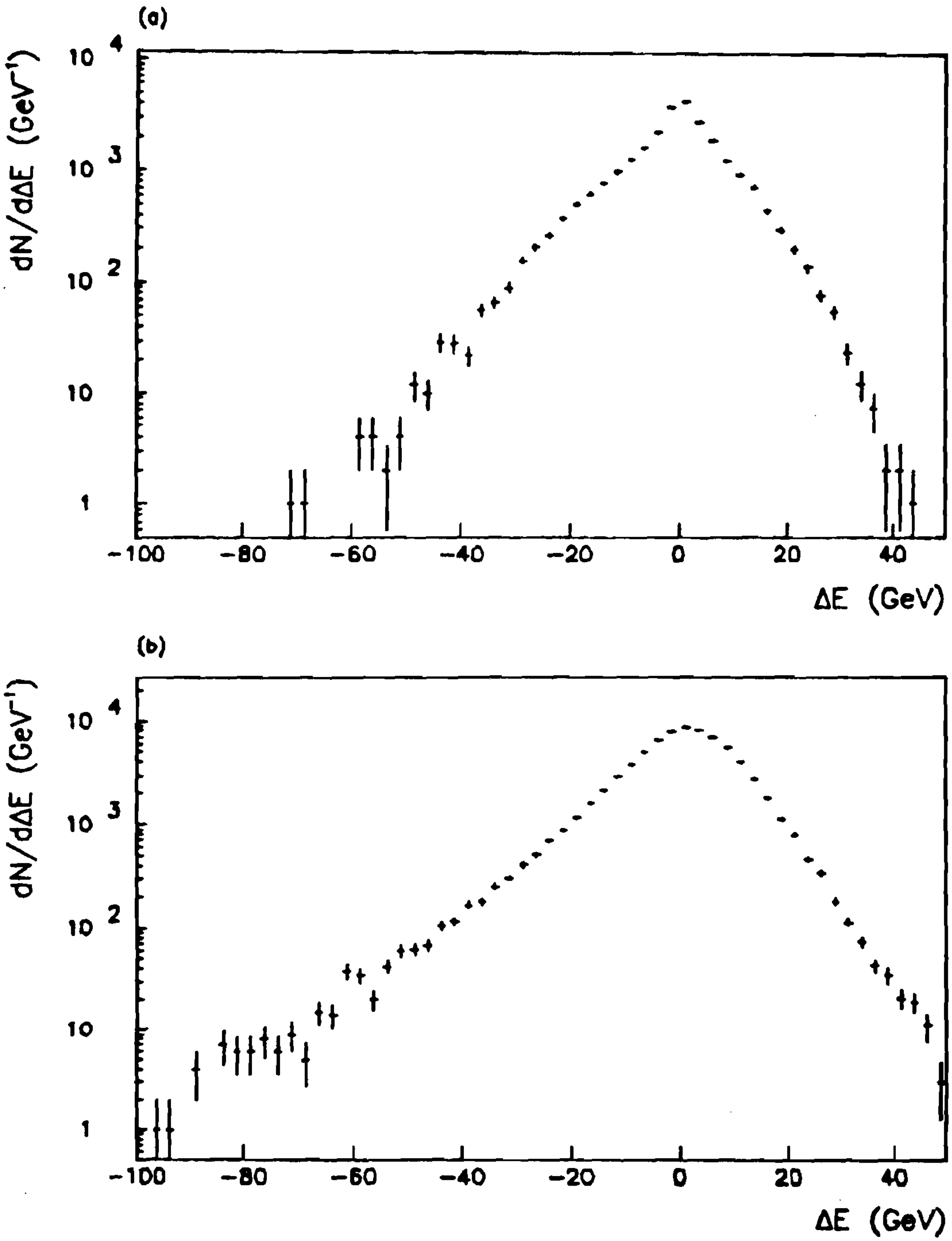

FIG. 3-6. Distribution of ΔE for all events. (a) LPS model. (b) QCD/brem model.

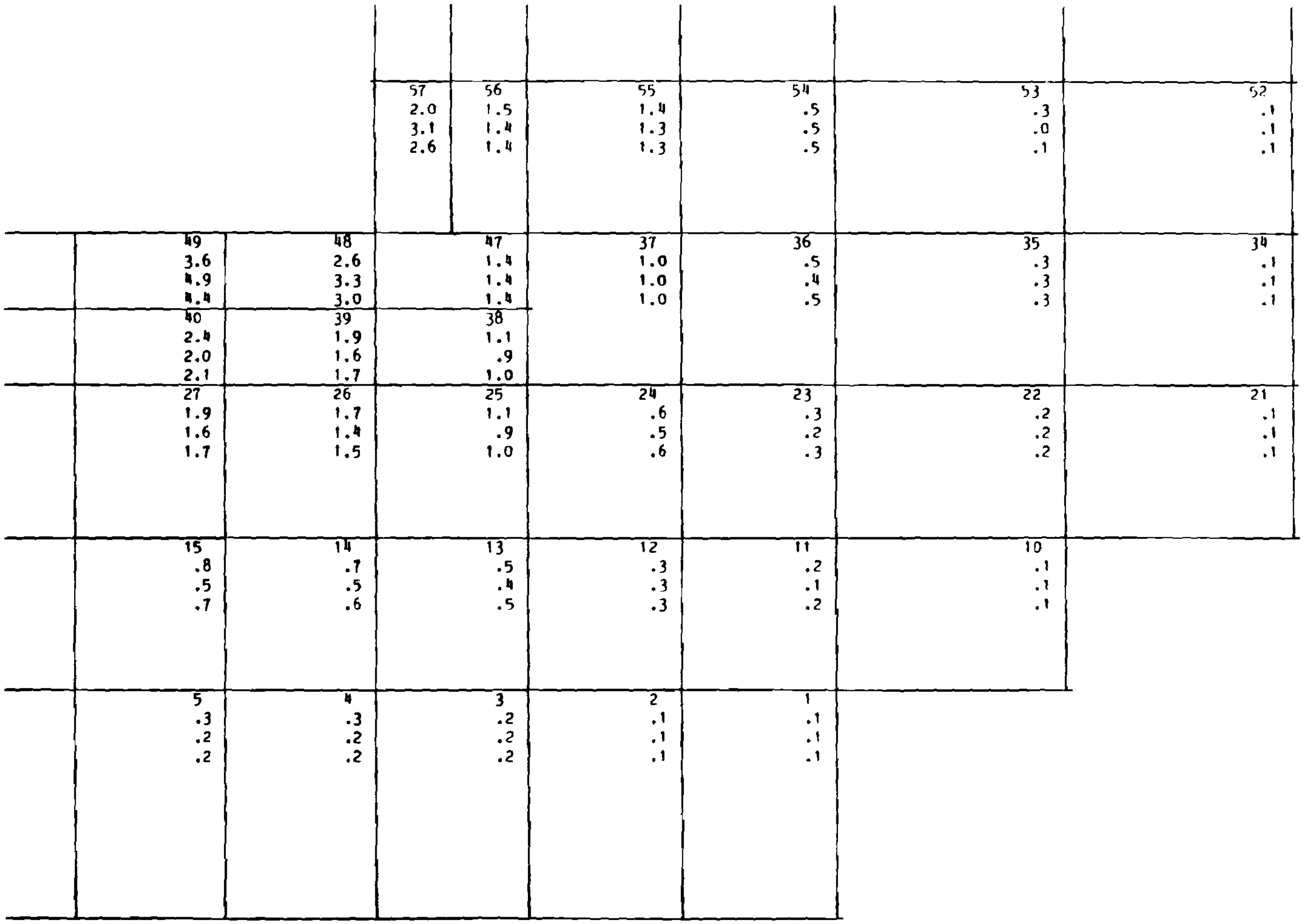

FIG. 3-7a. Module energy ratios for ΔE < −15 GeV; LPS data.

		57 2.2 2.5 2.4	56 1.5 1.6 1.5	55 1.3 1.4 1.4	54 .5 .6 .6	53 .3 .0 .2	52 .1 .1 .1
49 4.2 4.0 4.1	48 2.8 2.9 2.8		47 1.4 1.4 1.4	37 1.0 1.0 1.0	36 .5 .5 .5	35 .3 .3 .3	34 .1 .1 .1
40 2.3 2.1 2.2	39 1.7 1.7 1.7		38 1.0 .9 .9				
27 1.9 1.8 1.8	26 1.7 1.5 1.6		25 1.1 1.0 1.0	24 .6 .6 .6	23 .3 .3 .3	22 .2 .2 .2	21 .1 .1 .1
15 .7 .6 .7	14 .6 .6 .6		13 .5 .5 .5	12 .3 .3 .3	11 .2 .2 .2	10 .2 .2 .2	
5 .3 .3 .3	4 .3 .3 .3		3 .2 .2 .2	2 .2 .2 .2	1 .1 .1 .1		

FIG. 3-7b. Module energy ratios for $|\Delta E| < 15$ GeV; LPS data.

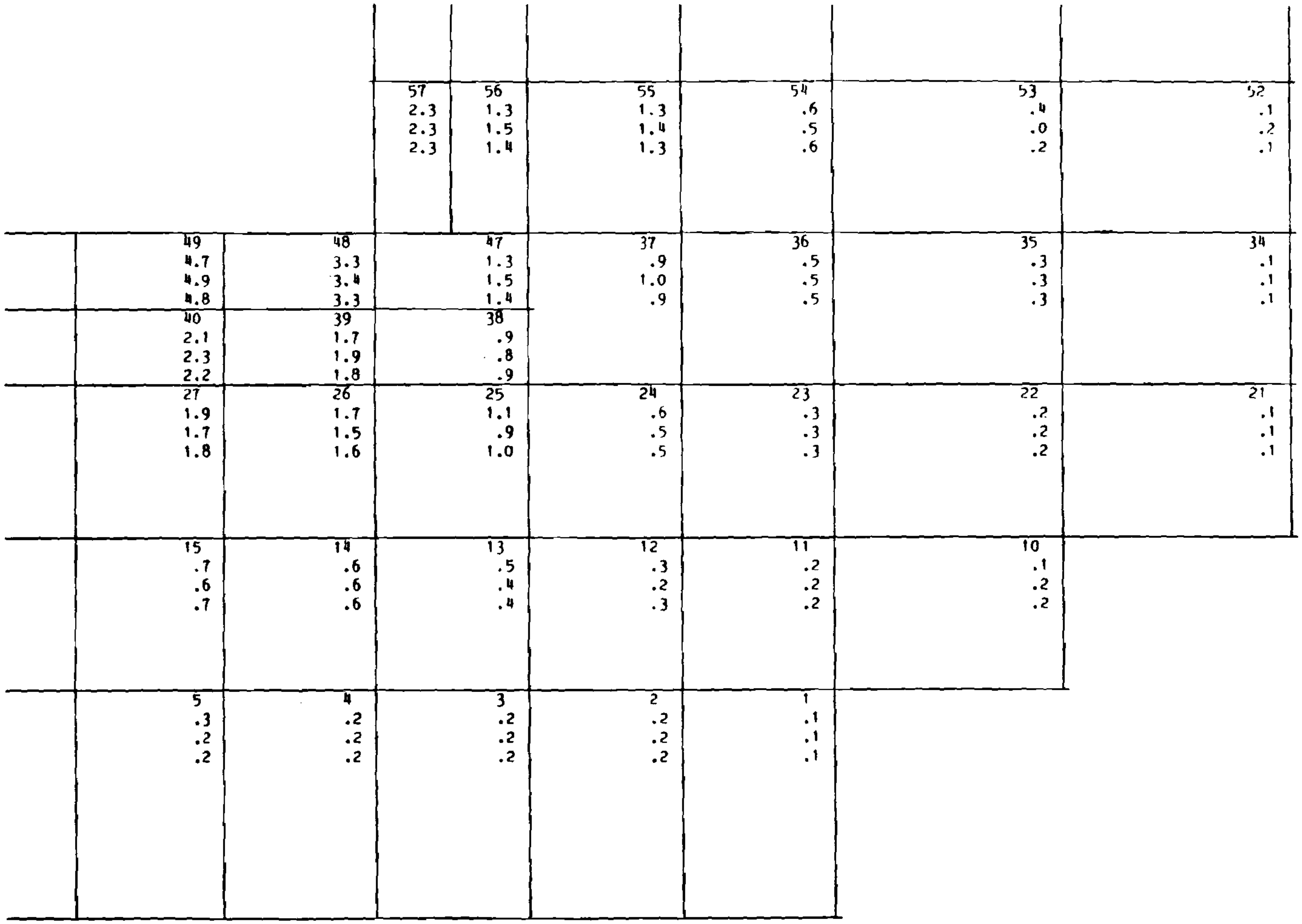

FIG. 3-7c. Module energy ratios for ΔE > 15 GeV; LPS data.

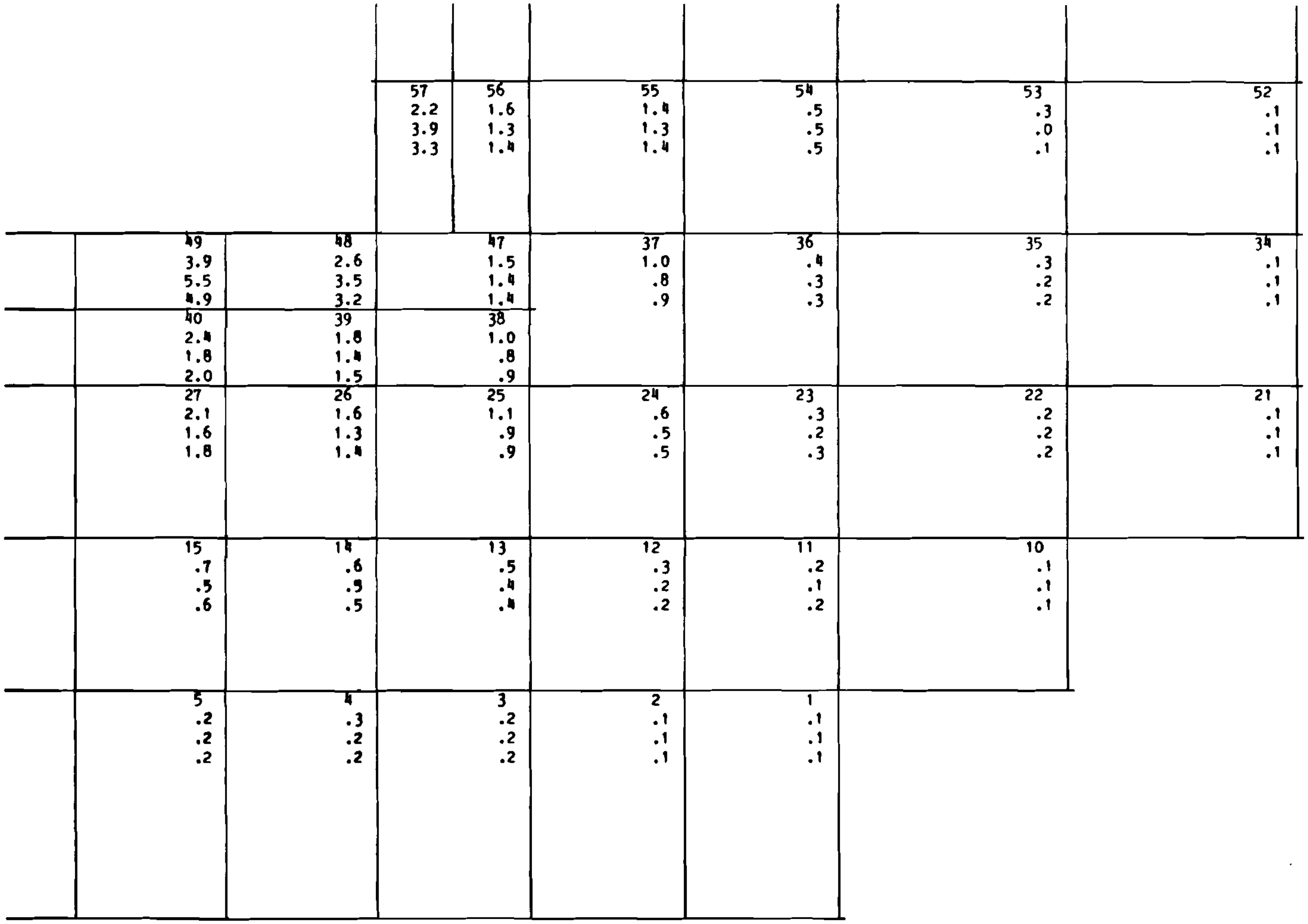

FIG. 3-8a. Module energy ratios for $\Delta E < -15$ GeV; QCD/brem data.

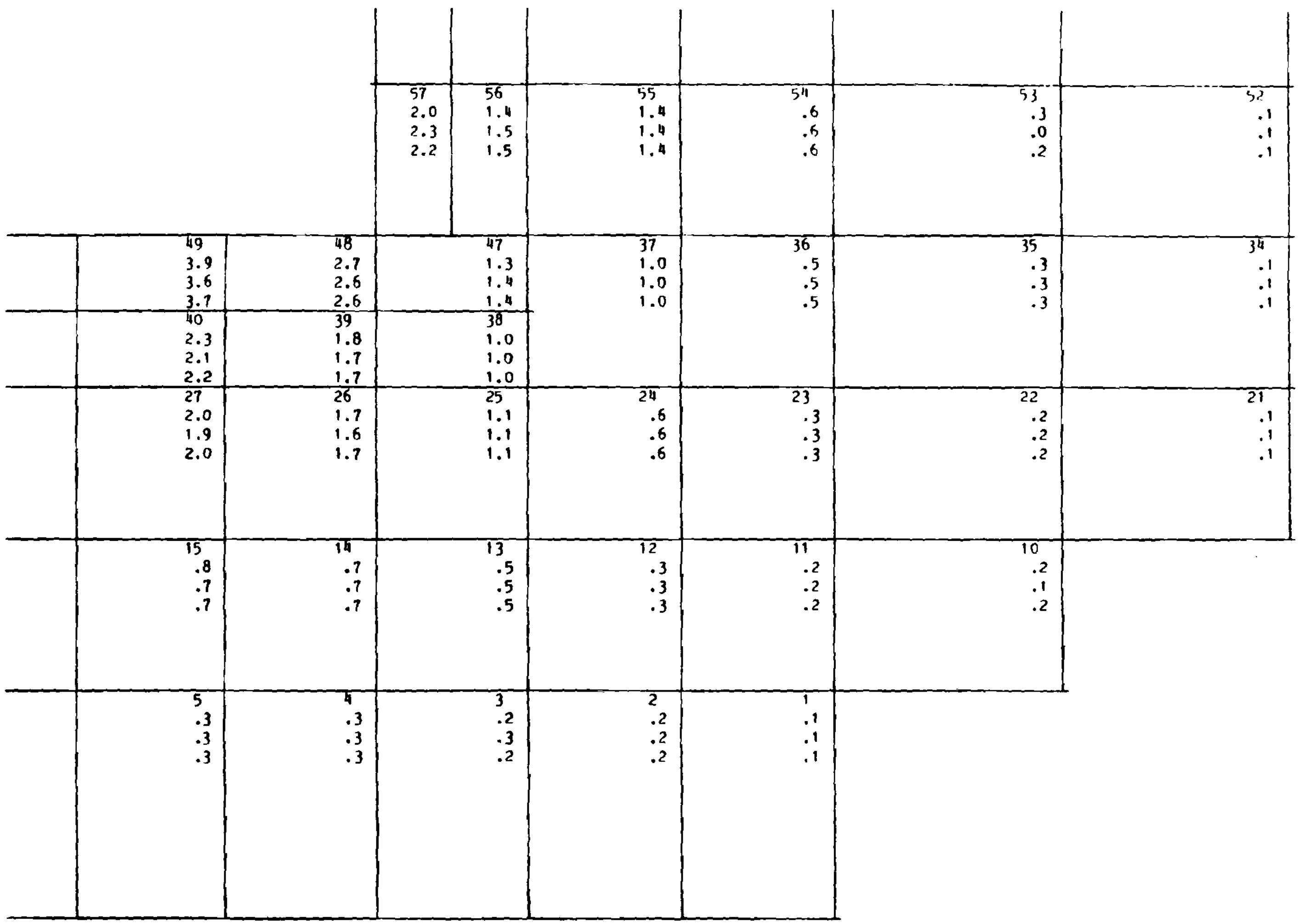

FIG. 3-8b. Module energy ratios for $|\Delta E| < 15$ GeV; QCD/brem data.

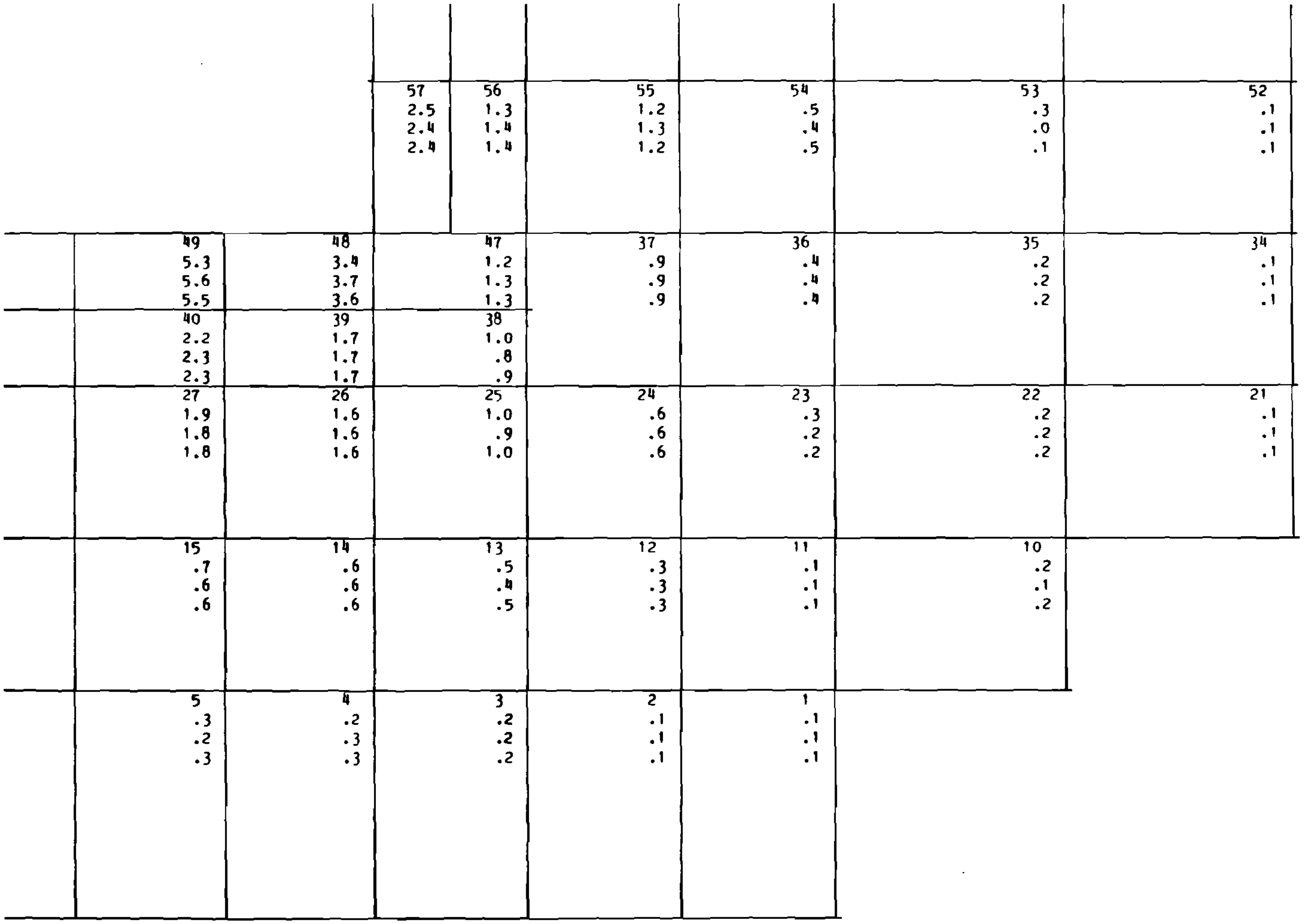

FIG. 3-8c. Module energy ratios for ΔE > 15 GeV; QCD/brem data.

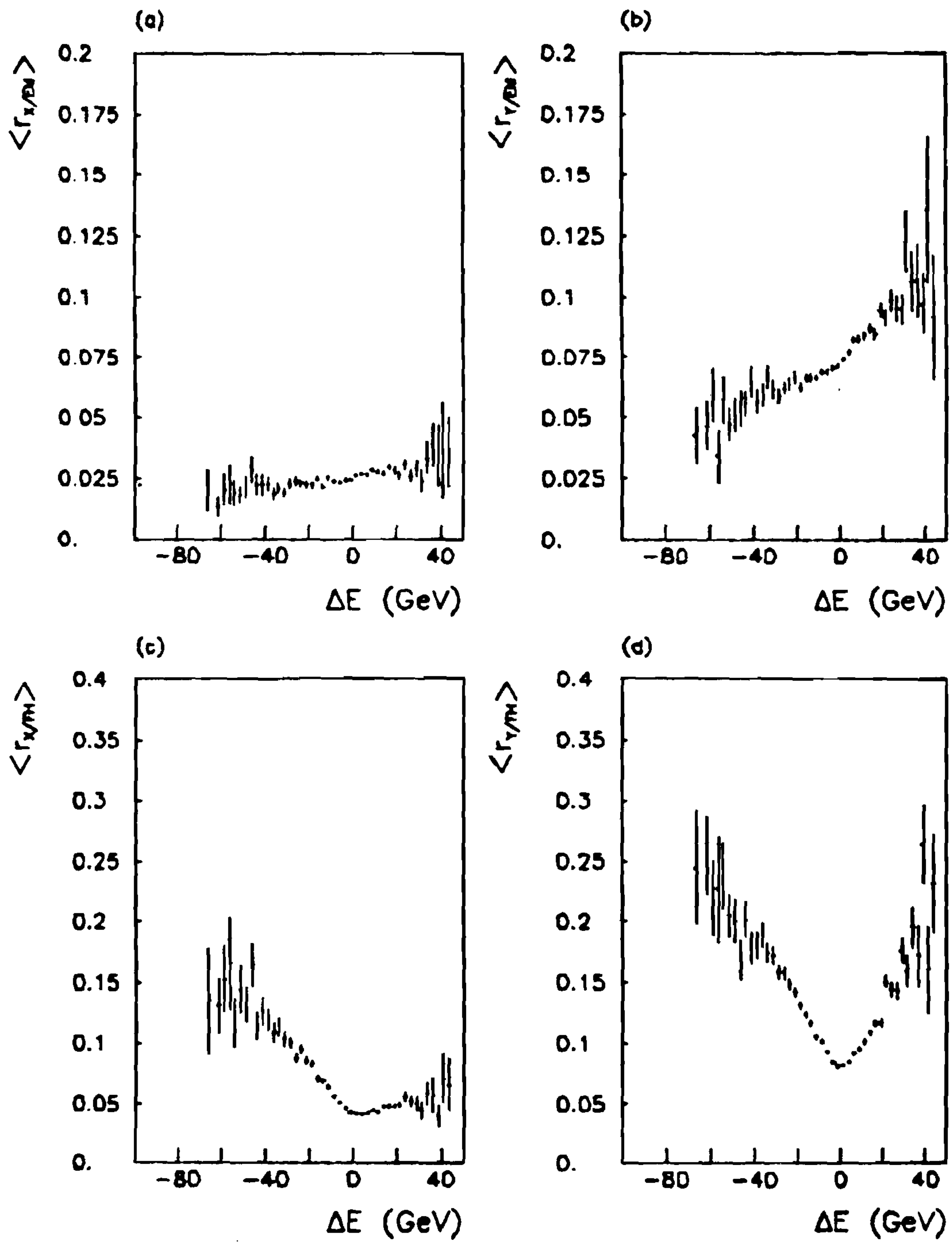

FIG. 3-9. Mean values of ring module energy ratios versus energy shifts. (a) $r_{x/EM}$. (b) $r_{y/EM}$. (c) $r_{x/FH}$. (d) $r_{y/FH}$.

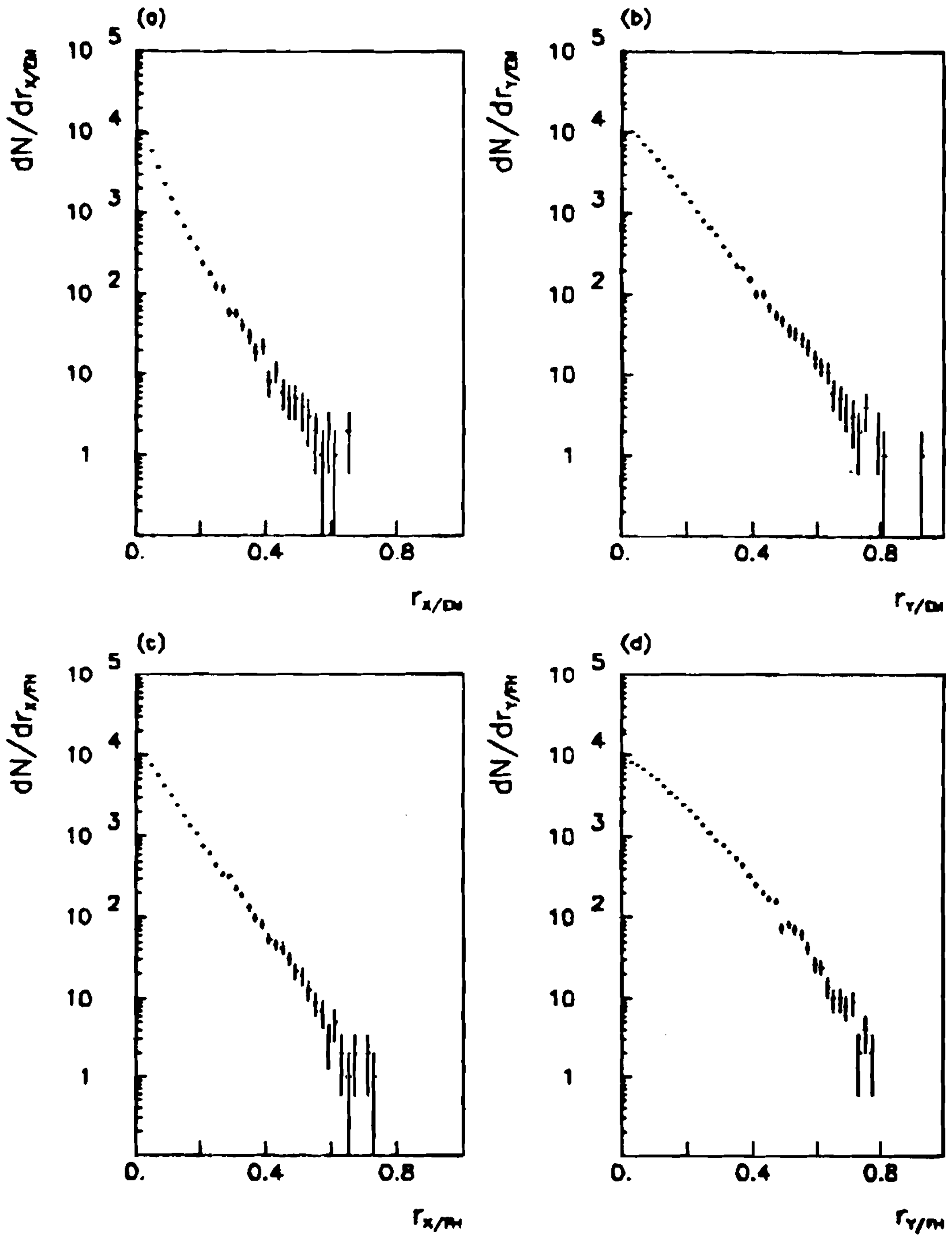

FIG. 3-10. Distributions of ring module energy ratios. (a) $r_{x/EM}$. (b) $r_{y/EM}$. (c) $r_{x/FH}$. (d) $r_{y/FH}$.

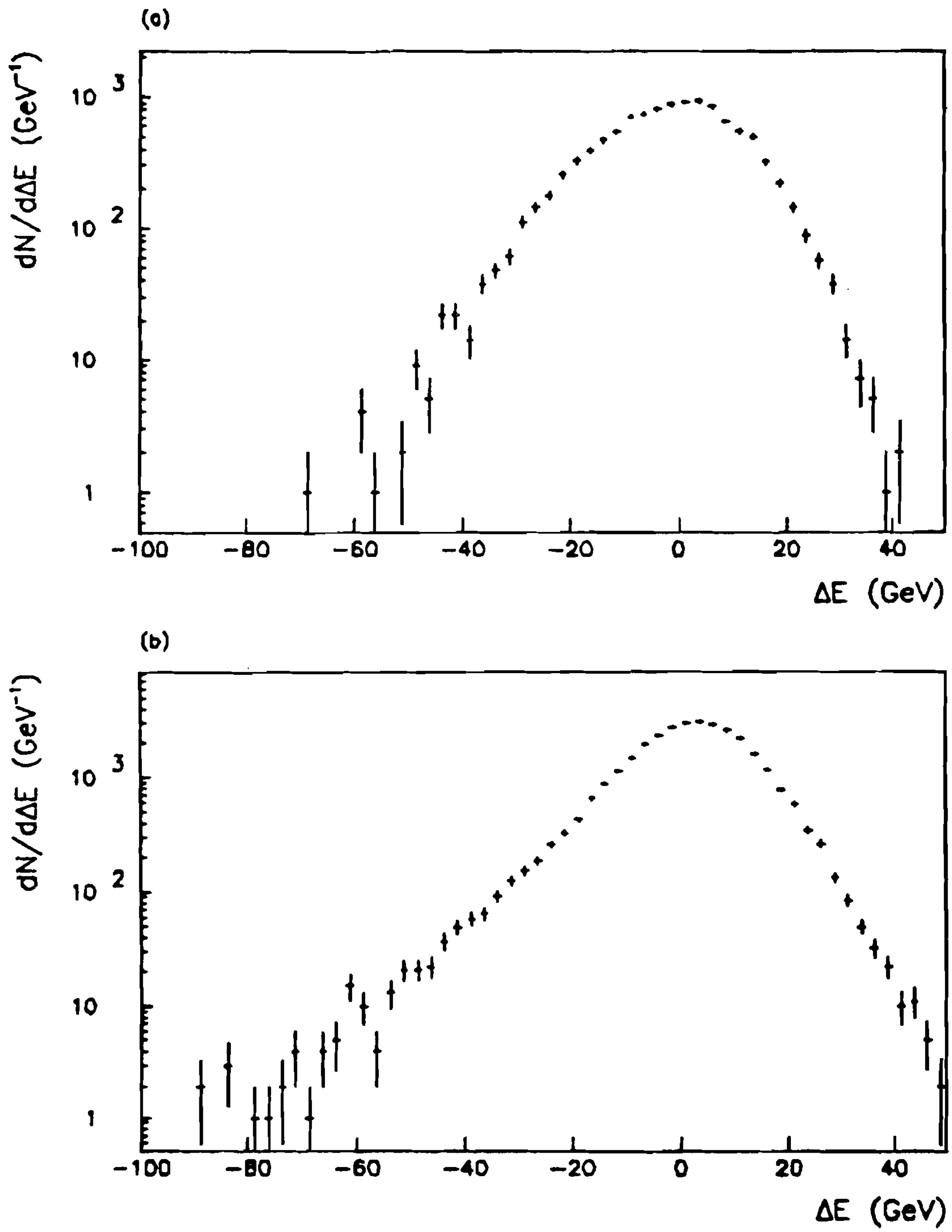

FIG. 3-11. Distribution of energy shift after cut on energy. (a) LPS. (b) QCD/brem.

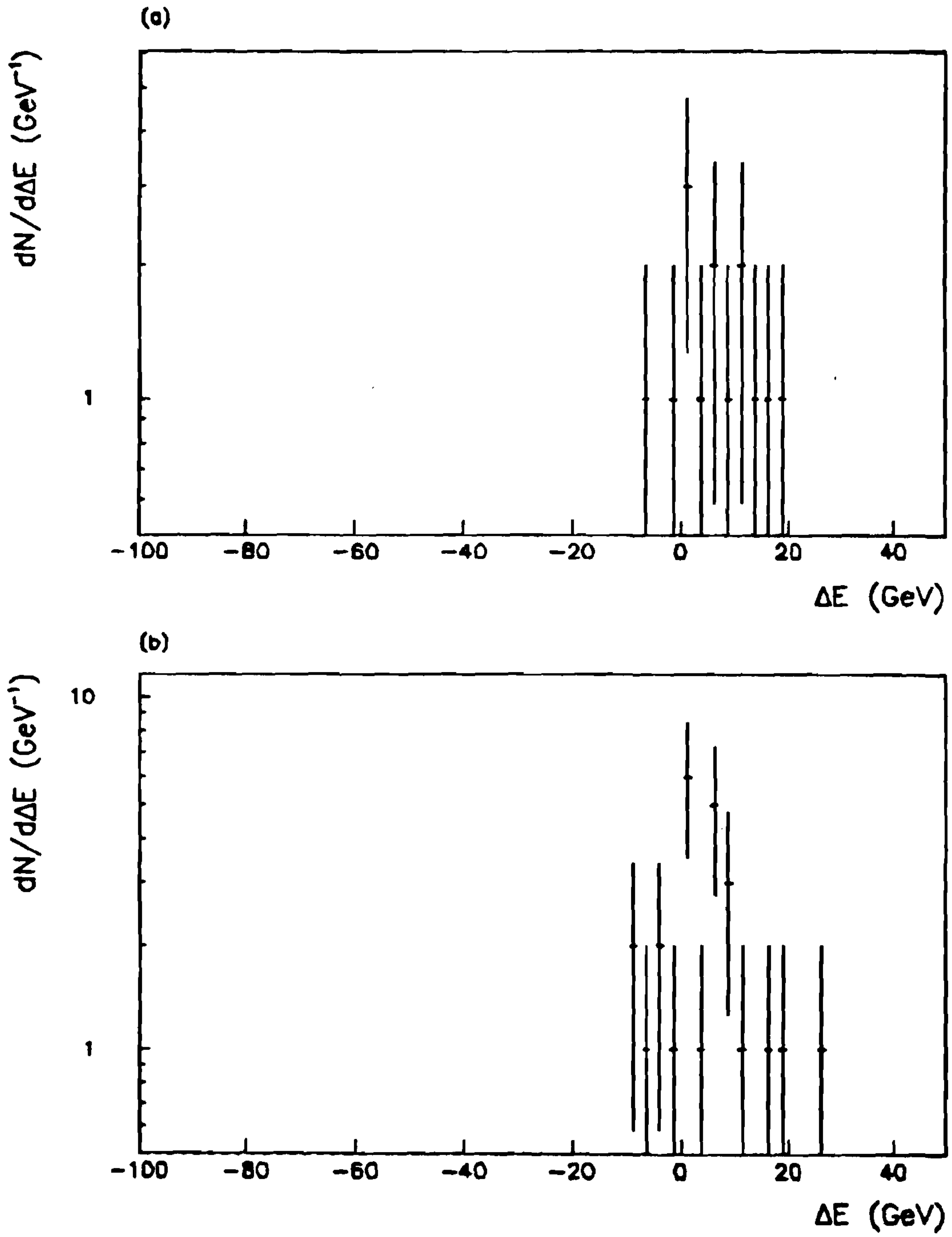

FIG. 3-12. Distribution of energy shift after cuts on energy and on ring module energy ratios. (a) LPS. (b) QCD/brem.

TABLE 3-1. Aperture acceptances and overlaps.

	Global	A-global	B 2/3	F 2/3	M 1/2
Global	7.86	7.54	4.89	4.91	4.33
A-global		7.54	4.89	4.91	4.33
B 2/3			4.89	2.26	3.37
F 2/3				4.91	3.22
M 1/2					4.33

NOTE: Diagonal entries are geometric acceptances of the corresponding apertures; off-diagonal entries are acceptances of the regions where the two corresponding apertures overlap. All entries are in units of steradians.

TABLE 3-2. Parametrizations of resolution functions.

Aperture	M_1 (10^{-3} GeV^{-1})	M_2	M_3 (10^{-3} GeV)
Global	-5.1 ± 0.3	1.074 ± 0.003	-3.6 ± 2.5
A-global	-5.4 ± 0.3	1.039 ± 0.003	0.3 ± 2.4
B 2/3	-8.9 ± 0.5	1.071 ± 0.004	21. ± 2.7
F 2/3	-12.2 ± 0.8	0.991 ± 0.004	9.1 ± 2.3
M 1/2	-13.4 ± 0.7	1.028 ± 0.005	25. ± 2.5

Aperture	S_1 (10^{-3})	S_2 (10^{-2} GeV)	S_3 (10^{-2} GeV^2)
Global	-2.4 ± 0.3	7.8 ± 0.2	0.53 ± 0.04
A-global	-1.3 ± 0.3	7.2 ± 0.2	0.51 ± 0.04
B 2/3	-1.5 ± 0.5	8.7 ± 0.2	1.55 ± 0.06
F 2/3	-0.6 ± 0.6	7.9 ± 0.2	0.83 ± 0.04
M 1/2	-1.9 ± 0.7	9.7 ± 0.3	1.38 ± 0.06

References for Chapter III

1. B. Brown et al., Phys. Rev. Lett. 49, 711 (1982).

2. C. DeMarzo et al., Phys. Lett. 112B, 173 (1982).

3. F. Lopez, Ph.D. dissertation, University of Illinois at Chicago, 1983; B. C. Brown et al., Phys. Rev. D 29, 1895 (1984).

4. T. Akesson and H.-U. Bengtsson, Phys. Lett. 120B, 233 (1983); J. C. Anjos et al., Universidade de Sao Paulo Instituto de Fisica preprint P-369, 1982 (unpublished).

CHAPTER IV

CROSS SECTIONS

In this chapter I present an analysis of cross sections for proton-proton and proton-nucleus scattering as a function of transverse energy deposited in each of the five full-azimuth geometrical apertures described in Chapter III. The dependence of the cross sections on the nucleon number A is discussed.

4.1. Luminosities

The cross section for some process P, $\sigma(P)$, is defined by

$$\sigma(P) = \frac{R(P)}{I_0 N_{scat}} , \tag{4-1}$$

where R(P) is the rate at which process P occurs in the target (dimensions are number of events per unit time), I_0 is the incident beam flux (particles per unit area per unit time), and N_{scat} is the number of scattering centers exposed to the beam. The quantities in this expression are determined from the counts recorded by the online scalers; each scaler incremented its count whenever a particular condition was met (see list of scalers in Table A-4). Quantities denoted below by s(name) are counts recorded by the scaler with the corresponding name.

N_{scat} is given in the thin target approximation by

$$N_{scat} = \frac{\rho N_0 \Delta z a \varepsilon}{A} , \tag{4-2}$$

where ρ is the mass density of the target, N_0 is Avogadro's number, Δz is the length of the target, a is the cross sectional area of the intersection of the beam and the target, ε is a dimensionless factor to correct for attenuation of the beam as it traverses the target, and A is the nucleon number of the target. In E557, incident protons are counted using the beam counters SA, SB, and SC (described in Appendix A), so for events originating in the fiducial hydrogen target region, ε must take into account 20 cm of hydrogen plus the material between the beam counters and the fiducial region. The result is $\varepsilon = 0.97$, giving $N_{scat} = a \ / \ (611 \text{ mb})$.

The rate divided by the flux, $R(P)/I_0$, should be roughly constant in time and equal to

$$\frac{R(P)}{I_0} = \frac{T(P)a}{s(\text{EFF BEAM})} . \tag{4-3}$$

Here T(P) is the number of times process P occurs in hydrogen target events while the trigger is "live" (ready to accept an event) and s(EFF BEAM) is the total number of beam particles entering the target while the trigger is live. The number of observed occurrences of P while the trigger is live is s(TRIGOR). To get the total number of events while the trigger is live, this must be increased by $\kappa \times$ s(PRETRIG) / s(STROBE) where κ is an acceptance factor to be discussed below and s(PRETRIG) / s(STROBE) accounts for events occuring in interactions which were not allowed to produce a trigger due to the presence of another beam particle within 130 ns or another interaction within 200 ns.

Because the trigger can be live while the spark chamber dead time has shut off data collection, the number of events written to tape, s(TRIG), is smaller than s(TRIGOR). I assume the fraction of events occurring in the hydrogen target is the same while the trigger is live as when data acquisition is live, so that for a run in which we are triggering on process P,

$$T(P) = \kappa \cdot s(\mathrm{TRIGOR})\left(\frac{N_H}{s(\mathrm{TRIG})}\right)\left(\frac{s(\mathrm{PRETRIG})}{s(\mathrm{STROBE})}\right) . \qquad (4\text{-}4)$$

Here N_H is the number of recorded events which come from a vertex reconstructed to be in the fiducial hydrogen target region.

The acceptance factor κ reflects the fact that not all recorded events have a successfully reconstructed vertex. There are two main error conditions in the vertex finding software. A type 34 error occurs when the vertex fit algorithm fails; a type 23 error indicates an overflow of a data buffer. Events with type 34 errors are primarily from interactions downstream of the target and so do not contribute significantly to the factor κ. An examination of events with and without type 23 errors suggests that type 23 error events generally have vertices distributed similarly to those of events without type 23 errors. Of the events with type 23 errors in a given run, the fraction that should be attributed to the hydrogen target is the same as the fraction of non-error events attributed to hydrogen. I have computed κ

accordingly.

The luminosity for the j'th run, L_j, is defined by

$$L_j = \frac{N_H}{\sigma(P)} = \frac{s(\mathrm{TRIG})}{\kappa s(\mathrm{TRIGOR})} \frac{s(\mathrm{STROBE})}{s(\mathrm{PRETRIG})} \frac{s(\mathrm{EFF\ BEAM})}{611\ \mathrm{mb}} , \tag{4-5}$$

and may be interpreted as the expected number of events of a given type to be found in that run divided by the cross section for such events, provided those events satisfy the online trigger requirements. In the case of the Interacting Beam trigger runs, the average value of $\sigma(P)$ was computed using a subset of the runs and luminosities were computed using this value, 28.3 millibarns, divided by N_H for each run. Values for L_j for each of the Global trigger runs are given in Table 4-1.

For three of the Global trigger runs in the data set (591, 592, and 593), scaler readings were unavailable and for a fourth (628) the luminosity computed from the scalers was not considered reliable due to a large number of vertex finding failures. Luminosities for these runs were computed in a manner to be described later.

4.2. Hydrogen cross sections

Hydrogen target data were selected using the vertices generated in the first stage of data processing. Vertices were required to lie within the hydrogen target fiducial region, the middle 40 cm length of the hydrogen target. A few events (about 25) for which the calorimeter measured an energy of more than 400 GeV were rejected. These fell into two categories: events not much larger than 400 GeV, which are consistent with upward fluctuations in the calorimeter, and "junk" events, where noise in the system produced nonsensical signals --

typically "calorimeter energies" of 2000 to 7000 GeV.

4.2.1. Uncorrected hydrogen cross sections (experimental)

Figure 4-1 shows the number of events as a function of Global E_t^C for several runs, where the number of events for each run has been divided by the luminosity for that run. If the online Global sum used to generate the trigger were very accurate, then these points all would lie on the same curve, the cross section as a function of E_t^C, which is the envelope of the curves in Fig. 4-1. Each run would "turn on" sharply at its threshold value of E_t^C. Instead, the turn-on is gradual and the points for a given run do not join up with those of the lower-threshold runs until about 1 GeV beyond the peak. There are errors in the online E_t^C sums due to pedestal drifts, errors in phototube gains, and the assumption that all events originate in the center of the hydrogen target. When E_t^C is computed offline, the turn-on is smeared.

For each Global trigger run, a cut on the Global transverse energy at a level of about 1 GeV beyond the peak in the E_t^C spectrum for that run was used to select events well beyond the trigger threshold. This corresponded to the value of E_t^C for which the trigger accepted essentially all events and the spectrum for that run joined up with the envelope of the spectrum for all runs. The events surviving this E_t^C cut were used in determining $d\sigma/dE_t^C$ for all values of E_t^C above the cut value. Table 4-1 lists the cut values for each Global trigger run. I refer to this procedure for determining cuts as the "envelope method."

One can also look at the number of events as a function of E_t^C in each of the four smaller apertures. The result is similar to what is seen with E_t^C. The existence of a threshold for Global E_t^C implies that for small enough values of the restricted aperture E_t^C the number of events seen will be suppressed; there is a gradual turn-on as E_t^C increases and the requirement on Global E_t^C becomes less and less inhibitory to production of the restricted aperture E_t^C. To compute $d\sigma/dE_t^C$ one must impose on each run a cut on E_t^C in the aperture under consideration. The events surviving this cut are not biased by the Global E_t^C threshold and may be used to compute the cross section for values of E_t^C above the cut value. The cuts have been determined by the envelope method as a function of the Global E_t^C cut and are listed in Table 4-2.

The approximate value of the cross section $d\sigma/dE_t^C$ evaluated at $E_t^C = E_{t0}^C$ for each aperture is given by

$$\left[\frac{d\sigma}{dE_t^C}\right]_{E_t^C=E_{t0}^C} = \frac{\Sigma\, N_{Hj}(E_{t0}^C,\Delta E_t^C)}{\Delta E_t^C\; \Sigma\, L_j}\;, \tag{4-6}$$

where the sums are over all runs for which the aperture transverse momentum cut is smaller than E_{t0}^C. Here $N_{Hj}(E_{t0}^C,\Delta E_t^C)$ is the number of events with a vertex in the fiducial hydrogen target region in run j with $E_{t0}^C < E_t^C < E_{t0}^C + \Delta E_t^C$; ΔE_t^C is small. Events from Interacting Beam trigger runs were used without transverse energy cuts, because no threshold bias was present. For this analysis I used a value of ΔE_t^C = 0.1 GeV; I then averaged the results over bins of width 0.5 GeV or more.

The cross sections for production of E_t^C into five calorimeter apertures are given in Table 4-3 and plotted in Fig. 4-2. The values given are the average values of $d\sigma/dE_t^C$ over the bins indicated in the plots by the horizontal error bars. Vertical error bars shown are statistical only. As mentioned earlier, luminosities for four Global trigger runs could not be computed from the scalers. These runs were not used in the first computation of the cross section for the Global aperture. Luminosities for these runs were then estimated by

$$L_j = \frac{\int (dN_j/dE_t^C)\ dE_t^C}{\int (d\sigma/dE_t^C)\ dE_t^C}\ , \tag{4-7}$$

where the integrals are from the E_t^C cut up. I then included these runs, using the estimated luminosities, in the final calculations of the cross sections. I have checked that inclusion of these runs does not substantially alter my results except to reduce the statistical errors.

Comparison of the spectra for the F2/3 and B2/3 apertures reveals a disturbing discrepancy. The two regions have similar acceptances and are approximately mirror images of each other with respect to $\theta^* = 90°$. Because the initial state (proton-proton) is symmetric with respect to $\theta^* = 90°$, we must expect the spectra for F2/3 and B2/3 to be nearly identical. Instead, the spectrum for F2/3 falls much more rapidly with E_t. The conclusion (if we are to retain our faith in Poincare invariance!) is that these spectra as they stand reflect some instrumental biases.

If the resolution functions described in the previous chapter adequately describe these biases, then the discrepancy should be disappear when the resolution functions are used to correct the transverse energy scales. This correction procedure will be discussed shortly.

4.2.2. LPS and QCD/Brem cross sections

First, however, I present cross section predictions from the Monte Carlos. Two sets of cross sections for the LPS data are presented in Tables 4-4 and 4-5; they are plotted in Figs. 4-3 and 4-4. The first set, $d\sigma/dE_t^C$, was computed from sums of simulated calorimeter module responses. The second set, $d\sigma/dE_t$, was computed from the actual transverse energies of the final state particles at the interaction vertex. The corresponding spectra for QCD/Brem Monte Carlo data are given in Figs. 4-5 and 4-6, and in Tables 4-6 and 4-7. Calculation of the cross sections was handled in much the same way as for the experimental Interacting Beam trigger data; the values of the luminosity were supplied by the Monte Carlo programs.

The F2/3 and B2/3 E_t cross sections are nearly identical, with a very slightly steeper slope for the F2/3 which seems reasonable in light of the small differences in acceptance. The F2/3 and B2/3 E_t^C spectra, however, show a discrepancy similar to what was seen in the hydrogen data. The simulation of the apparatus seems to be at least qualitatively successful in modelling the effects that give rise to the front-back asymmetry. These effects are present most strongly in the F2/3 data; there is a pronounced difference between the F2/3 E_t and E_t^C spectra, whereas for B2/3 the E_t and E_t^C spectra are much more similar to one another.

4.2.3. Corrections to E_t

The next step in understanding the E_t spectra is to use the resolution functions to determine corrections to be applied to the data, allowing an estimate of $d\sigma/dE_t$ from $d\sigma/dE_t^C$.

The method used was a modification of the one developed for the first E557 publication (Ref. 1). In the preceding chapter I wrote that the E_t spectrum is related to the E_t^C spectrum by

$$S_e^C(E_t^C) = \int_0^\infty S_e(E_t)\ R(E_t^C;E_t)\ dE_t \tag{4-8}$$

where $R(E_t^C;E_t)$ is the resolution function, obtained from the Hybrid Monte Carlo; $S_e^C(E_t^C) \equiv d\sigma/dE_t^C$ is the experimentally obtained spectrum described above; and $S_e(E_t) \equiv d\sigma/dE_t$ is what we want to solve for. Rigorous solution methods exist,[3] but for our purposes -- given the simple behavior of the spectra -- the more ad hoc procedure of "guessing" a solution and then verifying it by direct substitution is easier.

The prescription is as follows: first, I obtain a zeroth-order input spectrum of the form

$$S_0(E_t) \equiv A \exp\ (-\alpha E_t)\ . \tag{4-9}$$

The parameters A and α are determined by a least squares fit of the zeroth-order output spectrum,

$$S_0^C(E_t^C) \equiv \int_0^\infty S_0(E_t)\ R(E_t^C;E_t)\ dE_t \tag{4-10}$$

to $S_e^C(E_t^C)$ in the range of E_t^C from a few GeV up, where the observed spectrum is decreasing and is nearly exponential. Next, I compute

$$S_1(E_t) = S_0(E_t) \left[\frac{S_e^C(E_t^C)}{S_0^C(E_t^C)}\right] B \qquad (4\text{-}11)$$

where the functions of E_t^C are evaluated at $E_t^C = \mu(E_t)$, the mean value of the resolution function at E_t, and B is a normalization constant determined by the requirement

$$\int_0^\infty S_1(E_t)\, dE_t = \int_0^\infty S_e^C(E_t^C)\, dE_t^C \ . \qquad (4\text{-}12)$$

$S_1(E_t)$ is taken to be the final estimate of $d\sigma/dE_t$. By substitution into Eq. 4-8 I verify that this estimate is accurate. The primary differences between this method and that used for Ref. 1 are: first, Ref. 1 used resolution functions based on a subset of the LPS data and on a set of events consisting of tracks derived from the experimental calorimeter data, treated as input and run through the equipment simulation. Second, the resolution functions for Ref. 1 were parametrized by Gaussians normalized to unity from $E_t^C = -\infty$ to $+\infty$, rather than from 0 to $+\infty$ as in Eq. 3-2. Third, in the computation described by my Eq. 4-11, Ref. 1 evaluated the functions of E_t^C at $E_t^C = E_t$. Fourth, the normalization condition (eq. 4-12) was not imposed; B was set to 1. The second and fourth of these modifications are the principal reasons for the differences between my final cross sections and those of Ref. 1.

To check the procedure, I applied it to the Hybrid Monte Carlo events. Figures 4-7 and 4-8 show $d\sigma/dE_t^C$ and estimated $d\sigma/dE_t$, respectively, for the Hybrid data. Also shown in Fig. 4-8 are the actual shapes of the E_t spectra. Agreement is very good. The front/back asymmetries in the E_t spectra have been removed by the correction procedure.

I then applied the correction procedure to the experimental data. In Fig. 4-9 and Table 4-8 I present the corrected E_t spectra for the hydrogen data. Again, the front/back asymmetry has been much reduced; however, there remains a difference between F2/3 and B2/3 of up to nearly a factor of ten in cross section, corresponding to a transverse energy shift of about 1.5 GeV. This residual asymmetry will be discussed further in the next chapter. As in the QCD/Brem data, the F2/3 shows the largest correction of the five apertures.

4.3. Nuclear targets

Nuclear target data were selected using the vertices generated in the first stage of data processing. The positions of the nuclear targets were determined to within about 1 mm from an examination of the vertex positions and only events with vertices in the range $(z_1-0.026\ \mathrm{m}) < z_{vtx} < (z_1+0.134\ \mathrm{m})$ were accepted, where z_1 was the position of the upstream nuclear target ("Target 1"). This region fell between and excluded the peaks due to the end of the hydrogen target and the dE/dx counter, though a small fraction of the accepted events probably came from the tails of these peaks. Figure 4-10 shows the geometry of this nuclear target region and defines some notation.

Cuts similar to those used for hydrogen were imposed: calorimeter energy was required to be < 400 GeV and the Global transverse energy had to be at least 1 GeV above the hardware threshold in the Global trigger runs. In addition, cuts were imposed for each aperture on the transverse energy in that aperture. Studies using the envelope method indicated that the E_t^C cut values used for the hydrogen data (Tables 4-1 and 4-2) were appropriate also for the nuclear target data.

4.3.1. Vertex function fits

Figure 4-11 shows a typical histogram of vertex positions (z coordinate only) in the nuclear target region. Whereas with the hydrogen data, a fiducial region inside the target could be taken, and events with vertices inside that region could be used as an uncontaminated sample of hydrogen events, the nuclear targets are too thin and too close together to permit a clean separation according to vertex position. Instead, I have divided the nuclear target region events between Target 1, Target 2, and background according to the following procedure.

The data were binned according to E_t^C and a histogram of vertex z-coordinates was made for each bin. (The HBOOK histogram software package was used[2]). The histograms had eighty bins in z covering the entire nuclear target region, with each z bin 0.2 cm wide. The choice of E_t^C binning was, perhaps, not intuitively clear. E_t^C bins ranged in width from 0.5 to 2.0 GeV. Three criteria determined E_t^C bin sizes and boundaries: first, bins were made no narrower than necessary, to minimize problems due to the (already poor) statistics. Second, bins were made no wider than 2 GeV for the obvious reason that I am interested in changes in cross sections on scales of a few GeV. Finally, for each aperture, bin boundaries were imposed at the E_t^C cuts; this made analysis easier, because it eliminated threshold effects in any given histogram. For those E_t^C bins with enough events, a fit to a function -- the "vertex function" -- could then be made. The fit was performed using the HBOOK fitting routine, HFIT. The vertex function has components corresponding to each of the two targets, which can be separately integrated to estimate the number of events originating in each foil.

In E557's earlier analysis of nuclear target cross sections for two apertures, Global and Small Aperture,[4] the form chosen for the vertex function was a sum of four Gaussians plus a constant background term. Two of the Gaussians were centered on Target 1 and two on Target 2. A single Gaussian for each target had been tried and was found to give very poor fits; the observed shapes have longer tails than can be accounted for by single Gaussians. The fits were to data stored in histograms having forty bins, each 0.004 m wide. Because the positions of the targets (centers of the Gaussians) were well known, there were nine parameters for such a function -- the amplitude and width for each of the four Gaussians and the background amplitude. The normalization constraint (the integral of the vertex function must be the number of events observed) reduced the number of free parameters to eight.

A severe problem with this functional form is that the two Gaussians for each target are highly correlated. Crudely speaking, if HFIT finds it desireable to reduce the width of one, it then "wants" to increase the width of the other to compensate. The result is that the fit tends to be unstable, in the sense that one or more of the parameters either decreases or (more commonly) increases until it runs up against a user-imposed limit. Apparently HFIT then leaves the "runaway" parameters where they are and adjusts the others for the best fit. The resulting fit is often good enough, as measured by its χ^2, for our purposes. However, the covariance matrix returned by HFIT, necessary for a correct computation of errors, has deleted from it the rows and columns corresponding to the runaway parameters.

It was for this reason that I tried a fit to the following vertex function (the subscript j denotes quantities associated with the j'th E_t^C bin):

$$d_j(z) = \left(d_{1j}\lambda(z;z_1,\Gamma_{1j}) + d_{2j}\lambda(z;z_2,\Gamma_{2j}) + d_{BGj}b(z)\right)H_j \ , \qquad (4\text{-}13)$$

where z_1 and z_2 are defined in Fig. 4-10, H_j is the total number of entries in the histogram, $\lambda(z;z_i,\Gamma_{ij})$ is the Lorentzian function

$$\lambda(z;z_i,\Gamma_{ij}) = \frac{\Gamma_{ij}}{2\pi((z-z_i)^2 + (\Gamma_{ij}/2)^2)} \qquad (i = 1 \text{ or } 2) \ , \qquad (4\text{-}14)$$

and $b(z)$ is a uniform background within the nuclear target region,

$$\begin{aligned} b(z) &= \frac{1}{z_d - z_u} && \text{if } z_u < z < z_d \\ &= 0 && \text{otherwise} \ . \end{aligned} \qquad (4\text{-}15)$$

The limits z_u and z_d are defined in Fig. 4-10. The widths, Γ_{1j} and Γ_{2j}, and the amplitudes d_{1j} and d_{2j}, are the free parameters; the background amplitude, d_{BGj}, is determined by imposing the normalization condition.

The least squares procedure used by HFIT is based on the assumption that the relative error on the contents of each bin is small; for this condition to be satisfied one would like at least five entries, or better yet, ten in each bin. In fact, for the eighty-bin histogram, many bins had two, one, or zero entries. For this analysis I decided to combine adjacent bins to arrive at a coarser, nonuniform binning. The first such attempts used fifteen nonuniform bins in z with widths ranging from 4 mm near the target positions (where statistics are best and the function varies most rapidly) to 22 mm in the gap between the targets. Later the binning was coarsened still further to eight bins with widths from 8 mm to 58 mm (where the largest bin covered most of the region downstream of target 2). Figure 4-12 illustrates the binning scheme used.

A second advantage of the two-Lorentzian fit over the four-Gaussian fit now comes to light: the former has only four parameters to the latter's eight. Obviously the eight-parameter function would have been less suitable for the eight-bin fit.

I attempted the fit to fifteen nonuniform bins using a two-Gaussian function, a four-Gaussian function, and a two-Lorentzian function. The two-Gaussian form was clearly inferior. Comparing the latter two functions, only marginally better fits (as measured by the probability of the χ^2 of the fit) were obtained with the four-Gaussian form. In light of the fact that the two-Lorentzian form did not suffer from the instability problems that plagued the four-Gaussian function, I decided to use the former for this analysis.

However, none of the tested functions fit the data particularly well. Fits to histograms with large numbers of entries (>1000) were quite poor; the Lorentzian tails apparently are still not quite long enough. On the other hand, only a few of the histograms have enough statistics that the departure from a Lorentzian form is detectable. For the purposes of estimating the number of events under each peak in our limited quantity of data, it is doubtful that any improvement in the choice of the fitted function would significantly change the results.

Once the fit was made, the number of events in the nuclear target region ascribed to target i in E_t^C bin j was simply

$$D_{ij}(d_{ij},\Gamma_{ij}) = d_{ij} \int_{z_u}^{z_d} \lambda(z;z_i,\Gamma_{ij})\, dz \ . \tag{4-16}$$

I used the covariance matrix returned by HFIT and propagation of errors to determine the variance of D_{ij}; the term proportional to the variance in d_{ij} dominates.

4.3.2. Low statistics method

For many (in fact, most) bins of E_t^C the vertex histogram could not be fit reliably due to poor statistics. Fits were done for only those histograms in which each of the eight bins in z contained ten or more events. To estimate D_{ij} for those remaining histograms that had more than 35 entries, I used a different, cruder procedure. (Histograms with fewer than 35 entries could have been eliminated by rebinning. However, if different binnings were used for different targets, comparison of the nuclear target cross sections would have been more complicated, and the improvement in accuracy would have been marginal. These very low statistics E_t^C bins therefore were disregarded completely.) A value for d_{BGj} was assumed; for $E_t^C > 3$ GeV I chose $d_{BGj} = 0.15 \pm 0.10$, and for $E_t^C < 3$ GeV, 0.30 ± 0.20. Values of (1.5 ± 0.3) cm and (1.3 ± 0.3) cm were assumed for Γ_{1j} and Γ_{2j}, respectively. I based all these assumptions on the results and trends of the fits to histograms with better statistics. The number of events within 2.4 cm of each target, c_{1j} and c_{2j}, was estimated by summing the histogram entries within those boundaries (denoted z_{u1}, z_{d1}, z_{u2}, and z_{d2} in Fig. 4-10) and subtracting the estimated background:

$$c_{ij} = (\#\text{ events in } (z_{ui},z_{di}) \text{ for bin } j) - d_{BGj}H_j(z_{di}-z_{ui}) \;/\; (z_d-z_u) \;. \tag{4-17}$$

Finally, I estimated D_{ij} by multiplying c_{ij} by the appropriate factor:

$$D_{ij} = c_{ij}\,\frac{\Lambda(z_u,z_d;z_i,\Gamma_{ij})}{\Lambda(z_{iu},z_{id};z_i,\Gamma_{ij})} \tag{4-18}$$

where

$$\Lambda(z_a,z_b;z_i,\Gamma_{ij}) = \int_{z_a}^{z_b} \lambda(z;z_i,\Gamma_{ij})\,dz \;. \tag{4-19}$$

As a check of this procedure, I compared its results to the results of the fit for histograms where the fit could be done reliably; agreement was very good. About two-thirds of the measurements of D_{ij} had to be made with this procedure.

4.3.3. Nuclear cross sections

The cross section for nuclear target i, $(d\sigma/dE_t^C)_{A_i}$, in bin j is approximately $D_{ij}\sigma_i^0$, where

$$\sigma_i^0 = \frac{\varepsilon A_i}{\rho_i \Delta z_i N_0 \Delta E_t^C} \;. \tag{4-20}$$

Here ρ_i is the density of target i, Δz_i is its thickness, N_0 is Avogadro's number, ΔE_t^C is the width of the E_t^C bin, and ε is a beam attenuation factor. For our experiment there is negligible attenuation by the first nuclear target or between the two nuclear targets, so ε is the same for both, but larger than for hydrogen, since it includes the attenuation by the entire hydrogen target.

In principle one can get up to four measurements of average $d\sigma/dE_t^C$ for aluminum in each E_t^C bin, one from each of the four run groups. In practice, the measurement from group B seems to be unreliable (i.e. not very consistent with results from groups O, A, and P), due to poor statistics and a bad choice of target pairing: the thin aluminum target was used in combination with the lead target, and, especially at high E_t^C, the signal from aluminum was washed out by the much stronger signal from lead. Similar problems afflict the copper data from run group P, in addition to the fact that this run group includes no Global trigger data. The stronger aluminum signal from these runs, and the lead signal from run group B, appear to be good. The final uncorrected cross sections for aluminum are obtained from averaging up to three measurements per E_t^C bin, one from each of run groups O, A, and P. For copper, one measurement per E_t^C bin was used (run group A), and for lead, up to two measurements per E_t^C bin (groups O and B).

The uncorrected cross sections for all three targets and five apertures are presented in Figs. 4-13 (aluminum), 4-14 (copper), and 4-15 (lead), and in Table 4-9. Note the front-back asymmetry (the cross sections for the F2/3 aperture are steeper than those for B2/3) is stronger than for the hydrogen data. This behavior is consistent with the values of E_t/E (Chapter V) and with theoretical expectations.

4.3.4. E_t scale for nuclear target data

One would at this point like to apply corrections to the nuclear target E_t^C spectra to correct the E_t scale, as was done with the hydrogen data. There are two problems, however. First, the nuclear target data are arranged in coarse, nonuniform bins, with some large gaps (particularly for copper). The method used for the hydrogen data E_t corrections assumes the bins are be small (0.1 GeV), uniform, and mostly nonempty except at high E_t. Second, there is the problem of the production mechanism dependent resolution functions. If the Hybrid Monte Carlo is a mediocre simulation of the hydrogen data, one must expect it to be even worse as a simulation of the nuclear data; the LPS and QCD/Brem Monte Carlos, after all, are proton-proton simulations, not proton-nucleus (and their vertices are distributed in the hydrogen target only). I have no proton-nucleus Monte Carlo available.

What would be the likely result of corrections to the nuclear target spectra, if one could do them? For both the LPS and the QCD/Brem Monte Carlos we can compare $d\sigma/dE_t^C$ to the actual $d\sigma/dE_t$ (Figs. 4-3 to 4-6), and for the experimental data we can compare to the estimated $d\sigma/dE_t$ (Figs. 4-2 and 4-9). This is a rather disparate set of models, and we know the details of the resolution functions differ between them, but they have certain features in common. For most of the apertures, the corrections are small. Viewed as a horizontal E_t shift (rather than as a vertical $d\sigma/dE_t^C$ correction), for all but the F2/3 aperture the corrections generally are E_t shifts of about 0.5 GeV or less at the highest values of E_t (roughly a 3% shift). The corrections are largest for the F2/3 apertures, closer to a 1.0 GeV (6% to 10%) shift.

Given that the corrections are this small for events as different as those generated by LPS and QCD/Brem, it is reasonable to expect that the E_t shifts for the nuclear target data are also small. Given that the observed differences in event structure between the various nuclear targets are small (Chapter V), it is reasonable to expect that the corrections for the various nuclear targets will be similar. These expectations are based on extrapolations of what we know about the resolution functions and the nuclear target events. Like all extrapolations they must be taken cum grano salis until better data (or better analyses!) are available. Nevertheless, they seem reasonably safe.

I therefore will make no attempt to present corrected cross sections for the nuclear targets; the uncorrected cross sections already presented will be used for the following A-dependence studies, with the understanding that the transverse energy scales are uncertain at the highest transverse energies by about 5% for the Global, A-Global, B2/3, and M1/2 apertures and by about 10% for the F2/3 aperture. These uncertainties are systematic; the differences between the shifts for the various nuclear targets should be somewhat smaller than the shifts themselves.

4.3.5. Nucleon number dependence

As is customary in studies of A-dependence, I will parametrize the cross sections by

$$\left(\frac{d\sigma}{dE_t^C}\right)_A = sA^{\alpha(E_t^C)} \quad . \qquad (4\text{-}21)$$

Here s is the extrapolation of $d\theta/dE_t^C$ to A=1; typically hydrogen does not lie on such an extrapolation. The parameter α can be computed using ratios of numbers of events in a given run group from

$$\alpha(E^C_{tj}) = \frac{\ln(\sigma^\circ{}_2 / \sigma^\circ{}_1) + \ln(D_{2j} / D_{1j})}{\ln(A_2 / A_1)}$$

$$= \alpha_0 + \alpha_1 \ln(D_{2j} / D_{1j}) , \qquad (4\text{-}22)$$

or from fitting a straight line to the logarithm of the cross sections as a function of ln(A):

$$\ln (d\sigma/dE_t) = \alpha \ln (A) + \beta ; \qquad (4\text{-}23)$$

α and β are the parameters of the fit. Results from both methods are consistent, but the second gives smaller errors and was used for my final results. For many bins of E^C_t only two points on this line are available (aluminum and lead, usually) and a "fit" to a straight line is a less than Herculean task. Where data from all three targets are available, the linear relationship is found to hold well (Fig. 4-16).

The resulting values of α as a function of E^C_t are given in Fig. 4-17 and Table 4-9; the table also gives the correlation coefficients of the fits. A rise in α is seen in all apertures; clear evidence of an increase to values higher than 1.0 is seen in all but F 2/3, where $\alpha > 1.0$ in the last four bins, but by less than one standard deviation for three of the four.

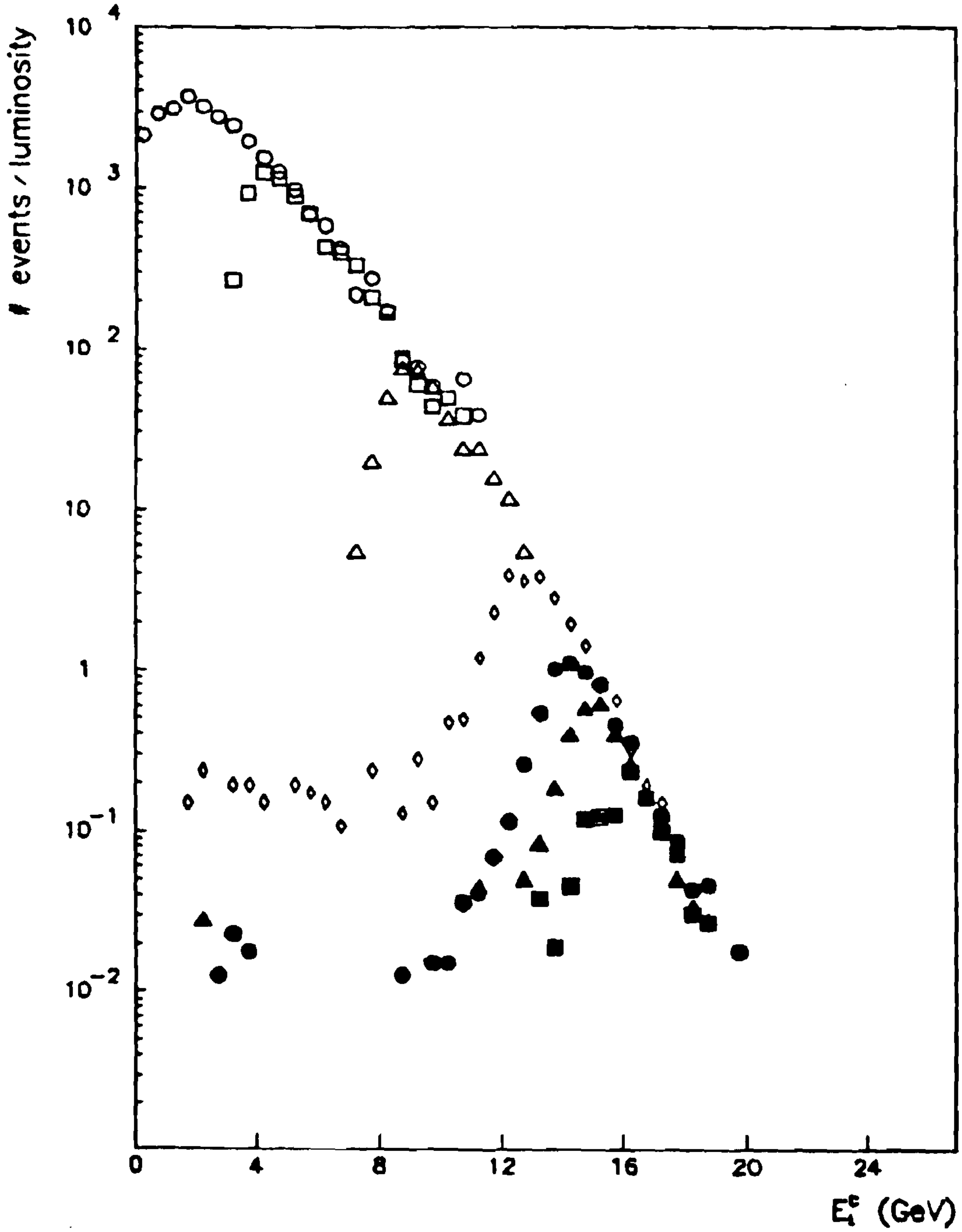

FIG. 4-1. Raw E_t distributions for several runs. ○ run 979. □ run 619. △ run 622. ◊ run 627. ● run 688. ▲ run 784. ■ run 772.

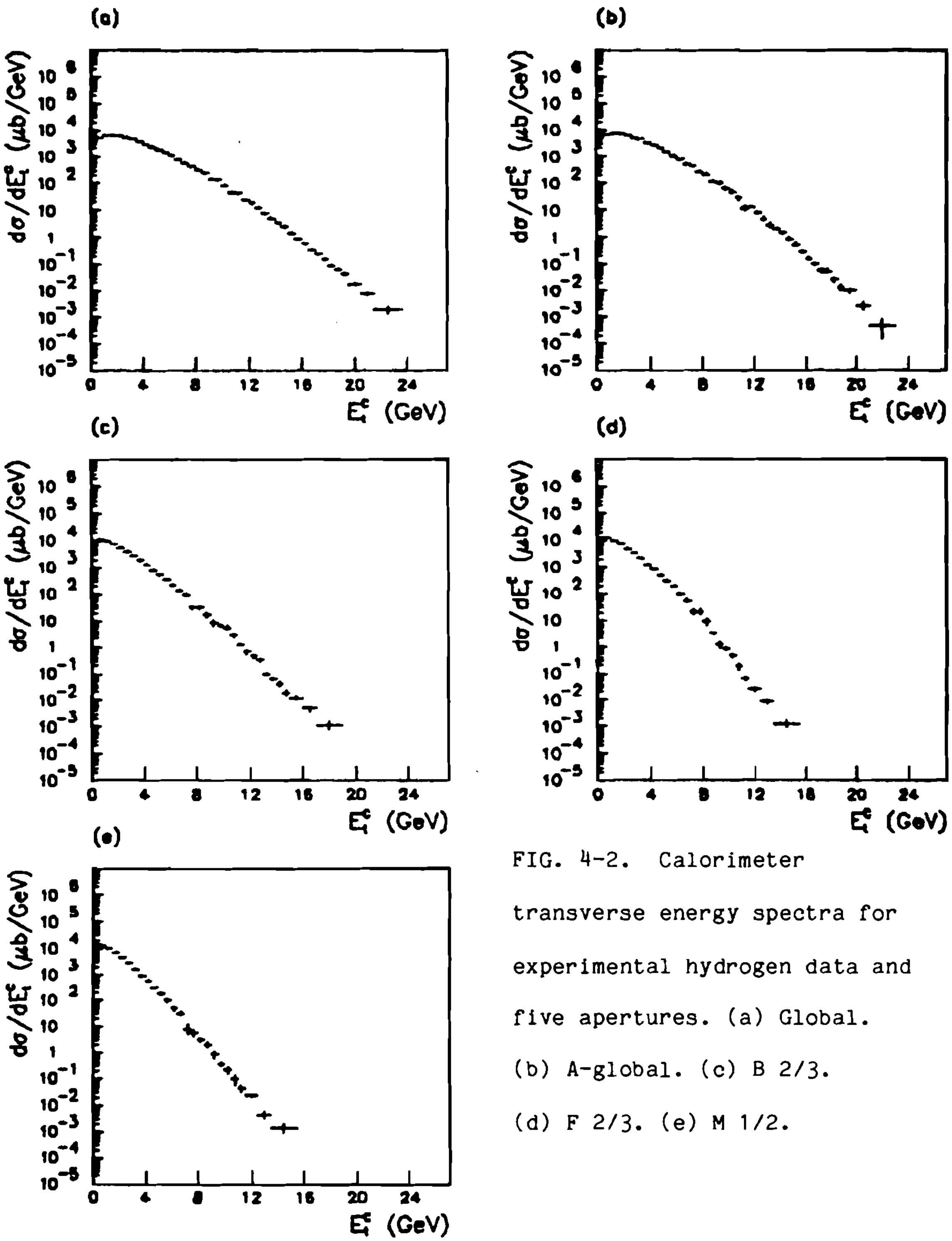

FIG. 4-2. Calorimeter transverse energy spectra for experimental hydrogen data and five apertures. (a) Global. (b) A-global. (c) B 2/3. (d) F 2/3. (e) M 1/2.

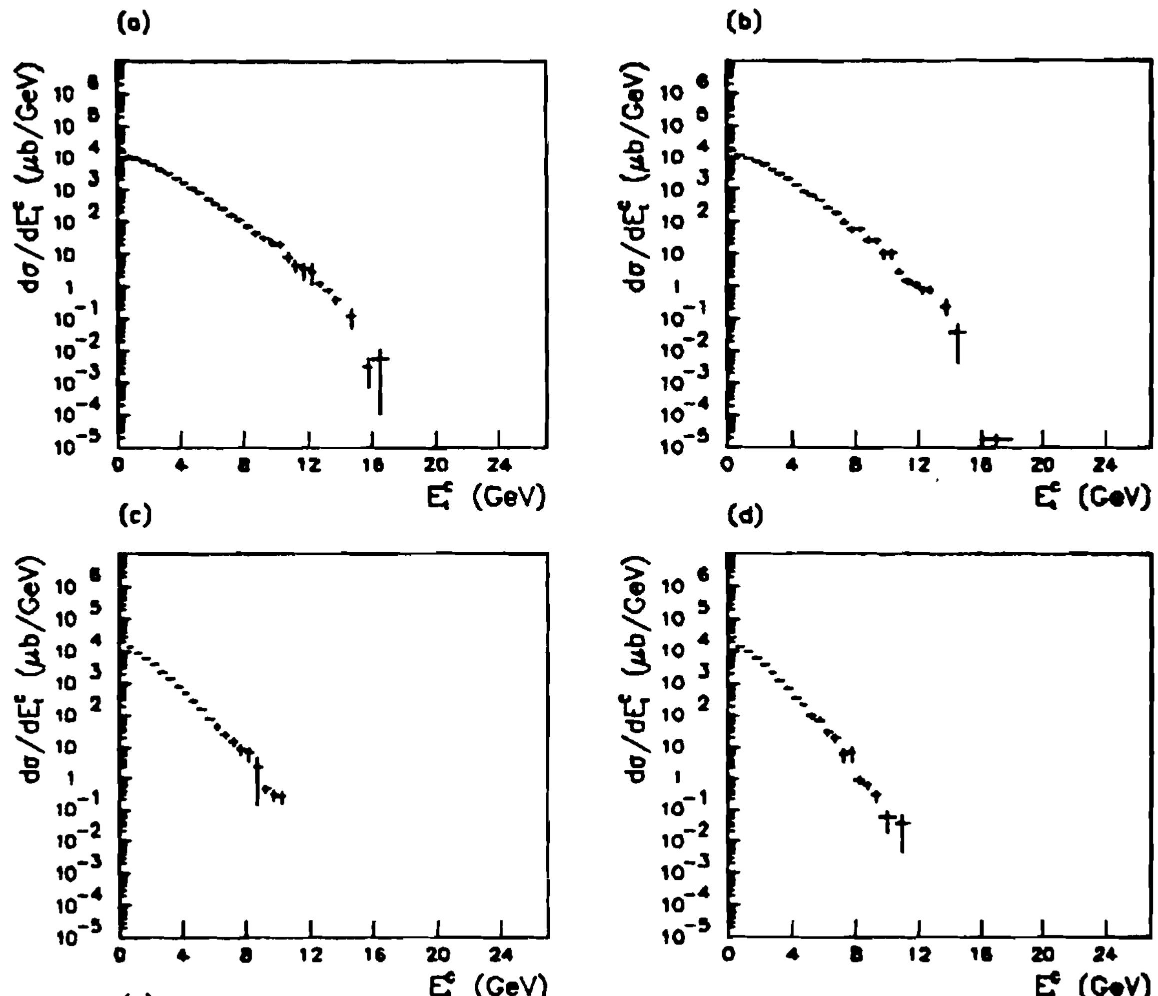

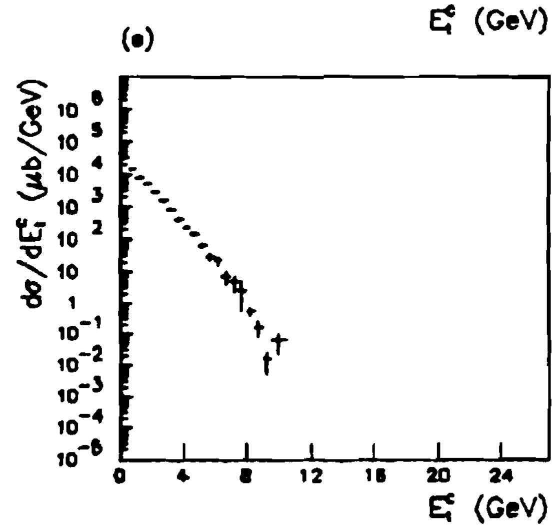

FIG. 4-3. Calorimeter transverse energy spectra for LPS Monte Carlo data and five apertures. (a) Global. (b) A-global. (c) B 2/3. (d) F 2/3. (e) M 1/2.

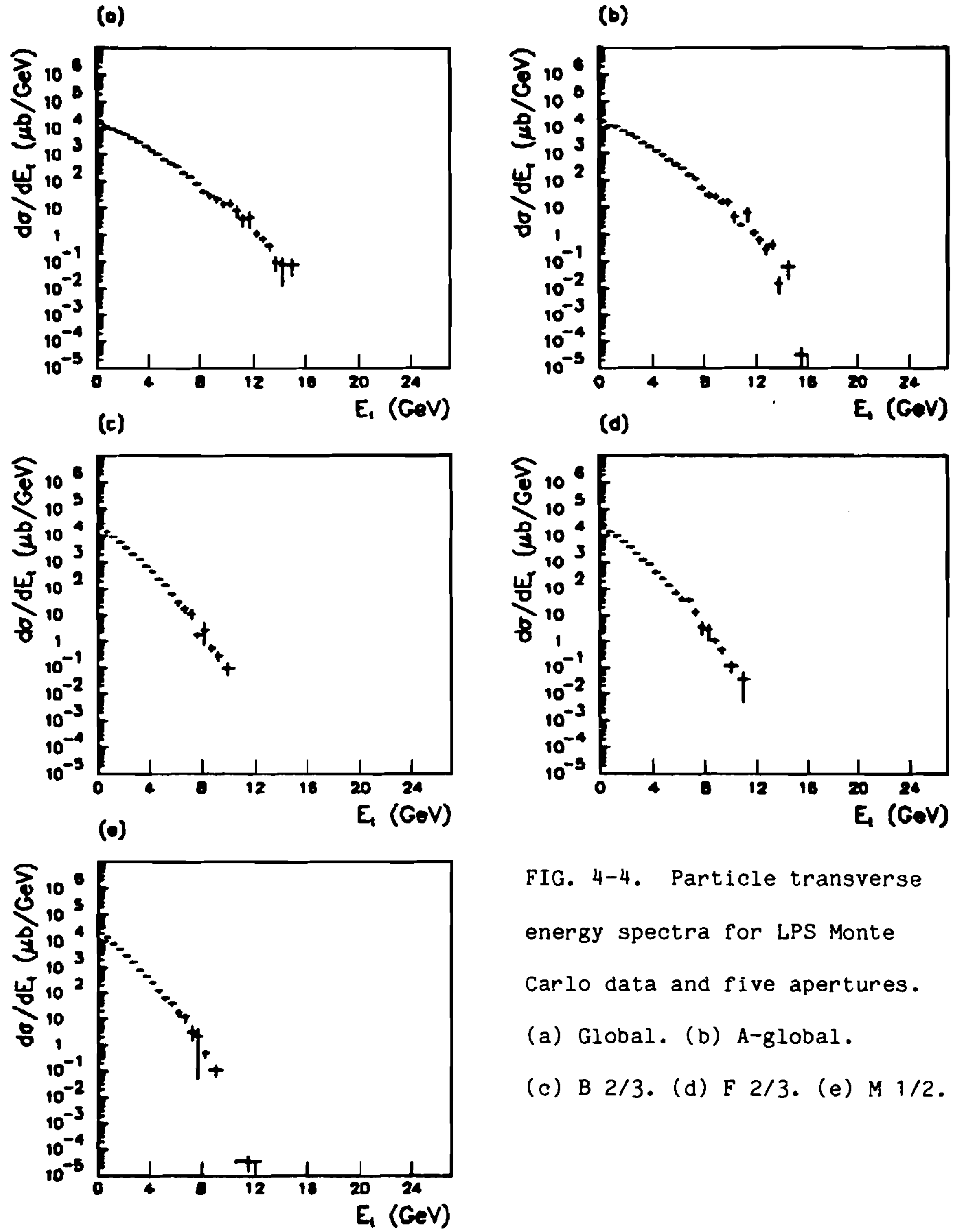

FIG. 4-4. Particle transverse energy spectra for LPS Monte Carlo data and five apertures. (a) Global. (b) A-global. (c) B 2/3. (d) F 2/3. (e) M 1/2.

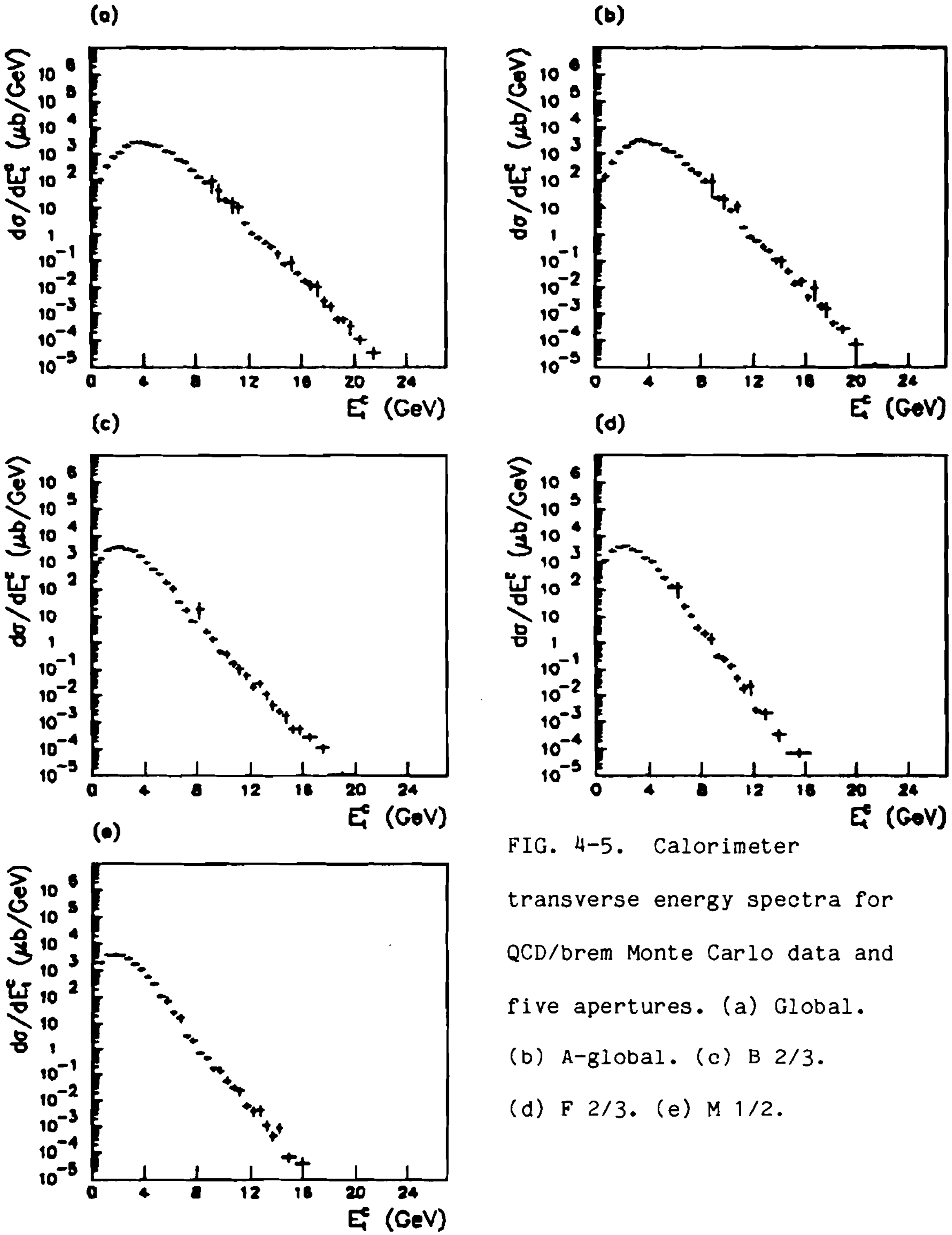

FIG. 4-5. Calorimeter transverse energy spectra for QCD/brem Monte Carlo data and five apertures. (a) Global. (b) A-global. (c) B 2/3. (d) F 2/3. (e) M 1/2.

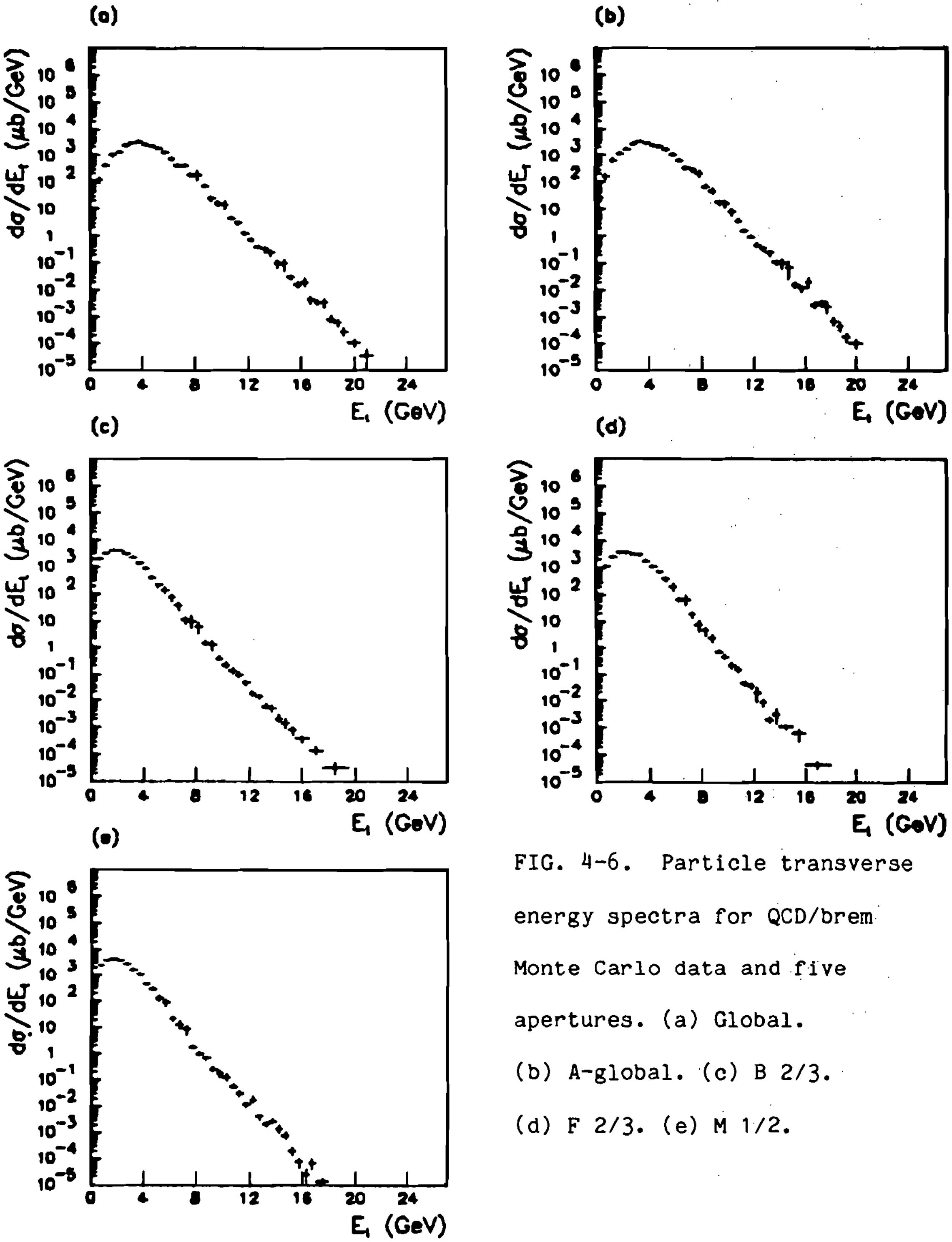

FIG. 4-6. Particle transverse energy spectra for QCD/brem Monte Carlo data and five apertures. (a) Global. (b) A-global. (c) B 2/3. (d) F 2/3. (e) M 1/2.

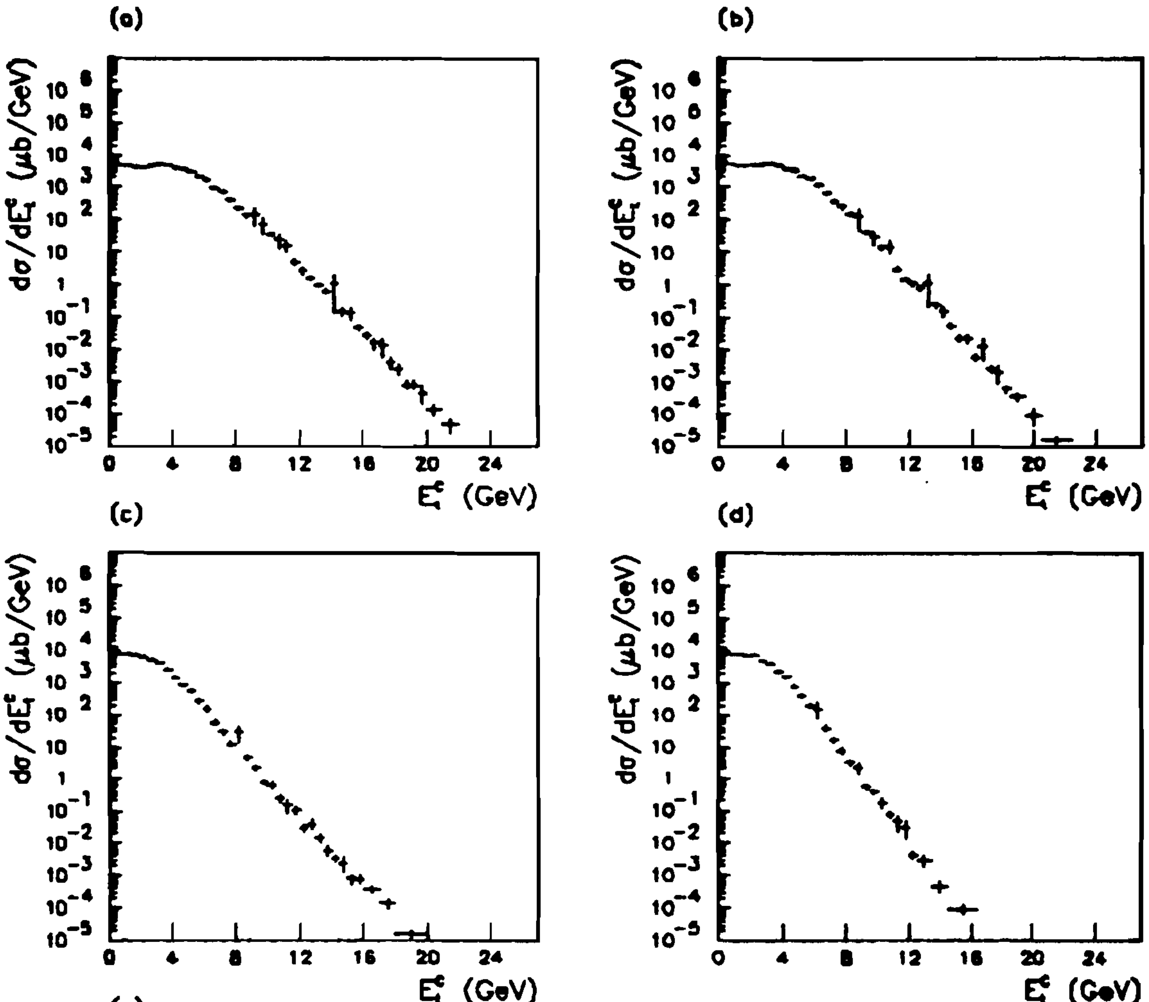

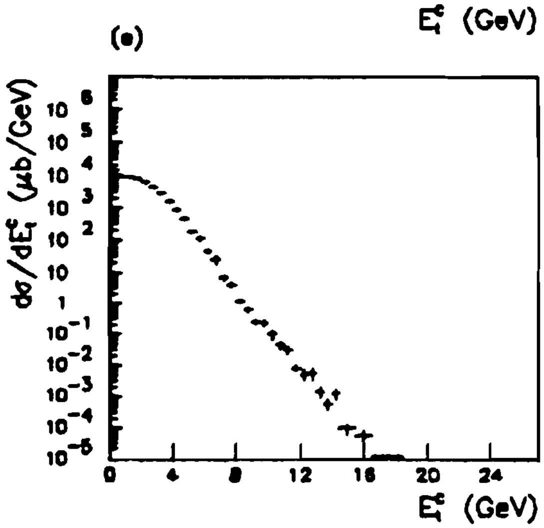

FIG. 4-7. Calorimeter transverse energy spectra for Hybrid Monte Carlo data and five apertures. (a) Global. (b) A-global. (c) B 2/3. (d) F 2/3. (e) M 1/2.

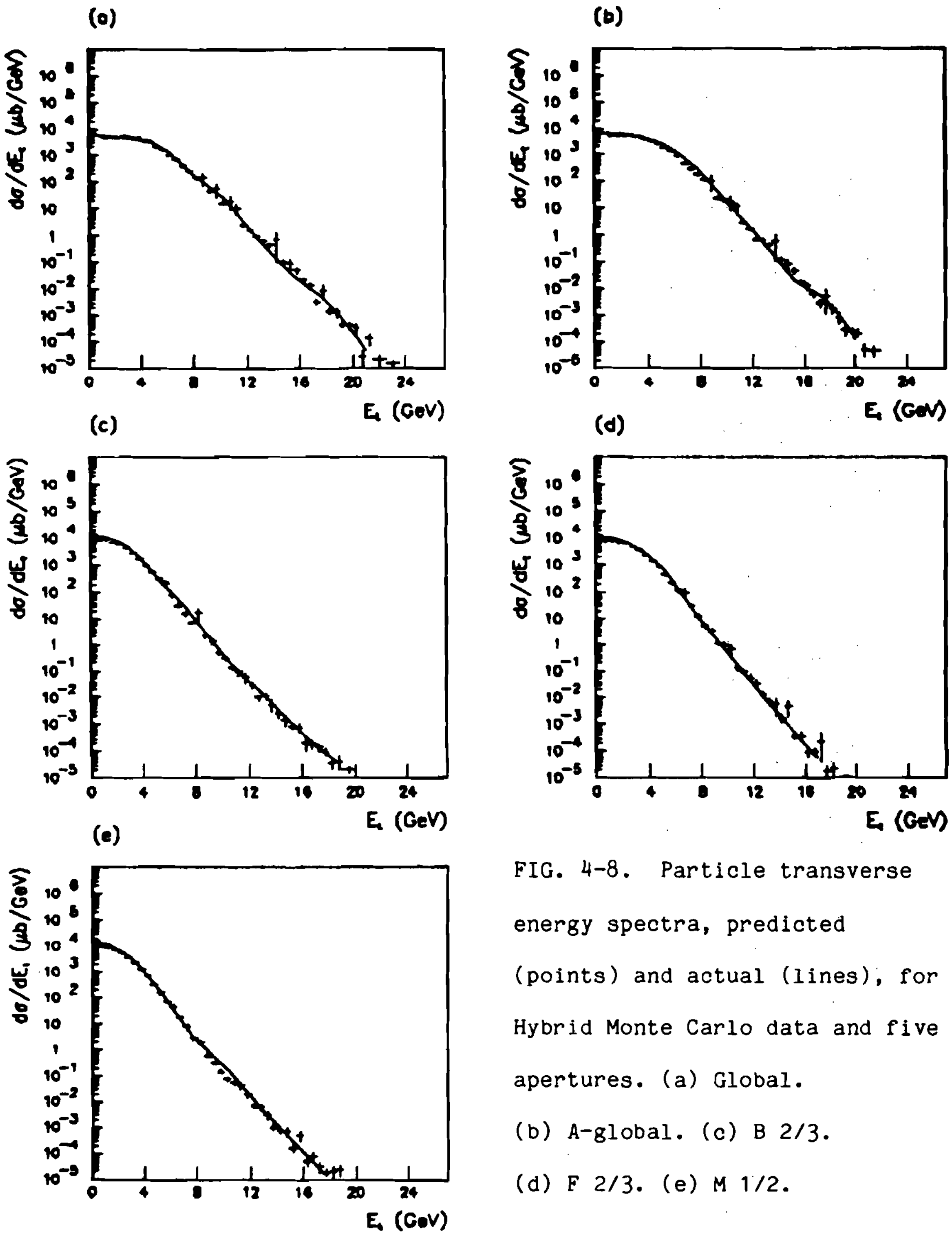

FIG. 4-8. Particle transverse energy spectra, predicted (points) and actual (lines), for Hybrid Monte Carlo data and five apertures. (a) Global. (b) A-global. (c) B 2/3. (d) F 2/3. (e) M 1/2.

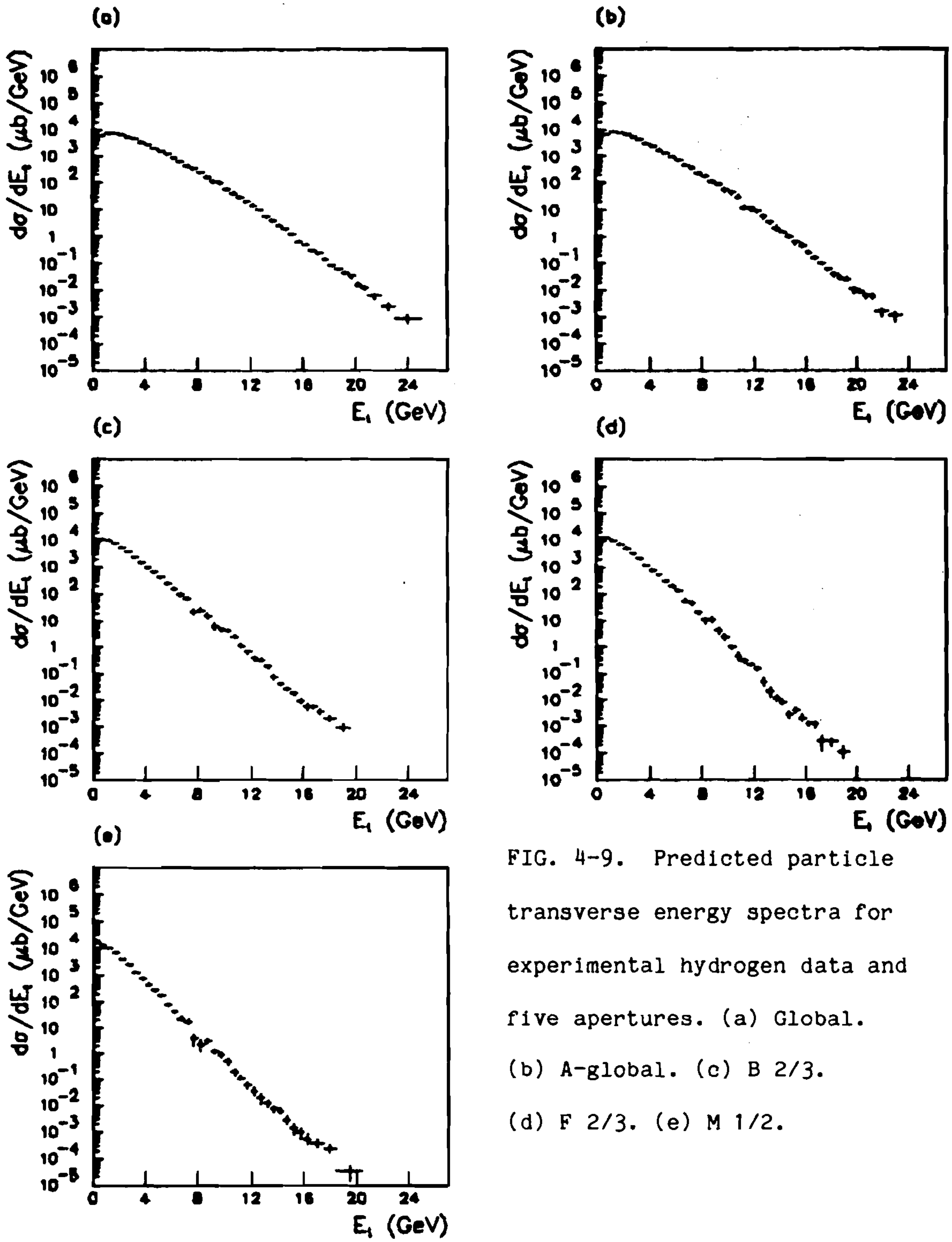

FIG. 4-9. Predicted particle transverse energy spectra for experimental hydrogen data and five apertures. (a) Global. (b) A-global. (c) B 2/3. (d) F 2/3. (e) M 1/2.

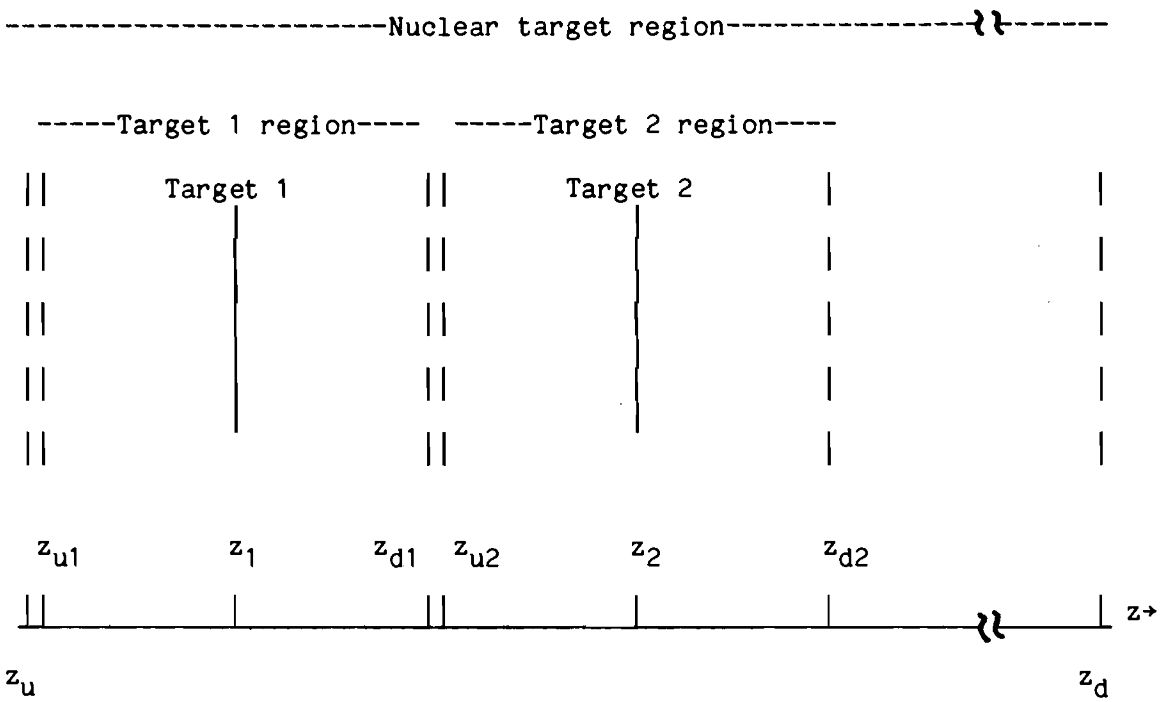

FIG. 4-10. Nuclear target region. The z coordinates are defined as follows: z_1 and z_2 are the physical target positions, separated by 50 mm (see Table 2-1). z_{u1}, z_{d1} = $z_1 \pm 24$ mm. z_{u2}, z_{d2} = $z_2 \pm 24$ mm. $z_u = z_1 - 26$ mm. $z_d = z_u + 160$ mm.

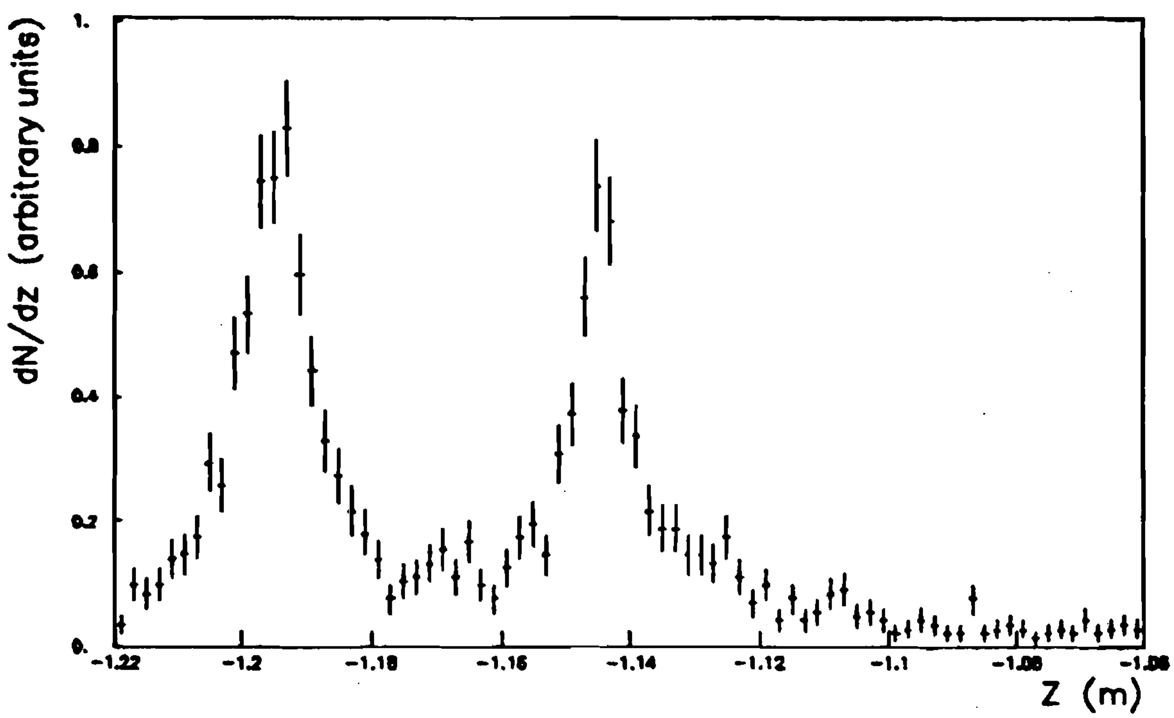

FIG. 4-11. Vertex positions in nuclear target region for events with $13.0 < \text{Global } E_t^C < 15.0$ GeV.

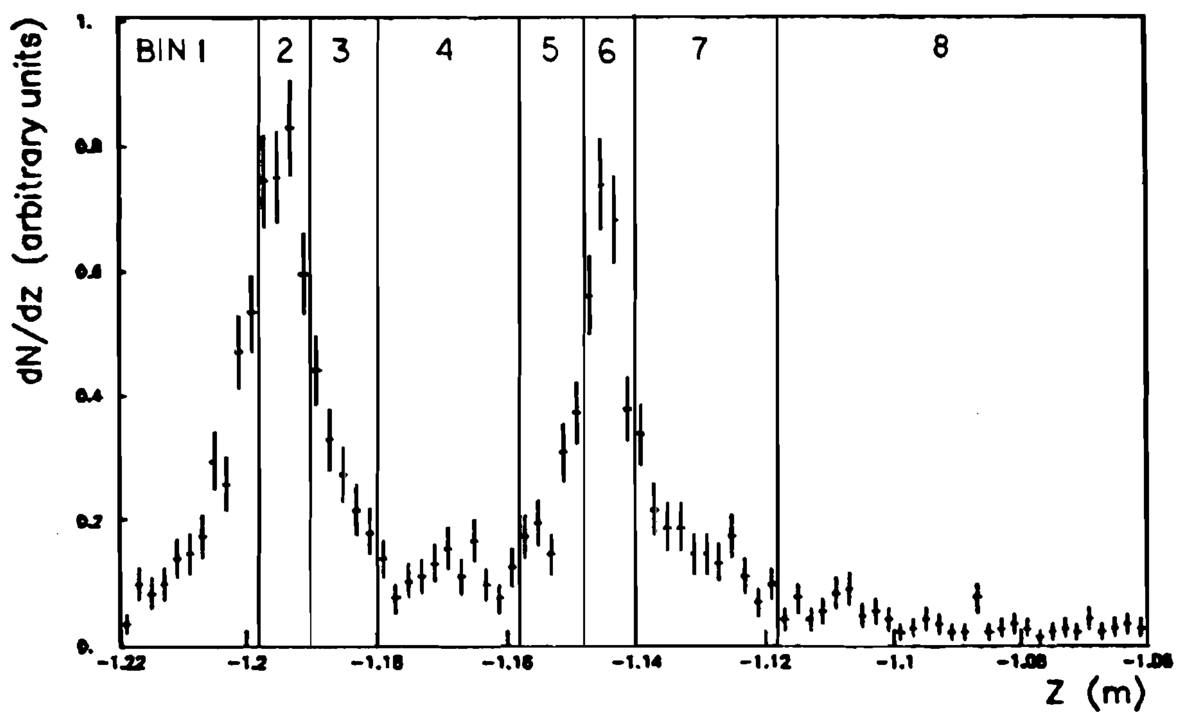

FIG. 4-12. Vertex positions in nuclear target region with eight nonuniform bins in z superimposed.

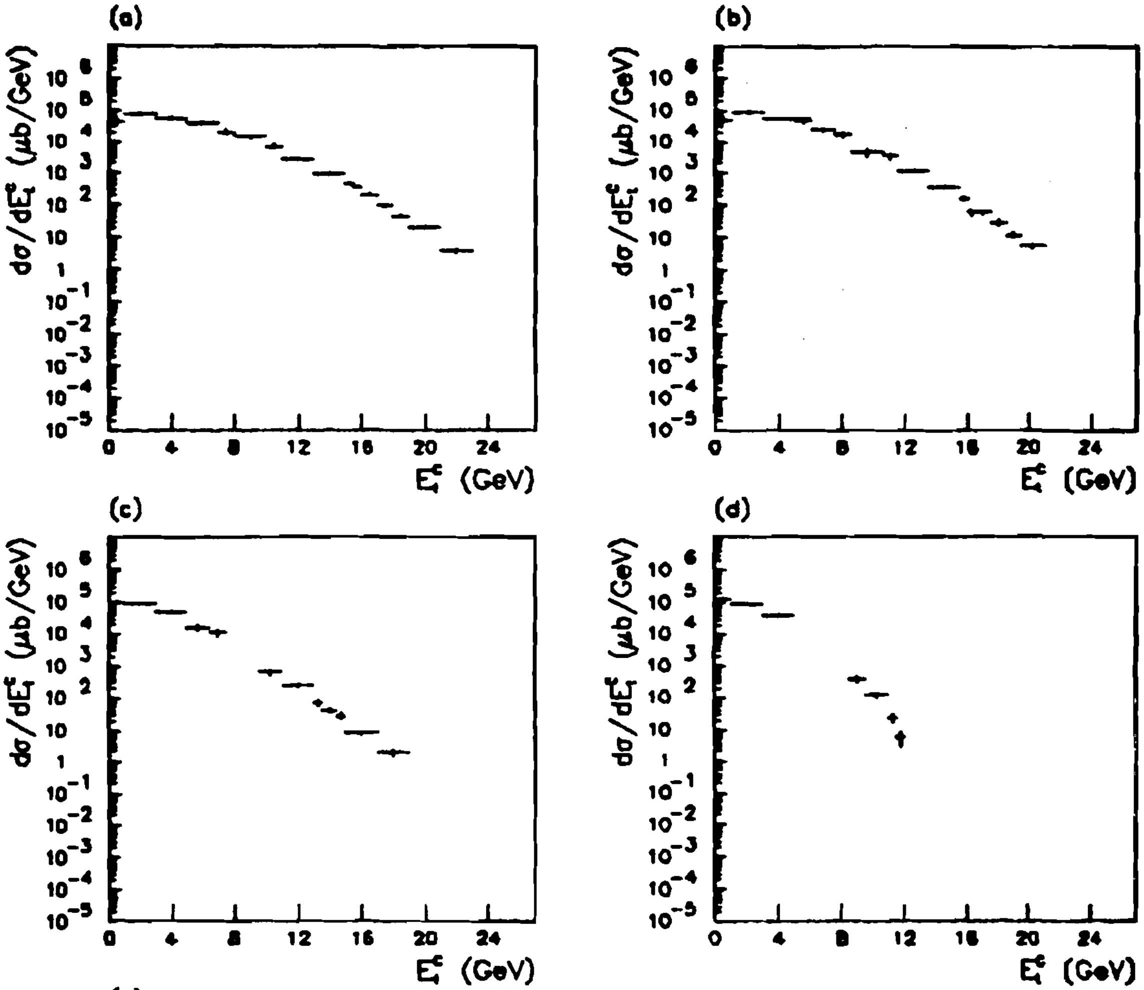

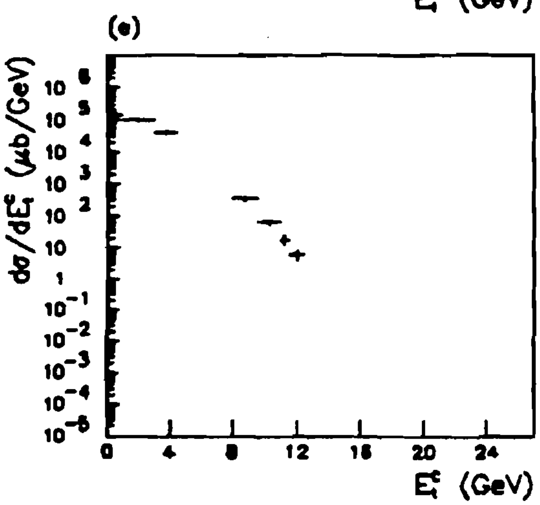

FIG. 4-13. Calorimeter transverse energy spectra for aluminum data and five apertures. (a) Global. (b) A-global. (c) B 2/3. (d) F 2/3. (e) M 1/2.

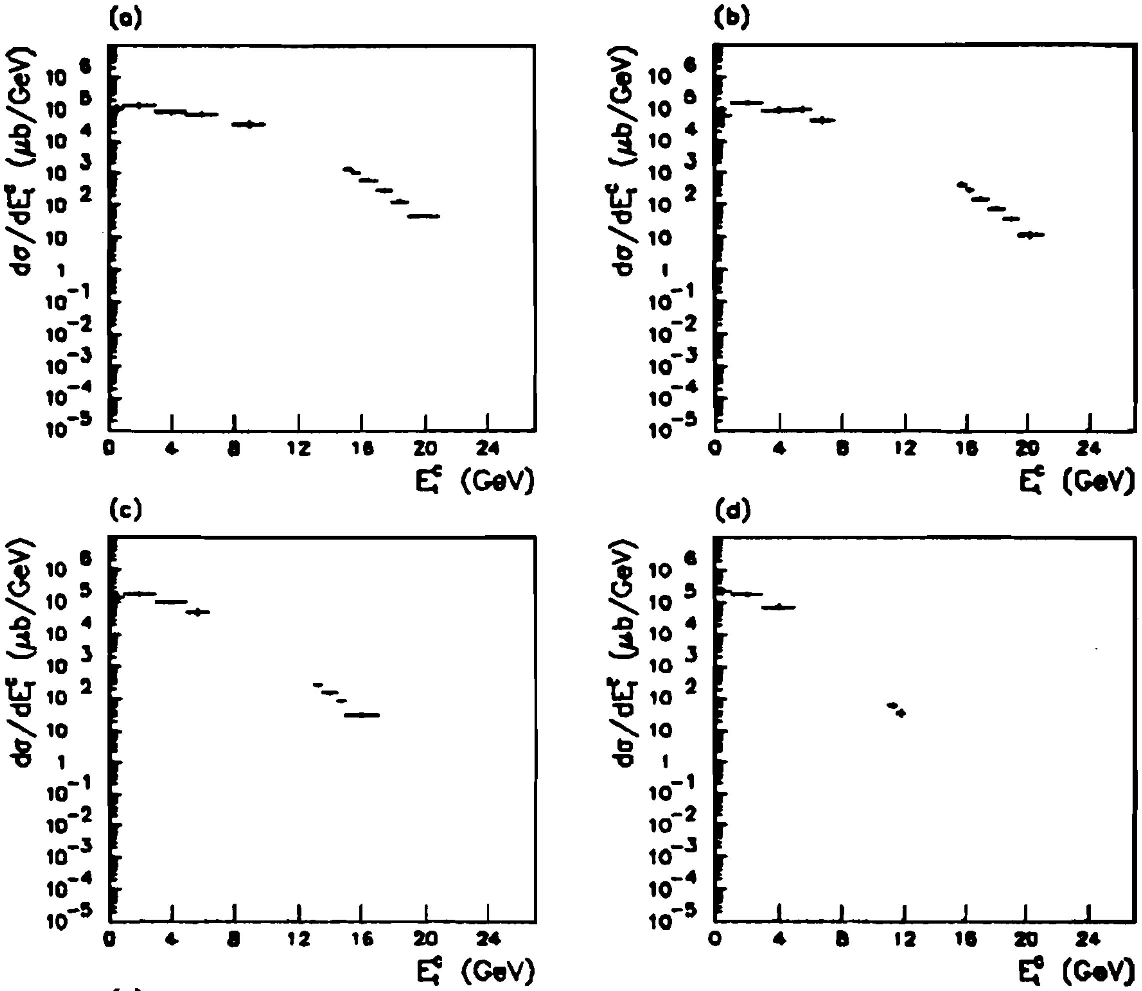

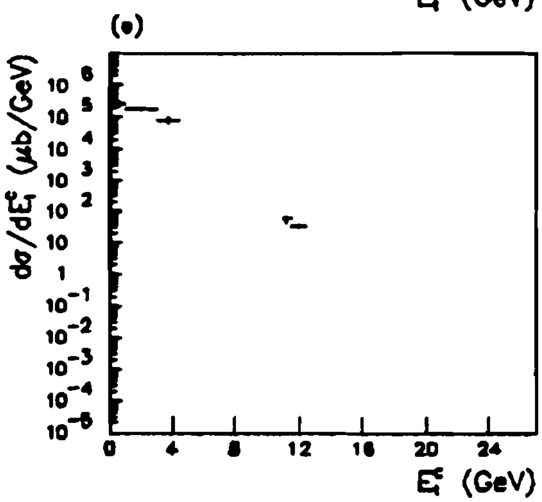

FIG. 4-14. Calorimeter transverse energy spectra for copper data and five apertures. (a) Global. (b) A-global. (c) B 2/3. (d) F 2/3. (e) M 1/2.

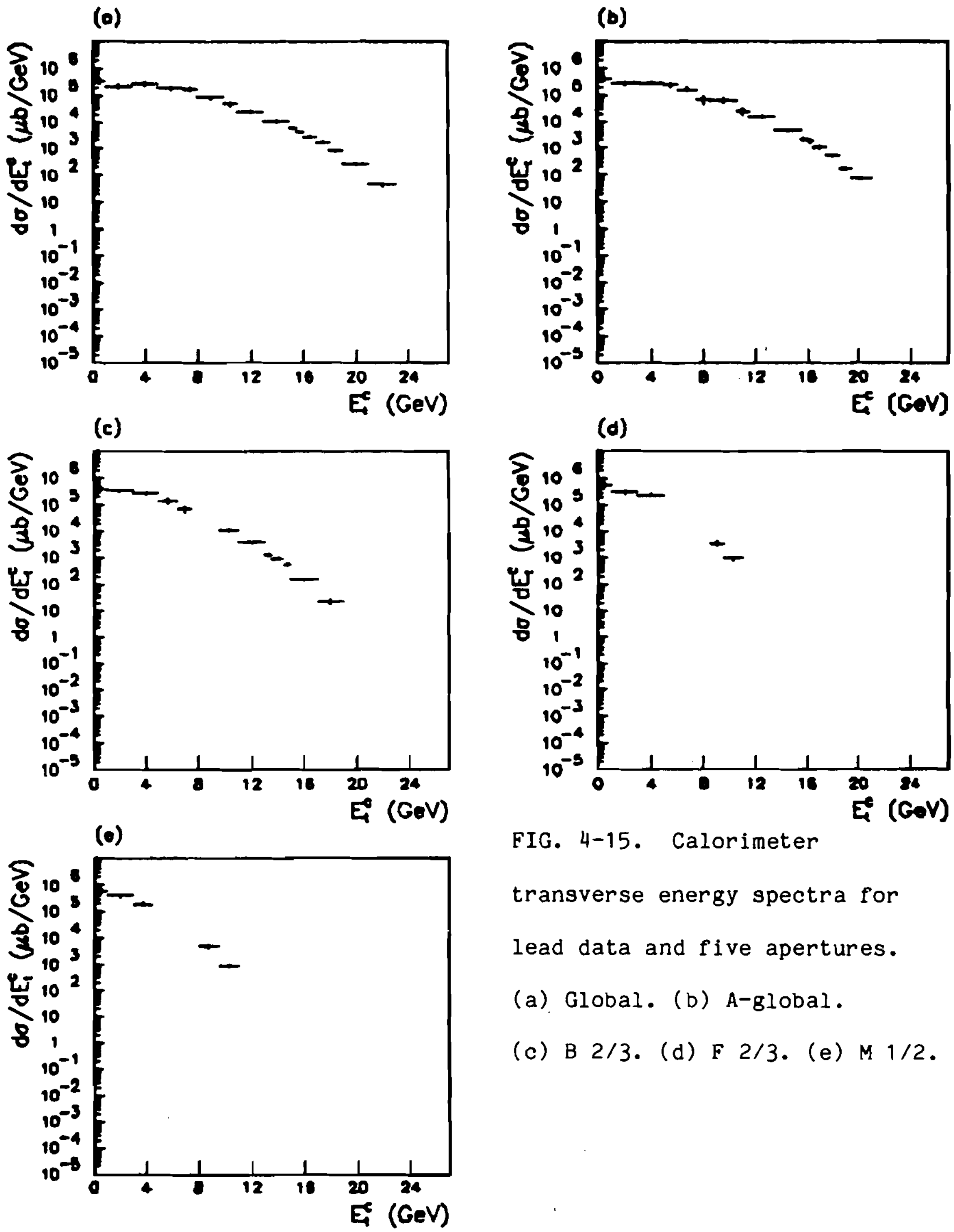

FIG. 4-15. Calorimeter transverse energy spectra for lead data and five apertures. (a) Global. (b) A-global. (c) B 2/3. (d) F 2/3. (e) M 1/2.

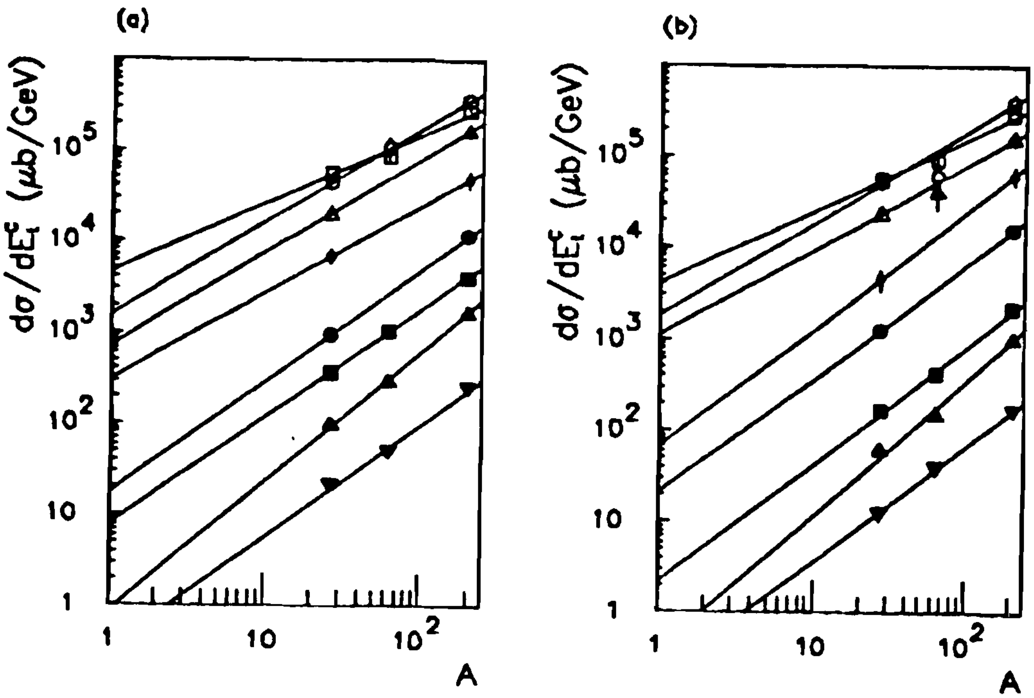

FIG. 4-16. $d\sigma/dE_t^C$ as a function of A for five apertures. Different symbols represent different E_t^C regions; for clarity, not all E_t^C bins are shown. (a) Global. ○ 0 GeV < E_t^C < 1 GeV. □ 3 GeV < E_t^C < 5 GeV. △ 7 GeV < E_t^C < 8 GeV. ◆ 10 GeV < E_t^C < 11 GeV. ● 13 GeV < E_t^C < 15 GeV. ■ 15.5 GeV < E_t^C < 16 GeV. ▲ 17 GeV < E_t^C < 18 GeV. ▼ 19 GeV < E_t^C < 21 GeV. (b) A-global. ○ 0 GeV < E_t^C < 1 GeV. □ 3 GeV < E_t^C < 5 GeV. △ 6 GeV < E_t^C < 7.5 GeV. ◆ 8.5 GeV < E_t^C < 10.5 GeV. ● 11.5 GeV < E_t^C < 13.5 GeV. ■ 15.5 GeV < E_t^C < 16 GeV. ▲ 16.5 GeV < E_t^C < 17.5 GeV. ▼ 18.5 GeV < E_t^C < 19.5 GeV.

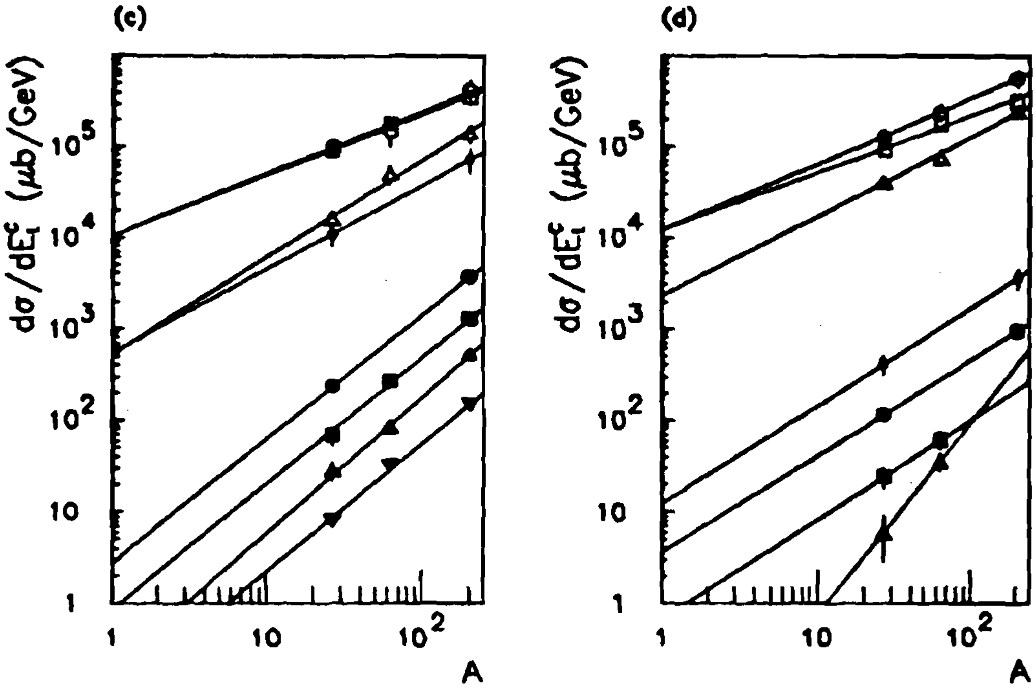

FIG. 4-16. (Continued). (c) B 2/3. ○ 0 GeV < E_t^C < 1 GeV. □ 1 GeV < E_t^C < 3 GeV. △ 5 GeV < E_t^C < 6.5 GeV. ◆ 6.5 GeV < E_t^C < 7.5 GeV. ● 11 GeV < E_t^C < 13 GeV. ■ 13 GeV < E_t^C < 13.5 GeV. ▲ 14.5 GeV < E_t^C < 15 GeV. ▼ 15 GeV < E_t^C < 17 GeV. (d) F 2/3. ○ 0 GeV < E_t^C < 1 GeV. □ 1 GeV < E_t^C < 3 GeV. △ 3 GeV < E_t^C < 5 GeV. ◆ 8.5 GeV < E_t^C < 9.5 GeV. ● 9.5 GeV < E_t^C < 11 GeV. ■ 11 GeV < E_t^C < 11.5 GeV. ▲ 11.5 GeV < E_t^C < 12 GeV.

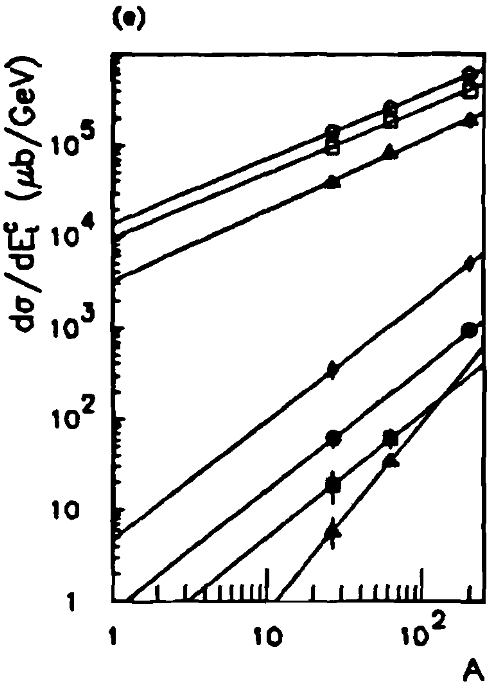

FIG. 4-16. (Continued). (e) M 1/2. ○ 0 GeV < E_t^C < 1 GeV. □ 1 GeV < E_t^C < 3 GeV. △ 3 GeV < E_t^C < 4 GeV. ◊ 8 GeV < E_t^C < 9.5 GeV. ● 9.5 GeV < E_t^C < 11 GeV. ■ 11 GeV < E_t^C < 11.5 GeV. ▲ 11.5 GeV < E_t^C < 12.5 GeV.

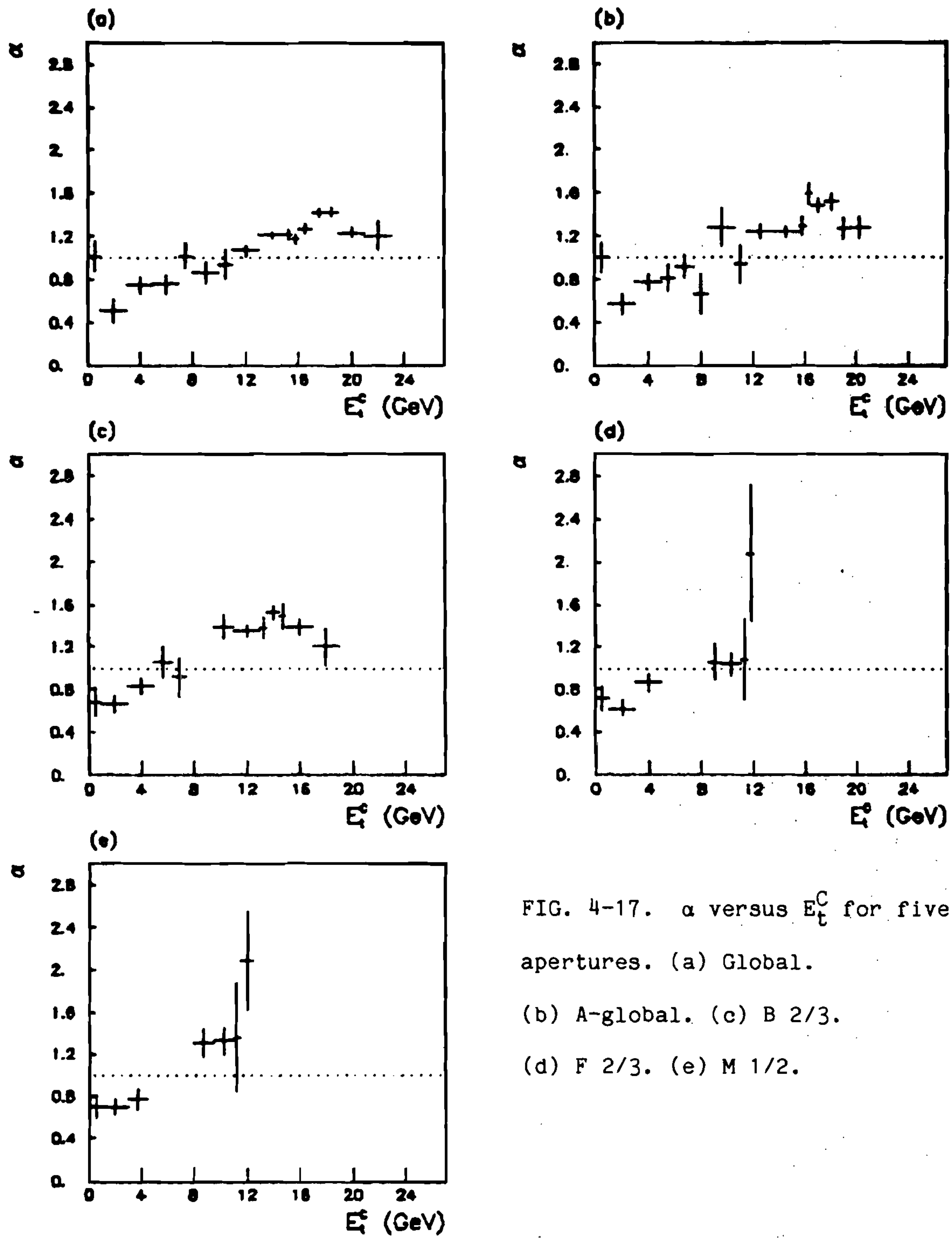

FIG. 4-17. α versus E_t^C for five apertures. (a) Global. (b) A-global. (c) B 2/3. (d) F 2/3. (e) M 1/2.

TABLE 4-1. Luminosities and Global E_t^C cuts for hydrogen data, Global trigger.

Run Group	Run Number	Luminosity (μb^{-1})	E_t^C cut (GeV)	Number of events
0	591	6.17[a]	13.0	71
	592	7.46[a]	13.0	86
	593	18.1[a]	11.0	1176
	619	0.186	7.0	190
	620	0.375	7.0	387
	621	0.565	10.0	68
	622	1.27	10.0	162
	625	5.92	13.0	88
	626	46.9	13.0	575
	627	55.2	13.0	614
	628	90.9[a]	17.0	31
	629	649.	18.0	85
	631	552.	18.0	99
	632	180.	18.0	31
Total				3663
A	663	149.	16.0	145
	672	66.2	16.0	44
	685	163.	15.5	209
	686	71.4	15.5	81
	688	395.	15.0	827
Total				1306
B	772	264.	17.0	67
	783	54.9	16.0	55

TABLE 4-1. (Continued)

Run Group	Run Number	Luminosity (μb^{-1})	E_t^C cut (GeV)	Number of events
	784	179.	16.0	128
	789	190.	15.5	201
	794	152.	15.0	300
Total				751
Grand total				5720

[a]Luminosity estimated using Global E_t^C cross section

TABLE 4-2. Restricted aperture E_t^C cuts as functions of Global E_t^C cuts.

E_t^C cut Global (GeV)	E_t^C cuts, restricted apertures (GeV) A-Global	B 2/3	F 2/3	M 1/2
7.0	7.5	6.5	6.0	5.5
10.0	10.5	9.0	8.0	7.5
11.0	11.5	9.5	8.5	8.0
13.0	13.5	11.0	9.5	9.5
15.0	15.5	13.0	11.0	11.0
15.5	16.0	13.0	11.0	11.5
16.0	16.5	13.5	11.5	11.5
17.0	17.5	14.5	12.0	12.5
18.0	18.5	15.0	12.5	13.0

TABLE 4-3. Calorimeter transverse energy spectra for experimental hydrogen data and five apertures.

GLOBAL

ET BIN EDGES (GEV)		CROSS SECTION (MICROBARNS)
.0	.5	(4.14 +/- .09) E+03
.5	1.0	(5.26 +/- .10) E+03
1.0	1.5	(6.51 +/- .11) E+03
1.5	2.0	(6.93 +/- .11) E+03
2.0	2.5	(6.32 +/- .11) E+03
2.5	3.0	(5.58 +/- .10) E+03
3.0	3.5	(4.77 +/- .09) E+03
3.5	4.0	(3.81 +/- .08) E+03
4.0	4.5	(3.02 +/- .07) E+03
4.5	5.0	(2.46 +/- .07) E+03
5.0	5.5	(1.91 +/- .06) E+03
5.5	6.0	(1.45 +/- .05) E+03
6.0	6.5	(1.18 +/- .05) E+03
6.5	7.0	(8.25 +/- .38) E+02
7.0	7.5	(5.99 +/- .27) E+02
7.5	8.0	(4.41 +/- .23) E+02
8.0	8.5	(3.44 +/- .20) E+02
8.5	9.0	(2.62 +/- .18) E+02
9.0	9.5	(1.55 +/- .14) E+02
9.5	10.0	(1.43 +/- .13) E+02
10.0	10.5	(8.59 +/- .70) E+01
10.5	11.0	(4.95 +/- .53) E+01
11.0	11.5	(4.41 +/- .20) E+01
11.5	12.0	(2.66 +/- .16) E+01
12.0	12.5	(2.06 +/- .14) E+01
12.5	13.0	(1.35 +/- .11) E+01
13.0	13.5	(7.88 +/- .33) E+00
13.5	14.0	(5.34 +/- .27) E+00
14.0	14.5	(3.57 +/- .22) E+00
14.5	15.0	(2.62 +/- .19) E+00
15.0	15.5	(1.53 +/- .07) E+00
15.5	16.0	(8.90 +/- .40) E-01
16.0	16.5	(6.10 +/- .28) E-01
16.5	17.0	(3.60 +/- .22) E-01
17.0	17.5	(2.51 +/- .16) E-01
17.5	18.0	(1.62 +/- .13) E-01
18.0	18.5	(9.45 +/- .76) E-02
18.5	19.0	(6.54 +/- .63) E-02
19.0	19.5	(4.67 +/- .54) E-02
19.5	20.5	(1.88 +/- .24) E-02
20.5	21.5	(7.57 +/- 1.55) E-03
21.5	23.5	(1.97 +/- .57) E-03

TABLE 4-3. (Continued)

A-GLOBAL

ET BIN EDGES (GEV)		CROSS SECTION (MICROBARNS)
.0	.5	(5.14 +/- .10) E+03
.5	1.0	(6.43 +/- .11) E+03
1.0	1.5	(7.66 +/- .12) E+03
1.5	2.0	(7.36 +/- .11) E+03
2.0	2.5	(6.47 +/- .11) E+03
2.5	3.0	(5.47 +/- .10) E+03
3.0	3.5	(4.62 +/- .09) E+03
3.5	4.0	(3.36 +/- .08) E+03
4.0	4.5	(2.66 +/- .07) E+03
4.5	5.0	(1.96 +/- .06) E+03
5.0	5.5	(1.49 +/- .05) E+03
5.5	6.0	(1.09 +/- .04) E+03
6.0	6.5	(8.00 +/- .38) E+02
6.5	7.0	(5.51 +/- .31) E+02
7.0	7.5	(4.44 +/- .28) E+02
7.5	8.0	(2.74 +/- .18) E+02
8.0	8.5	(2.16 +/- .16) E+02
8.5	9.0	(1.24 +/- .12) E+02
9.0	9.5	(1.06 +/- .11) E+02
9.5	10.0	(6.67 +/- .90) E+01
10.0	10.5	(4.89 +/- .77) E+01
10.5	11.0	(2.85 +/- .41) E+01
11.0	11.5	(1.20 +/- .27) E+01
11.5	12.0	(1.37 +/- .11) E+01
12.0	12.5	(8.33 +/- .88) E+00
12.5	13.0	(4.91 +/- .68) E+00
13.0	13.5	(2.96 +/- .53) E+00
13.5	14.0	(2.05 +/- .17) E+00
14.0	14.5	(1.44 +/- .14) E+00
14.5	15.0	(8.79 +/- 1.12) E-01
15.0	15.5	(5.30 +/- .87) E-01
15.5	16.0	(2.90 +/- .29) E-01
16.0	16.5	(1.60 +/- .17) E-01
16.5	17.0	(1.02 +/- .12) E-01
17.0	17.5	(5.75 +/- .87) E-02
17.5	18.0	(5.31 +/- .75) E-02
18.0	18.5	(2.50 +/- .52) E-02
18.5	19.0	(1.27 +/- .28) E-02
19.0	20.0	(9.69 +/- 1.74) E-03
20.0	21.0	(2.73 +/- .96) E-03
21.0	23.0	(4.54 +/- 3.21) E-04

TABLE 4-3. (Continued)

B 2/3

ET BIN EDGES (GEV)		CROSS SECTION (MICROBARNS)
.0	.5	(1.01 +/- .01) E+04
.5	1.0	(1.06 +/- .01) E+04
1.0	1.5	(9.84 +/- .13) E+03
1.5	2.0	(7.70 +/- .12) E+03
2.0	2.5	(5.80 +/- .10) E+03
2.5	3.0	(4.14 +/- .09) E+03
3.0	3.5	(2.92 +/- .07) E+03
3.5	4.0	(1.86 +/- .06) E+03
4.0	4.5	(1.31 +/- .05) E+03
4.5	5.0	(8.10 +/- .38) E+02
5.0	5.5	(5.53 +/- .31) E+02
5.5	6.0	(3.31 +/- .24) E+02
6.0	6.5	(2.15 +/- .20) E+02
6.5	7.0	(1.32 +/- .13) E+02
7.0	7.5	(9.65 +/- 1.08) E+01
7.5	8.0	(3.46 +/- .65) E+01
8.0	8.5	(3.46 +/- .65) E+01
8.5	9.0	(1.79 +/- .48) E+01
9.0	9.5	(8.54 +/- 2.28) E+00
9.5	10.0	(6.95 +/- .81) E+00
10.0	10.5	(5.65 +/- .73) E+00
10.5	11.0	(2.96 +/- .53) E+00
11.0	11.5	(1.26 +/- .13) E+00
11.5	12.0	(6.56 +/- .97) E-01
12.0	12.5	(4.74 +/- .83) E-01
12.5	13.0	(3.21 +/- .68) E-01
13.0	13.5	(9.68 +/- 1.33) E-02
13.5	14.0	(6.90 +/- .95) E-02
14.0	14.5	(4.22 +/- .75) E-02
14.5	15.0	(1.88 +/- .45) E-02
15.0	16.0	(1.21 +/- .19) E-02
16.0	17.0	(4.85 +/- 1.25) E-03
17.0	19.0	(1.21 +/- .46) E-03

TABLE 4-3. (Continued)

F 2/3

ET BIN EDGES (GEV)		CROSS SECTION (MICROBARNS)
.0	.5	(1.24 +/- .01) E+04
.5	1.0	(1.19 +/- .01) E+04
1.0	1.5	(1.02 +/- .01) E+04
1.5	2.0	(7.66 +/- .12) E+03
2.0	2.5	(5.29 +/- .10) E+03
2.5	3.0	(3.46 +/- .08) E+03
3.0	3.5	(2.20 +/- .06) E+03
3.5	4.0	(1.24 +/- .05) E+03
4.0	4.5	(8.44 +/- .39) E+02
4.5	5.0	(5.08 +/- .30) E+02
5.0	5.5	(3.13 +/- .24) E+02
5.5	6.0	(2.00 +/- .19) E+02
6.0	6.5	(9.18 +/- 1.05) E+01
6.5	7.0	(5.60 +/- .83) E+01
7.0	7.5	(2.14 +/- .52) E+01
7.5	8.0	(2.14 +/- .52) E+01
8.0	8.5	(9.11 +/- 2.35) E+00
8.5	9.0	(3.43 +/- .57) E+00
9.0	9.5	(1.20 +/- .35) E+00
9.5	10.0	(8.37 +/- 1.09) E-01
10.0	10.5	(4.60 +/- .81) E-01
10.5	11.0	(1.81 +/- .52) E-01
11.0	11.5	(6.46 +/- 1.09) E-02
11.5	12.5	(2.52 +/- .39) E-02
12.5	13.5	(9.09 +/- 1.69) E-03
13.5	15.5	(1.36 +/- .48) E-03

TABLE 4-3. (Continued)

M 1/2

ET BIN EDGES (GEV)		CROSS SECTION (MICROBARNS)
.0	.5	(1.48 +/- .02) E+04
.5	1.0	(1.31 +/- .02) E+04
1.0	1.5	(1.04 +/- .01) E+04
1.5	2.0	(7.04 +/- .11) E+03
2.0	2.5	(4.51 +/- .09) E+03
2.5	3.0	(2.78 +/- .07) E+03
3.0	3.5	(1.62 +/- .05) E+03
3.5	4.0	(9.05 +/- .40) E+02
4.0	4.5	(5.83 +/- .32) E+02
4.5	5.0	(3.01 +/- .23) E+02
5.0	5.5	(1.81 +/- .18) E+02
5.5	6.0	(9.41 +/- 1.07) E+01
6.0	6.5	(5.00 +/- .78) E+01
6.5	7.0	(3.34 +/- .64) E+01
7.0	7.5	(8.34 +/- 3.41) E+00
7.5	8.0	(5.69 +/- 1.90) E+00
8.0	8.5	(2.96 +/- .53) E+00
8.5	9.0	(2.04 +/- .44) E+00
9.0	9.5	(8.33 +/- 2.95) E-01
9.5	10.0	(3.63 +/- .73) E-01
10.0	10.5	(2.09 +/- .56) E-01
10.5	11.0	(9.77 +/- 3.99) E-02
11.0	11.5	(4.34 +/- 1.16) E-02
11.5	12.5	(2.43 +/- .40) E-02
12.5	13.5	(4.51 +/- 1.41) E-03
13.5	15.5	(1.36 +/- .48) E-03

TABLE 4-4. Calorimeter transverse energy spectra for LPS Monte Carlo data and five apertures.

GLOBAL

ET BIN EDGES (GEV)		CROSS SECTION (MICROBARNS)
.0	.5	(1.49 +/- .03) E+04
.5	1.0	(1.15 +/- .03) E+04
1.0	1.5	(9.59 +/- .25) E+03
1.5	2.0	(7.69 +/- .22) E+03
2.0	2.5	(6.02 +/- .19) E+03
2.5	3.0	(4.40 +/- .15) E+03
3.0	3.5	(3.26 +/- .12) E+03
3.5	4.0	(2.30 +/- .09) E+03
4.0	4.5	(1.62 +/- .07) E+03
4.5	5.0	(1.15 +/- .06) E+03
5.0	5.5	(8.66 +/- .48) E+02
5.5	6.0	(5.42 +/- .33) E+02
6.0	6.5	(3.97 +/- .27) E+02
6.5	7.0	(2.65 +/- .21) E+02
7.0	7.5	(1.69 +/- .16) E+02
7.5	8.0	(1.22 +/- .16) E+02
8.0	8.5	(7.69 +/- 1.08) E+01
8.5	9.0	(4.61 +/- .81) E+01
9.0	9.5	(3.28 +/- .67) E+01
9.5	10.0	(2.36 +/- .56) E+01
10.0	10.5	(2.12 +/- .53) E+01
10.5	11.0	(8.92 +/- 3.00) E+00
11.0	11.5	(4.81 +/- 1.77) E+00
11.5	12.0	(3.46 +/- 1.87) E+00
12.0	12.5	(3.09 +/- 1.94) E+00
12.5	13.0	(1.30 +/- .23) E+00
13.0	13.5	(7.95 +/- 1.76) E-01
13.5	14.0	(4.13 +/- 1.32) E-01
14.5	15.0	(1.31 +/- .79) E-01
15.5	16.0	(3.19 +/- 2.45) E-03
16.0	17.0	(5.87 +/- 5.76) E-03

TABLE 4-4. (Continued)

A-GLOBAL

ET BIN EDGES (GEV)		CROSS SECTION (MICROBARNS)
.0	.5	(1.65 +/- .03) E+04
.5	1.0	(1.23 +/- .03) E+04
1.0	1.5	(9.80 +/- .25) E+03
1.5	2.0	(7.67 +/- .21) E+03
2.0	2.5	(5.80 +/- .18) E+03
2.5	3.0	(4.10 +/- .14) E+03
3.0	3.5	(2.89 +/- .11) E+03
3.5	4.0	(1.96 +/- .08) E+03
4.0	4.5	(1.33 +/- .06) E+03
4.5	5.0	(8.79 +/- .46) E+02
5.0	5.5	(6.41 +/- .39) E+02
5.5	6.0	(4.58 +/- .30) E+02
6.0	6.5	(2.79 +/- .22) E+02
6.5	7.0	(1.87 +/- .19) E+02
7.0	7.5	(9.80 +/- 1.23) E+01
7.5	8.0	(5.82 +/- .92) E+01
8.0	8.5	(5.59 +/- .90) E+01
8.5	9.0	(2.60 +/- .58) E+01
9.0	9.5	(2.53 +/- .58) E+01
9.5	10.0	(1.03 +/- .35) E+01
10.0	10.5	(9.96 +/- 3.46) E+00
10.5	11.0	(2.79 +/- .33) E+00
11.0	11.5	(1.45 +/- .22) E+00
11.5	12.0	(1.11 +/- .21) E+00
12.0	12.5	(7.66 +/- 1.76) E-01
12.5	13.0	(7.48 +/- 1.76) E-01
13.5	14.0	(2.39 +/- 1.04) E-01
14.0	15.0	(3.63 +/- 3.22) E-02
16.0	18.0	(1.73 +/- 1.30) E-05

TABLE 4-4. (Continued)

B 2/3

ET BIN EDGES (GEV)		CROSS SECTION (MICROBARNS)
.0	.5	(2.61 +/- .04) E+04
.5	1.0	(1.41 +/- .03) E+04
1.0	1.5	(9.46 +/- .23) E+03
1.5	2.0	(5.97 +/- .17) E+03
2.0	2.5	(3.86 +/- .13) E+03
2.5	3.0	(2.34 +/- .09) E+03
3.0	3.5	(1.35 +/- .06) E+03
3.5	4.0	(7.91 +/- .45) E+02
4.0	4.5	(4.61 +/- .30) E+02
4.5	5.0	(2.81 +/- .24) E+02
5.0	5.5	(1.57 +/- .18) E+02
5.5	6.0	(7.50 +/- 1.05) E+01
6.0	6.5	(4.23 +/- .78) E+01
6.5	7.0	(2.46 +/- .58) E+01
7.0	7.5	(1.47 +/- .45) E+01
7.5	8.0	(8.65 +/- 3.52) E+00
8.0	8.5	(6.47 +/- 3.14) E+00
8.5	9.0	(2.37 +/- 2.25) E+00
9.0	9.5	(4.65 +/- 1.40) E-01
9.5	10.0	(2.96 +/- 1.14) E-01
10.0	10.5	(2.65 +/- 1.15) E-01

TABLE 4-4. (Continued)

F 2/3

ET BIN EDGES (GEV)		CROSS SECTION (MICROBARNS)
.0	.5	(2.66 +/- .04) E+04
.5	1.0	(1.42 +/- .03) E+04
1.0	1.5	(9.78 +/- .23) E+03
1.5	2.0	(5.89 +/- .17) E+03
2.0	2.5	(3.65 +/- .12) E+03
2.5	3.0	(2.08 +/- .08) E+03
3.0	3.5	(1.25 +/- .06) E+03
3.5	4.0	(7.28 +/- .43) E+02
4.0	4.5	(3.56 +/- .27) E+02
4.5	5.0	(2.14 +/- .19) E+02
5.0	5.5	(9.31 +/- 1.31) E+01
5.5	6.0	(7.29 +/- 1.04) E+01
6.0	6.5	(2.87 +/- .62) E+01
6.5	7.0	(1.93 +/- .51) E+01
7.0	7.5	(5.85 +/- 2.53) E+00
7.5	8.0	(6.66 +/- 3.12) E+00
8.0	8.5	(8.40 +/- 1.82) E-01
8.5	9.0	(5.95 +/- 1.55) E-01
9.0	9.5	(2.81 +/- 1.03) E-01
9.5	10.5	(5.95 +/- 4.06) E-02
10.5	11.5	(3.70 +/- 3.24) E-02

TABLE 4-4. (Continued)

M 1/2

ET BIN EDGES (GEV)		CROSS SECTION (MICROBARNS)
.0	.5	(3.05 +/- .04) E+04
.5	1.0	(1.48 +/- .03) E+04
1.0	1.5	(8.40 +/- .21) E+03
1.5	2.0	(5.15 +/- .15) E+03
2.0	2.5	(2.80 +/- .10) E+03
2.5	3.0	(1.58 +/- .07) E+03
3.0	3.5	(8.46 +/- .48) E+02
3.5	4.0	(4.03 +/- .29) E+02
4.0	4.5	(2.37 +/- .22) E+02
4.5	5.0	(1.40 +/- .17) E+02
5.0	5.5	(6.20 +/- .95) E+01
5.5	6.0	(2.83 +/- .62) E+01
6.0	6.5	(2.16 +/- .56) E+01
6.5	7.0	(6.98 +/- 3.09) E+00
7.0	7.5	(4.75 +/- 2.64) E+00
7.5	8.0	(2.62 +/- 2.10) E+00
8.0	8.5	(5.18 +/- 1.48) E-01
8.5	9.0	(1.51 +/- .77) E-01
9.0	9.5	(1.50 +/- 1.02) E-02
9.5	10.5	(6.14 +/- 4.04) E-02

TABLE 4-5. Particle transverse energy spectra for LPS Monte Carlo data and five apertures.

GLOBAL

ET BIN EDGES (GEV)		CROSS SECTION (MICROBARNS)
.0	.5	(1.54 +/- .03) E+04
.5	1.0	(1.21 +/- .03) E+04
1.0	1.5	(9.80 +/- .25) E+03
1.5	2.0	(7.64 +/- .22) E+03
2.0	2.5	(5.93 +/- .18) E+03
2.5	3.0	(4.34 +/- .15) E+03
3.0	3.5	(3.07 +/- .12) E+03
3.5	4.0	(2.07 +/- .08) E+03
4.0	4.5	(1.45 +/- .07) E+03
4.5	5.0	(1.09 +/- .05) E+03
5.0	5.5	(6.79 +/- .38) E+02
5.5	6.0	(4.94 +/- .33) E+02
6.0	6.5	(3.79 +/- .25) E+02
6.5	7.0	(2.08 +/- .20) E+02
7.0	7.5	(1.60 +/- .16) E+02
7.5	8.0	(8.40 +/- 1.13) E+01
8.0	8.5	(4.33 +/- .78) E+01
8.5	9.0	(2.92 +/- .62) E+01
9.0	9.5	(2.24 +/- .53) E+01
9.5	10.0	(1.45 +/- .38) E+01
10.0	10.5	(1.54 +/- .45) E+01
10.5	11.0	(7.89 +/- 3.04) E+00
11.0	11.5	(3.96 +/- 1.82) E+00
11.5	12.0	(4.46 +/- 2.70) E+00
12.0	12.5	(1.17 +/- .21) E+00
12.5	13.0	(7.19 +/- 1.69) E-01
13.0	13.5	(4.00 +/- 1.32) E-01
13.5	14.0	(1.02 +/- .58) E-01
14.0	14.5	(7.65 +/- 6.32) E-02
14.5	15.5	(7.74 +/- 4.78) E-02

TABLE 4-5. (Continued)

A-GLOBAL

ET BIN EDGES (GEV)		CROSS SECTION (MICROBARNS)
.0	.5	(1.65 +/- .03) E+04
.5	1.0	(1.25 +/- .03) E+04
1.0	1.5	(1.02 +/- .03) E+04
1.5	2.0	(7.50 +/- .21) E+03
2.0	2.5	(5.61 +/- .17) E+03
2.5	3.0	(4.06 +/- .14) E+03
3.0	3.5	(2.81 +/- .11) E+03
3.5	4.0	(1.91 +/- .08) E+03
4.0	4.5	(1.28 +/- .06) E+03
4.5	5.0	(9.36 +/- .49) E+02
5.0	5.5	(5.98 +/- .36) E+02
5.5	6.0	(4.23 +/- .29) E+02
6.0	6.5	(2.86 +/- .23) E+02
6.5	7.0	(1.63 +/- .16) E+02
7.0	7.5	(1.13 +/- .13) E+02
7.5	8.0	(5.36 +/- .87) E+01
8.0	8.5	(3.08 +/- .65) E+01
8.5	9.0	(2.55 +/- .58) E+01
9.0	9.5	(1.70 +/- .45) E+01
9.5	10.0	(1.61 +/- .45) E+01
10.0	10.5	(4.76 +/- 1.77) E+00
10.5	11.0	(2.31 +/- .30) E+00
11.0	11.5	(6.09 +/- 3.18) E+00
11.5	12.0	(1.16 +/- .22) E+00
12.0	12.5	(6.44 +/- 1.62) E-01
12.5	13.0	(2.89 +/- 1.03) E-01
13.0	13.5	(4.28 +/- 1.40) E-01
13.5	14.0	(1.62 +/- 1.01) E-02
14.0	15.0	(6.27 +/- 4.01) E-02
15.0	16.0	(3.24 +/- 2.71) E-05

TABLE 4-5. (Continued)

B 2/3

ET BIN EDGES (GEV)		CROSS SECTION (MICROBARNS)
.0	.5	(2.71 +/- .04) E+04
.5	1.0	(1.45 +/- .03) E+04
1.0	1.5	(9.10 +/- .23) E+03
1.5	2.0	(5.83 +/- .17) E+03
2.0	2.5	(3.62 +/- .12) E+03
2.5	3.0	(2.00 +/- .08) E+03
3.0	3.5	(1.25 +/- .06) E+03
3.5	4.0	(7.25 +/- .42) E+02
4.0	4.5	(4.21 +/- .30) E+02
4.5	5.0	(2.16 +/- .21) E+02
5.0	5.5	(1.33 +/- .15) E+02
5.5	6.0	(6.09 +/- .95) E+01
6.0	6.5	(2.87 +/- .62) E+01
6.5	7.0	(1.66 +/- .48) E+01
7.0	7.5	(1.09 +/- .39) E+01
7.5	8.0	(1.62 +/- .25) E+00
8.0	8.5	(2.71 +/- 2.05) E+00
8.5	9.0	(5.24 +/- 1.40) E-01
9.0	9.5	(2.72 +/- 1.15) E-01
9.5	10.5	(1.00 +/- .46) E-01

TABLE 4-5. (Continued)

F 2/3

ET BIN EDGES (GEV)		CROSS SECTION (MICROBARNS)
.0	.5	(2.58 +/- .04) E+04
.5	1.0	(1.44 +/- .03) E+04
1.0	1.5	(9.68 +/- .23) E+03
1.5	2.0	(5.94 +/- .17) E+03
2.0	2.5	(3.89 +/- .13) E+03
2.5	3.0	(2.18 +/- .09) E+03
3.0	3.5	(1.31 +/- .06) E+03
3.5	4.0	(8.45 +/- .48) E+02
4.0	4.5	(4.35 +/- .31) E+02
4.5	5.0	(2.56 +/- .22) E+02
5.0	5.5	(1.44 +/- .18) E+02
5.5	6.0	(7.10 +/- 1.03) E+01
6.0	6.5	(4.12 +/- .76) E+01
6.5	7.0	(3.63 +/- .72) E+01
7.0	7.5	(1.36 +/- .42) E+01
7.5	8.0	(3.67 +/- 1.85) E+00
8.0	8.5	(2.98 +/- 1.96) E+00
8.5	9.0	(1.07 +/- .21) E+00
9.0	9.5	(4.85 +/- 1.40) E-01
9.5	10.5	(1.14 +/- .45) E-01
10.5	11.5	(3.72 +/- 3.23) E-02

TABLE 4-5. (Continued)

M 1/2

ET BIN EDGES (GEV)		CROSS SECTION (MICROBARNS)
.0	.5	(3.08 +/- .04) E+04
.5	1.0	(1.45 +/- .03) E+04
1.0	1.5	(8.44 +/- .21) E+03
1.5	2.0	(5.04 +/- .15) E+03
2.0	2.5	(2.83 +/- .11) E+03
2.5	3.0	(1.58 +/- .07) E+03
3.0	3.5	(7.96 +/- .46) E+02
3.5	4.0	(4.66 +/- .33) E+02
4.0	4.5	(2.60 +/- .24) E+02
4.5	5.0	(1.21 +/- .17) E+02
5.0	5.5	(6.05 +/- .95) E+01
5.5	6.0	(3.84 +/- .74) E+01
6.0	6.5	(1.67 +/- .48) E+01
6.5	7.0	(1.18 +/- .42) E+01
7.0	7.5	(3.34 +/- 1.89) E+00
7.5	8.0	(2.33 +/- 2.29) E+00
8.0	8.5	(4.66 +/- 1.40) E-01
8.5	9.5	(1.08 +/- .45) E-01
10.5	12.5	(3.29 +/- 2.04) E-05

TABLE 4-6. Calorimeter transverse energy spectra for QCD/brem Monte Carlo data and five apertures.

GLOBAL

ET BIN EDGES (GEV)		CROSS SECTION (MICROBARNS)
.5	1.0	(1.09 +/- .29) E+02
1.0	1.5	(3.66 +/- .58) E+02
1.5	2.0	(7.92 +/- .88) E+02
2.0	2.5	(1.23 +/- .11) E+03
2.5	3.0	(2.09 +/- .20) E+03
3.0	3.5	(2.94 +/- .21) E+03
3.5	4.0	(2.89 +/- .18) E+03
4.0	4.5	(2.59 +/- .14) E+03
4.5	5.0	(2.32 +/- .14) E+03
5.0	5.5	(2.08 +/- .13) E+03
5.5	6.0	(1.36 +/- .09) E+03
6.0	6.5	(1.18 +/- .09) E+03
6.5	7.0	(6.29 +/- .52) E+02
7.0	7.5	(5.28 +/- .56) E+02
7.5	8.0	(2.85 +/- .35) E+02
8.0	8.5	(1.57 +/- .19) E+02
8.5	9.0	(9.20 +/- 1.38) E+01
9.0	9.5	(1.04 +/- .67) E+02
9.5	10.0	(4.94 +/- 3.03) E+01
10.0	10.5	(2.15 +/- .40) E+01
10.5	11.0	(1.71 +/- 1.04) E+01
11.0	11.5	(1.12 +/- .50) E+01
11.5	12.0	(2.86 +/- .48) E+00
12.0	12.5	(1.24 +/- .19) E+00
12.5	13.0	(7.94 +/- 1.31) E-01
13.0	13.5	(5.37 +/- .84) E-01
13.5	14.0	(3.74 +/- .79) E-01
14.0	14.5	(1.95 +/- .66) E-01
14.5	15.0	(7.72 +/- 1.62) E-02
15.0	15.5	(9.30 +/- 4.55) E-02
15.5	16.0	(3.77 +/- .89) E-02
16.0	16.5	(1.84 +/- .36) E-02
16.5	17.0	(1.30 +/- .51) E-02
17.0	17.5	(1.11 +/- .68) E-02
17.5	18.0	(3.12 +/- 1.26) E-03
18.0	18.5	(2.08 +/- .81) E-03
18.5	19.0	(6.42 +/- 1.89) E-04
19.0	19.5	(6.54 +/- 1.82) E-04
19.5	20.0	(3.73 +/- 2.14) E-04
20.0	21.0	(1.13 +/- .44) E-04
21.0	22.0	(3.78 +/- 1.80) E-05

TABLE 4-6. (Continued)

A-GLOBAL

ET BIN EDGES (GEV)		CROSS SECTION (MICROBARNS)
.0	.5	(1.25 +/- .58) E+01
.5	1.0	(1.58 +/- .34) E+02
1.0	1.5	(5.00 +/- .65) E+02
1.5	2.0	(1.20 +/- .17) E+03
2.0	2.5	(1.95 +/- .15) E+03
2.5	3.0	(2.61 +/- .18) E+03
3.0	3.5	(3.19 +/- .20) E+03
3.5	4.0	(2.97 +/- .18) E+03
4.0	4.5	(2.36 +/- .14) E+03
4.5	5.0	(2.27 +/- .13) E+03
5.0	5.5	(1.50 +/- .10) E+03
5.5	6.0	(1.22 +/- .09) E+03
6.0	6.5	(7.86 +/- .72) E+02
6.5	7.0	(4.24 +/- .37) E+02
7.0	7.5	(2.65 +/- .33) E+02
7.5	8.0	(1.78 +/- .25) E+02
8.0	8.5	(9.65 +/- 1.46) E+01
8.5	9.0	(9.61 +/- 6.88) E+01
9.0	9.5	(2.30 +/- .40) E+01
9.5	10.0	(1.97 +/- 1.02) E+01
10.0	10.5	(7.87 +/- 1.69) E+00
10.5	11.0	(1.13 +/- .50) E+01
11.0	11.5	(1.89 +/- .28) E+00
11.5	12.0	(8.38 +/- .97) E-01
12.0	12.5	(5.92 +/- .85) E-01
12.5	13.0	(3.72 +/- .74) E-01
13.0	13.5	(2.46 +/- .54) E-01
13.5	14.0	(1.07 +/- .20) E-01
14.0	14.5	(1.04 +/- .46) E-01
14.5	15.0	(4.16 +/- .86) E-02
15.0	15.5	(1.39 +/- .33) E-02
15.5	16.0	(1.77 +/- .57) E-02
16.0	16.5	(4.30 +/- 1.02) E-03
16.5	17.0	(1.03 +/- .70) E-02
17.0	17.5	(2.00 +/- .54) E-03
17.5	18.0	(1.56 +/- .83) E-03
18.0	18.5	(4.55 +/- 1.14) E-04
18.5	19.5	(2.73 +/- .65) E-04
19.5	20.5	(6.93 +/- 3.54) E-05
20.5	22.5	(1.19 +/- .85) E-05

TABLE 4-6. (Continued)

B 2/3

ET BIN EDGES (GEV)		CROSS SECTION (MICROBARNS)
.0	.5	(4.55 +/- .72) E+02
.5	1.0	(1.43 +/- .11) E+03
1.0	1.5	(2.98 +/- .23) E+03
1.5	2.0	(3.57 +/- .19) E+03
2.0	2.5	(3.64 +/- .20) E+03
2.5	3.0	(3.21 +/- .17) E+03
3.0	3.5	(2.60 +/- .15) E+03
3.5	4.0	(1.69 +/- .12) E+03
4.0	4.5	(9.57 +/- .69) E+02
4.5	5.0	(5.74 +/- .52) E+02
5.0	5.5	(3.71 +/- .38) E+02
5.5	6.0	(1.78 +/- .25) E+02
6.0	6.5	(1.09 +/- .29) E+02
6.5	7.0	(3.54 +/- .56) E+01
7.0	7.5	(1.72 +/- .36) E+01
7.5	8.0	(6.98 +/- .79) E+00
8.0	8.5	(2.00 +/- 1.16) E+01
8.5	9.0	(2.71 +/- .51) E+00
9.0	9.5	(1.40 +/- .33) E+00
9.5	10.0	(4.79 +/- .76) E-01
10.0	10.5	(3.72 +/- .97) E-01
10.5	11.0	(1.64 +/- .45) E-01
11.0	11.5	(1.09 +/- .45) E-01
11.5	12.0	(5.87 +/- 1.77) E-02
12.0	12.5	(2.21 +/- .57) E-02
12.5	13.0	(2.88 +/- .92) E-02
13.0	13.5	(1.14 +/- .37) E-02
13.5	14.0	(4.59 +/- 1.72) E-03
14.0	14.5	(2.60 +/- .64) E-03
14.5	15.0	(1.78 +/- .89) E-03
15.0	15.5	(6.07 +/- 2.04) E-04
15.5	16.0	(5.83 +/- 2.08) E-04
16.0	17.0	(2.91 +/- .74) E-04
17.0	18.0	(1.10 +/- .34) E-04
18.0	20.0	(1.23 +/- .85) E-05

TABLE 4-6. (Continued)

F 2/3

ET BIN EDGES (GEV)		CROSS SECTION (MICROBARNS)
.0	.5	(2.74 +/- .44) E+02
.5	1.0	(1.19 +/- .10) E+03
1.0	1.5	(2.82 +/- .18) E+03
1.5	2.0	(3.64 +/- .23) E+03
2.0	2.5	(4.33 +/- .22) E+03
2.5	3.0	(3.23 +/- .17) E+03
3.0	3.5	(2.69 +/- .15) E+03
3.5	4.0	(1.53 +/- .10) E+03
4.0	4.5	(1.06 +/- .09) E+03
4.5	5.0	(5.49 +/- .60) E+02
5.0	5.5	(2.66 +/- .29) E+02
5.5	6.0	(1.27 +/- .18) E+02
6.0	6.5	(1.13 +/- .66) E+02
6.5	7.0	(2.36 +/- .49) E+01
7.0	7.5	(1.12 +/- .22) E+01
7.5	8.0	(3.89 +/- .96) E+00
8.0	8.5	(2.24 +/- .56) E+00
8.5	9.0	(1.41 +/- .61) E+00
9.0	9.5	(3.14 +/- .55) E-01
9.5	10.0	(2.36 +/- .53) E-01
10.0	10.5	(1.31 +/- .42) E-01
10.5	11.0	(4.82 +/- 1.03) E-02
11.0	11.5	(1.95 +/- .68) E-02
11.5	12.0	(2.32 +/- 1.24) E-02
12.0	12.5	(3.12 +/- .65) E-03
12.5	13.5	(2.26 +/- .90) E-03
13.5	14.5	(3.59 +/- 1.45) E-04
14.5	16.5	(7.52 +/- 2.44) E-05

TABLE 4-6. (Continued)

M 1/2

ET BIN EDGES (GEV)		CROSS SECTION (MICROBARNS)
.0	.5	(6.51 +/- .80) E+02
.5	1.0	(2.04 +/- .12) E+03
1.0	1.5	(3.98 +/- .25) E+03
1.5	2.0	(4.29 +/- .21) E+03
2.0	2.5	(3.84 +/- .21) E+03
2.5	3.0	(2.93 +/- .16) E+03
3.0	3.5	(1.87 +/- .12) E+03
3.5	4.0	(1.12 +/- .09) E+03
4.0	4.5	(6.02 +/- .64) E+02
4.5	5.0	(3.09 +/- .38) E+02
5.0	5.5	(1.09 +/- .14) E+02
5.5	6.0	(7.63 +/- 1.83) E+01
6.0	6.5	(2.70 +/- .52) E+01
6.5	7.0	(1.66 +/- .55) E+01
7.0	7.5	(3.49 +/- .61) E+00
7.5	8.0	(2.24 +/- .39) E+00
8.0	8.5	(6.90 +/- .85) E-01
8.5	9.0	(4.15 +/- .72) E-01
9.0	9.5	(1.74 +/- .28) E-01
9.5	10.0	(1.46 +/- .41) E-01
10.0	10.5	(5.65 +/- 1.58) E-02
10.5	11.0	(3.10 +/- .78) E-02
11.0	11.5	(2.29 +/- .72) E-02
11.5	12.0	(6.28 +/- 1.60) E-03
12.0	12.5	(3.85 +/- 1.56) E-03
12.5	13.0	(4.32 +/- 1.80) E-03
13.0	13.5	(1.09 +/- .42) E-03
13.5	14.0	(4.42 +/- 1.78) E-04
14.0	14.5	(8.77 +/- 3.38) E-04
14.5	15.5	(6.86 +/- 2.62) E-05
15.5	16.5	(3.88 +/- 2.13) E-05
16.5	18.5	(9.26 +/- 5.34) E-06

TABLE 4-7. Particle transverse energy spectra for QCD/brem Monte Carlo data and five apertures.

GLOBAL

ET BIN EDGES (GEV)		CROSS SECTION (MICROBARNS)
.5	1.0	(1.14 +/- .25) E+02
1.0	1.5	(4.21 +/- .65) E+02
1.5	2.0	(1.00 +/- .16) E+03
2.0	2.5	(1.34 +/- .10) E+03
2.5	3.0	(2.43 +/- .19) E+03
3.0	3.5	(2.92 +/- .17) E+03
3.5	4.0	(3.32 +/- .20) E+03
4.0	4.5	(2.57 +/- .14) E+03
4.5	5.0	(2.31 +/- .15) E+03
5.0	5.5	(1.95 +/- .12) E+03
5.5	6.0	(1.34 +/- .10) E+03
6.0	6.5	(7.64 +/- .59) E+02
6.5	7.0	(4.24 +/- .32) E+02
7.0	7.5	(4.12 +/- .54) E+02
7.5	8.0	(1.92 +/- .24) E+02
8.0	8.5	(1.81 +/- .66) E+02
8.5	9.0	(7.54 +/- 1.26) E+01
9.0	9.5	(2.57 +/- .39) E+01
9.5	10.0	(1.64 +/- .31) E+01
10.0	10.5	(1.48 +/- .49) E+01
10.5	11.0	(4.82 +/- .61) E+00
11.0	11.5	(3.10 +/- .50) E+00
11.5	12.0	(1.25 +/- .12) E+00
12.0	12.5	(7.25 +/- .88) E-01
12.5	13.0	(4.23 +/- .60) E-01
13.0	13.5	(3.46 +/- .68) E-01
13.5	14.0	(2.44 +/- .66) E-01
14.0	14.5	(9.75 +/- 3.26) E-02
14.5	15.0	(9.82 +/- 4.61) E-02
15.0	15.5	(3.05 +/- .52) E-02
15.5	16.0	(1.60 +/- .36) E-02
16.0	16.5	(2.17 +/- .79) E-02
16.5	17.0	(4.47 +/- 1.18) E-03
17.0	17.5	(3.55 +/- .79) E-03
17.5	18.0	(3.59 +/- 1.22) E-03
18.0	18.5	(8.34 +/- 2.31) E-04
18.5	19.0	(6.52 +/- 2.12) E-04
19.0	19.5	(2.92 +/- .97) E-04
19.5	20.5	(1.10 +/- .35) E-04
20.5	21.5	(3.75 +/- 3.61) E-05

TABLE 4-7. (Continued)

A-GLOBAL

ET BIN EDGES (GEV)		CROSS SECTION (MICROBARNS)
.0	.5	(2.70 +/- 2.43) E+01
.5	1.0	(1.72 +/- .35) E+02
1.0	1.5	(6.59 +/- 1.50) E+02
1.5	2.0	(1.17 +/- .10) E+03
2.0	2.5	(1.75 +/- .12) E+03
2.5	3.0	(2.77 +/- .19) E+03
3.0	3.5	(3.38 +/- .21) E+03
3.5	4.0	(2.96 +/- .17) E+03
4.0	4.5	(2.43 +/- .15) E+03
4.5	5.0	(2.14 +/- .13) E+03
5.0	5.5	(1.71 +/- .11) E+03
5.5	6.0	(1.06 +/- .08) E+03
6.0	6.5	(6.23 +/- .53) E+02
6.5	7.0	(3.38 +/- .29) E+02
7.0	7.5	(2.90 +/- .47) E+02
7.5	8.0	(2.04 +/- .63) E+02
8.0	8.5	(6.95 +/- .84) E+01
8.5	9.0	(4.98 +/- 1.11) E+01
9.0	9.5	(1.76 +/- .22) E+01
9.5	10.0	(1.69 +/- .53) E+01
10.0	10.5	(7.81 +/- 2.11) E+00
10.5	11.0	(3.90 +/- .66) E+00
11.0	11.5	(1.67 +/- .24) E+00
11.5	12.0	(9.04 +/- .87) E-01
12.0	12.5	(4.91 +/- .62) E-01
12.5	13.0	(3.67 +/- .63) E-01
13.0	13.5	(2.48 +/- .58) E-01
13.5	14.0	(1.09 +/- .17) E-01
14.0	14.5	(1.03 +/- .34) E-01
14.5	15.0	(7.36 +/- 4.78) E-02
15.0	15.5	(1.63 +/- .34) E-02
15.5	16.0	(1.23 +/- .30) E-02
16.0	16.5	(2.06 +/- .80) E-02
16.5	17.0	(2.88 +/- .61) E-03
17.0	17.5	(3.36 +/- .77) E-03
17.5	18.0	(2.66 +/- 1.23) E-03
18.0	18.5	(7.43 +/- 2.18) E-04
18.5	19.0	(4.49 +/- 1.76) E-04
19.0	19.5	(1.72 +/- .59) E-04
19.5	20.5	(1.01 +/- .35) E-04

TABLE 4-7. (Continued)

B 2/3

ET BIN EDGES (GEV)		CROSS SECTION (MICROBARNS)
.0	.5	(6.07 +/- .67) E+02
.5	1.0	(1.91 +/- .20) E+03
1.0	1.5	(3.00 +/- .17) E+03
1.5	2.0	(3.99 +/- .20) E+03
2.0	2.5	(3.91 +/- .22) E+03
2.5	3.0	(3.09 +/- .16) E+03
3.0	3.5	(2.24 +/- .14) E+03
3.5	4.0	(1.32 +/- .09) E+03
4.0	4.5	(8.84 +/- .78) E+02
4.5	5.0	(4.12 +/- .35) E+02
5.0	5.5	(2.07 +/- .26) E+02
5.5	6.0	(1.44 +/- .31) E+02
6.0	6.5	(7.58 +/- 2.09) E+01
6.5	7.0	(3.60 +/- 1.09) E+01
7.0	7.5	(1.08 +/- .31) E+01
7.5	8.0	(9.83 +/- 4.59) E+00
8.0	8.5	(5.93 +/- 2.58) E+00
8.5	9.0	(1.41 +/- .23) E+00
9.0	9.5	(1.25 +/- .46) E+00
9.5	10.0	(3.93 +/- .69) E-01
10.0	10.5	(2.22 +/- .47) E-01
10.5	11.0	(1.39 +/- .35) E-01
11.0	11.5	(9.60 +/- 2.03) E-02
11.5	12.0	(4.74 +/- .88) E-02
12.0	12.5	(1.88 +/- .46) E-02
12.5	13.0	(1.43 +/- .33) E-02
13.0	13.5	(6.07 +/- 1.16) E-03
13.5	14.0	(5.17 +/- 1.21) E-03
14.0	14.5	(2.23 +/- .62) E-03
14.5	15.0	(1.50 +/- .54) E-03
15.0	15.5	(7.83 +/- 2.42) E-04
15.5	16.5	(3.97 +/- 1.10) E-04
16.5	17.5	(1.48 +/- .47) E-04
17.5	19.5	(3.39 +/- 1.53) E-05

TABLE 4-7. (Continued)

F 2/3

ET BIN EDGES (GEV)		CROSS SECTION (MICROBARNS)
.0	.5	(2.76 +/- .42) E+02
.5	1.0	(1.07 +/- .09) E+03
1.0	1.5	(2.48 +/- .19) E+03
1.5	2.0	(3.67 +/- .20) E+03
2.0	2.5	(3.76 +/- .20) E+03
2.5	3.0	(3.27 +/- .18) E+03
3.0	3.5	(3.15 +/- .19) E+03
3.5	4.0	(1.75 +/- .10) E+03
4.0	4.5	(1.04 +/- .08) E+03
4.5	5.0	(6.56 +/- .68) E+02
5.0	5.5	(3.78 +/- .52) E+02
5.5	6.0	(1.95 +/- .61) E+02
6.0	6.5	(6.56 +/- .85) E+01
6.5	7.0	(6.39 +/- 2.77) E+01
7.0	7.5	(1.84 +/- .46) E+01
7.5	8.0	(7.32 +/- 3.04) E+00
8.0	8.5	(4.53 +/- 1.35) E+00
8.5	9.0	(2.39 +/- .86) E+00
9.0	9.5	(6.89 +/- .85) E-01
9.5	10.0	(4.43 +/- .85) E-01
10.0	10.5	(2.26 +/- .50) E-01
10.5	11.0	(1.50 +/- .39) E-01
11.0	11.5	(4.73 +/- .80) E-02
11.5	12.0	(3.83 +/- .83) E-02
12.0	12.5	(2.20 +/- 1.22) E-02
12.5	13.0	(8.67 +/- 2.34) E-03
13.0	13.5	(2.10 +/- .39) E-03
13.5	14.0	(3.37 +/- 1.95) E-03
14.0	15.0	(1.09 +/- .22) E-03
15.0	16.0	(6.36 +/- 3.09) E-04
16.0	18.0	(4.67 +/- 1.33) E-05

TABLE 4-7. (Continued)

M 1/2

ET BIN EDGES (GEV)		CROSS SECTION (MICROBARNS)
.0	.5	(7.93 +/- .77) E+02
.5	1.0	(2.46 +/- .19) E+03
1.0	1.5	(3.79 +/- .21) E+03
1.5	2.0	(4.41 +/- .22) E+03
2.0	2.5	(3.86 +/- .20) E+03
2.5	3.0	(2.80 +/- .16) E+03
3.0	3.5	(1.65 +/- .11) E+03
3.5	4.0	(1.09 +/- .08) E+03
4.0	4.5	(4.64 +/- .42) E+02
4.5	5.0	(2.83 +/- .40) E+02
5.0	5.5	(1.27 +/- .27) E+02
5.5	6.0	(8.73 +/- 2.47) E+01
6.0	6.5	(2.20 +/- .36) E+01
6.5	7.0	(1.30 +/- .46) E+01
7.0	7.5	(8.36 +/- 3.24) E+00
7.5	8.0	(1.72 +/- .17) E+00
8.0	8.5	(9.92 +/- 1.44) E-01
8.5	9.0	(6.60 +/- 1.12) E-01
9.0	9.5	(2.57 +/- .34) E-01
9.5	10.0	(1.63 +/- .45) E-01
10.0	10.5	(1.23 +/- .39) E-01
10.5	11.0	(5.84 +/- 1.06) E-02
11.0	11.5	(3.01 +/- .66) E-02
11.5	12.0	(1.15 +/- .21) E-02
12.0	12.5	(1.81 +/- .49) E-02
12.5	13.0	(4.07 +/- .80) E-03
13.0	13.5	(2.09 +/- .45) E-03
13.5	14.0	(2.78 +/- .73) E-03
14.0	14.5	(1.43 +/- .45) E-03
14.5	15.0	(7.77 +/- 2.72) E-04
15.0	15.5	(1.99 +/- .73) E-04
15.5	16.0	(7.06 +/- 2.87) E-05
16.0	16.5	(2.39 +/- 1.24) E-05
16.5	17.0	(6.33 +/- 2.69) E-05
17.0	18.0	(1.34 +/- .64) E-05

TABLE 4-8. Predicted particle transverse energy spectra for experimental hydrogen data and five apertures.

GLOBAL

ET BIN EDGES (GEV)		CROSS SECTION (MICROBARNS)
.0	.5	(4.34 +/- .10) E+03
.5	1.0	(6.12 +/- .13) E+03
1.0	1.5	(7.21 +/- .15) E+03
1.5	2.0	(7.56 +/- .15) E+03
2.0	2.5	(6.40 +/- .13) E+03
2.5	3.0	(5.55 +/- .12) E+03
3.0	3.5	(4.57 +/- .10) E+03
3.5	4.0	(3.47 +/- .09) E+03
4.0	4.5	(2.89 +/- .08) E+03
4.5	5.0	(2.15 +/- .06) E+03
5.0	5.5	(1.62 +/- .05) E+03
5.5	6.0	(1.27 +/- .05) E+03
6.0	6.5	(9.19 +/- .40) E+02
6.5	7.0	(6.34 +/- .30) E+02
7.0	7.5	(4.52 +/- .23) E+02
7.5	8.0	(3.60 +/- .20) E+02
8.0	8.5	(2.60 +/- .17) E+02
8.5	9.0	(1.74 +/- .14) E+02
9.0	9.5	(1.16 +/- .11) E+02
9.5	10.0	(1.05 +/- .10) E+02
10.0	10.5	(5.79 +/- .53) E+01
10.5	11.0	(4.34 +/- .38) E+01
11.0	11.5	(2.98 +/- .15) E+01
11.5	12.0	(1.94 +/- .12) E+01
12.0	12.5	(1.54 +/- .11) E+01
12.5	13.0	(9.90 +/- .81) E+00
13.0	13.5	(5.73 +/- .25) E+00
13.5	14.0	(4.13 +/- .21) E+00
14.0	14.5	(2.75 +/- .17) E+00
14.5	15.0	(2.01 +/- .15) E+00
15.0	15.5	(1.29 +/- .05) E+00
15.5	16.0	(6.91 +/- .33) E-01
16.0	16.5	(5.26 +/- .24) E-01
16.5	17.0	(3.14 +/- .17) E-01
17.0	17.5	(2.45 +/- .14) E-01
17.5	18.0	(1.51 +/- .11) E-01
18.0	18.5	(8.80 +/- .79) E-02
18.5	19.0	(6.27 +/- .52) E-02
19.0	19.5	(4.55 +/- .44) E-02
19.5	20.0	(3.38 +/- .38) E-02
20.0	20.5	(1.67 +/- .27) E-02
20.5	21.0	(1.25 +/- .23) E-02
21.0	22.0	(5.96 +/- 1.13) E-03
22.0	23.0	(2.44 +/- .74) E-03
23.0	25.0	(9.03 +/- 3.19) E-04

TABLE 4-8. (Continued)

A-GLOBAL

ET BIN EDGES (GEV)		CROSS SECTION (MICROBARNS)
.0	.5	(5.32 +/- .13) E+03
.5	1.0	(6.96 +/- .17) E+03
1.0	1.5	(8.19 +/- .19) E+03
1.5	2.0	(7.64 +/- .18) E+03
2.0	2.5	(6.41 +/- .15) E+03
2.5	3.0	(5.45 +/- .13) E+03
3.0	3.5	(4.37 +/- .11) E+03
3.5	4.0	(3.14 +/- .09) E+03
4.0	4.5	(2.43 +/- .07) E+03
4.5	5.0	(1.77 +/- .06) E+03
5.0	5.5	(1.35 +/- .05) E+03
5.5	6.0	(9.59 +/- .41) E+02
6.0	6.5	(7.28 +/- .35) E+02
6.5	7.0	(4.93 +/- .29) E+02
7.0	7.5	(3.91 +/- .25) E+02
7.5	8.0	(2.37 +/- .16) E+02
8.0	8.5	(1.86 +/- .14) E+02
8.5	9.0	(1.18 +/- .11) E+02
9.0	9.5	(9.11 +/- .95) E+01
9.5	10.0	(5.68 +/- .75) E+01
10.0	10.5	(4.45 +/- .66) E+01
10.5	11.0	(3.01 +/- .47) E+01
11.0	11.5	(1.23 +/- .24) E+01
11.5	12.0	(1.12 +/- .18) E+01
12.0	12.5	(8.92 +/- .79) E+00
12.5	13.0	(5.53 +/- .62) E+00
13.0	13.5	(3.45 +/- .48) E+00
13.5	14.0	(2.08 +/- .37) E+00
14.0	14.5	(1.51 +/- .12) E+00
14.5	15.0	(1.05 +/- .10) E+00
15.0	15.5	(6.14 +/- .77) E-01
15.5	16.0	(4.93 +/- .68) E-01
16.0	16.5	(2.64 +/- .42) E-01
16.5	17.0	(1.65 +/- .17) E-01
17.0	17.5	(1.01 +/- .11) E-01
17.5	18.0	(6.15 +/- .71) E-02
18.0	18.5	(3.91 +/- .56) E-02
18.5	19.0	(3.02 +/- .46) E-02
19.0	19.5	(2.65 +/- .41) E-02
19.5	20.0	(1.06 +/- .26) E-02
20.0	20.5	(9.43 +/- 1.83) E-03
20.5	21.0	(5.95 +/- 1.45) E-03
21.0	21.5	(5.84 +/- 1.43) E-03
21.5	22.5	(1.57 +/- .53) E-03
22.5	23.5	(1.07 +/- .44) E-03

TABLE 4-8. (Continued)

B 2/3

ET BIN EDGES (GEV)		CROSS SECTION (MICROBARNS)
.0	.5	(1.12 +/- .02) E+04
.5	1.0	(1.15 +/- .02) E+04
1.0	1.5	(1.04 +/- .02) E+04
1.5	2.0	(7.49 +/- .16) E+03
2.0	2.5	(5.63 +/- .13) E+03
2.5	3.0	(3.72 +/- .09) E+03
3.0	3.5	(2.41 +/- .07) E+03
3.5	4.0	(1.46 +/- .05) E+03
4.0	4.5	(9.68 +/- .41) E+02
4.5	5.0	(6.45 +/- .33) E+02
5.0	5.5	(4.23 +/- .26) E+02
5.5	6.0	(2.40 +/- .19) E+02
6.0	6.5	(1.54 +/- .15) E+02
6.5	7.0	(9.80 +/- .97) E+01
7.0	7.5	(6.86 +/- .80) E+01
7.5	8.0	(2.21 +/- .45) E+01
8.0	8.5	(2.49 +/- .47) E+01
8.5	9.0	(1.57 +/- .37) E+01
9.0	9.5	(6.23 +/- 1.83) E+00
9.5	10.0	(4.81 +/- .82) E+00
10.0	10.5	(4.21 +/- .50) E+00
10.5	11.0	(2.49 +/- .38) E+00
11.0	11.5	(1.10 +/- .22) E+00
11.5	12.0	(6.37 +/- .73) E-01
12.0	12.5	(3.62 +/- .54) E-01
12.5	13.0	(3.18 +/- .50) E-01
13.0	13.5	(1.85 +/- .37) E-01
13.5	14.0	(7.76 +/- 1.98) E-02
14.0	14.5	(4.25 +/- .59) E-02
14.5	15.0	(2.69 +/- .41) E-02
15.0	15.5	(1.86 +/- .33) E-02
15.5	16.0	(9.33 +/- 2.17) E-03
16.0	16.5	(5.79 +/- 1.39) E-03
16.5	17.0	(5.66 +/- 1.19) E-03
17.0	17.5	(3.83 +/- .97) E-03
17.5	18.5	(2.15 +/- .50) E-03
18.5	19.5	(9.71 +/- 3.26) E-04

TABLE 4-8. (Continued)

F 2/3

ET BIN EDGES (GEV)		CROSS SECTION (MICROBARNS)
.0	.5	(1.26 +/- .05) E+04
.5	1.0	(1.22 +/- .05) E+04
1.0	1.5	(1.01 +/- .04) E+04
1.5	2.0	(7.42 +/- .31) E+03
2.0	2.5	(5.26 +/- .21) E+03
2.5	3.0	(3.35 +/- .13) E+03
3.0	3.5	(2.10 +/- .09) E+03
3.5	4.0	(1.25 +/- .06) E+03
4.0	4.5	(7.77 +/- .39) E+02
4.5	5.0	(5.44 +/- .30) E+02
5.0	5.5	(3.23 +/- .22) E+02
5.5	6.0	(1.90 +/- .16) E+02
6.0	6.5	(1.36 +/- .13) E+02
6.5	7.0	(5.73 +/- .70) E+01
7.0	7.5	(4.63 +/- .57) E+01
7.5	8.0	(2.07 +/- .37) E+01
8.0	8.5	(1.03 +/- .26) E+01
8.5	9.0	(1.09 +/- .26) E+01
9.0	9.5	(4.42 +/- 1.26) E+00
9.5	10.0	(2.34 +/- .61) E+00
10.0	10.5	(9.13 +/- 1.88) E-01
10.5	11.0	(4.45 +/- 1.29) E-01
11.0	11.5	(2.89 +/- .49) E-01
11.5	12.0	(2.17 +/- .32) E-01
12.0	12.5	(1.44 +/- .25) E-01
12.5	13.0	(4.88 +/- 1.43) E-02
13.0	13.5	(2.12 +/- .80) E-02
13.5	14.0	(1.17 +/- .23) E-02
14.0	14.5	(8.45 +/- 1.64) E-03
14.5	15.0	(3.04 +/- .91) E-03
15.0	15.5	(4.30 +/- .93) E-03
15.5	16.0	(2.18 +/- .55) E-03
16.0	16.5	(1.36 +/- .36) E-03
16.5	17.0	(1.27 +/- .33) E-03
17.0	17.5	(2.77 +/- 1.64) E-04
17.5	18.5	(2.70 +/- .92) E-04
18.5	19.5	(1.23 +/- .56) E-04

TABLE 4-8. (Continued)

M 1/2

ET BIN EDGES (GEV)		CROSS SECTION (MICROBARNS)
.0	.5	(1.58 +/- .04) E+04
.5	1.0	(1.35 +/- .04) E+04
1.0	1.5	(1.05 +/- .03) E+04
1.5	2.0	(6.79 +/- .18) E+03
2.0	2.5	(4.16 +/- .11) E+03
2.5	3.0	(2.45 +/- .07) E+03
3.0	3.5	(1.37 +/- .05) E+03
3.5	4.0	(7.76 +/- .35) E+02
4.0	4.5	(4.70 +/- .26) E+02
4.5	5.0	(2.67 +/- .19) E+02
5.0	5.5	(1.65 +/- .15) E+02
5.5	6.0	(8.18 +/- .89) E+01
6.0	6.5	(4.47 +/- .59) E+01
6.5	7.0	(2.31 +/- .41) E+01
7.0	7.5	(1.79 +/- .35) E+01
7.5	8.0	(3.71 +/- 1.66) E+00
8.0	8.5	(2.31 +/- 1.13) E+00
8.5	9.0	(3.29 +/- .89) E+00
9.0	9.5	(1.17 +/- .22) E+00
9.5	10.0	(9.02 +/- 1.91) E-01
10.0	10.5	(4.97 +/- 1.40) E-01
10.5	11.0	(1.92 +/- .66) E-01
11.0	11.5	(1.15 +/- .24) E-01
11.5	12.0	(5.97 +/- 1.69) E-02
12.0	12.5	(3.57 +/- 1.28) E-02
12.5	13.0	(1.91 +/- .83) E-02
13.0	13.5	(1.18 +/- .30) E-02
13.5	14.0	(7.19 +/- 1.75) E-03
14.0	14.5	(6.19 +/- 1.35) E-03
14.5	15.0	(2.79 +/- .86) E-03
15.0	15.5	(1.31 +/- .60) E-03
15.5	16.0	(9.54 +/- 4.38) E-04
16.0	16.5	(5.72 +/- 2.39) E-04
16.5	17.5	(3.91 +/- 1.27) E-04
17.5	18.5	(2.52 +/- .92) E-04
18.5	20.5	(3.45 +/- 2.05) E-05

TABLE 4-9. Calorimeter transverse energy spectra for nuclear target data, and parameter α and correlation coefficient of fit to A^{α}, for five apertures.

GLOBAL

ET LIMITS	DS/DET (AL)	DS/DET (CU)	DS/DET (PB)	ALPHA	CORRELATION
.0 1.0	(4.40 +/- .83) E+04	(1.08 +/- .30) E+05	(3.49 +/- .73) E+05	1.015 +/- .138	1.000
1.0 3.0	(7.84 +/- .83) E+04	(1.34 +/- .21) E+05	(2.13 +/- .43) E+05	.507 +/- .108	.991
3.0 5.0	(5.57 +/- .46) E+04	(8.32 +/- 1.19) E+04	(2.64 +/- .35) E+05	.748 +/- .076	.988
5.0 7.0	(4.04 +/- .38) E+04	(6.91 +/- 1.20) E+04	(1.91 +/- .28) E+05	.757 +/- .086	.998
7.0 8.0	(2.05 +/- .37) E+04	. . . .	(1.64 +/- .26) E+05	1.021 +/- .118	1.000
8.0 10.0	(1.43 +/- .17) E+04	(3.49 +/- .81) E+04	(8.24 +/- 1.32) E+04	.863 +/- .098	.998
10.0 11.0	(6.84 +/- 1.16) E+03	. . . .	(4.69 +/- .95) E+04	.944 +/- .130	1.000
11.0 13.0	(2.74 +/- .19) E+03	. . . .	(2.42 +/- .17) E+04	1.070 +/- .049	1.000
13.0 15.0	(9.58 +/- .47) E+02	. . . .	(1.14 +/- .04) E+04	1.213 +/- .030	1.000
15.0 15.5	(4.82 +/- .33) E+02	(1.35 +/- .05) E+03	(5.72 +/- .40) E+03	1.214 +/- .047	1.000
15.5 16.0	(3.63 +/- .24) E+02	(1.06 +/- .04) E+03	(4.06 +/- .25) E+03	1.176 +/- .044	.999
16.0 17.0	(2.13 +/- .14) E+02	(6.11 +/- .17) E+02	(2.81 +/- .17) E+03	1.271 +/- .043	1.000
17.0 18.0	(1.00 +/- .09) E+02	(3.05 +/- .13) E+02	(1.70 +/- .07) E+03	1.417 +/- .040	1.000
18.0 19.0	(4.75 +/- .43) E+01	(1.37 +/- .08) E+02	(8.00 +/- .36) E+02	1.420 +/- .044	.999
19.0 21.0	(2.12 +/- .15) E+01	(4.89 +/- .29) E+01	(2.49 +/- .15) E+02	1.230 +/- .045	.995
21.0 23.0	(3.98 +/- .83) E+00	. . . .	(4.67 +/- .83) E+01	1.208 +/- .134	1.000

A-GLOBAL

ET LIMITS	DS/DET (AL)	DS/DET (CU)	DS/DET (PB)	ALPHA	CORRELATION
.0 1.0	(5.12 +/- .98) E+04	(6.18 +/- 3.55) E+04	(3.96 +/- .84) E+05	1.005 +/- .140	.988
1.0 3.0	(8.59 +/- .84) E+04	(1.55 +/- .20) E+05	(2.65 +/- .45) E+05	.568 +/- .094	.993
3.0 5.0	(5.63 +/- .47) E+04	(8.79 +/- 1.38) E+04	(2.82 +/- .36) E+05	.780 +/- .074	.992
5.0 6.0	(4.49 +/- .65) E+04	(9.60 +/- 1.92) E+04	(2.33 +/- .50) E+05	.813 +/- .127	.999
6.0 7.5	(2.43 +/- .33) E+04	(4.24 +/- 1.04) E+04	(1.60 +/- .29) E+05	.920 +/- .110	.994
7.5 8.5	(1.68 +/- .33) E+04	. . . .	(6.59 +/- 2.13) E+04	.669 +/- .185	1.000
8.5 10.5	(4.50 +/- 1.23) E+03	. . . .	(6.08 +/- 1.32) E+04	1.277 +/- .172	1.000
10.5 11.5	(3.55 +/- .81) E+03	. . . .	(2.39 +/- .66) E+04	.936 +/- .176	1.000
11.5 13.5	(1.25 +/- .13) E+03	. . . .	(1.58 +/- .12) E+04	1.243 +/- .064	1.000
13.5 15.5	(3.61 +/- .28) E+02	. . . .	(4.51 +/- .25) E+03	1.238 +/- .047	1.000
15.5 16.0	(1.66 +/- .22) E+02	(4.14 +/- .31) E+02	(2.18 +/- .26) E+03	1.287 +/- .086	.995
16.0 16.5	(6.37 +/- 1.37) E+01	(2.87 +/- .20) E+02	(1.80 +/- .19) E+03	1.588 +/- .091	.999
16.5 17.5	(6.15 +/- .69) E+01	(1.55 +/- .09) E+02	(1.07 +/- .08) E+03	1.478 +/- .061	.993
17.5 18.5	(2.99 +/- .55) E+01	(7.72 +/- .63) E+01	(5.26 +/- .48) E+02	1.509 +/- .084	.995
18.5 19.5	(1.21 +/- .22) E+01	(3.79 +/- .55) E+01	(1.63 +/- .18) E+02	1.268 +/- .098	1.000
19.5 21.0	(5.67 +/- .92) E+00	(1.22 +/- .25) E+01	(7.33 +/- .95) E+01	1.277 +/- .100	.995

TABLE 4-9. (continued)

B 2/3

ET LIMITS		DS/DET (AL)	DS/DET (CU)	DS/DET (PB)	ALPHA	CORRELATION
.0	1.0	(1.01 +/- .14) E+05	(1.44 +/- .45) E+05	(4.14 +/- .97) E+05	.682 +/- .133	.991
1.0	3.0	(9.03 +/- .71) E+04	(1.75 +/- .18) E+05	(3.38 +/- .51) E+05	.667 +/- .080	.995
3.0	5.0	(4.95 +/- .43) E+04	(9.99 +/- 1.47) E+04	(2.70 +/- .34) E+05	.831 +/- .075	1.000
5.0	6.5	(1.60 +/- .32) E+04	(4.95 +/- 1.09) E+04	(1.39 +/- .32) E+05	1.058 +/- .148	.993
6.5	7.5	(1.08 +/- .26) E+04	. . . .	(6.96 +/- 2.05) E+04	.913 +/- .186	1.000
7.5	9.0	. . . .	. . . .	. . . .	. . . .	. . .
9.0	9.5	. . . .	. . . .	. . . .	. . . .	. . .
9.5	11.0	(6.56 +/- 1.29) E+02	. . . .	(1.13 +/- .12) E+04	1.397 +/- .109	1.000
11.0	13.0	(2.36 +/- .24) E+02	. . . .	(3.74 +/- .21) E+03	1.354 +/- .057	1.000
13.0	13.5	(6.79 +/- 1.52) E+01	(2.65 +/- .20) E+02	(1.27 +/- .15) E+03	1.380 +/- .102	.998
13.5	14.5	(4.11 +/- .55) E+01	(1.47 +/- .08) E+02	(9.12 +/- .80) E+02	1.531 +/- .070	1.000
14.5	15.0	(2.79 +/- .64) E+01	(8.54 +/- 1.18) E+01	(5.42 +/- .77) E+02	1.490 +/- .120	.999
15.0	17.0	(8.10 +/- 1.20) E+00	(3.15 +/- .37) E+01	(1.47 +/- .12) E+02	1.390 +/- .076	.999
17.0	19.0	(1.90 +/- .54) E+00	. . . .	(2.20 +/- .54) E+01	1.200 +/- .184	1.000

F 2/3

ET LIMITS		DS/DET (AL)	DS/DET (CU)	DS/DET (PB)	ALPHA	CORRELATION
.0	1.0	(1.28 +/- .15) E+05	(2.36 +/- .50) E+05	(5.53 +/- 1.12) E+05	.717 +/- .114	1.000
1.0	3.0	(9.15 +/- .63) E+04	(1.74 +/- .18) E+05	(3.09 +/- .47) E+05	.623 +/- .077	.992
3.0	5.0	(4.06 +/- .38) E+04	(7.48 +/- 1.26) E+04	(2.38 +/- .31) E+05	.863 +/- .079	.998
5.0	6.0	. . . .	. . . .	. . . .	. . . .	. . .
6.0	8.0	. . . .	. . . .	. . . .	. . . .	. . .
8.0	8.5	. . . .	. . . .	. . . .	. . . .	. . .
8.5	9.5	(4.10 +/- .97) E+02	. . . .	(3.57 +/- .87) E+03	1.062 +/- .167	1.000
9.5	11.0	(1.14 +/- .17) E+02	. . . .	(9.61 +/- 1.55) E+02	1.043 +/- .109	1.000
11.0	11.5	(2.35 +/- .63) E+01	(5.96 +/- 1.12) E+01	. . . .	1.084 +/- .382	1.000
11.5	12.0	(5.88 +/- 2.95) E+00	(3.48 +/- .72) E+01	. . . .	2.075 +/- .633	1.000

M 1/2

ET LIMITS		DS/DET (AL)	DS/DET (CU)	DS/DET (PB)	ALPHA	CORRELATION
.0	1.0	(1.41 +/- .16) E+05	(2.53 +/- .48) E+05	(5.90 +/- 1.23) E+05	.701 +/- .113	1.000
1.0	3.0	(9.50 +/- .70) E+04	(1.80 +/- .17) E+05	(3.90 +/- .52) E+05	.699 +/- .072	.999
3.0	4.5	(3.99 +/- .43) E+04	(8.25 +/- 1.51) E+04	(1.90 +/- .32) E+05	.769 +/- .097	.999
4.5	5.5	. . . .	. . . .	. . . .	. . . .	. . .
5.5	7.5	. . . .	. . . .	. . . .	. . . .	. . .
7.5	8.0	. . . .	. . . .	. . . .	. . . .	. . .
8.0	9.5	(3.45 +/- .78) E+02	. . . .	(4.94 +/- .85) E+03	1.306 +/- .139	1.000
9.5	11.0	(6.12 +/- 1.29) E+01	. . . .	(9.23 +/- 1.42) E+02	1.331 +/- .128	1.000
11.0	11.5	(1.89 +/- .72) E+01	(6.04 +/- 1.40) E+01	. . . .	1.358 +/- .520	1.000
11.5	12.5	(5.97 +/- 2.21) E+00	(3.56 +/- .53) E+01	. . . .	2.084 +/- .466	1.000

References for Chapter IV

1. B. Brown et al., Phys. Rev. Lett. 49, 711 (1982).
2. R. Brun, I. Ivanchenko, and P. Palazzi, CERN Computer Centre program library long write-up Y250, 1979 (unpublished).
3. C. E. Fichtel and J. I. Trombka, Gamma Ray Astrophysics (NASA SP-453, Washington DC, 1981), ch. 13; M. A. Dris, Nucl. Inst. Meth. 161, 311 (1979).
4. B. Brown et al., Phys. Rev. Lett. 50, 11 (1983).

CHAPTER V

EVENT STRUCTURE

The principal goal of E557 was to study properties of events in which a hard parton-parton collision appeared to have occurred. The Global trigger was intended to select such events: however, one finds that Global trigger events are predominantly non-jetlike and show no clear signs of having come from hard scatters. In this chapter I discuss the properties of events as functions of the transverse energy in each of five full-azimuth apertures and report on the extent to which jetlike events can be found in an unbiased way in our data. I also discuss a possible background, evidence for which appears in the event structure analysis.

5.1. Planarity definition

We wish to study the structure -- the "shape" in which the energy is distributed -- of events with high transverse energy in each of several apertures. In particular, we would like to know whether high E_t events have the characteristic jet configuration expected in simple theories of hard parton-parton scattering.

A number of measures of the "jettiness" of an event's structure have been proposed, among them sphericity,[1] thrust,[2] and planarity.[3] Sphericity and thrust are the most commonly used in e^+e^- experiments.

The NA5 collaboration defined planarity for use in its analysis of high transverse energy hadronic collisions; it is somewhat similar to sphericity, but two-dimensional: i.e., based on transverse momenta rather than three-momenta. For this analysis, I will use the planarity parameter, defined as follows. Consider a set of n particles with transverse momenta $\vec{p}_{t1}$, $\vec{p}_{t2}$, ... $\vec{p}_{tn}$. (These transverse momenta are two-vectors in the plane transverse to the beam). Each $\vec{p}_{ti}$ can be decomposed into components parallel and perpendicular to some direction $\hat{n}$; if $A(\hat{n})$ denotes the sum of the squared magnitudes of the parallel components and $B(\hat{n})$ the sum of the squared magnitudes of the perpendicular components, then the planarity, P, is defined as the maximum with respect to variation of $\hat{n}$ of

$$P(\hat{n}) = \frac{A(\hat{n}) - B(\hat{n})}{A(\hat{n}) + B(\hat{n})} . \qquad (5\text{-}1)$$

The direction $\hat{n}_P$ which maximizes $P(\hat{n})$ is called the planarity axis. Operationally, one finds the planarity axis by diagonalizing the tensor

$$I_{\alpha\beta} = \sum_{i=1}^{n} (p_{ti}^2 \delta_{\alpha\beta} - p_{ti\alpha} p_{ti\beta}) \qquad (\alpha,\beta = x,y) \qquad (5\text{-}2)$$

(which is analogous to the inertia tensor in mechanics); then, if ϕ_i denotes the angle between $\vec{p}_{ti}$ and $\hat{n}_P$,

$$P = \frac{\Sigma\, p_{ti}^2 (\cos^2\phi_i - \sin^2\phi_i)}{\Sigma\, p_{ti}^2} . \qquad (5\text{-}3)$$

For any configuration in which all particle trajectories are straight lines emanating from the interaction point and lie in a plane containing the beam direction -- two back-to-back particles, for example -- the planarity axis is the line formed by the intersection of that plane with the transverse plane; then $B(\hat{n}_p) = 0$ and $P = 1$, the maximum possible value. For configurations of particles whose directions are distributed isotropically and without correlation with their transverse momenta, as $n\to\infty$, $P\to 0$ (see Fig. 5-1).

Effects such as bending of particle trajectories by the magnet and secondary interactions will tend to distort the planarity. We include the former effect in our simulations and, as will be shown below, the planarity distortion is negligible. Secondary scatters are not simulated but their effect is expected to be small. The amount of material between the center of the hydrogen target and the calorimeter is about 4.8 g/cm^2, and to significantly affect the planarity requires that a secondary scatter involve one of the high-momentum particles and that enough momentum be transferred to substantially alter the transverse energy of the event. Such secondary scattering would affect not only the planarity but the event rate. Lopez[4] has investigated the contributions of secondary scattering to the cross sections for E557's limited-$\Delta\phi$ triggers and found them to be negligible. However, a somewhat different situation exists just after a hard collision in a nucleus, before the scattered partons have hadronized; the entire event structure is being carried by a small number of particles in an extremely dense medium. Multiple scattering of partons inside the nucleus, which has been widely credited with causing the anomalous nuclear enhancement, can also be expected to decrease planarity.

A hard parton-parton scatter will initially produce two high-p_t partons back to back in their center of mass frame. If their initial transverse momenta in the proton-proton center of mass frame are not too large, and if they each hadronize into a jet of particles whose p_t with respect to the parton direction is limited (as discussed in Chapter I), then the final state particles will lie near a plane. The fragments of the beam and target remnants will be distributed isotropically but will have relatively low p_t, while the planarity of the high-p_t final-state particles will be large. (The converse is untrue: because planarity is insensitive to collimation, or its lack, in θ, a high-planarity event can be non-jetlike).

For the experimental data, we have available not particle transverse momenta but calorimeter module transverse energies. One can define a "calorimeter planarity," P^C, analogous to the above "particle planarity," by doing sums over modules instead of particles and substituting module transverse energies, ε_{ti}, for p_{ti}. Particle planarities can be computed for the Monte Carlo events, with the convention that only particles entering the EM calorimeter are included in the sums.

The main advantages to using planarity are that it can be computed quickly and easily; it has an easily-interpreted meaning (via the momentum-tensor metaphor), and that use of planarity facilitates comparison of our results with those of NA5. To compute thrust requires that one find, by a tree-search algorithm, the set of particles whose total momentum is a maximum. This is consumes considerably more computer time, for large multiplicities, than does the computation of planarity. Thrust has the advantage of being linear in the particle momenta, so that if one particle is split into two (via a decay or instrumentally), so long as the angle between them is small, the thrust remains unchanged. Thus it is relatively insensitive to the history of the secondaries.[5] A variable similar to thrust has been used by the AFS collaboration[6] to study event structure within a small aperture. No maximization is done to find the thrust axis; instead, the axis used is the direction of the summed momenta in the aperture. This variable retains most of thrust's advantages and is easily computed. However, it is not applicable to studies of full-azimuth apertures. A two-dimensional analog has been used by Lopez in the analysis of the E557 small-$\Delta\phi$ apertures.[4,7]

5.2. Monte Carlo event structure

As examples of two classes of events with very different distributions of planarity, let us consider the LPS and QCD/brem Monte Carlo data. Figures 5-2 and 5-3 show, respectively, mean values of P^C and of P as functions of E_t^C and of E_t for the LPS model. The numerical values are tabulated in Tables 5-1 and 5-2. The results from the QCD/Brem model are given in Figs. 5-4 and 5-5, and in Tables 5-3 and 5-4. The differences in event structure between these two models is readily apparent. In both, mean planarity is fairly high at low transverse energy, due to the preponderance of very low multiplicity events (less than about five particles in the calorimeter) which tend to have high planarity. (Events with zero particles entering the calorimeter are included, with planarity arbitrarily set at zero -- hence in some cases there is a dip in mean planarity at zero transverse energy). However, the jets in the QCD/Brem model, though somewhat masked by gluon bremsstrahlung, still dominate at large transverse energy and cause a distinct rise in mean planarity. The isotropic LPS events get less and less planar as transverse energy increases and the multiplicity grows.

It should be emphasized that, while the apertures over which the transverse energy sum is taken differ from one plot to the next, I always do the sums in the planarity definitions over all particles entering the EM calorimeter (for P) or over all modules in the complete calorimeter (for P^C). The restricted-aperture transverse energy sums are being used to select events, but we are interested in the structure of all the large-angle energy.

Comparison of plots shows that, for both LPS and QCD/Brem data, the shape and normalization of mean P versus E_t and of mean P^C versus E_t^C are very similar. Positions in transverse energy are shifted by a small amount which is consistent with the E_t shifts described by the calorimeter resolution function. The E557 calorimeter does not significantly distort the planarity distributions.

It is of interest to examine the size of the high-planarity component of the data. Figure 5-6 and Table 5-5 give the fraction of events having $P^C > 0.7$ for the LPS data. The QCD/brem results are in Fig. 5-7 and Table 5-6. For all apertures, only a few percent of high-E_t^C LPS events have high planarity, while in QCD/brem the fraction rises with E_t^C to about 80% or more.

A second quantifier of event structure is the ratio of Global transverse energy in the calorimeter to Global energy in the calorimeter (E^C, defined as the sum of the energies in the modules):

$$\frac{E_t^C}{E^C} = \frac{\Sigma\ \varepsilon_{ti}^C \sin\ \theta_i}{\Sigma\ \varepsilon_{ti}^C} \ . \tag{5-4}$$

Writing this quantity in terms of module energies makes it clear that E_t^C/E^C is in fact an energy-weighted average of sin θ for the event. Mean values of E_t^C/E^C and the corresponding particle quantity, E_t/E, in the Monte Carlos are given in Tables 5-7 and 5-8 for large E_t^C in each of the apertures.

5.3. Hydrogen data event structure

Figure 5-8 and Table 5-9 give the mean planarity in the hydrogen data as a function of E_t^C. As was stated in Ref. 8, no rise in planarity with Global aperture transverse energy is seen; for high Global E_t^C, mean planarity is nearly constant with a value of 0.4. Essentially the same behavior is seen for A-Global E_t^C.

The data are consistent with a very slight rise in mean planarity as a function of transverse energy in the B 2/3 aperture, and a moderate increase with M 1/2 transverse energy. However, mean planarity increases dramatically with increasing E_t^C in the F 2/3 aperture. The increase is seen primarily in the last two bins of Fig. 5-8d. There are nine events in the last bin, with $E_t^C > 13.5$ GeV and mean planarity 0.82. In the bin from 12.5 to 13.5 GeV there are thirty events with a mean planarity of 0.58. By contrast, mean calorimeter planarity for events with high B 2/3 transverse energy goes up to only about 0.50 -- higher than for high Global E_t^C events, but only slightly.

Figure 5-9 and Table 5-10 present the fraction of events with high P^C (> 0.7) as a function of transverse energy for the hydrogen data. As has been reported previously,[8] the fraction of events with high P^C is constant for large E_t^C in the Global aperture, with a value of about 8%. The behavior as a function of E_t^C in A-global is similar. The high-planarity component for large E_t^C in B 2/3 is slightly larger, about 12%, and rises only slightly with E_t^C, if at all. However, the high-P^C component is enhanced in events with high E_t^C in M 1/2 -- (39 ± 12)% above 12.5 GeV -- and a dramatic rise to (78 ± 19)% is seen at high E_t^C in F 2/3.

The structure of the events with high F 2/3 transverse energy is very different from that of the events with high B 2/3 E_t^C. Once again we are faced with asymmetric results from symmetric apertures. No such asymmetry is seen in the Monte Carlo data. Whatever its cause, it is something not simulated in our models.

Mean values of E_t^C/E^C for the hydrogen data are given in Table 5-11.

5.4. Mechanisms for the asymmetry

One or the other of Figs. 5-8c and 5-8d, or both, must be reflecting an instrumental effect not simulated in the Monte Carlo; the true average structure of proton-proton events must be symmetric with respect to reflections about 90°. Therefore, either the highly planar events with high F 2/3 E_t^C must have been faked by some mechanism, or their counterparts in the B 2/3 aperture must have been swamped or suppressed by some mechanism. In the following discussion, I will use the phrase "F 2/3 event" to mean "event with high E_t^C in F 2/3," and similarly for "B 2/3 event."

Pictures of the nine events with E_t^C in the F 2/3 aperture greater than 13.5 GeV are shown in Figs. 5-10b to 5-10j. In these "Lego plots" the two horizontal axes are ϕ and cos θ^*. For each module with ϵ_{ti}^C above 0.15 GeV an entry was made in the plot at the (cos θ^*, ϕ) corresponding to the center of the module with height proportional to

ϵ^C_{ti}. (Figure 5-10a shows the area of these plots covered by the calorimeter as well as the axis definitions).

An event with two high-p_t jets would appear as two clusters, limited in ϕ and cos θ^* and with centers separated by about 180° in ϕ. Several such events appear in Figs. 5-11a to 5-11i, typical F 2/3 events from the QCD/Brem Monte Carlo. Most of the Monte Carlo events and those from the experimental data approach this ideal to a greater or lesser degree. Only two of the nine events from the experiment have $P^C < 0.7$; these events do not look very "jetty."

No problems with the experimental data are obvious from these pictures; E^C_t seems to be fairly well balanced, with the jets (there seems to be no reason to call them anything else) always close to 180° apart and of comparable size.

Figures 12 and 13 show pictures of some typical events with E^C_t in the B 2/3 aperture larger than 14.8 GeV, for the hydrogen data and the QCD/brem model, respectively.

Could the low-planarity B 2/3 events be incorrect? Perhaps there is some source of low-planarity background events which preferentially occur in the backward direction (in the nominal proton-proton center-of-mass system whose origin is in the hydrogen target). If so, then there should be about as many high-planarity events in a sample chosen by a particle E_t cut in the B 2/3 aperture as for the same cut in the F 2/3 aperture; the low-planarity background should appear as additional events in the B 2/3 sample and not in the F 2/3 sample.

Cutting on particle E_t is not possible, but with some care one can try the test with a cut on E^C_t. I used the resolution function to determine approximately equivalent E^C_t cuts for the F 2/3 and B 2/3 apertures as follows: Assuming the F 2/3 events to be free of asymmetric background, one can predict the background-free B 2/3 E_t^C spectrum by applying the B 2/3 resolution function to the F 2/3 E_t spectrum, obtained as described in Chapter IV. Then, for a given F 2/3 E_t^C cut, one can determine an "equivalent" B 2/3 E_t^C cut by requiring equal background-free cross sections integrated above the cuts for the two apertures. According to this prescription, the cut equivalent to $E_t^C > 12.5$ GeV in F 2/3 (which selects the 39 events in the last two bins of Fig. 5-8d) is $E_t^C > 13.8$ GeV in B 2/3. I refer to these as the "high cuts." For $E_t^C > 10.0$ GeV in F 2/3, the equivalent cut in B 2/3 is $E_t^C > 11.2$ GeV. These are the "low cuts."

I applied these cuts to subsets of the experimental data. To avoid threshold effects, I used only runs in which the cuts for <u>both</u> apertures were higher than the threshold cuts described in Chapter IV.

The low cuts selected 56 F 2/3 and 174 B 2/3 events. If there were no background, or if the background were symmetric in the nominal center-of-mass frame, approximately equal numbers of events would be expected. Of these, 11 of the F 2/3 and 18 of the B 2/3 events had $P^C > 0.7$ For the high cuts, 22 F 2/3 and 102 B 2/3 events were selected, of which 12 and 16, respectively, had $P^C > 0.7$. Given the statistics and the uncertainties of the resolution function, these numbers are quite consistent with a forward-backward symmetric, high-planarity signal plus an asymmetric (backward), low-planarity background, probably with a small high-planarity tail.

If we assume F 2/3 events to be background-free, then the differences between the numbers of B 2/3 and F 2/3 events provide a rough estimate of the size of the background in the B 2/3 data: about

70% of the signal for $E_t^C > 11.2$, rising to 80% for $E_t^C > 13.8$. About 5% of this estimated background has $P^C > 0.7$ -- less than, but comparable to, the high-planarity component in events with moderate amounts of E_t^C in F 2/3 or B 2/3.

In Chapter IV, after applying corrections to the cross sections, a difference of a factor of about 10 remained between the F 2/3 and B 2/3 spectra at high E_t. A background of 70% to 80% would eliminate most of this difference. The remaining discrepancy in the cross sections could very easily be explained by uncertainties in the (asymmetric) resolution functions.

Further evidence for a background, and information on its nature, comes from a study of the vertex positions for high-E_t^C events. Table 5-12 shows, for each of the Global trigger run groups, information on the positions of the vertices in the plane transverse to the beam for events above and below the "high cuts," 12.5 GeV in F 2/3 or 13.8 GeV in B 2/3. (Events below these cuts are still required to be above the threshold cuts. Again, runs where the high cuts were less than the threshold cuts were excluded.) Shown are the number of events in each category, the mean vertex position $\bar{x}$ and $\bar{y}$, and the standard deviations, σ_x and σ_y. Only for run group GA were there enough F 2/3 events (barely) to quote numbers. In dealing with these data one has to be careful, because the beam position and size varied from run to run. However, comparisons within each run group show that the B 2/3 events, above or below the 13.8 GeV threshold, come from vertices which are spread more widely than those of the F 2/3 events.

In the laboratory frame, B 2/3 events should have lower average particle energies than the equivalent F 2/3 events. These lower-energy tracks will be more susceptible to secondary scattering, implying a greater uncertainty in the vertex finding. On the other hand, they will occur at wider angles -- a fact which should improve the vertex finding. On the whole, it is not clear that vertices should be inherently more or less accurately found for B 2/3 events than for F 2/3 events. In any case, the errors in the x and y positions of the vertex computed by the vertex finding algorithm are much smaller than the width of the beam, typically less than or about equal to 0.1 mm. If the vertex position discrepancy is due to errors in vertex finding, the cause must be something drastic, not accounted for in the algorithm.

One such possibility is secondary scattering. If some of the tracks used to find the vertex came in fact from a scattering of one of the final-state particles of the first scatter, an erroneous vertex position might be computed. (Note that secondary scattering is not modelled in the apparatus simulation in our Monte Carlos). However, this seems an unlikely explanation for the present problem. Drastic changes in the transverse energy or topology of an event due to secondary scattering are very unlikely: the high multiplicity of the main, high-E_t event means the average energies of the secondaries are rather low, yet one is requiring one of them to give rise to a <u>second</u> high-multiplicity scatter with enough transverse energy in the B 2/3 aperture to compete with single high-E_t scatters.

A more reasonable possibility is that the vertex position discrepancy arises from a real difference in the actual vertex positions, owing to a <u>prior</u> scatter of the beam particle. Such a scatter at a moderate angle would decrease the particle's velocity in the z direction so that the products of the second, high-E_t collision would tend to go backward in the nominal center-of-mass frame. The initial scatter provides a mechanism for artificially increasing the apparent transverse energy of the second scatter; because the planarity increase seen in the F 2/3 events occurs only in the last bins of E_t^C, and because of the steeply-falling cross section, a rather modest E_t boost would suffice to swamp the uncontaminated high-planarity events with lower-E_t, lower-planarity events.

It is easy to show that an event initiated by a particle emerging from a prior scatter at an angle θ with respect to the nominal beam direction in the laboratory frame of reference will, for small angles, have a transverse energy <u>relative to the nominal beam direction</u> which is boosted with respect to the transverse energy <u>relative to the direction of the intermediate particle</u> by approximately $E^C \sin\theta$. Thus the transverse energy boost depends on the event structure and on the aperture being considered. The maximum boost occurs when all the final-state energy enters the aperture; it is about equal to the transverse momentum of the initiating particle relative to the nominal beam direction. For high-E_t^C Global aperture data, E^C is typically about 200 GeV, or half the incident energy.

At high E_t, the difference in $d\sigma/dE_t$ between the F 2/3 and B 2/3 apertures corresponds to an E_t shift of about 1.5 GeV. Furthermore, the region of E_t^C in which a planarity rise is seen is about 3 GeV wide, suggesting that to bury a similar rise in the B 2/3 aperture requires that at least some events be shifted upward by about 3 GeV or more, so that the intermediate particle had to have a transverse momentum of at least 3 GeV -- large, but not outrageous. The situation is somewhat analogous to what is widely believed to occur in high-p_t production from nuclear targets: the rate is boosted substantially above A times the rate for proton targets by a multiple-scattering contribution.

No vertex position anomaly is seen at low transverse energy (Table 5-13), nor in the nuclear target data (Table 5-14). For the latter, all events whose vertex was within 2.5 cm in z of one of the nuclear targets were attributed to that target; the thresholds were chosen arbitrarily. The absence of the vertex position anomaly in the nuclear target data suggests that for these events the asymmetric background is negligible. (A more direct check by forward-backward symmetry arguments fails for pA collisions.) This can be attributed to the anomalous nuclear enhancement: the cross sections fall more slowly with E_t than for hydrogen, with the result that true high-E_t events are not so easily swamped by a lower-E_t background.

The vertex data also suggest that the background affects the other three apertures as well, but to a lesser degree than in B 2/3. Table 5-15 shows vertex position widths increasing significantly with E_t^C in A-global, Global, and M 1/2. (Here again, the thresholds for these three apertures were selected arbitrarily).

5.5. Nuclear targets

Event structure in the nuclear targets was studied by assigning events with vertices within 2.5 cm in z of a nuclear target to that target. As was mentioned in the previous section, the absence of a vertex position anomaly suggests that the suspected asymmetric background is negligible in the nuclear target events.

In Figs. 5-14, 5-15, and 5-16, and in Tables 5-16, 5-17, and 5-18, I present mean calorimeter planarity versus E_t^C for aluminum, copper, and lead targets, respectively. The fraction of events having $P^C > 0.7$ as a function of E_t^C is given in Figs. 5-17, 5-18, and 5-19, and in Tables 5-19, 5-20, and 5-21. No strong evidence of any emerging planar component is seen for any aperture with any nuclear target.

Table 5-22 presents mean values of E_t^C/E_t for the nuclear targets. Note that nuclear target events tend to distribute energy more backwards than do the hydrogen events.

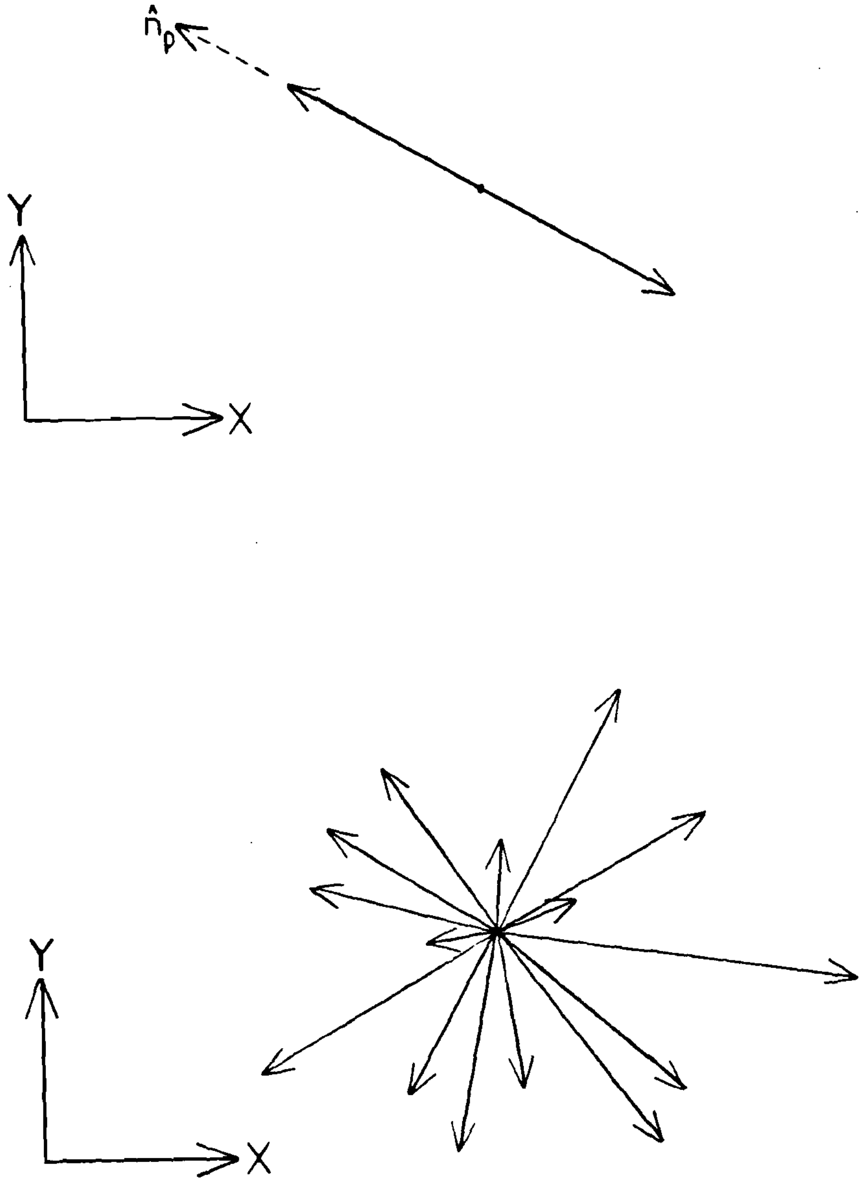

FIG. 5-1. Events with (a) P = 1 and (b) P = 0.

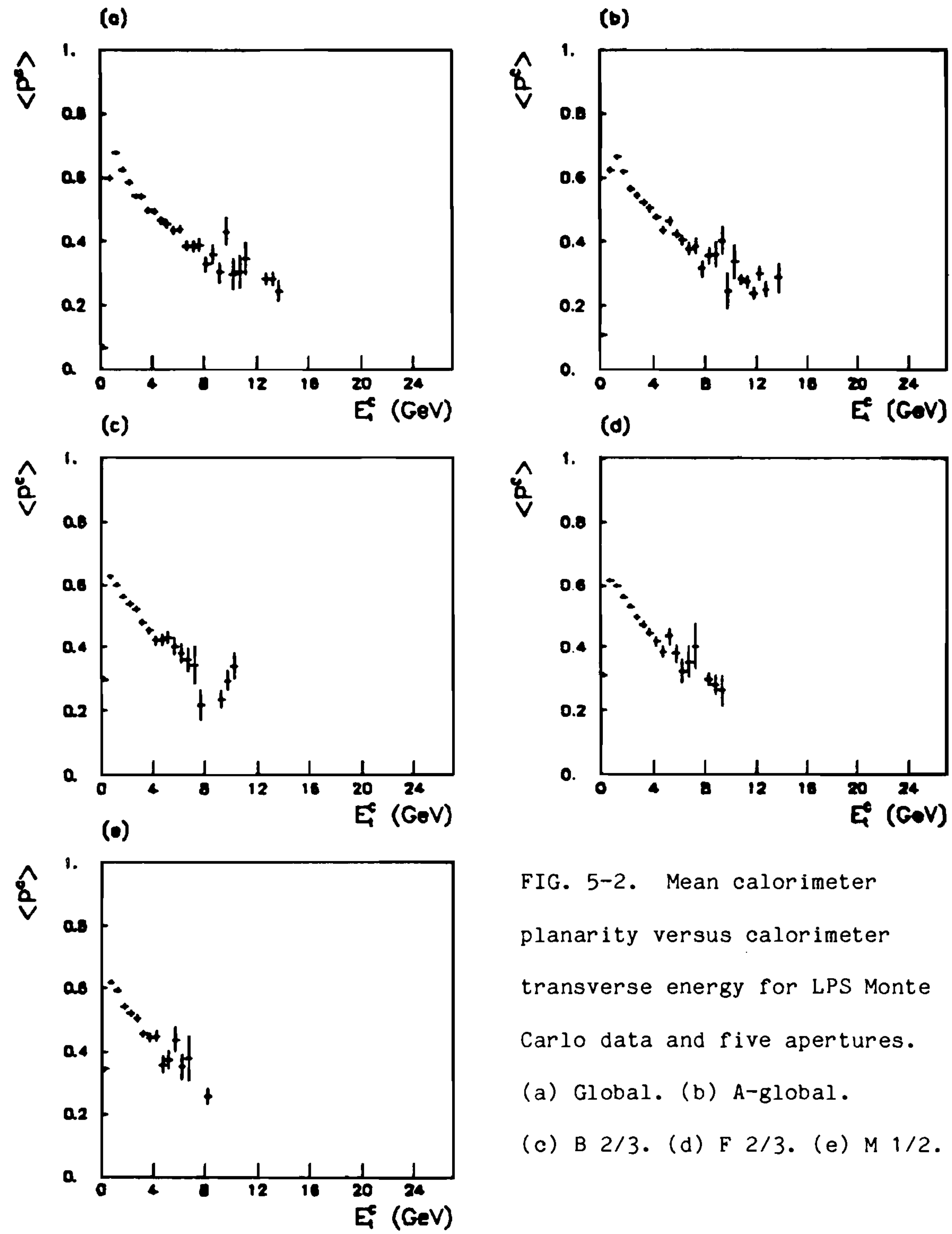

FIG. 5-2. Mean calorimeter planarity versus calorimeter transverse energy for LPS Monte Carlo data and five apertures. (a) Global. (b) A-global. (c) B 2/3. (d) F 2/3. (e) M 1/2.

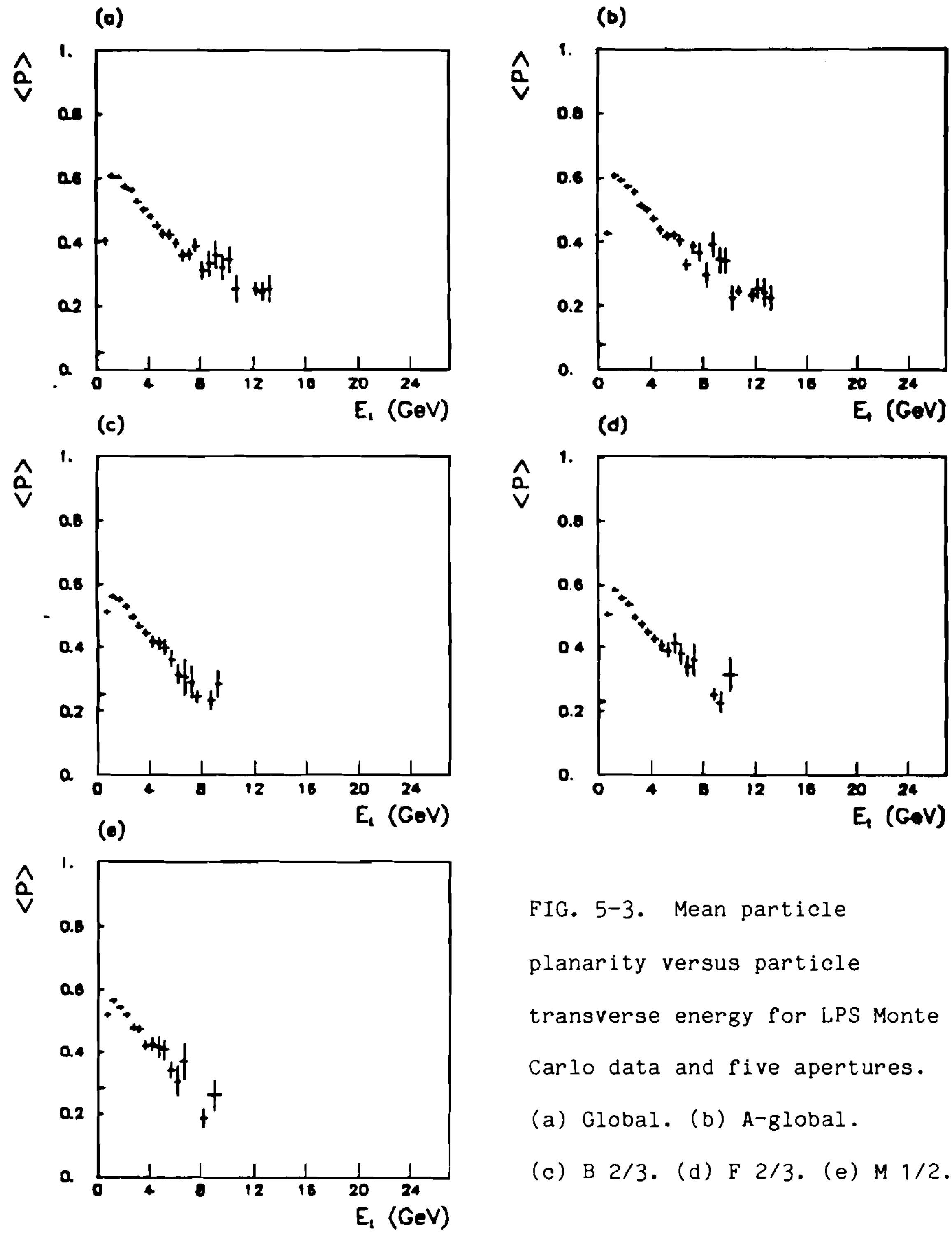

FIG. 5-3. Mean particle planarity versus particle transverse energy for LPS Monte Carlo data and five apertures. (a) Global. (b) A-global. (c) B 2/3. (d) F 2/3. (e) M 1/2.

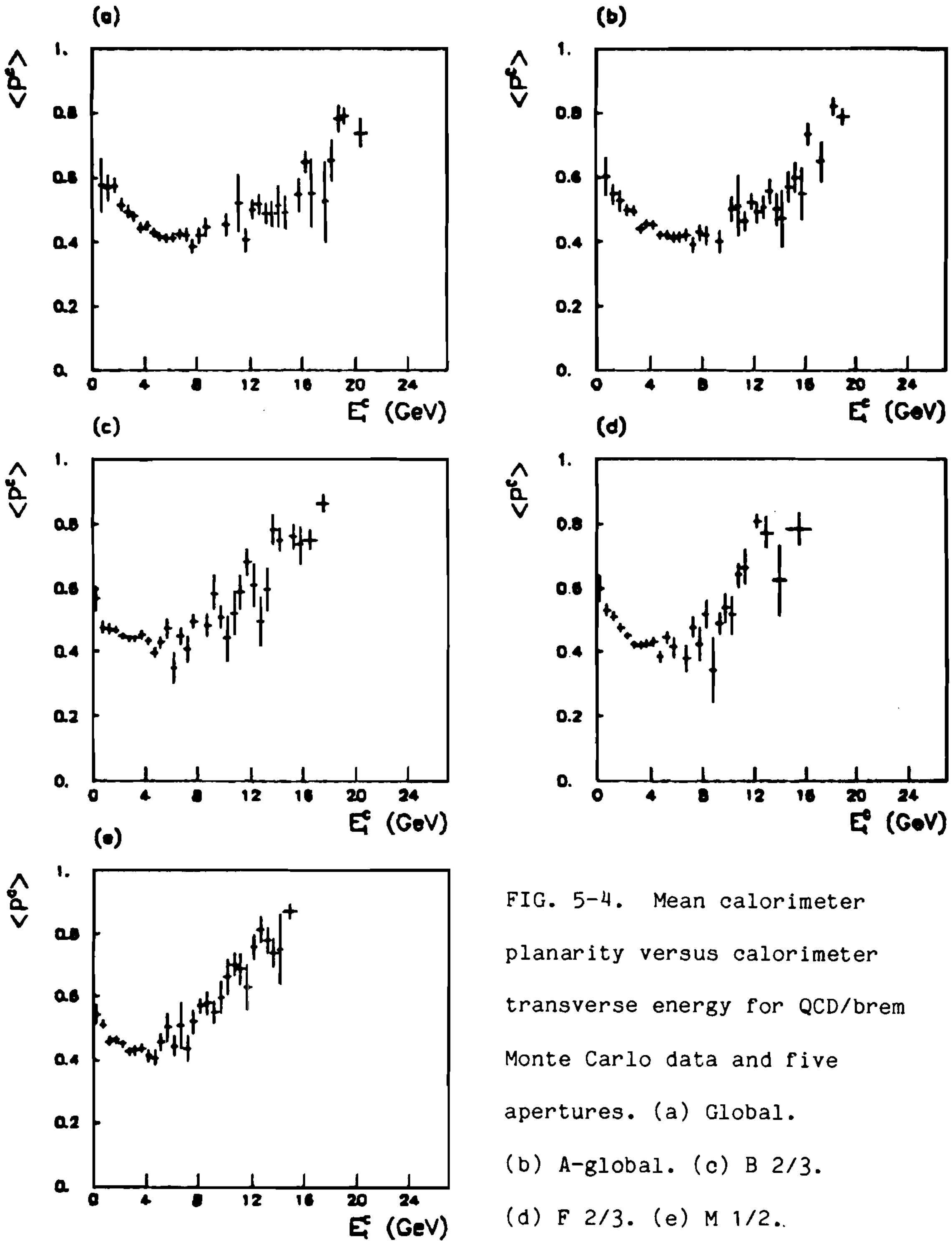

FIG. 5-4. Mean calorimeter planarity versus calorimeter transverse energy for QCD/brem Monte Carlo data and five apertures. (a) Global. (b) A-global. (c) B 2/3. (d) F 2/3. (e) M 1/2.

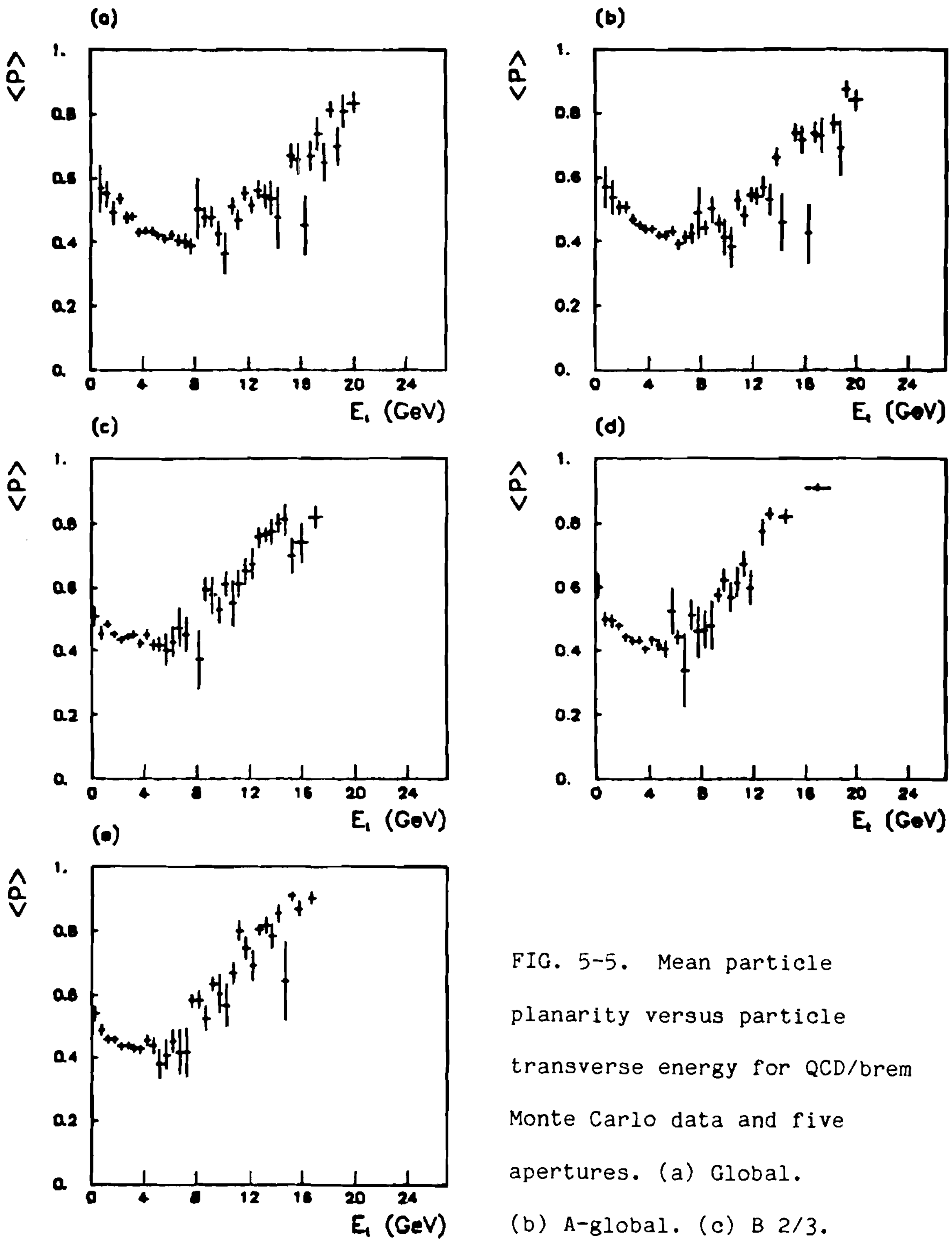

FIG. 5-5. Mean particle planarity versus particle transverse energy for QCD/brem Monte Carlo data and five apertures. (a) Global. (b) A-global. (c) B 2/3. (d) F 2/3. (e) M 1/2.

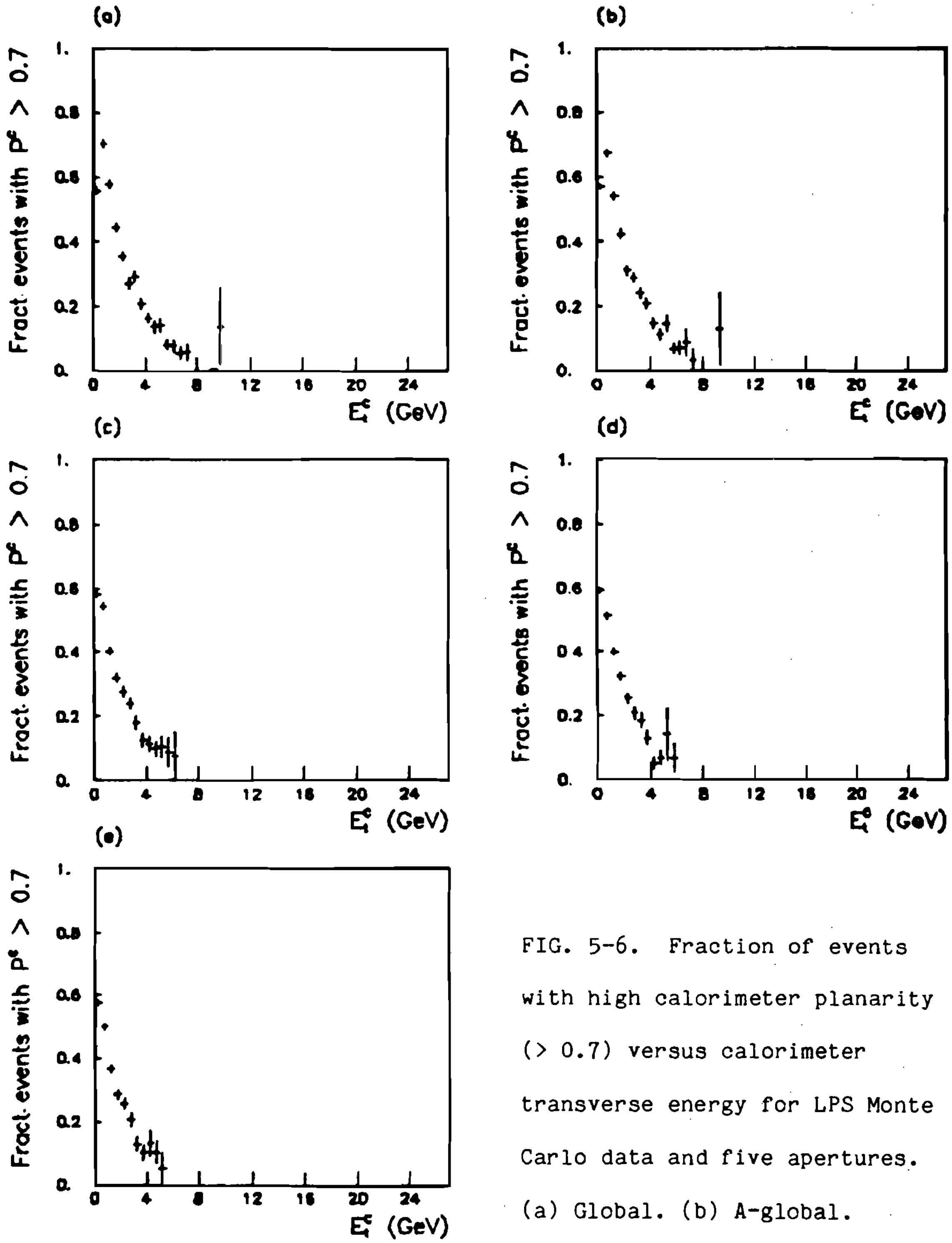

FIG. 5-6. Fraction of events with high calorimeter planarity (> 0.7) versus calorimeter transverse energy for LPS Monte Carlo data and five apertures. (a) Global. (b) A-global. (c) B 2/3. (d) F 2/3. (e) M 1/2.

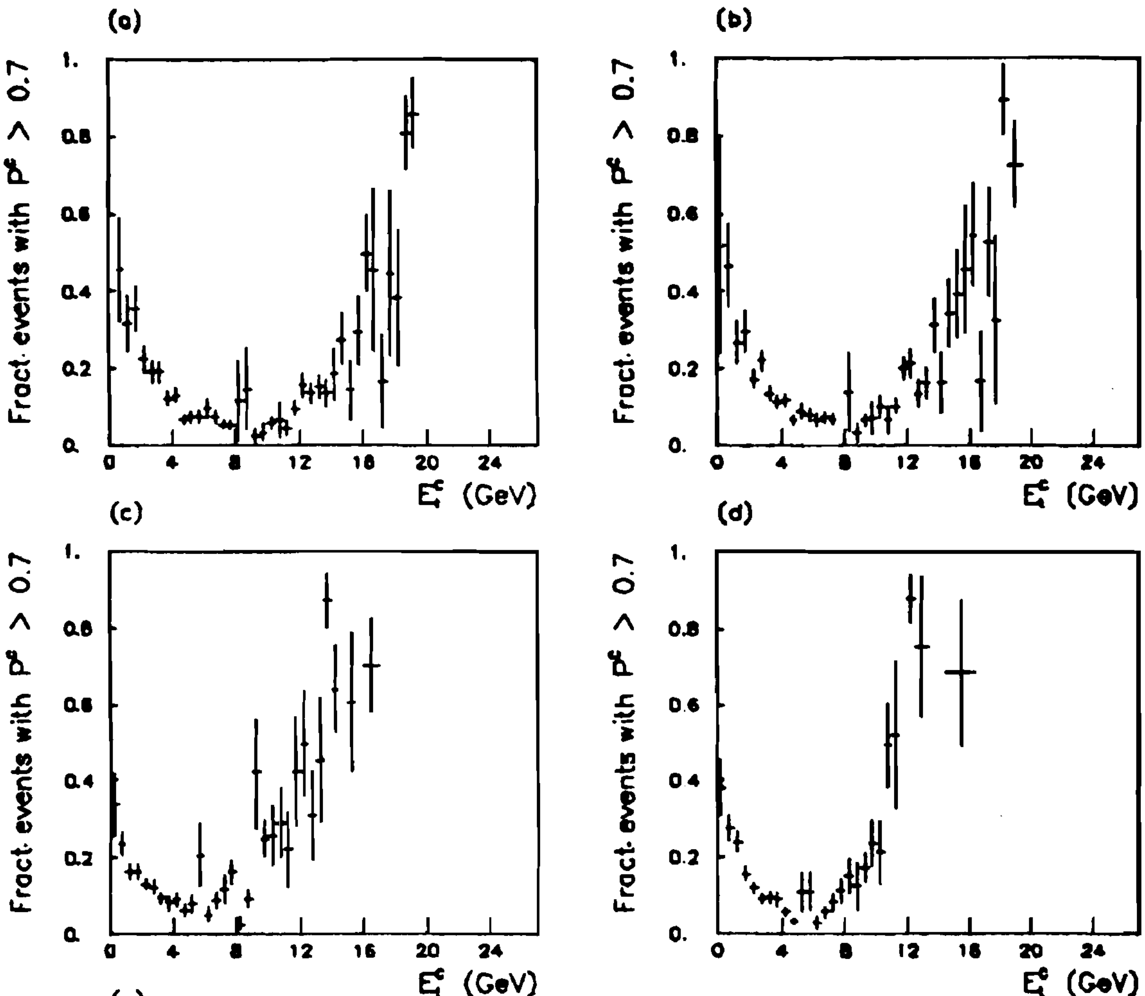

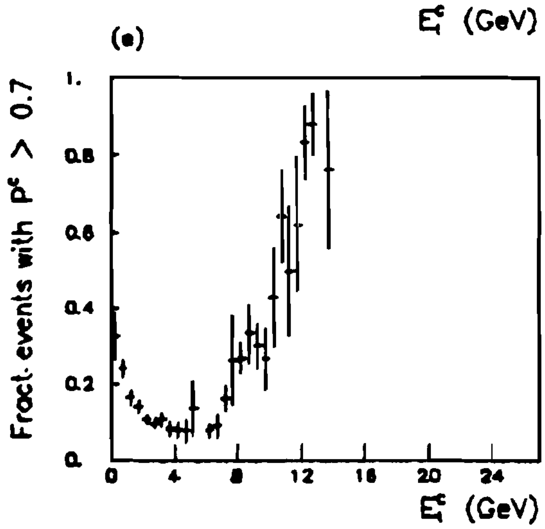

FIG. 5-7. Fraction of events with high calorimeter planarity (> 0.7) versus calorimeter transverse energy for QCD/brem Monte Carlo data and five apertures. (a) Global. (b) A-global. (c) B 2/3. (d) F 2/3. (e) M 1/2.

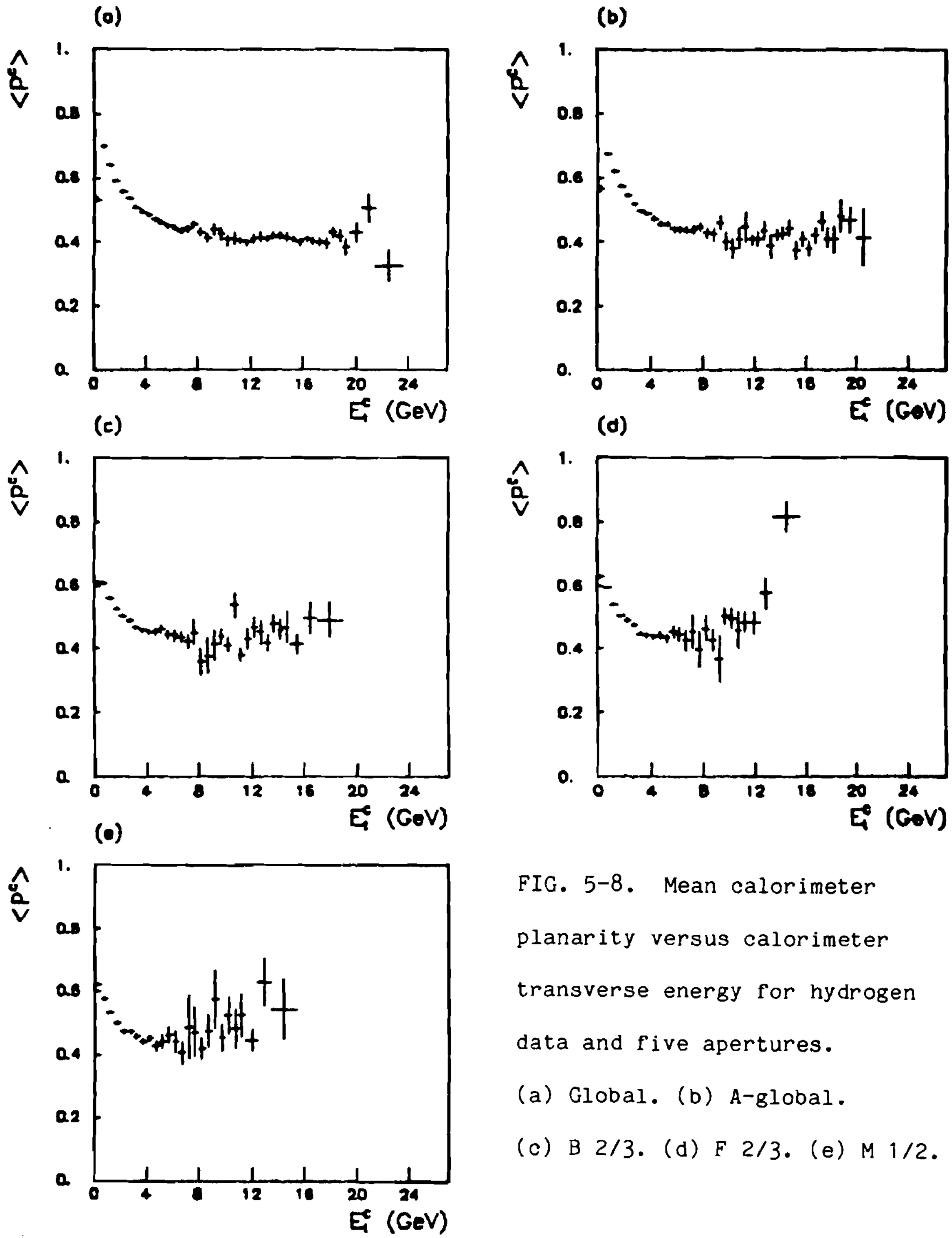

FIG. 5-8. Mean calorimeter planarity versus calorimeter transverse energy for hydrogen data and five apertures.
(a) Global. (b) A-global.
(c) B 2/3. (d) F 2/3. (e) M 1/2.

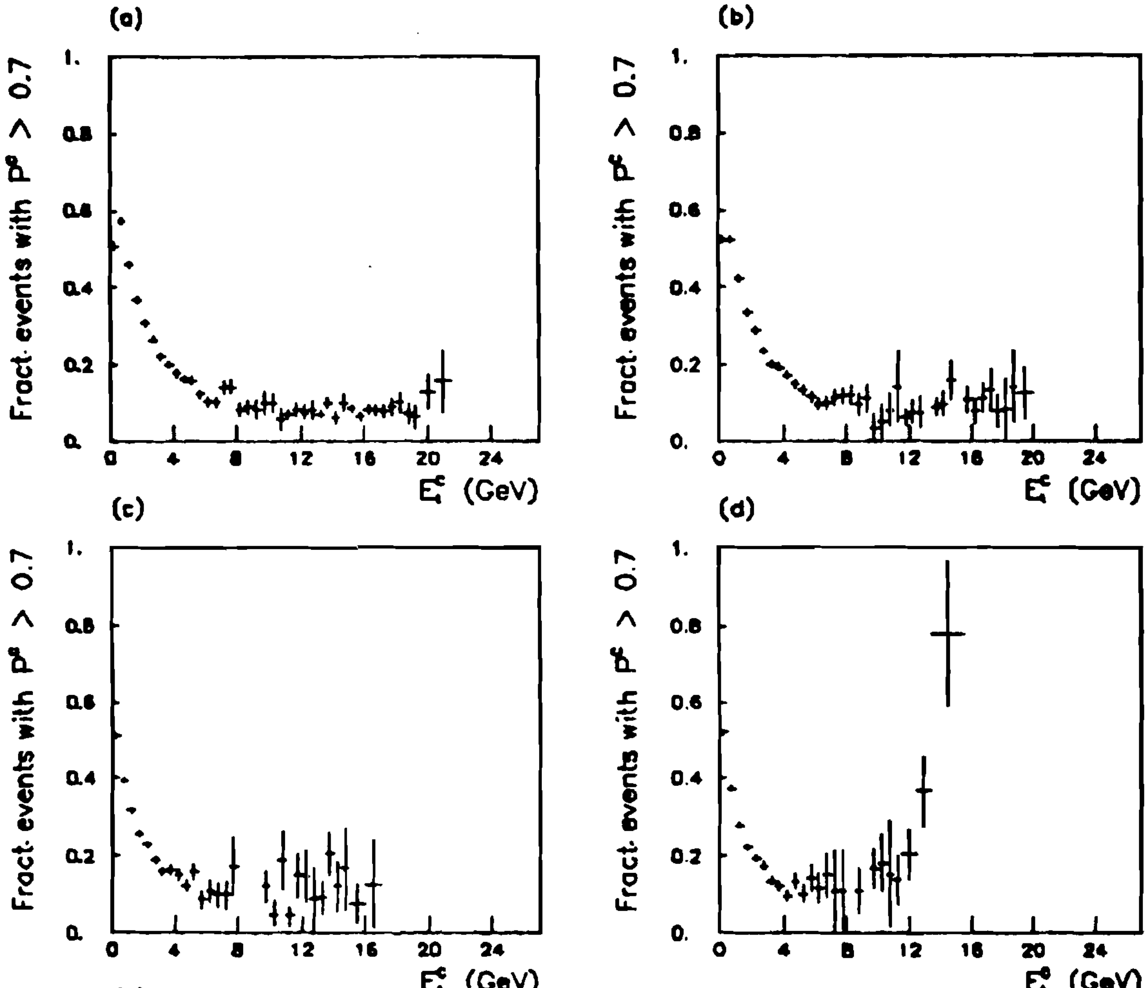

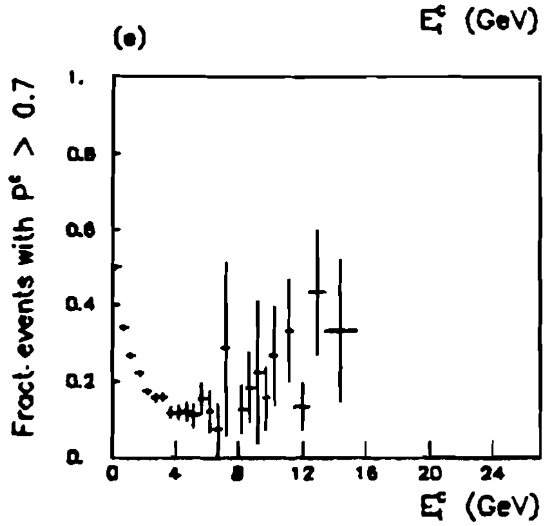

FIG. 5-9. Fraction of events with high calorimeter planarity (> 0.7) versus calorimeter transverse energy for hydrogen data and five apertures. (a) Global. (b) A-global. (c) B 2/3. (d) F 2/3. (e) M 1/2.

(a)

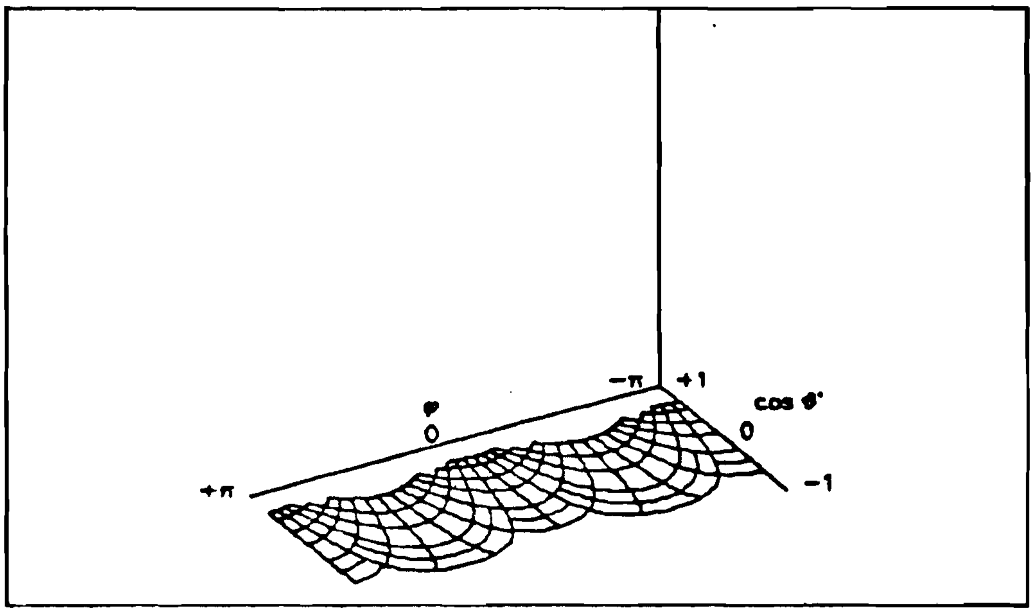

FIG. 5-10. (a) Axis definitions and calorimeter acceptance region for following "Lego plots." (b-j) Transverse energy versus cos θ^* and ϕ for nine events from the experimental hydrogen data with E_t^C in F 2/3 greater than 13.5 GeV.

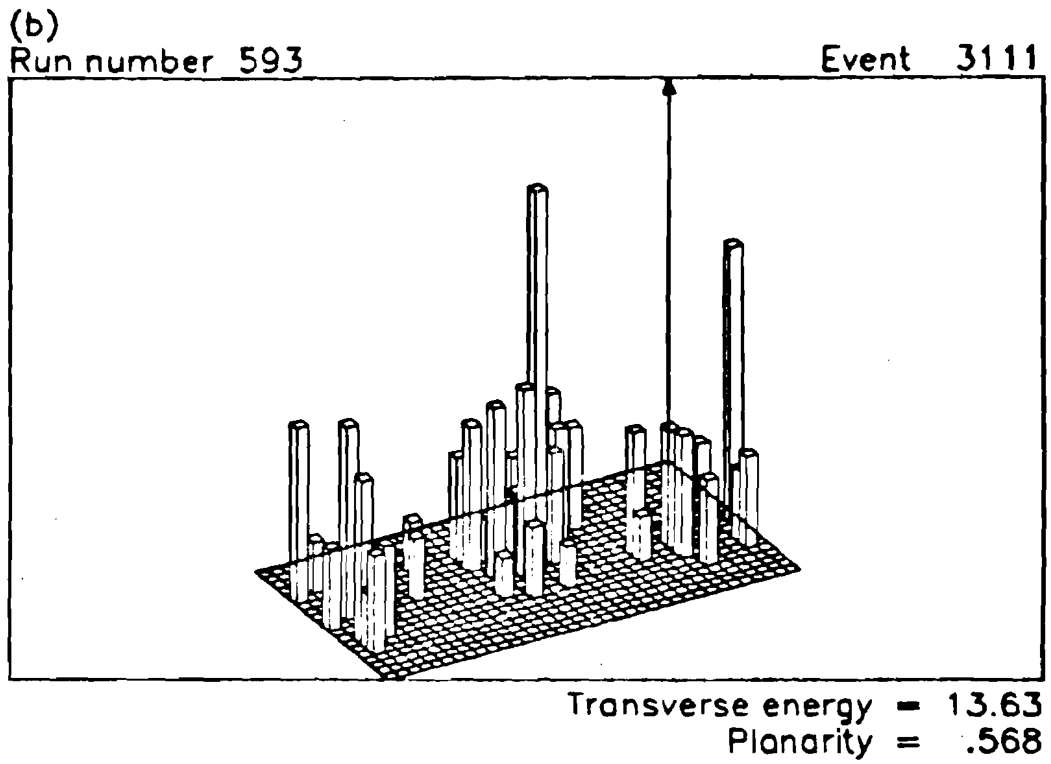

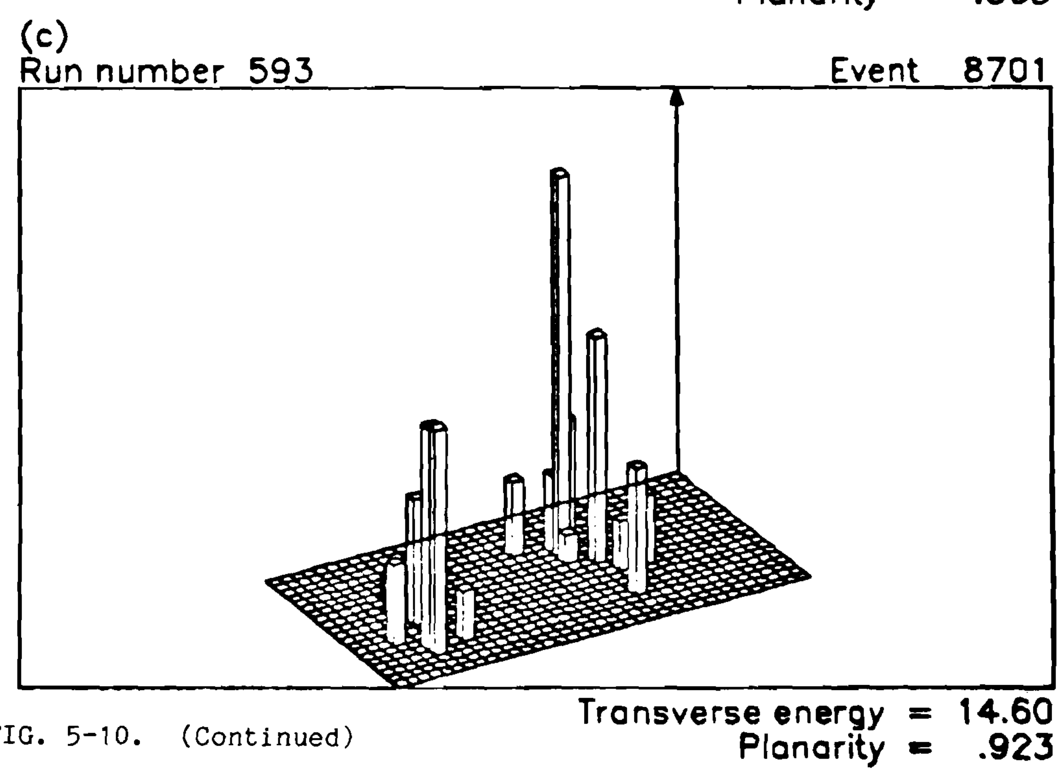

FIG. 5-10. (Continued)

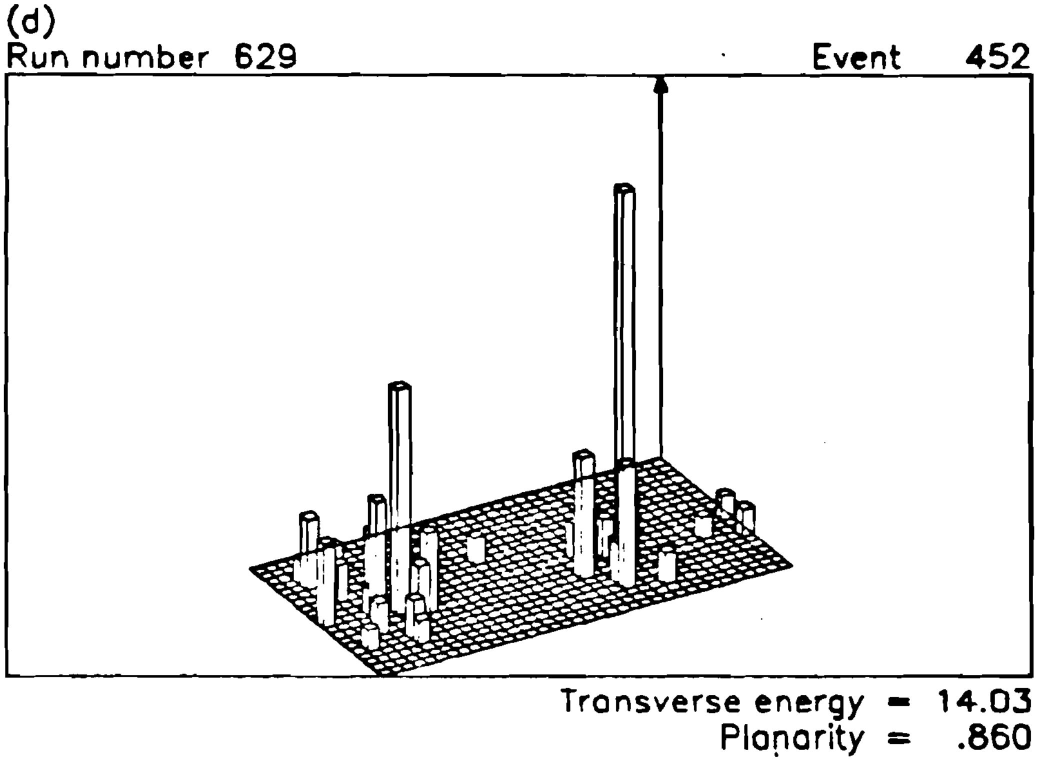

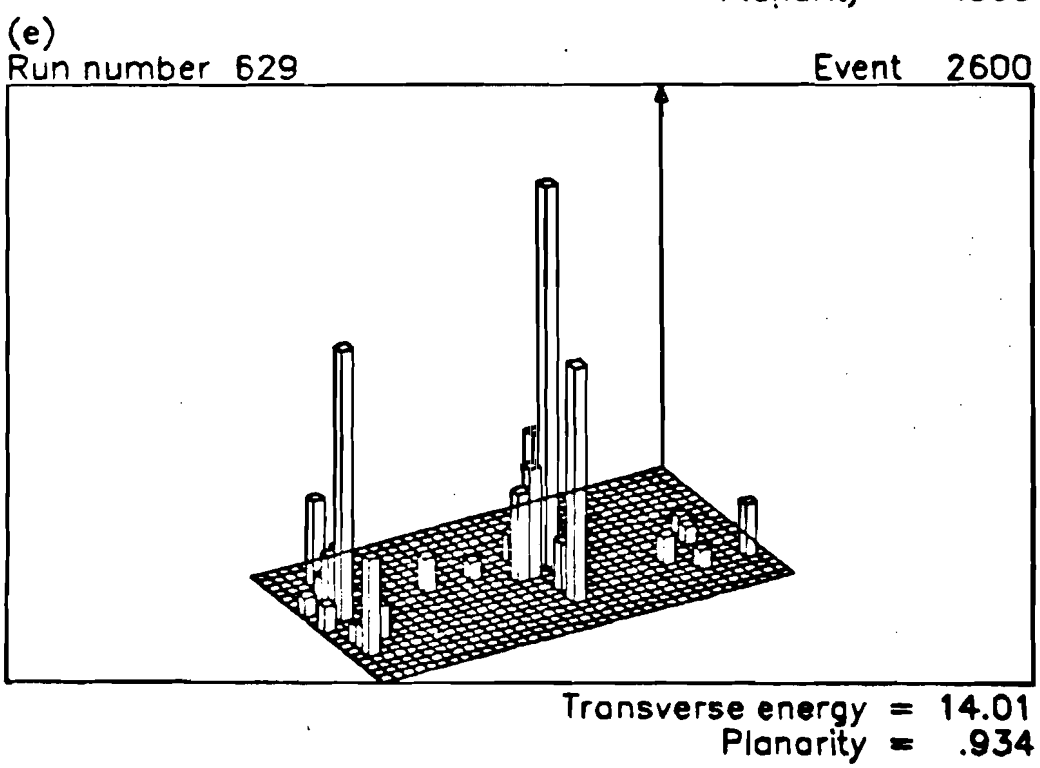

FIG. 5-10. (Continued)

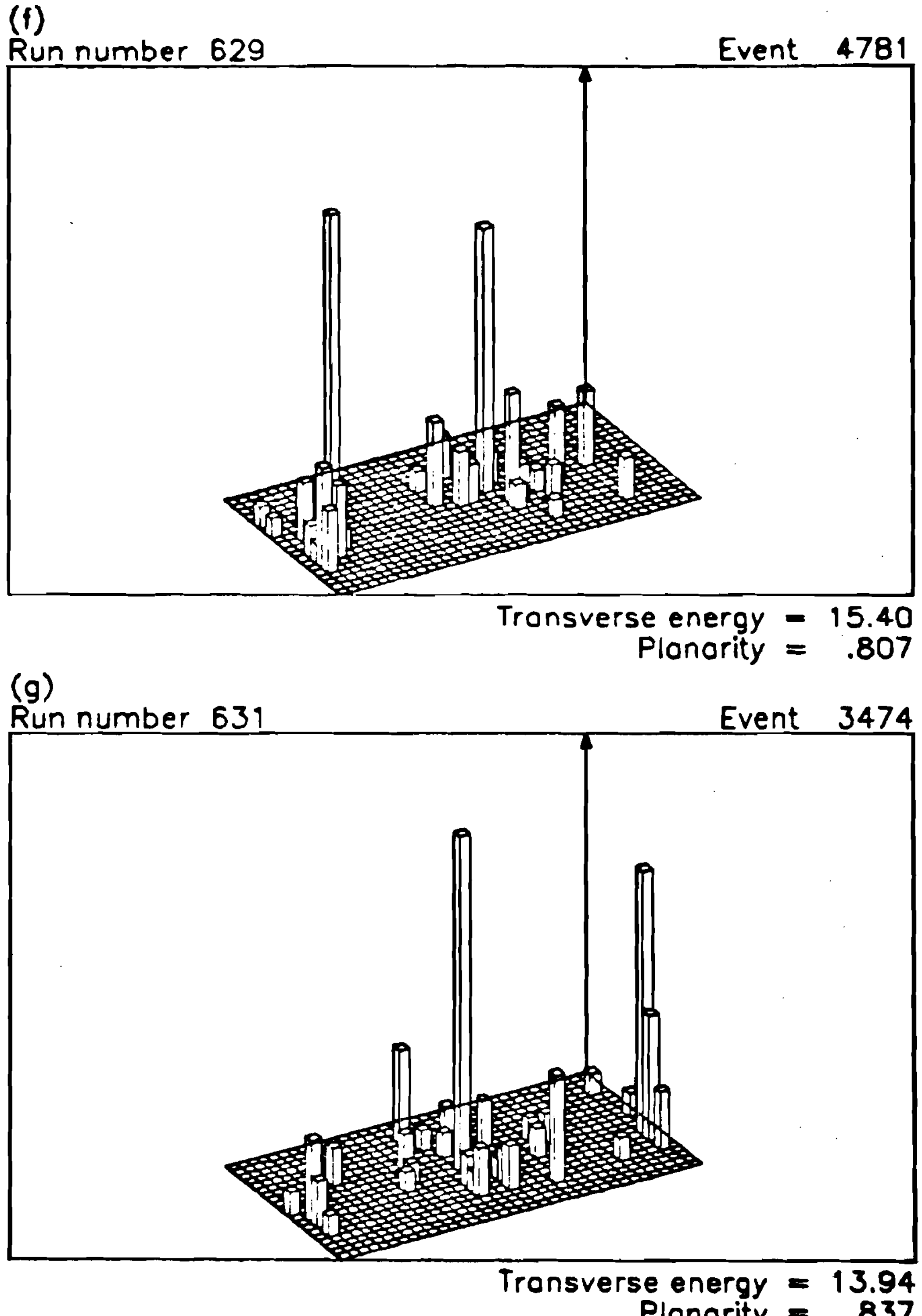

FIG. 5-10. (Continued)

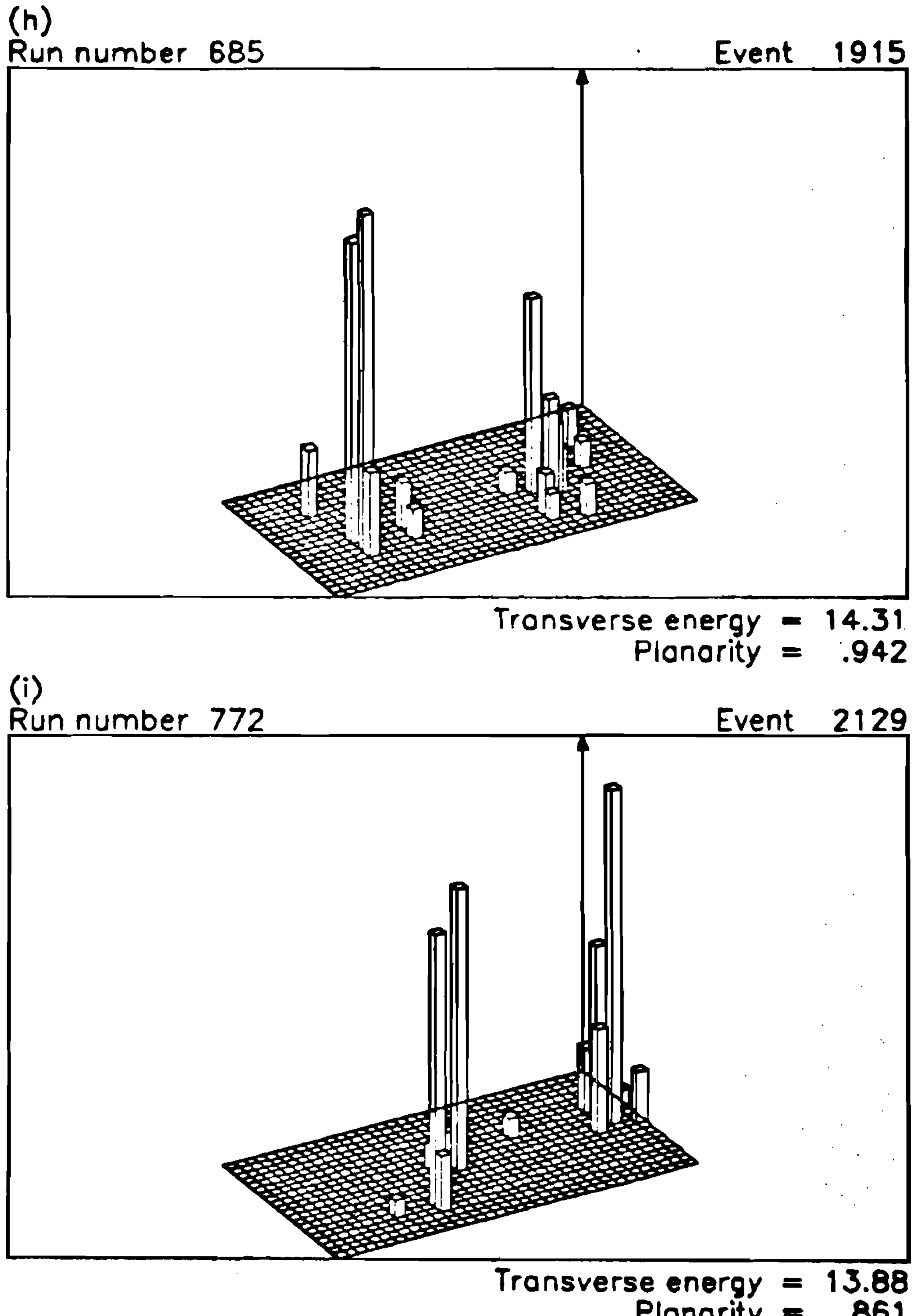

FIG. 5-10. (Continued)

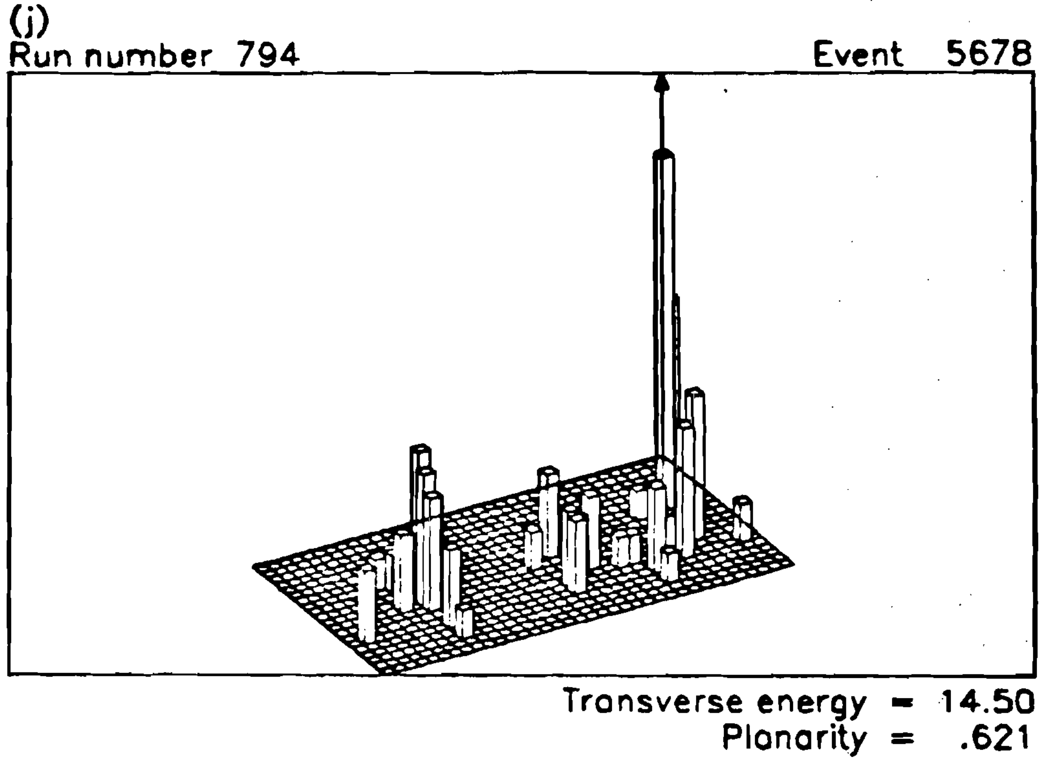

FIG. 5-10. (Continued)

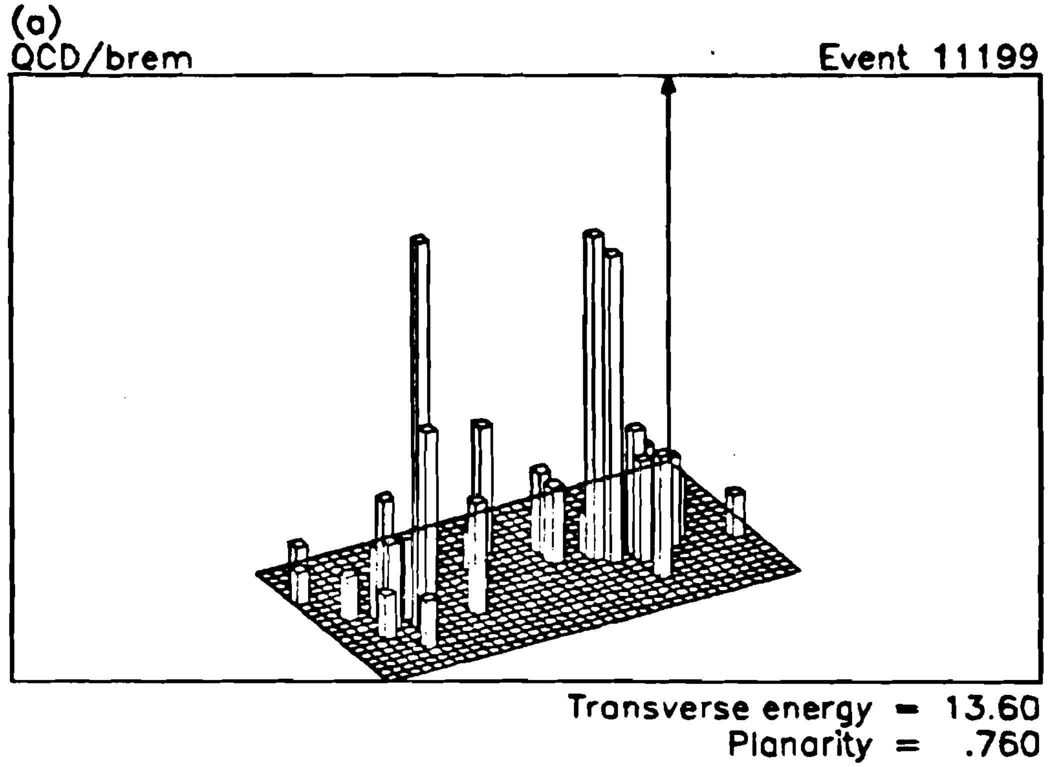

FIG. 5-11. Transverse energy versus cos θ^* and ϕ for nine events from the QCD/brem Monte Carlo data with E_t^C in F 2/3 greater than 13.5 GeV.

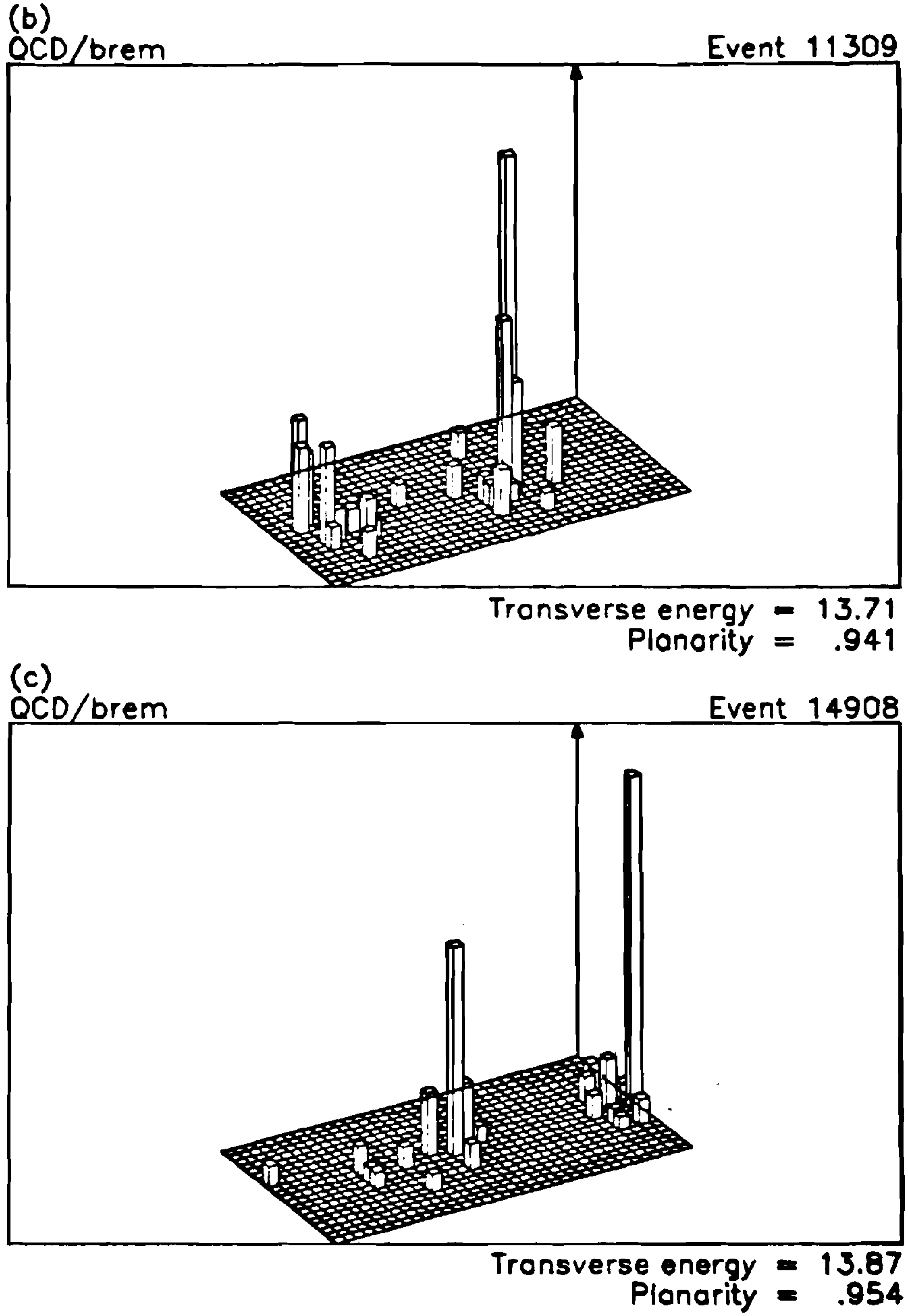

FIG. 5-11. (Continued)

(d)

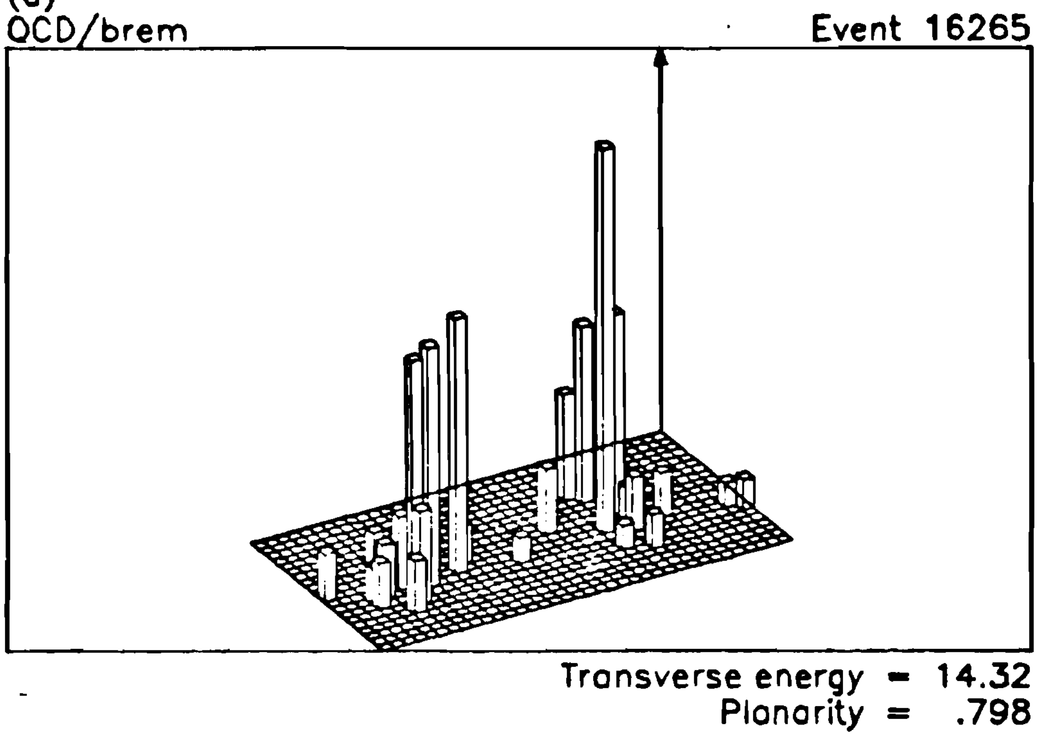

(e)

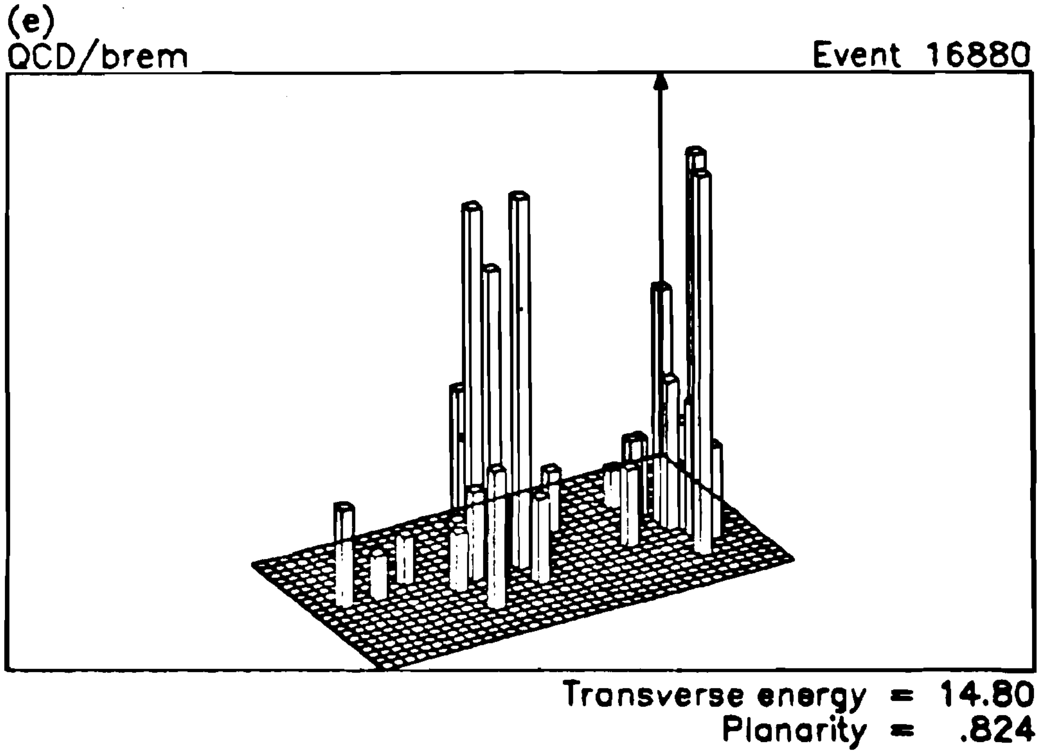

FIG. 5-11. (Continued)

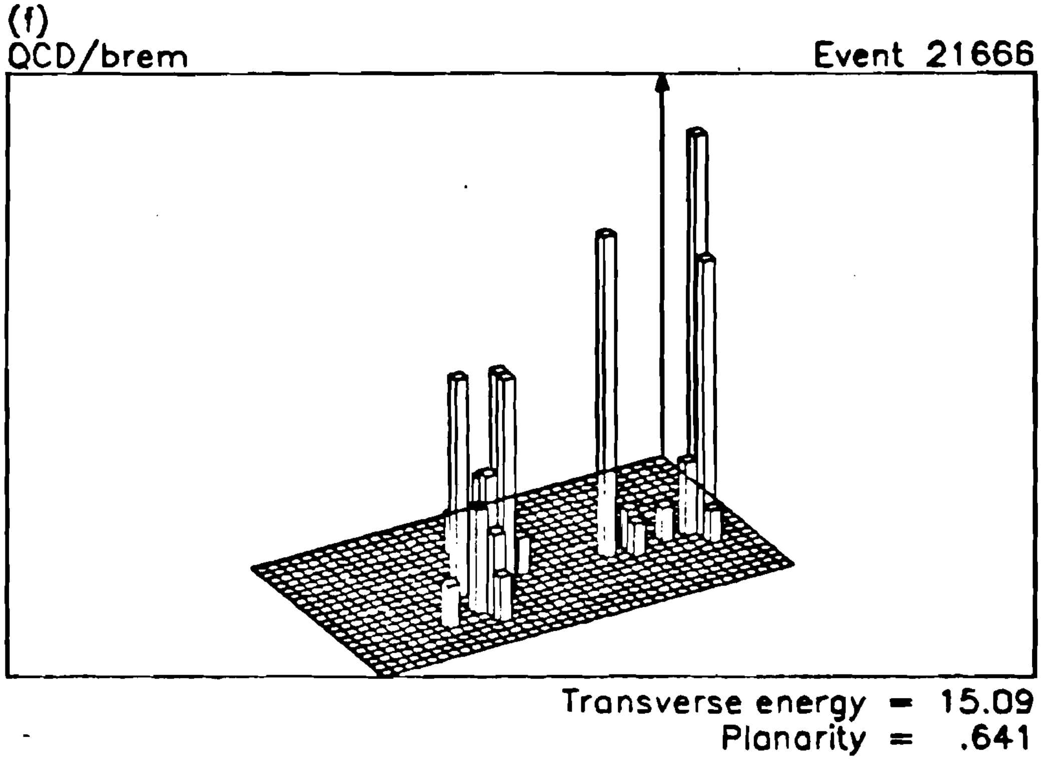

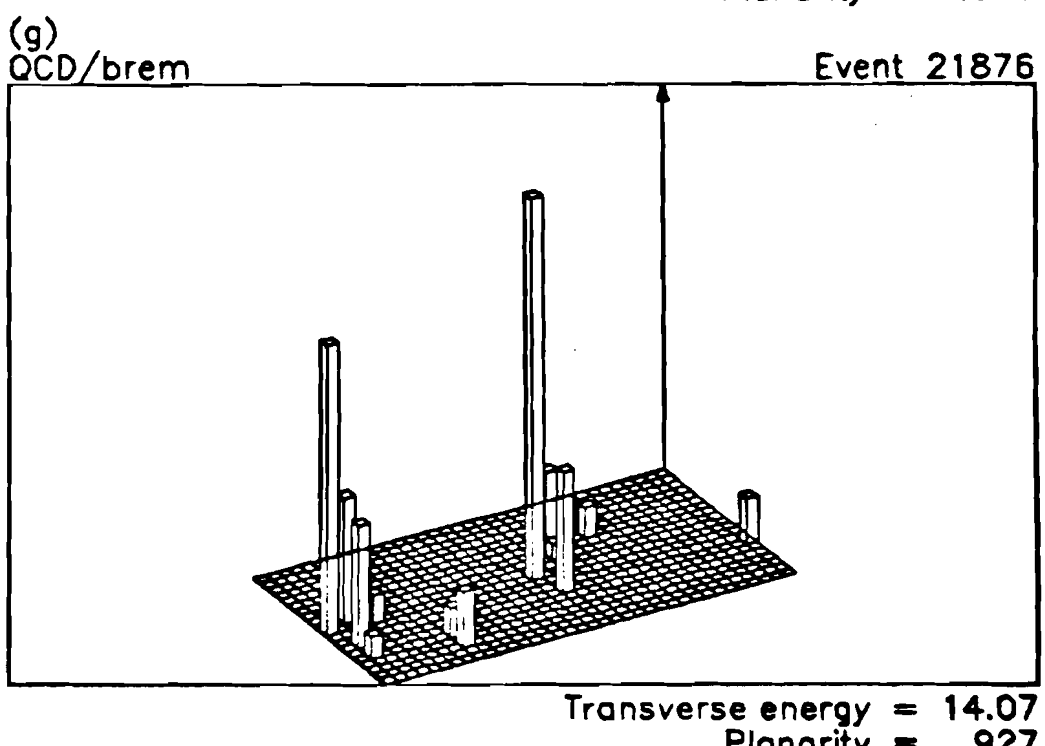

FIG. 5-11. (Continued)

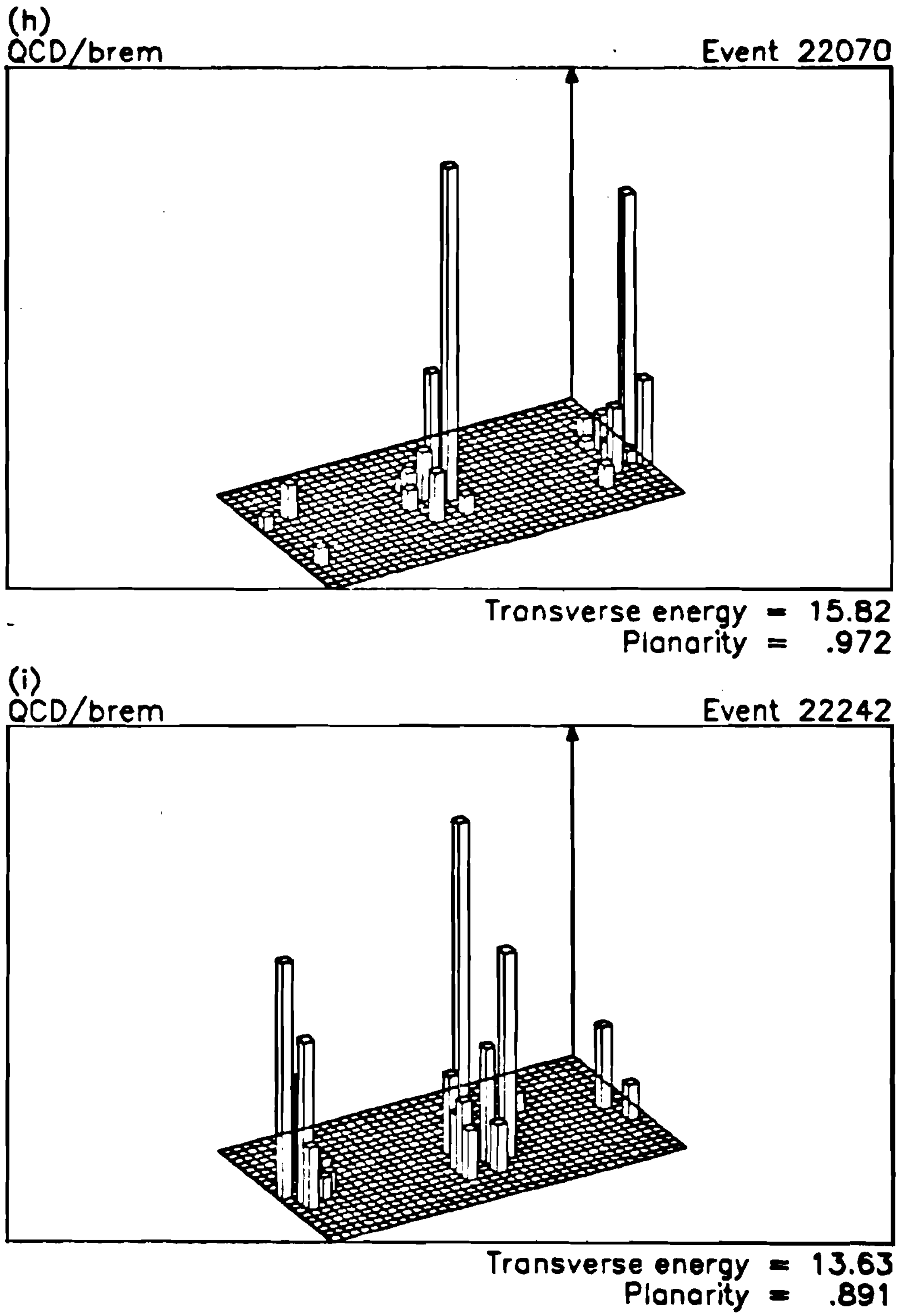

FIG. 5-11. (Continued)

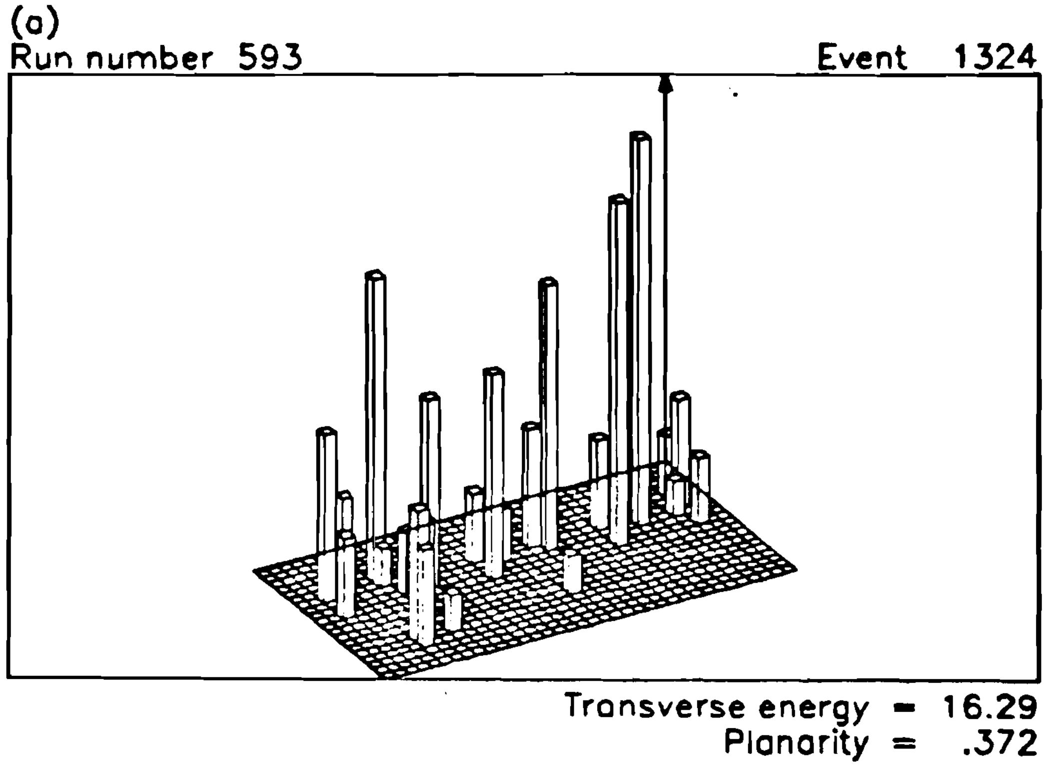

FIG. 5-12. Transverse energy versus cos θ^* and ϕ for nine events from the experimental hydrogen data with E_t^C in B 2/3 greater than 14.8 GeV.

(b)

Run number 593 Event 4862

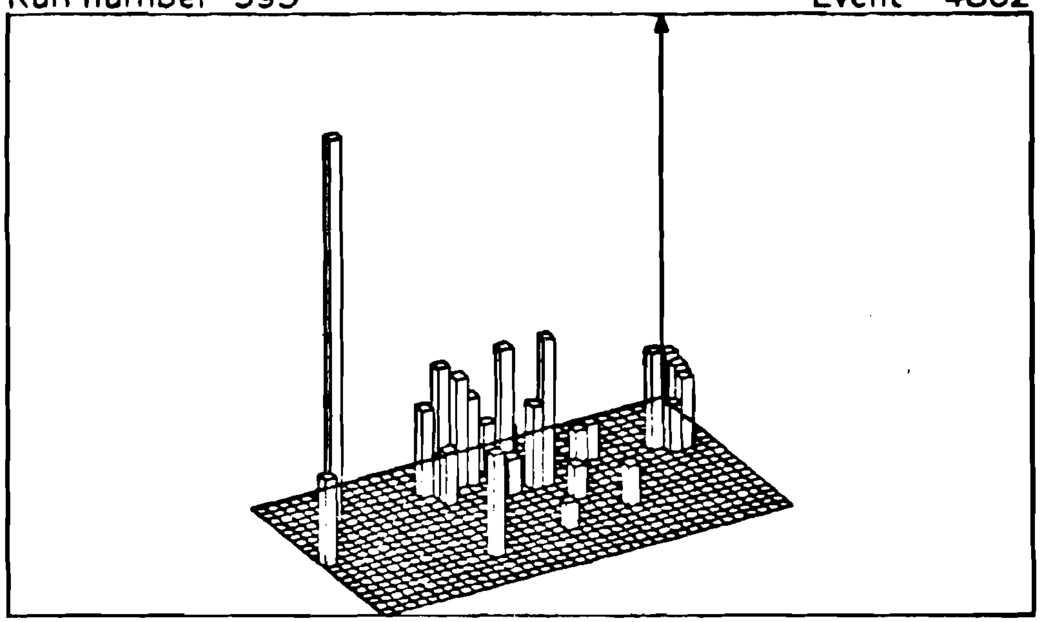

Transverse energy = 15.30
Planarity = .400

(c)

Run number 626 Event 1966

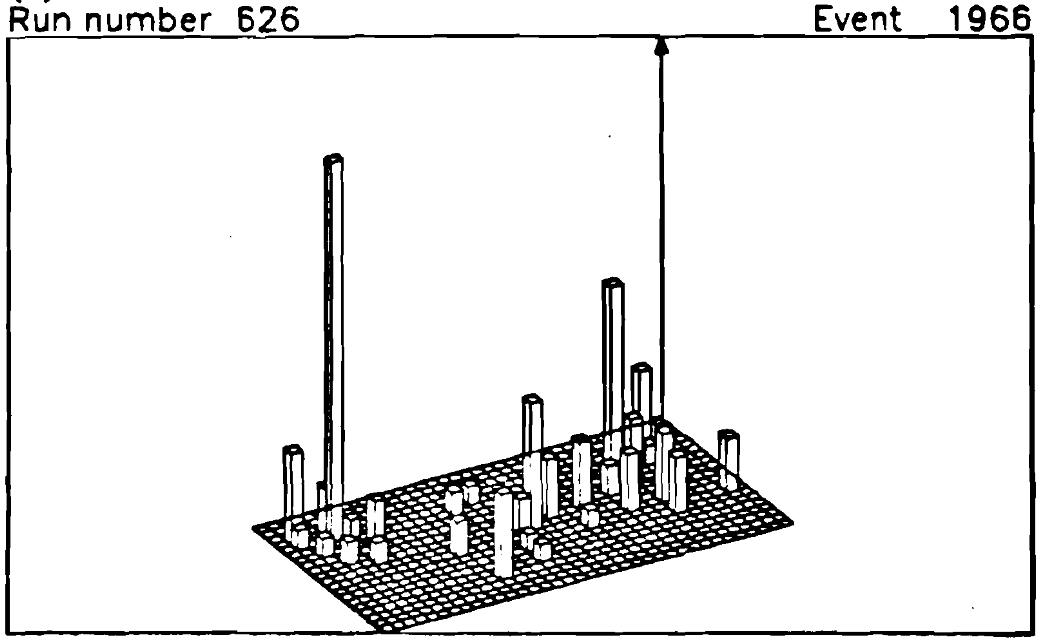

Transverse energy = 17.42
Planarity = .494

FIG. 5-12. (Continued)

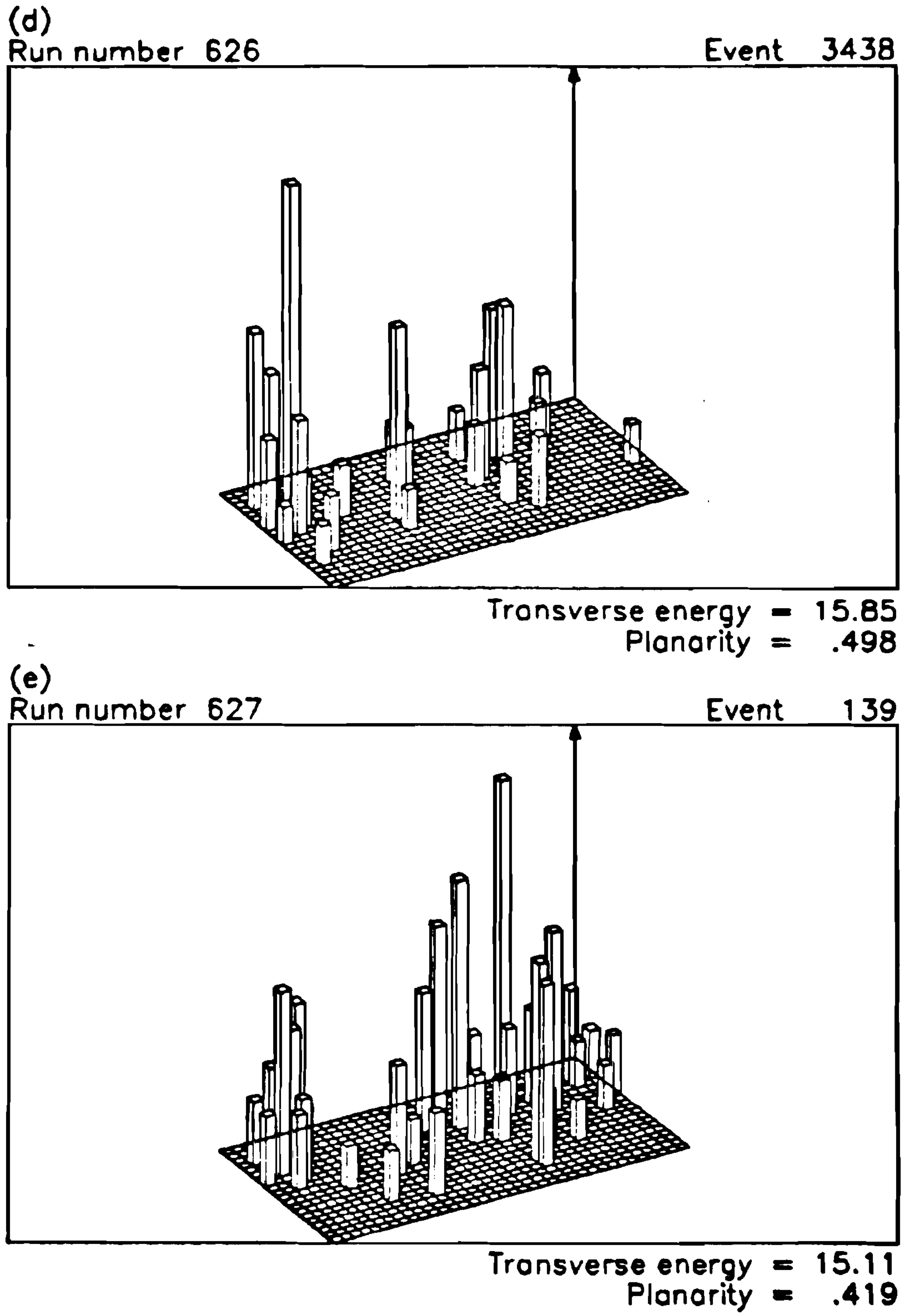

FIG. 5-12. (Continued)

(f)

Run number 628 Event 1716

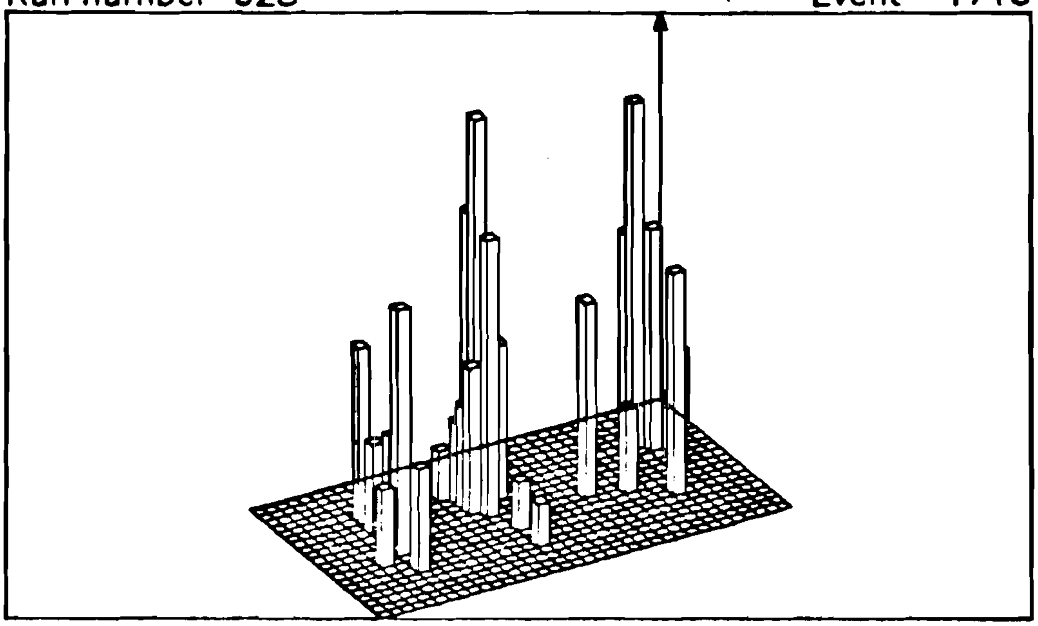

Transverse energy = 16.12

Planarity = .467

(g)

Run number 663 Event 381

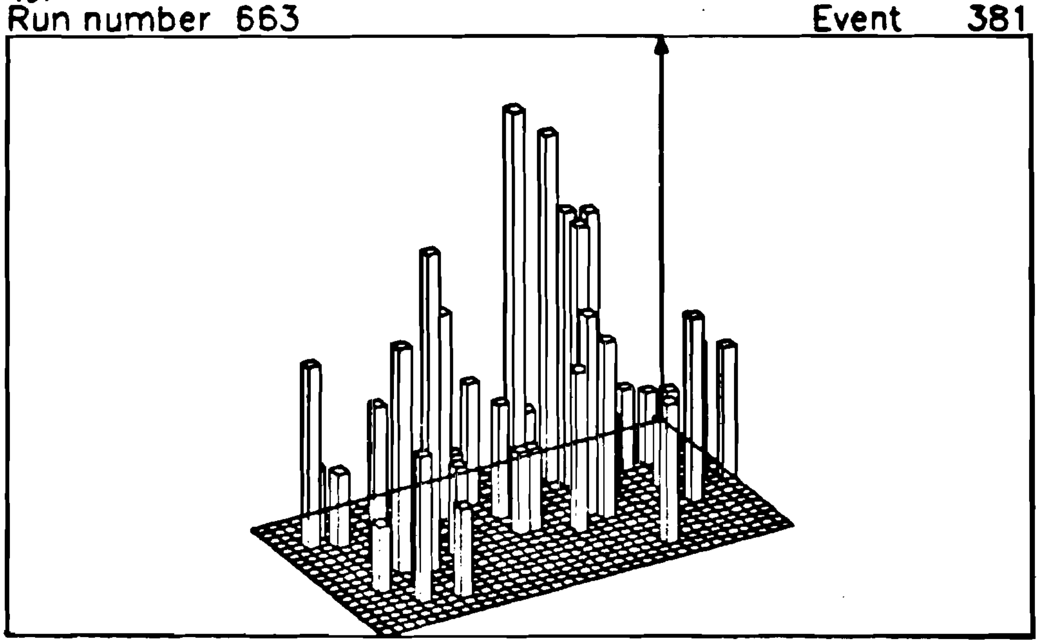

Transverse energy = 15.58

Planarity = .422

FIG. 5-12. (Continued)

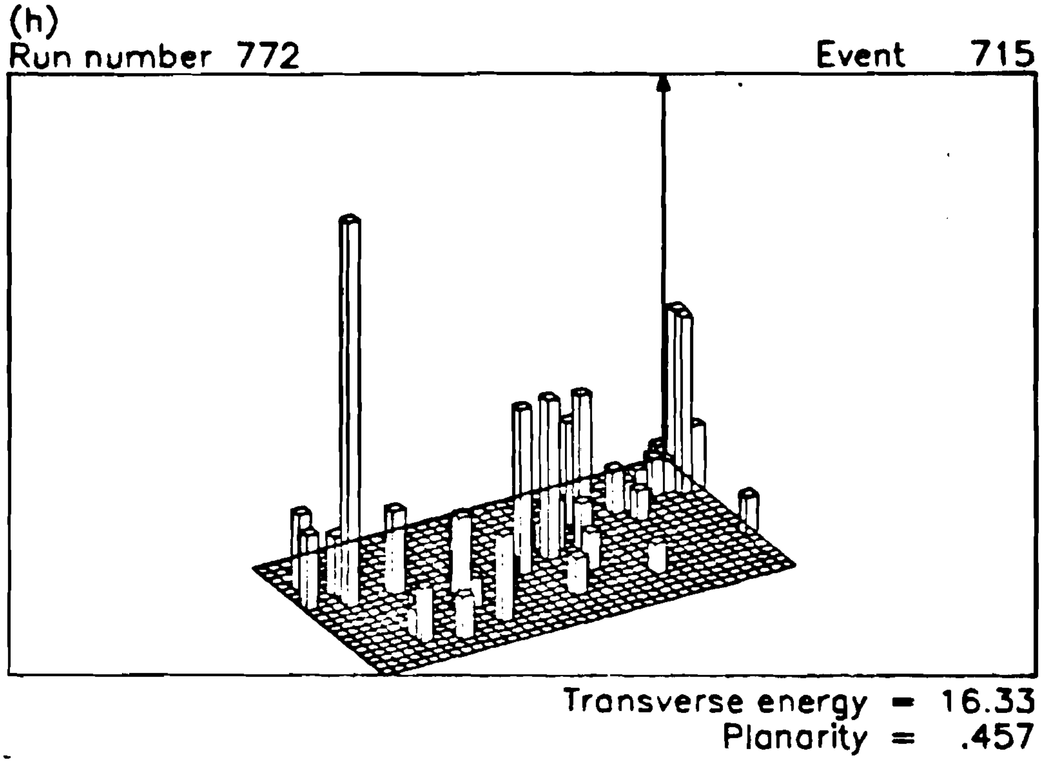

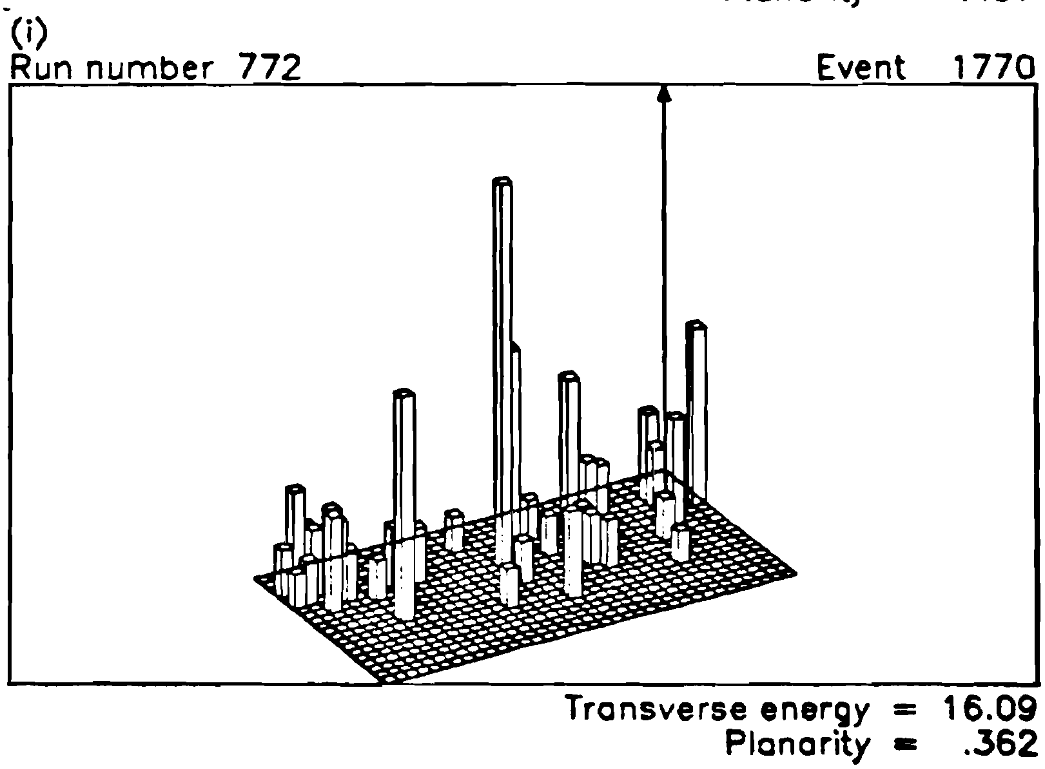

FIG. 5-12. (Continued)

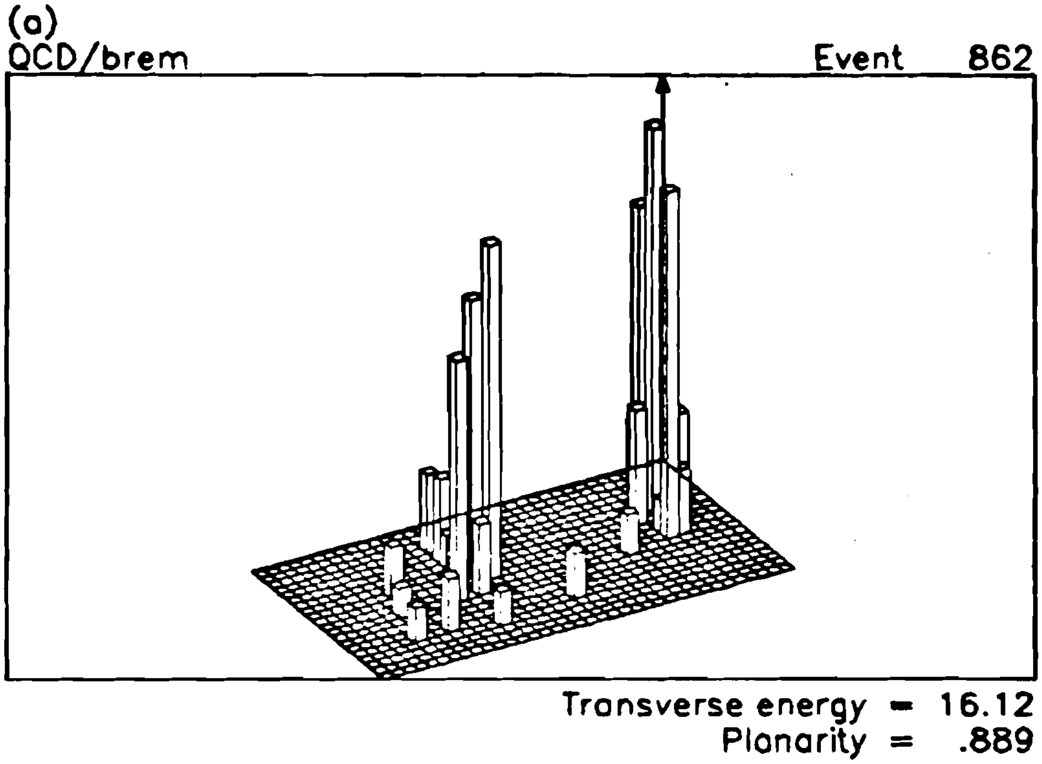

FIG. 5-13. Transverse energy versus cos θ^* and ϕ for nine events from the QCD/brem Monte Carlo data with E_t^C in B 2/3 greater than 14.5 GeV.

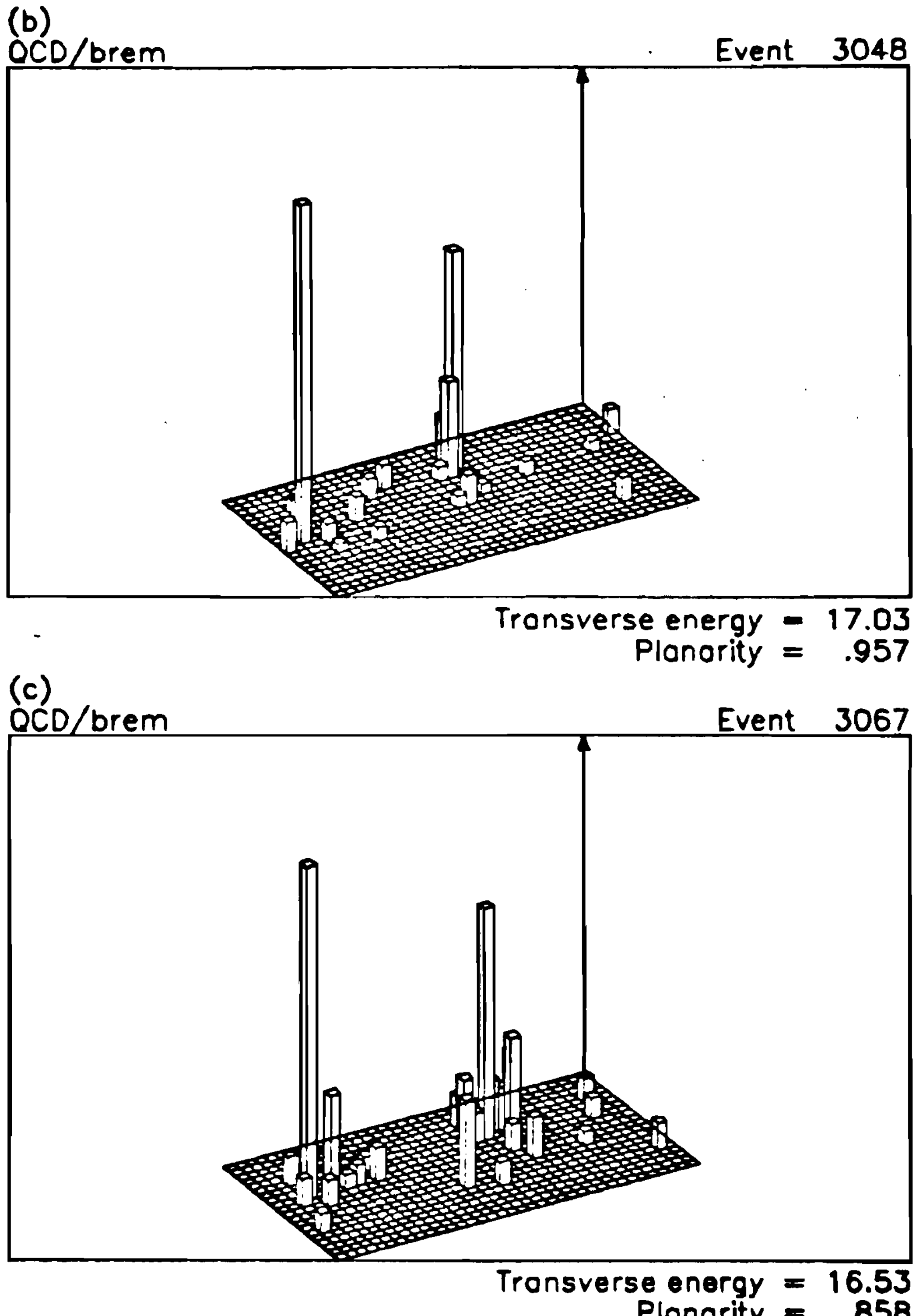

FIG. 5-13. (Continued)

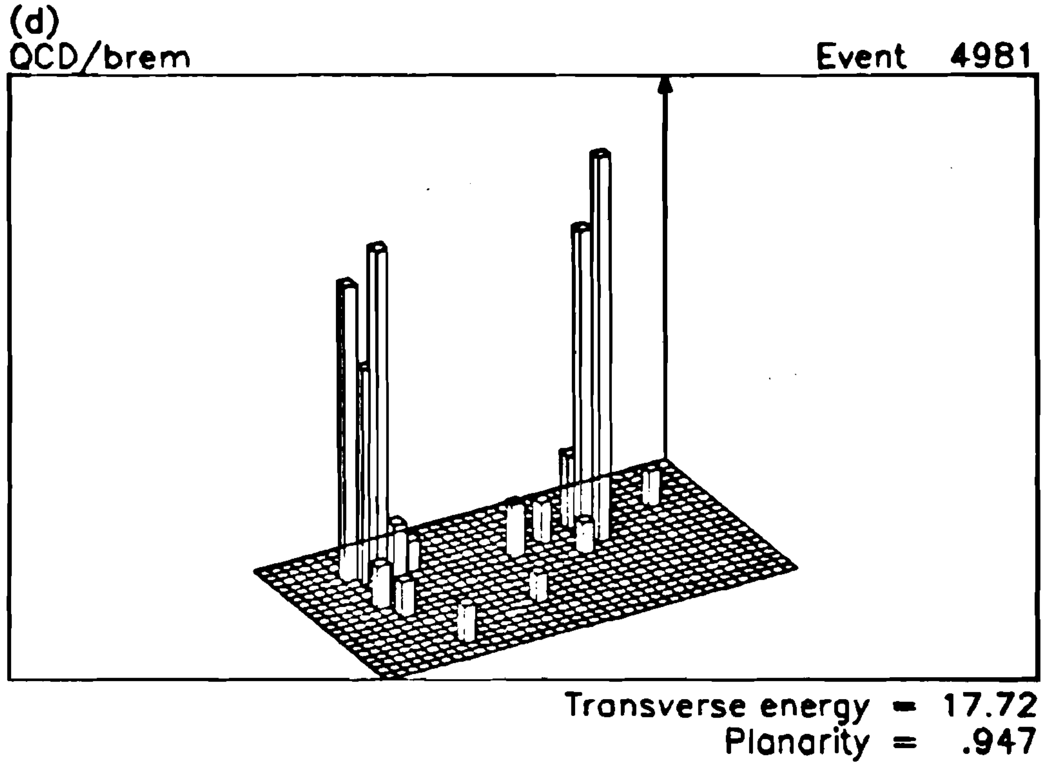

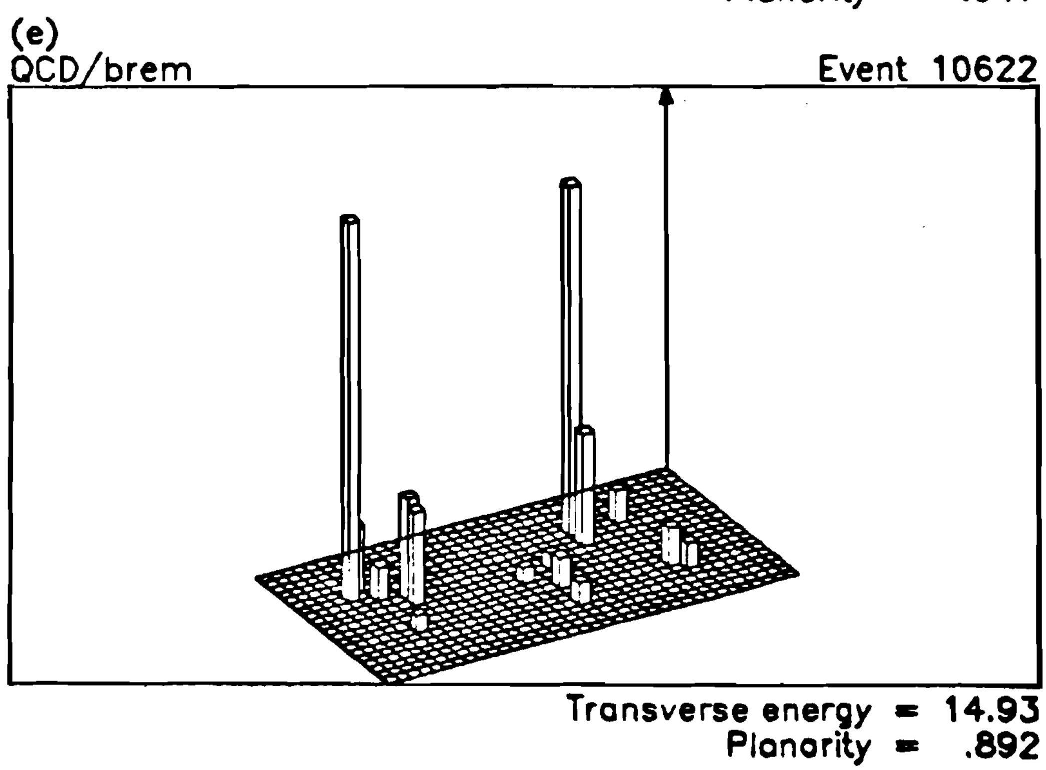

FIG. 5-13. (Continued)

(f)

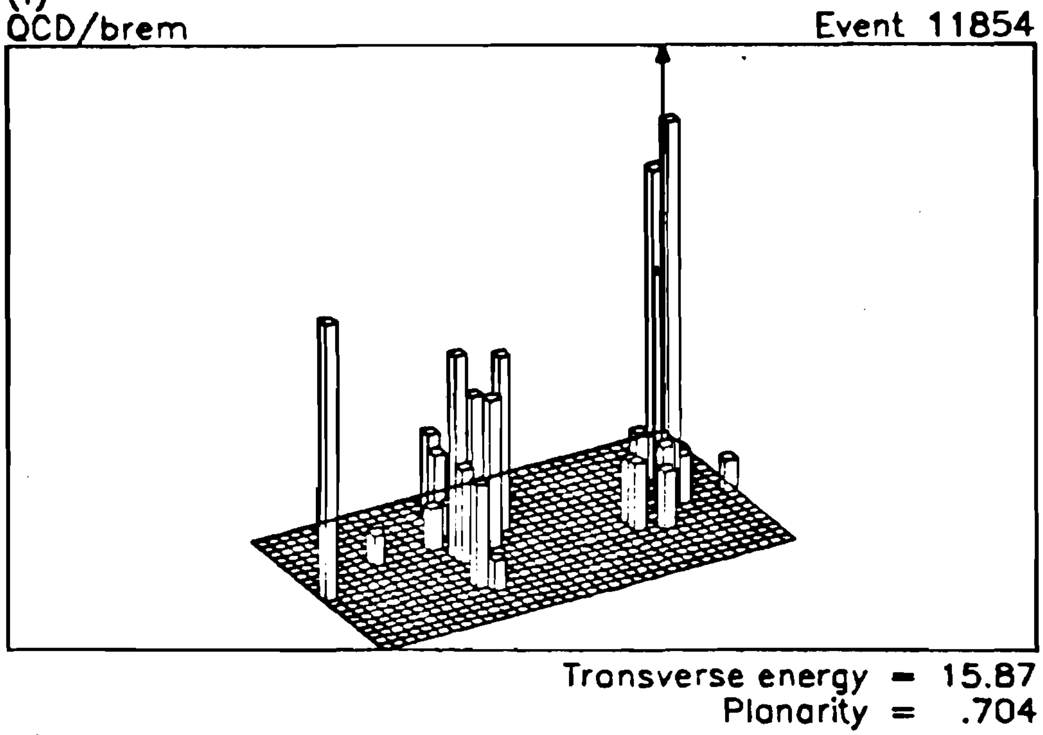

(g)

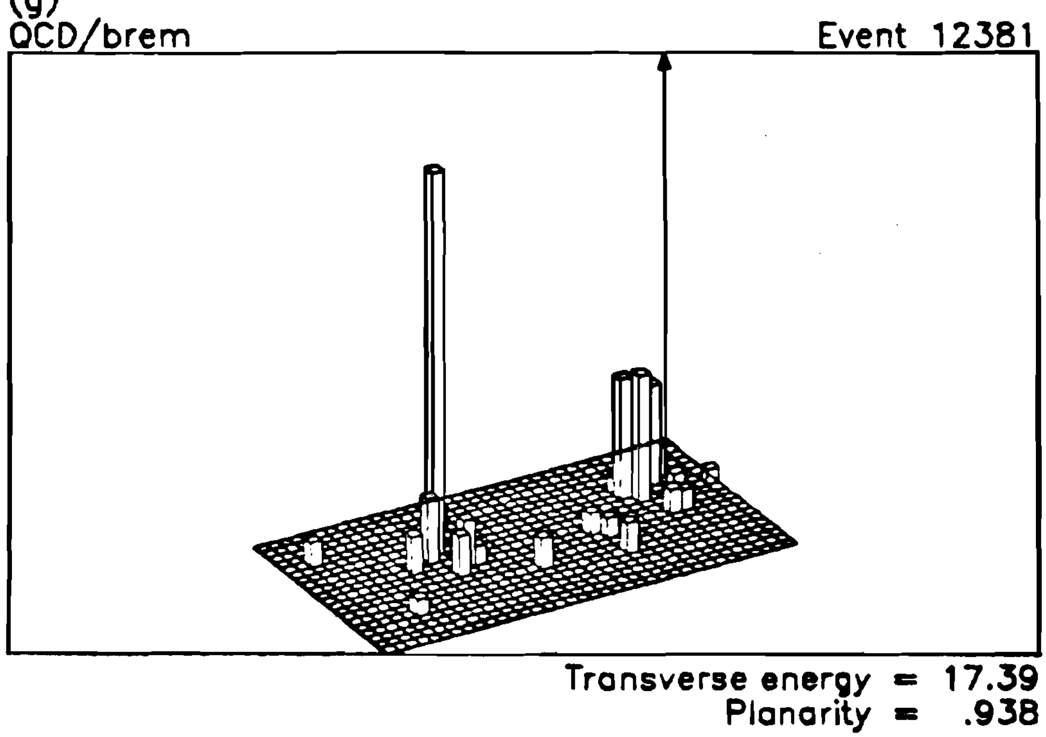

FIG. 5-13. (Continued)

(h)
QCD/brem Event 13784

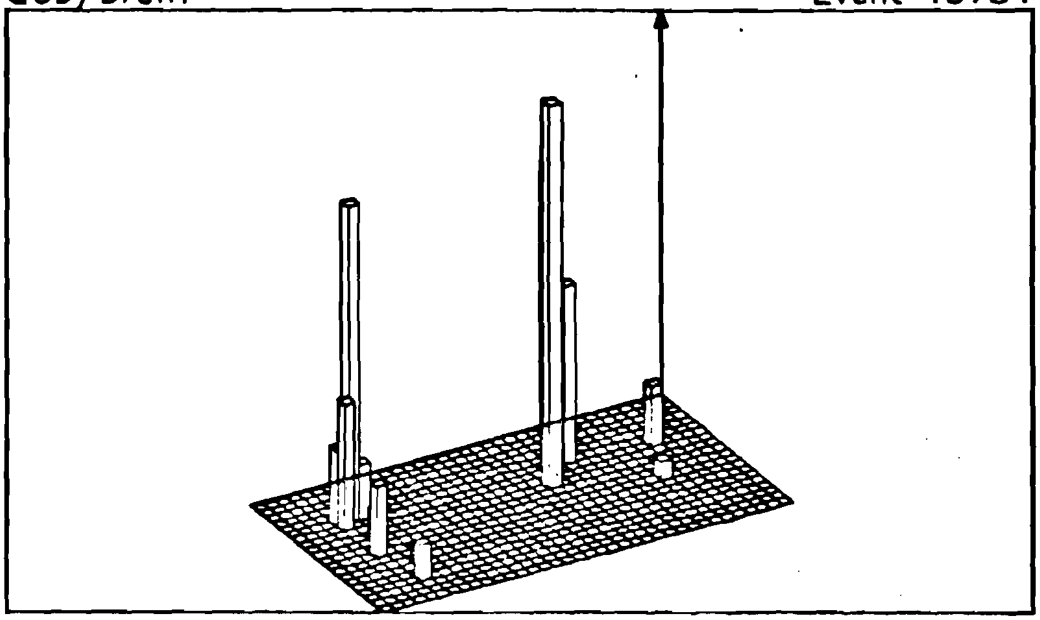

Transverse energy = 16.30
Planarity = .926

(i)
QCD/brem Event 15800

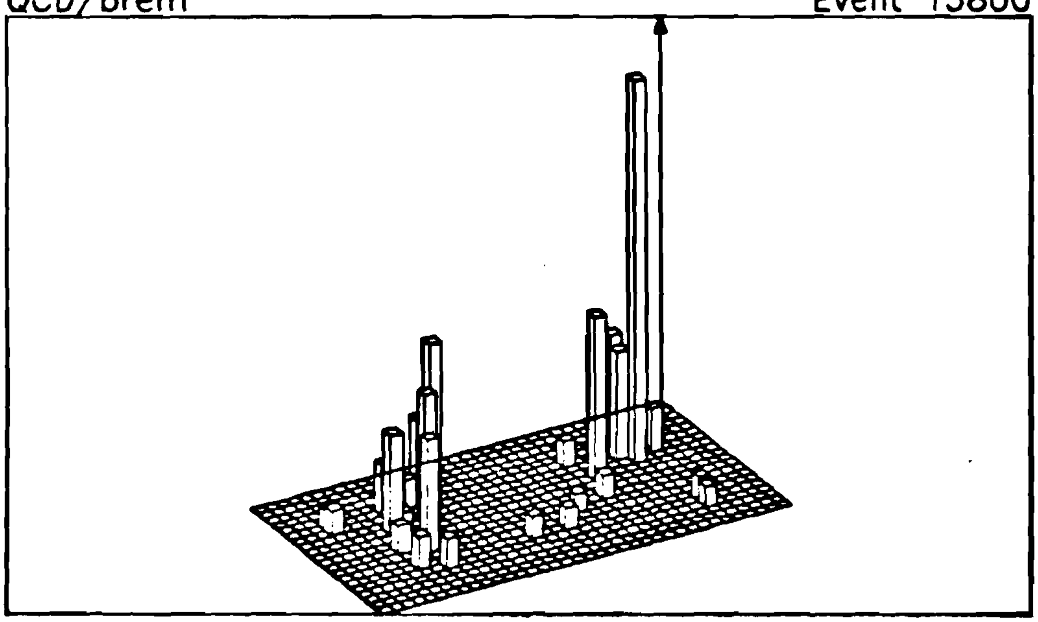

Transverse energy = 16.68
Planarity = .831

FIG. 5-13. (Continued)

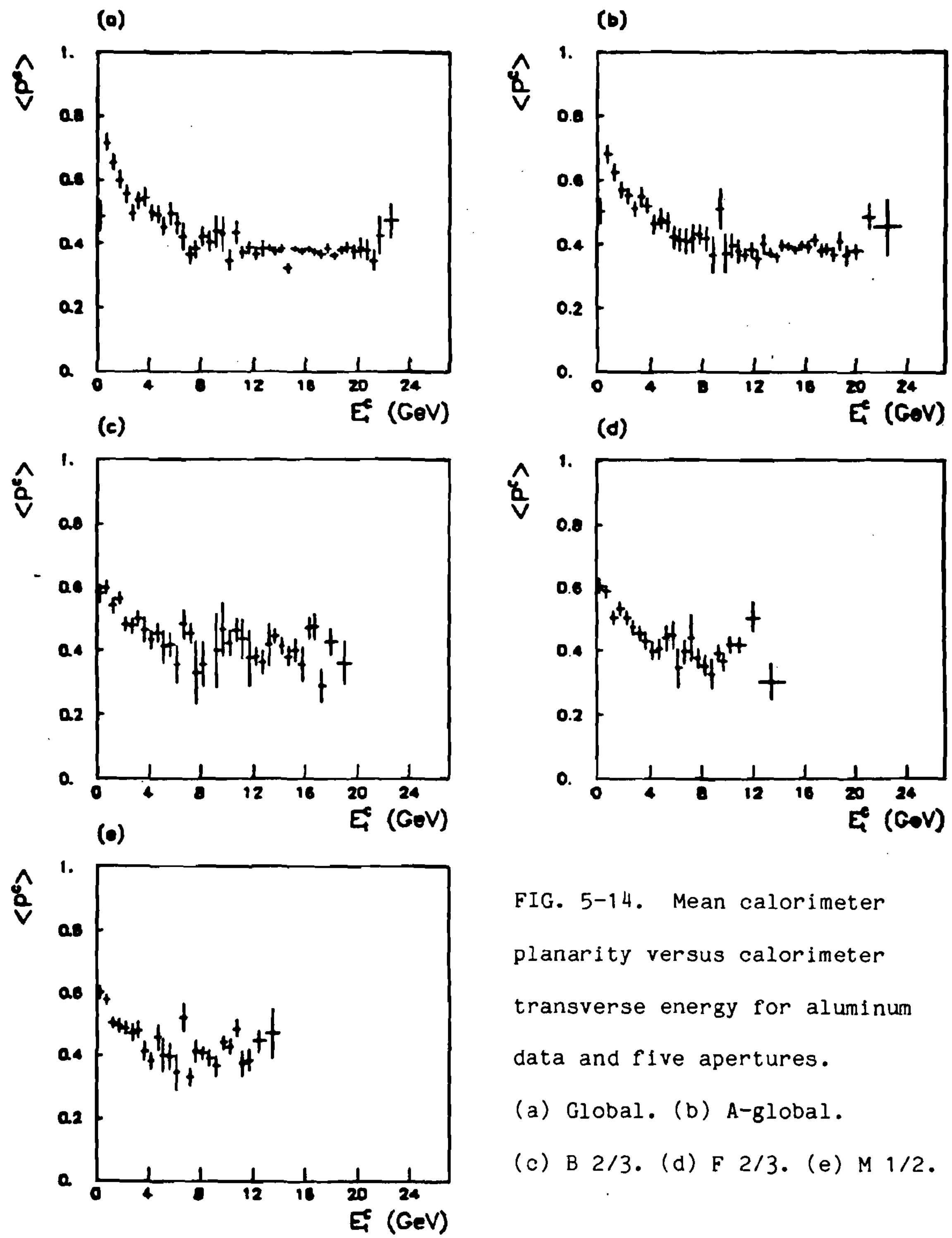

FIG. 5-14. Mean calorimeter planarity versus calorimeter transverse energy for aluminum data and five apertures. (a) Global. (b) A-global. (c) B 2/3. (d) F 2/3. (e) M 1/2.

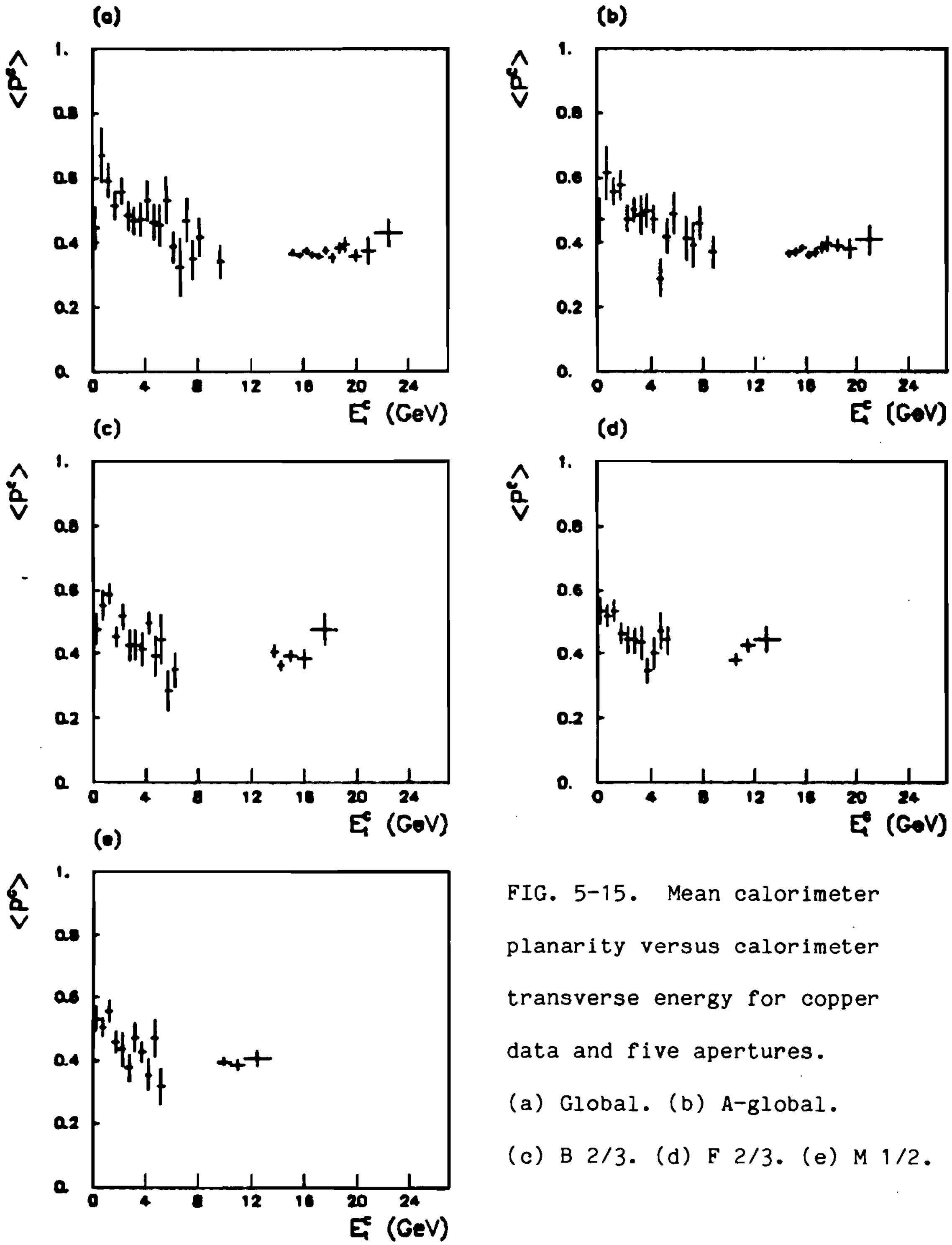

FIG. 5-15. Mean calorimeter planarity versus calorimeter transverse energy for copper data and five apertures. (a) Global. (b) A-global. (c) B 2/3. (d) F 2/3. (e) M 1/2.

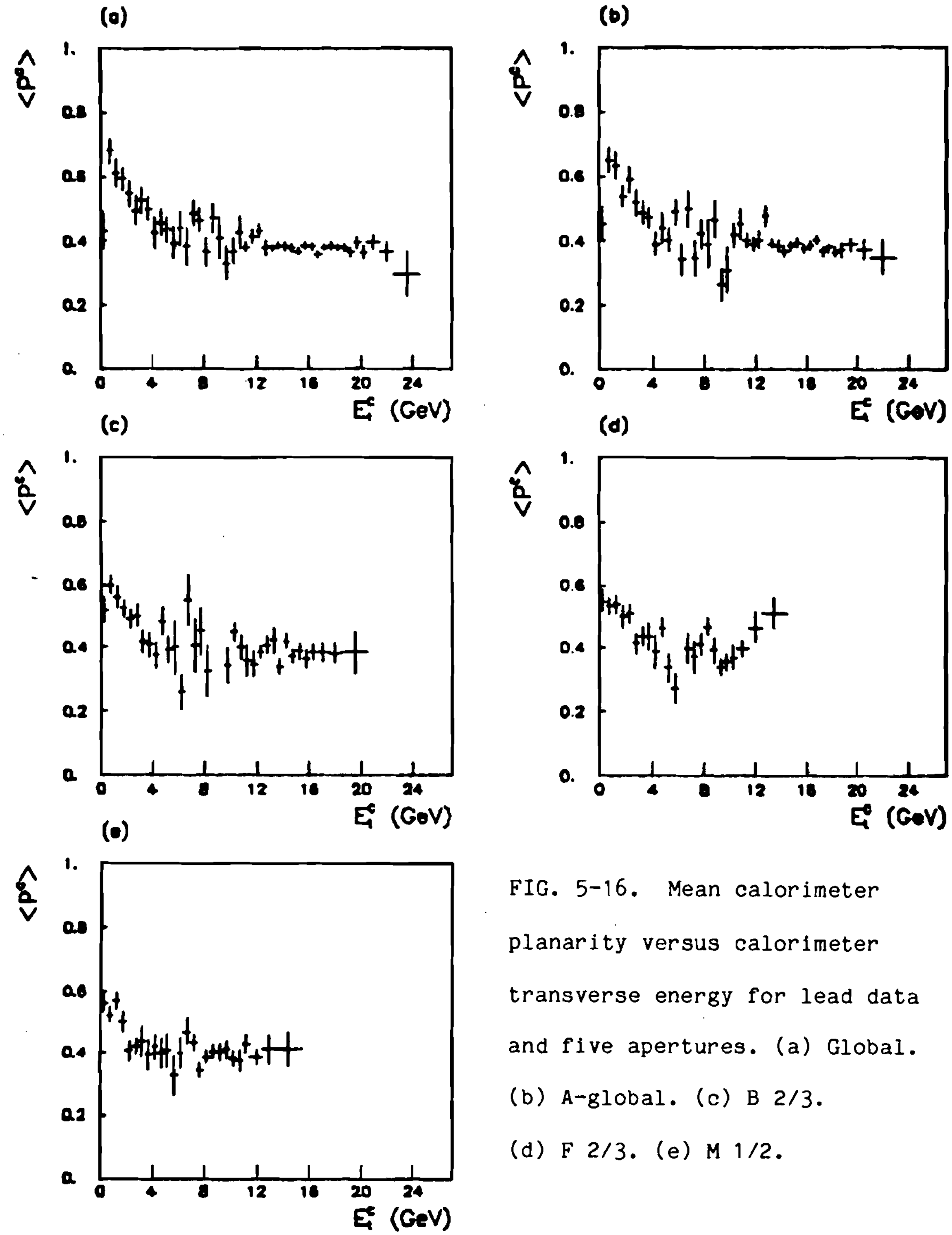

FIG. 5-16. Mean calorimeter planarity versus calorimeter transverse energy for lead data and five apertures. (a) Global. (b) A-global. (c) B 2/3. (d) F 2/3. (e) M 1/2.

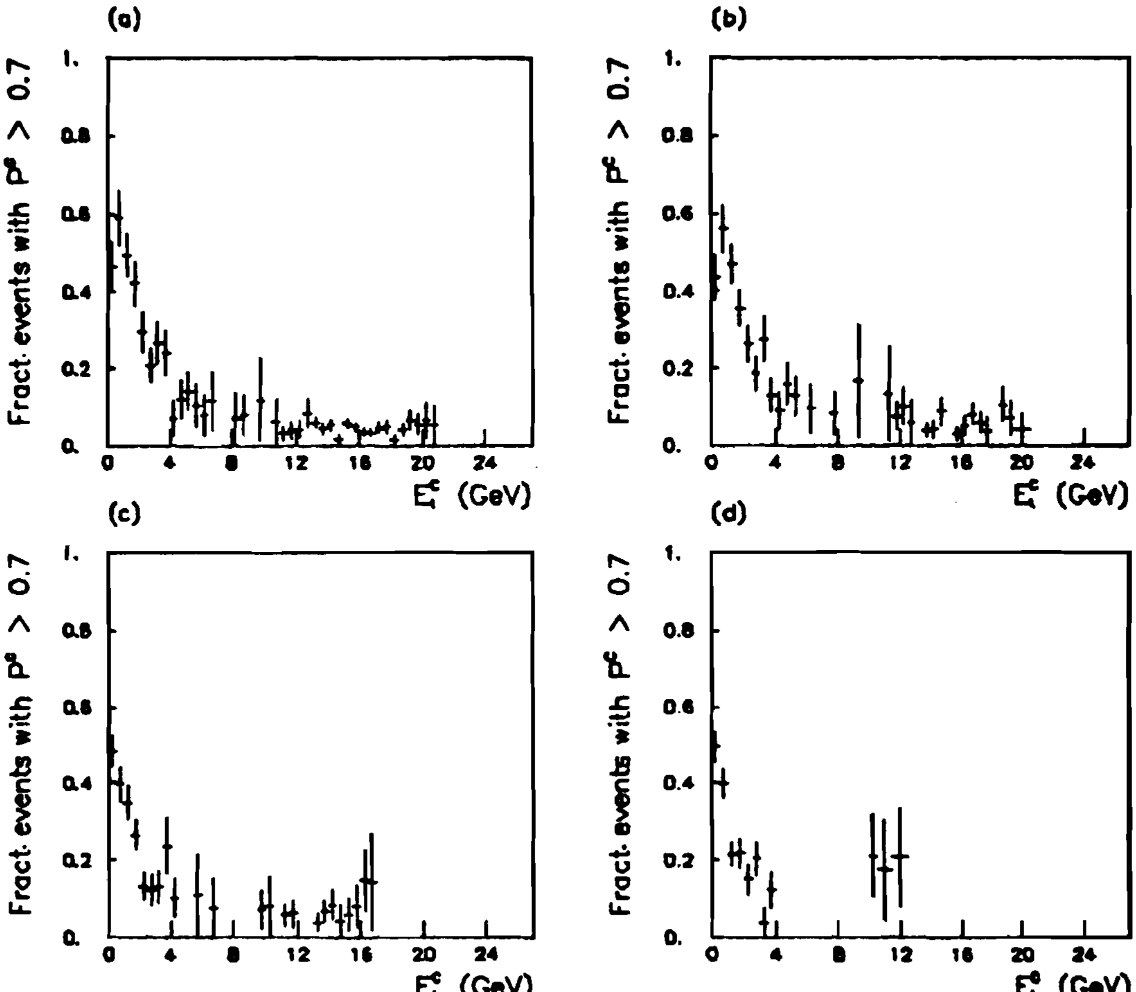

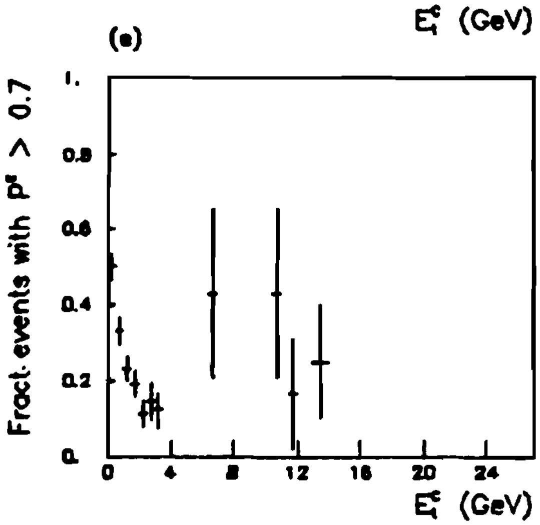

FIG. 5-17. Fraction of events with high calorimeter planarity (> 0.7) versus calorimeter transverse energy for aluminum data and five apertures. (a) Global. (b) A-global. (c) B 2/3. (d) F 2/3. (e) M 1/2.

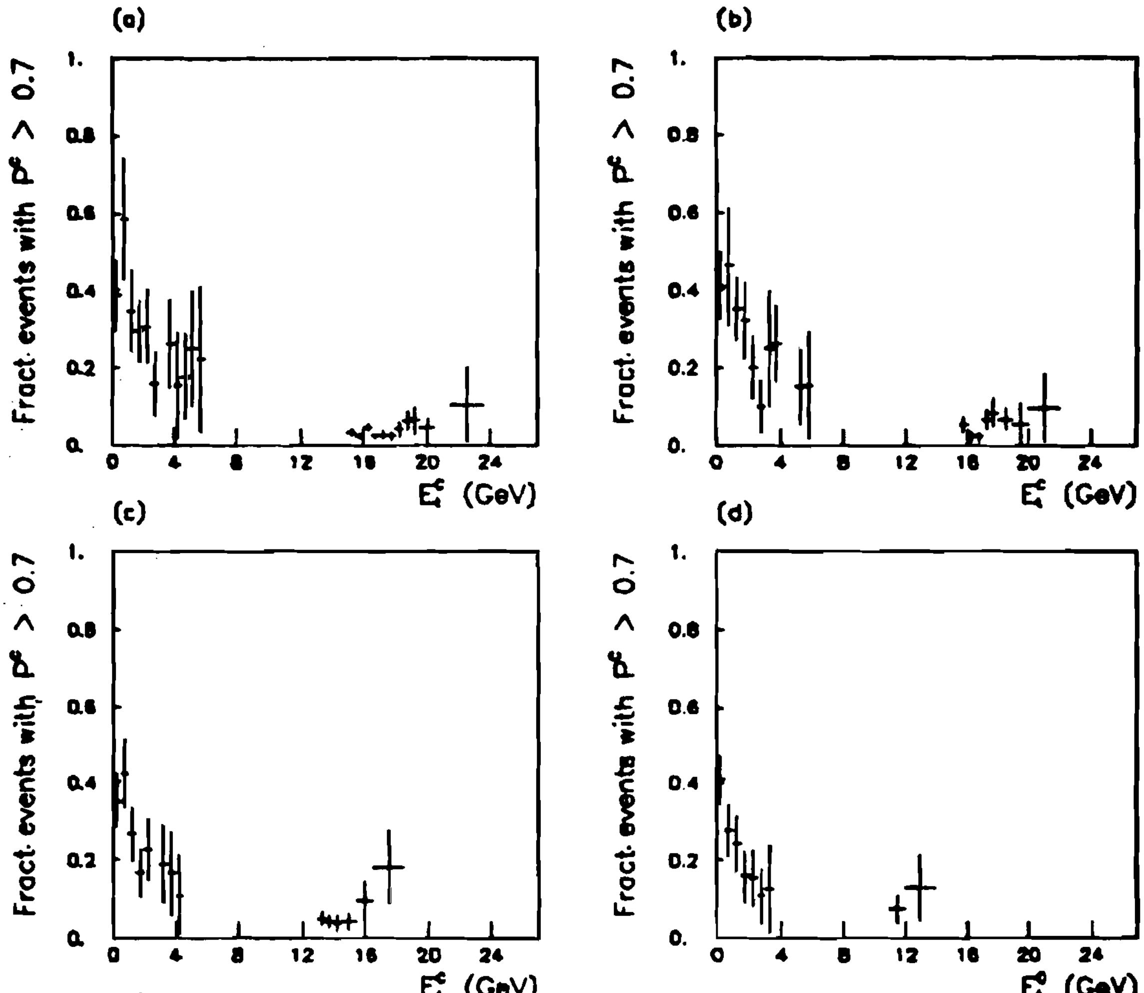

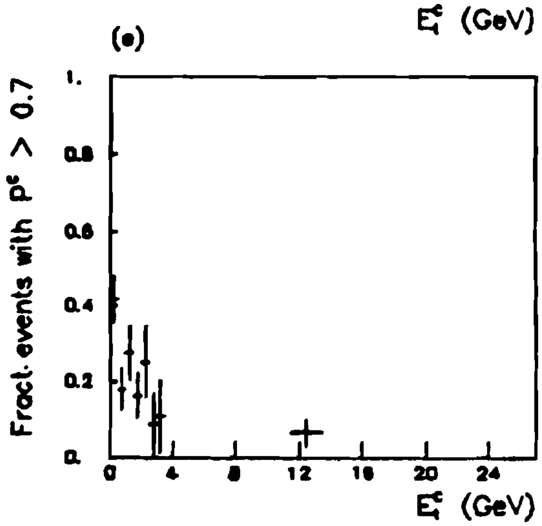

FIG. 5-18. Fraction of events with high calorimeter planarity (> 0.7) versus calorimeter transverse energy for copper data and five apertures.
(a) Global. (b) A-global.
(c) B 2/3. (d) F 2/3. (e) M 1/2.

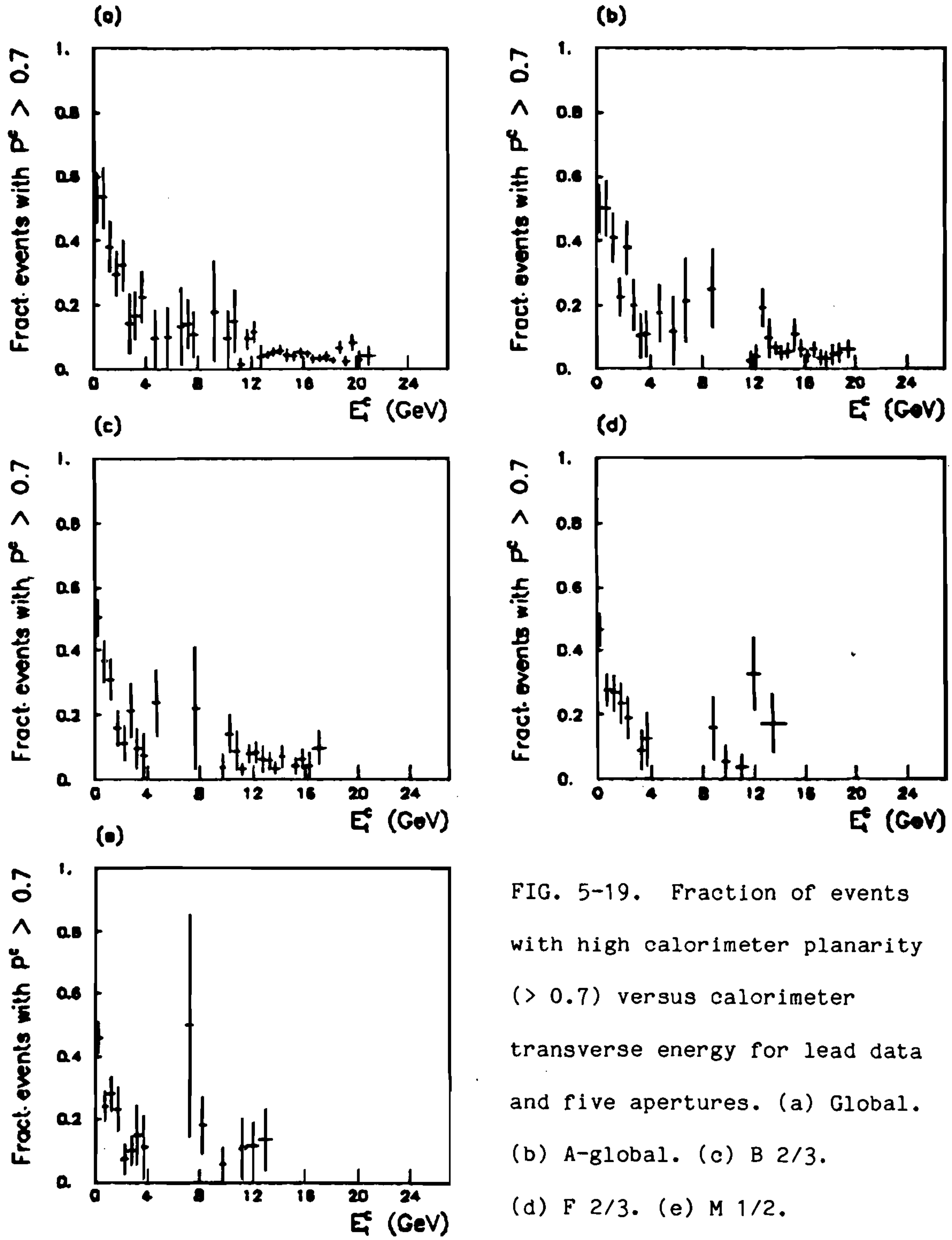

FIG. 5-19. Fraction of events with high calorimeter planarity (> 0.7) versus calorimeter transverse energy for lead data and five apertures. (a) Global. (b) A-global. (c) B 2/3. (d) F 2/3. (e) M 1/2.

TABLE 5-1. Mean calorimeter planarity versus calorimeter transverse energy for LPS Monte Carlo data and five apertures.

GLOBAL

ET BIN EDGES (GEV)		MEAN PLANARITY
.0	.5	.068+/- .005
.5	1.0	.598+/- .009
1.0	1.5	.677+/- .007
1.5	2.0	.625+/- .007
2.0	2.5	.586+/- .007
2.5	3.0	.542+/- .008
3.0	3.5	.541+/- .008
3.5	4.0	.496+/- .009
4.0	4.5	.494+/- .009
4.5	5.0	.467+/- .010
5.0	5.5	.455+/- .011
5.5	6.0	.434+/- .012
6.0	6.5	.439+/- .012
6.5	7.0	.385+/- .015
7.0	7.5	.383+/- .018
7.5	8.0	.389+/- .022
8.0	8.5	.329+/- .022
8.5	9.0	.359+/- .028
9.0	9.5	.303+/- .031
9.5	10.0	.433+/- .045
10.0	10.5	.298+/- .048
10.5	11.0	.305+/- .050
11.0	11.5	.346+/- .051
12.5	13.0	.284+/- .016
13.0	13.5	.282+/- .021
13.5	14.0	.248+/- .034

TABLE 5-1. (Continued)

A-GLOBAL

ET BIN EDGES (GEV)		MEAN PLANARITY
.0	.5	.109+/- .006
.5	1.0	.622+/- .008
1.0	1.5	.663+/- .006
1.5	2.0	.617+/- .007
2.0	2.5	.564+/- .007
2.5	3.0	.543+/- .008
3.0	3.5	.522+/- .008
3.5	4.0	.503+/- .009
4.0	4.5	.476+/- .009
4.5	5.0	.436+/- .011
5.0	5.5	.464+/- .012
5.5	6.0	.424+/- .012
6.0	6.5	.404+/- .015
6.5	7.0	.377+/- .018
7.0	7.5	.386+/- .023
7.5	8.0	.315+/- .025
8.0	8.5	.356+/- .024
8.5	9.0	.358+/- .038
9.0	9.5	.403+/- .044
9.5	10.0	.248+/- .054
10.0	10.5	.336+/- .054
10.5	11.0	.282+/- .013
11.0	11.5	.274+/- .018
11.5	12.0	.240+/- .018
12.0	12.5	.300+/- .021
12.5	13.0	.252+/- .023
13.5	14.0	.287+/- .043

TABLE 5-1. (Continued)

B 2/3

ET BIN EDGES (GEV)		MEAN PLANARITY
.0	.5	.299+/- .006
.5	1.0	.627+/- .006
1.0	1.5	.602+/- .006
1.5	2.0	.562+/- .007
2.0	2.5	.539+/- .008
2.5	3.0	.524+/- .009
3.0	3.5	.481+/- .010
3.5	4.0	.454+/- .011
4.0	4.5	.421+/- .014
4.5	5.0	.422+/- .017
5.0	5.5	.432+/- .020
5.5	6.0	.404+/- .027
6.0	6.5	.381+/- .031
6.5	7.0	.359+/- .037
7.0	7.5	.345+/- .059
7.5	8.0	.218+/- .044
9.0	9.5	.237+/- .028
9.5	10.0	.294+/- .032
10.0	10.5	.342+/- .039

F 2/3

ET BIN EDGES (GEV)		MEAN PLANARITY
.0	.5	.311+/- .006
.5	1.0	.615+/- .006
1.0	1.5	.599+/- .006
1.5	2.0	.563+/- .007
2.0	2.5	.533+/- .008
2.5	3.0	.500+/- .009
3.0	3.5	.473+/- .011
3.5	4.0	.447+/- .012
4.0	4.5	.419+/- .014
4.5	5.0	.386+/- .017
5.0	5.5	.433+/- .028
5.5	6.0	.380+/- .028
6.0	6.5	.324+/- .037
6.5	7.0	.352+/- .048
7.0	7.5	.404+/- .073
8.0	8.5	.300+/- .018
8.5	9.0	.281+/- .028
9.0	9.5	.264+/- .048

TABLE 5-1. (Continued)

M 1/2

ET BIN EDGES (GEV)		MEAN PLANARITY
.0	.5	.344+/- .006
.5	1.0	.617+/- .006
1.0	1.5	.593+/- .006
1.5	2.0	.542+/- .007
2.0	2.5	.519+/- .008
2.5	3.0	.505+/- .010
3.0	3.5	.456+/- .011
3.5	4.0	.444+/- .014
4.0	4.5	.450+/- .018
4.5	5.0	.358+/- .026
5.0	5.5	.374+/- .028
5.5	6.0	.438+/- .039
6.0	6.5	.351+/- .041
6.5	7.0	.378+/- .070
8.0	8.5	.257+/- .024

TABLE 5-2. Mean particle planarity versus particle transverse energy for LPS Monte Carlo data and five apertures.

GLOBAL

ET BIN EDGES (GEV)		MEAN PLANARITY
.0	.5	.053+/- .004
.5	1.0	.404+/- .009
1.0	1.5	.605+/- .008
1.5	2.0	.603+/- .007
2.0	2.5	.573+/- .007
2.5	3.0	.562+/- .008
3.0	3.5	.529+/- .008
3.5	4.0	.500+/- .008
4.0	4.5	.480+/- .009
4.5	5.0	.451+/- .010
5.0	5.5	.427+/- .012
5.5	6.0	.424+/- .013
6.0	6.5	.397+/- .013
6.5	7.0	.359+/- .017
7.0	7.5	.364+/- .015
7.5	8.0	.391+/- .021
8.0	8.5	.313+/- .028
8.5	9.0	.332+/- .040
9.0	9.5	.361+/- .042
9.5	10.0	.323+/- .037
10.0	10.5	.346+/- .039
10.5	11.0	.256+/- .042
12.0	12.5	.257+/- .021
12.5	13.0	.246+/- .028
13.0	13.5	.254+/- .042

TABLE 5-2. (Continued)

A-GLOBAL

ET BIN EDGES (GEV)		MEAN PLANARITY
.0	.5	.079+/- .005
.5	1.0	.425+/- .009
1.0	1.5	.606+/- .007
1.5	2.0	.593+/- .007
2.0	2.5	.571+/- .007
2.5	3.0	.555+/- .008
3.0	3.5	.513+/- .008
3.5	4.0	.501+/- .009
4.0	4.5	.472+/- .010
4.5	5.0	.438+/- .011
5.0	5.5	.418+/- .012
5.5	6.0	.421+/- .014
6.0	6.5	.404+/- .016
6.5	7.0	.330+/- .016
7.0	7.5	.386+/- .017
7.5	8.0	.369+/- .027
8.0	8.5	.297+/- .036
8.5	9.0	.392+/- .038
9.0	9.5	.346+/- .039
9.5	10.0	.343+/- .039
10.0	10.5	.224+/- .037
10.5	11.0	.247+/- .014
11.5	12.0	.236+/- .021
12.0	12.5	.255+/- .030
12.5	13.0	.243+/- .041
13.0	13.5	.225+/- .037

TABLE 5-2. (Continued)

B 2/3

ET BIN EDGES (GEV)		MEAN PLANARITY
.0	.5	.252+/- .006
.5	1.0	.513+/- .007
1.0	1.5	.561+/- .007
1.5	2.0	.551+/- .007
2.0	2.5	.532+/- .008
2.5	3.0	.500+/- .009
3.0	3.5	.470+/- .010
3.5	4.0	.448+/- .012
4.0	4.5	.419+/- .015
4.5	5.0	.413+/- .019
5.0	5.5	.399+/- .022
5.5	6.0	.363+/- .024
6.0	6.5	.315+/- .030
6.5	7.0	.307+/- .055
7.0	7.5	.292+/- .047
7.5	8.0	.246+/- .019
8.5	9.0	.235+/- .029
9.0	9.5	.283+/- .042

F 2/3

ET BIN EDGES (GEV)		MEAN PLANARITY
.0	.5	.229+/- .006
.5	1.0	.509+/- .007
1.0	1.5	.583+/- .006
1.5	2.0	.557+/- .007
2.0	2.5	.540+/- .007
2.5	3.0	.498+/- .008
3.0	3.5	.475+/- .011
3.5	4.0	.453+/- .012
4.0	4.5	.427+/- .014
4.5	5.0	.406+/- .019
5.0	5.5	.391+/- .022
5.5	6.0	.414+/- .029
6.0	6.5	.381+/- .034
6.5	7.0	.341+/- .029
7.0	7.5	.363+/- .048
8.5	9.0	.252+/- .019
9.0	9.5	.228+/- .031
9.5	10.5	.315+/- .052

TABLE 5-2. (Continued)

M 1/2

ET BIN EDGES (GEV)		MEAN PLANARITY
.0	.5	.282+/- .005
.5	1.0	.520+/- .007
1.0	1.5	.565+/- .007
1.5	2.0	.545+/- .007
2.0	2.5	.522+/- .009
2.5	3.0	.481+/- .009
3.0	3.5	.475+/- .012
3.5	4.0	.421+/- .014
4.0	4.5	.424+/- .020
4.5	5.0	.415+/- .033
5.0	5.5	.407+/- .032
5.5	6.0	.341+/- .024
6.0	6.5	.304+/- .046
6.5	7.0	.370+/- .058
8.0	8.5	.188+/- .028
8.5	9.5	.259+/- .049

TABLE 5-3. Mean calorimeter planarity versus calorimeter transverse energy for QCD/brem Monte Carlo data and five apertures.

GLOBAL

ET BIN EDGES (GEV)		MEAN PLANARITY
.5	1.0	.575+/- .081
1.0	1.5	.567+/- .039
1.5	2.0	.574+/- .024
2.0	2.5	.516+/- .019
2.5	3.0	.495+/- .020
3.0	3.5	.479+/- .015
3.5	4.0	.445+/- .013
4.0	4.5	.451+/- .011
4.5	5.0	.430+/- .011
5.0	5.5	.418+/- .012
5.5	6.0	.413+/- .012
6.0	6.5	.414+/- .014
6.5	7.0	.425+/- .015
7.0	7.5	.423+/- .018
7.5	8.0	.390+/- .021
8.0	8.5	.419+/- .022
8.5	9.0	.446+/- .027
10.0	10.5	.454+/- .034
11.0	11.5	.522+/- .086
11.5	12.0	.408+/- .034
12.0	12.5	.502+/- .029
12.5	13.0	.518+/- .031
13.0	13.5	.491+/- .032
13.5	14.0	.489+/- .036
14.0	14.5	.512+/- .065
14.5	15.0	.491+/- .051
15.5	16.0	.547+/- .052
16.0	16.5	.647+/- .032
16.5	17.0	.552+/- .105
17.5	18.0	.525+/- .123
18.0	18.5	.652+/- .062
18.5	19.0	.780+/- .042
19.0	19.5	.790+/- .025
20.0	21.0	.737+/- .045

TABLE 5-3. (Continued)

A-GLOBAL

ET BIN EDGES (GEV)		MEAN PLANARITY
.5	1.0	.601+/- .058
1.0	1.5	.545+/- .032
1.5	2.0	.524+/- .031
2.0	2.5	.497+/- .016
2.5	3.0	.496+/- .015
3.0	3.5	.439+/- .014
3.5	4.0	.456+/- .011
4.0	4.5	.450+/- .012
4.5	5.0	.419+/- .011
5.0	5.5	.422+/- .013
5.5	6.0	.415+/- .014
6.0	6.5	.416+/- .016
6.5	7.0	.422+/- .016
7.0	7.5	.392+/- .022
7.5	8.0	.430+/- .024
8.0	8.5	.420+/- .028
9.0	9.5	.402+/- .035
10.0	10.5	.500+/- .037
10.5	11.0	.511+/- .092
11.0	11.5	.464+/- .028
11.5	12.0	.523+/- .022
12.0	12.5	.491+/- .031
12.5	13.0	.505+/- .033
13.0	13.5	.555+/- .037
13.5	14.0	.500+/- .049
14.0	14.5	.471+/- .087
14.5	15.0	.569+/- .046
15.0	15.5	.598+/- .047
15.5	16.0	.547+/- .078
16.0	16.5	.733+/- .034
17.0	17.5	.647+/- .061
18.0	18.5	.818+/- .027
18.5	19.5	.785+/- .026

TABLE 5-3. (Continued)

B 2/3

ET BIN EDGES (GEV)		MEAN PLANARITY
.0	.5	.569+/- .038
.5	1.0	.480+/- .018
1.0	1.5	.473+/- .016
1.5	2.0	.470+/- .011
2.0	2.5	.451+/- .011
2.5	3.0	.443+/- .011
3.0	3.5	.442+/- .011
3.5	4.0	.455+/- .014
4.0	4.5	.434+/- .014
4.5	5.0	.400+/- .015
5.0	5.5	.430+/- .020
5.5	6.0	.475+/- .030
6.0	6.5	.349+/- .047
6.5	7.0	.451+/- .027
7.0	7.5	.411+/- .041
7.5	8.0	.498+/- .022
8.5	9.0	.488+/- .037
9.0	9.5	.587+/- .052
9.5	10.0	.512+/- .037
10.0	10.5	.444+/- .072
10.5	11.0	.524+/- .065
11.0	11.5	.589+/- .054
11.5	12.0	.684+/- .041
12.0	12.5	.610+/- .066
12.5	13.0	.497+/- .078
13.0	13.5	.598+/- .065
13.5	14.0	.783+/- .048
14.0	14.5	.751+/- .037
15.0	15.5	.761+/- .040
15.5	16.0	.735+/- .058
16.0	17.0	.751+/- .031
17.0	18.0	.864+/- .027

TABLE 5-3. (Continued)

F 2/3

ET BIN EDGES (GEV)		MEAN PLANARITY
.0	.5	.599+/- .037
.5	1.0	.533+/- .019
1.0	1.5	.511+/- .014
1.5	2.0	.478+/- .012
2.0	2.5	.451+/- .010
2.5	3.0	.421+/- .011
3.0	3.5	.420+/- .011
3.5	4.0	.422+/- .014
4.0	4.5	.430+/- .015
4.5	5.0	.386+/- .017
5.0	5.5	.447+/- .019
5.5	6.0	.413+/- .029
6.5	7.0	.379+/- .038
7.0	7.5	.479+/- .031
7.5	8.0	.425+/- .054
8.0	8.5	.518+/- .043
8.5	9.0	.345+/- .101
9.0	9.5	.489+/- .035
9.5	10.0	.538+/- .043
10.0	10.5	.517+/- .059
10.5	11.0	.639+/- .037
11.0	11.5	.664+/- .054
12.0	12.5	.809+/- .020
12.5	13.5	.771+/- .047
13.5	14.5	.624+/- .109
14.5	16.5	.783+/- .050

TABLE 5-3. (Continued)

M 1/2

ET BIN EDGES (GEV)		MEAN PLANARITY
.0	.5	.540+/- .028
.5	1.0	.510+/- .013
1.0	1.5	.459+/- .013
1.5	2.0	.464+/- .010
2.0	2.5	.453+/- .010
2.5	3.0	.428+/- .011
3.0	3.5	.431+/- .013
3.5	4.0	.438+/- .016
4.0	4.5	.416+/- .018
4.5	5.0	.408+/- .023
5.0	5.5	.456+/- .026
5.5	6.0	.504+/- .043
6.0	6.5	.448+/- .031
6.5	7.0	.509+/- .071
7.0	7.5	.439+/- .040
7.5	8.0	.521+/- .037
8.0	8.5	.569+/- .023
8.5	9.0	.578+/- .035
9.0	9.5	.550+/- .033
9.5	10.0	.595+/- .050
10.0	10.5	.661+/- .057
10.5	11.0	.702+/- .034
11.0	11.5	.690+/- .050
11.5	12.0	.628+/- .071
12.0	12.5	.757+/- .040
12.5	13.0	.816+/- .042
13.0	13.5	.780+/- .040
13.5	14.0	.740+/- .048
14.0	14.5	.751+/- .113
14.5	15.5	.871+/- .023

TABLE 5-4. Mean particle planarity versus particle transverse energy for QCD/brem Monte Carlo data and five apertures.

GLOBAL

ET BIN EDGES (GEV)		MEAN PLANARITY
.5	1.0	.566+/- .075
1.0	1.5	.551+/- .040
1.5	2.0	.491+/- .034
2.0	2.5	.535+/- .017
2.5	3.0	.476+/- .017
3.0	3.5	.480+/- .012
3.5	4.0	.430+/- .013
4.0	4.5	.436+/- .011
4.5	5.0	.435+/- .011
5.0	5.5	.421+/- .011
5.5	6.0	.410+/- .014
6.0	6.5	.421+/- .013
6.5	7.0	.405+/- .014
7.0	7.5	.402+/- .023
7.5	8.0	.388+/- .024
8.0	8.5	.502+/- .095
8.5	9.0	.476+/- .027
9.0	9.5	.478+/- .030
9.5	10.0	.428+/- .038
10.0	10.5	.362+/- .063
10.5	11.0	.511+/- .024
11.0	11.5	.468+/- .031
11.5	12.0	.551+/- .021
12.0	12.5	.514+/- .026
12.5	13.0	.561+/- .026
13.0	13.5	.543+/- .036
13.5	14.0	.537+/- .054
14.0	14.5	.475+/- .094
15.0	15.5	.667+/- .036
15.5	16.0	.657+/- .047
16.0	16.5	.451+/- .089
16.5	17.0	.670+/- .046
17.0	17.5	.736+/- .049
17.5	18.0	.647+/- .058
18.0	18.5	.812+/- .026
18.5	19.0	.699+/- .057
19.0	19.5	.806+/- .050
19.5	20.5	.834+/- .031

TABLE 5-4. (Continued)

A-GLOBAL

ET BIN EDGES (GEV)		MEAN PLANARITY
.5	1.0	.567+/- .062
1.0	1.5	.538+/- .051
1.5	2.0	.506+/- .019
2.0	2.5	.506+/- .016
2.5	3.0	.469+/- .014
3.0	3.5	.452+/- .013
3.5	4.0	.438+/- .012
4.0	4.5	.439+/- .012
4.5	5.0	.419+/- .011
5.0	5.5	.417+/- .012
5.5	6.0	.433+/- .014
6.0	6.5	.392+/- .015
6.5	7.0	.413+/- .016
7.0	7.5	.425+/- .031
7.5	8.0	.488+/- .078
8.0	8.5	.442+/- .022
8.5	9.0	.500+/- .040
9.0	9.5	.454+/- .026
9.5	10.0	.413+/- .055
10.0	10.5	.383+/- .060
10.5	11.0	.527+/- .029
11.0	11.5	.480+/- .031
11.5	12.0	.543+/- .021
12.0	12.5	.541+/- .025
12.5	13.0	.570+/- .031
13.0	13.5	.530+/- .048
13.5	14.0	.663+/- .027
14.0	14.5	.459+/- .086
15.0	15.5	.737+/- .026
15.5	16.0	.715+/- .040
16.0	16.5	.425+/- .089
16.5	17.0	.737+/- .032
17.0	17.5	.729+/- .051
18.0	18.5	.766+/- .031
18.5	19.0	.690+/- .085
19.0	19.5	.874+/- .024
19.5	20.5	.839+/- .032

TABLE 5-4. (Continued)

B 2/3

ET BIN EDGES (GEV)		MEAN PLANARITY
.0	.5	.511+/- .029
.5	1.0	.458+/- .024
1.0	1.5	.488+/- .012
1.5	2.0	.455+/- .010
2.0	2.5	.435+/- .012
2.5	3.0	.444+/- .010
3.0	3.5	.451+/- .012
3.5	4.0	.424+/- .012
4.0	4.5	.454+/- .016
4.5	5.0	.418+/- .015
5.0	5.5	.420+/- .023
5.5	6.0	.405+/- .049
6.0	6.5	.428+/- .048
6.5	7.0	.473+/- .061
7.0	7.5	.453+/- .056
8.0	8.5	.374+/- .092
8.5	9.0	.596+/- .034
9.0	9.5	.577+/- .057
9.5	10.0	.531+/- .041
10.0	10.5	.611+/- .038
10.5	11.0	.552+/- .070
11.0	11.5	.612+/- .042
11.5	12.0	.651+/- .040
12.0	12.5	.674+/- .047
12.5	13.0	.756+/- .031
13.0	13.5	.767+/- .022
13.5	14.0	.776+/- .037
14.0	14.5	.801+/- .029
14.5	15.0	.812+/- .048
15.0	15.5	.700+/- .054
15.5	16.5	.740+/- .060
16.5	17.5	.820+/- .034

TABLE 5-4. (Continued)

F 2/3

ET BIN EDGES (GEV)		MEAN PLANARITY
.0	.5	.605+/- .037
.5	1.0	.503+/- .021
1.0	1.5	.496+/- .017
1.5	2.0	.480+/- .011
2.0	2.5	.443+/- .011
2.5	3.0	.430+/- .011
3.0	3.5	.432+/- .010
3.5	4.0	.405+/- .011
4.0	4.5	.433+/- .014
4.5	5.0	.418+/- .018
5.0	5.5	.405+/- .024
5.5	6.0	.528+/- .071
6.0	6.5	.445+/- .023
6.5	7.0	.342+/- .114
7.0	7.5	.515+/- .047
7.5	8.0	.463+/- .079
8.0	8.5	.469+/- .059
8.5	9.0	.481+/- .075
9.0	9.5	.578+/- .022
9.5	10.0	.624+/- .035
10.0	10.5	.572+/- .045
10.5	11.0	.617+/- .044
11.0	11.5	.673+/- .037
11.5	12.0	.601+/- .055
12.5	13.0	.773+/- .040
13.0	13.5	.831+/- .017
14.0	15.0	.820+/- .023
16.0	18.0	.909+/- .010

TABLE 5-4. (Continued)

M 1/2

ET BIN EDGES (GEV)		MEAN PLANARITY
.0	.5	.539+/- .023
.5	1.0	.488+/- .016
1.0	1.5	.459+/- .012
1.5	2.0	.455+/- .011
2.0	2.5	.436+/- .011
2.5	3.0	.437+/- .010
3.0	3.5	.428+/- .013
3.5	4.0	.426+/- .013
4.0	4.5	.453+/- .018
4.5	5.0	.437+/- .026
5.0	5.5	.377+/- .046
5.5	6.0	.406+/- .045
6.0	6.5	.452+/- .036
6.5	7.0	.417+/- .069
7.0	7.5	.416+/- .075
7.5	8.0	.582+/- .018
8.0	8.5	.585+/- .028
8.5	9.0	.525+/- .040
9.0	9.5	.634+/- .022
9.5	10.0	.602+/- .059
10.0	10.5	.565+/- .067
10.5	11.0	.667+/- .034
11.0	11.5	.802+/- .029
11.5	12.0	.746+/- .034
12.0	12.5	.691+/- .045
12.5	13.0	.805+/- .018
13.0	13.5	.818+/- .024
13.5	14.0	.785+/- .037
14.0	14.5	.853+/- .026
14.5	15.0	.640+/- .122
15.0	15.5	.908+/- .015
15.5	16.0	.869+/- .021
16.5	17.0	.903+/- .018

TABLE 5-5. Fraction of events with high calorimeter planarity (> 0.7) versus calorimeter transverse energy for LPS Monte Carlo data and five apertures.

GLOBAL

ET BIN EDGES (GEV)		FRACTION OF EVENTS WITH P(CALR) > .7
.0	.5	.556 +/- .010
.5	1.0	.701 +/- .011
1.0	1.5	.575 +/- .013
1.5	2.0	.443 +/- .014
2.0	2.5	.355 +/- .015
2.5	3.0	.272 +/- .016
3.0	3.5	.292 +/- .018
3.5	4.0	.209 +/- .018
4.0	4.5	.165 +/- .017
4.5	5.0	.137 +/- .018
5.0	5.5	.143 +/- .022
5.5	6.0	.081 +/- .015
6.0	6.5	.078 +/- .018
6.5	7.0	.056 +/- .019
7.0	7.5	.059 +/- .025
9.0	9.5	.003 +/- .003
9.5	10.0	.140 +/- .121

A-GLOBAL

ET BIN EDGES (GEV)		FRACTION OF EVENTS WITH P(CALR) > .7
.0	.5	.569 +/- .010
.5	1.0	.671 +/- .011
1.0	1.5	.538 +/- .013
1.5	2.0	.424 +/- .014
2.0	2.5	.312 +/- .014
2.5	3.0	.290 +/- .016
3.0	3.5	.243 +/- .017
3.5	4.0	.208 +/- .018
4.0	4.5	.147 +/- .018
4.5	5.0	.111 +/- .017
5.0	5.5	.147 +/- .025
5.5	6.0	.068 +/- .015
6.0	6.5	.070 +/- .020
6.5	7.0	.088 +/- .043
7.0	7.5	.035 +/- .031
9.0	9.5	.130 +/- .114

TABLE 5-5. (Continued)

B 2/3

ET BIN EDGES (GEV)		FRACTION OF EVENTS WITH P(CALR) > .7
.0	.5	.582 +/- .008
.5	1.0	.545 +/- .010
1.0	1.5	.405 +/- .012
1.5	2.0	.320 +/- .014
2.0	2.5	.276 +/- .016
2.5	3.0	.239 +/- .018
3.0	3.5	.182 +/- .021
3.5	4.0	.125 +/- .021
4.0	4.5	.113 +/- .025
4.5	5.0	.099 +/- .024
5.0	5.5	.105 +/- .033
5.5	6.0	.088 +/- .047
6.0	6.5	.077 +/- .072

F 2/3

ET BIN EDGES (GEV)		FRACTION OF EVENTS WITH P(CALR) > .7
.0	.5	.595 +/- .008
.5	1.0	.513 +/- .010
1.0	1.5	.400 +/- .012
1.5	2.0	.322 +/- .014
2.0	2.5	.254 +/- .016
2.5	3.0	.208 +/- .018
3.0	3.5	.186 +/- .022
3.5	4.0	.132 +/- .024
4.0	4.5	.050 +/- .016
4.5	5.0	.069 +/- .023
5.0	5.5	.140 +/- .082
5.5	6.0	.068 +/- .045

TABLE 5-5. (Continued)

M 1/2

ET BIN EDGES (GEV)		FRACTION OF EVENTS WITH P(CALR) > .7
.0	.5	.574 +/- .007
.5	1.0	.498 +/- .010
1.0	1.5	.367 +/- .012
1.5	2.0	.285 +/- .014
2.0	2.5	.256 +/- .018
2.5	3.0	.205 +/- .020
3.0	3.5	.129 +/- .022
3.5	4.0	.101 +/- .024
4.0	4.5	.130 +/- .043
4.5	5.0	.105 +/- .035
5.0	5.5	.053 +/- .049

TABLE 5-6. Fraction of events with high calorimeter planarity (> 0.7) versus calorimeter transverse energy for QCD/brem Monte Carlo data and five apertures.

GLOBAL

ET BIN EDGES (GEV)		FRACTION OF EVENTS WITH P(CALR) > .7
.5	1.0	.457 +/- .133
1.0	1.5	.319 +/- .071
1.5	2.0	.356 +/- .058
2.0	2.5	.225 +/- .036
2.5	3.0	.192 +/- .028
3.0	3.5	.190 +/- .026
3.5	4.0	.123 +/- .019
4.0	4.5	.131 +/- .017
4.5	5.0	.066 +/- .012
5.0	5.5	.074 +/- .014
5.5	6.0	.076 +/- .015
6.0	6.5	.097 +/- .025
6.5	7.0	.075 +/- .018
7.0	7.5	.054 +/- .011
7.5	8.0	.054 +/- .012
8.0	8.5	.118 +/- .104
8.5	9.0	.147 +/- .107
9.0	9.5	.026 +/- .018
9.5	10.0	.036 +/- .023
10.0	10.5	.059 +/- .018
10.5	11.0	.068 +/- .046
11.0	11.5	.045 +/- .021
11.5	12.0	.098 +/- .019
12.0	12.5	.156 +/- .031
12.5	13.0	.137 +/- .027
13.0	13.5	.153 +/- .031
13.5	14.0	.135 +/- .034
14.0	14.5	.186 +/- .070
14.5	15.0	.278 +/- .066
15.0	15.5	.144 +/- .080
15.5	16.0	.298 +/- .091
16.0	16.5	.498 +/- .099
16.5	17.0	.455 +/- .209
17.0	17.5	.168 +/- .121
17.5	18.0	.448 +/- .215
18.0	18.5	.385 +/- .175
18.5	19.0	.809 +/- .094
19.0	19.5	.859 +/- .090

TABLE 5-6. (Continued)

A-GLOBAL

ET BIN EDGES (GEV)		FRACTION OF EVENTS WITH P(CALR) > .7
.0	.5	.519 +/- .281
.5	1.0	.465 +/- .107
1.0	1.5	.269 +/- .056
1.5	2.0	.299 +/- .054
2.0	2.5	.173 +/- .025
2.5	3.0	.220 +/- .028
3.0	3.5	.135 +/- .018
3.5	4.0	.112 +/- .018
4.0	4.5	.116 +/- .017
4.5	5.0	.067 +/- .012
5.0	5.5	.085 +/- .021
5.5	6.0	.078 +/- .017
6.0	6.5	.067 +/- .017
6.5	7.0	.073 +/- .015
7.0	7.5	.068 +/- .015
8.0	8.5	.140 +/- .103
8.5	9.0	.033 +/- .025
9.0	9.5	.066 +/- .014
9.5	10.0	.072 +/- .042
10.0	10.5	.101 +/- .031
10.5	11.0	.065 +/- .036
11.0	11.5	.102 +/- .018
11.5	12.0	.201 +/- .029
12.0	12.5	.212 +/- .037
12.5	13.0	.134 +/- .035
13.0	13.5	.163 +/- .041
13.5	14.0	.312 +/- .069
14.0	14.5	.162 +/- .079
14.5	15.0	.343 +/- .086
15.0	15.5	.392 +/- .112
15.5	16.0	.455 +/- .162
16.0	16.5	.544 +/- .132
16.5	17.0	.167 +/- .130
17.0	17.5	.525 +/- .138
17.5	18.0	.326 +/- .217
18.0	18.5	.893 +/- .090
18.5	19.5	.724 +/- .111

TABLE 5-6. (Continued)

B 2/3

ET BIN EDGES (GEV)		FRACTION OF EVENTS WITH P(CALR) > .7
.0	.5	.339 +/- .081
.5	1.0	.237 +/- .029
1.0	1.5	.162 +/- .021
1.5	2.0	.165 +/- .021
2.0	2.5	.131 +/- .015
2.5	3.0	.123 +/- .018
3.0	3.5	.097 +/- .015
3.5	4.0	.083 +/- .018
4.0	4.5	.093 +/- .019
4.5	5.0	.065 +/- .016
5.0	5.5	.080 +/- .026
5.5	6.0	.208 +/- .083
6.0	6.5	.053 +/- .020
6.5	7.0	.088 +/- .023
7.0	7.5	.118 +/- .039
7.5	8.0	.162 +/- .030
8.0	8.5	.029 +/- .017
8.5	9.0	.095 +/- .023
9.0	9.5	.421 +/- .142
9.5	10.0	.249 +/- .048
10.0	10.5	.258 +/- .077
10.5	11.0	.291 +/- .089
11.0	11.5	.221 +/- .100
11.5	12.0	.425 +/- .143
12.0	12.5	.500 +/- .137
12.5	13.0	.311 +/- .118
13.0	13.5	.456 +/- .166
13.5	14.0	.874 +/- .070
14.0	14.5	.643 +/- .117
15.0	15.5	.608 +/- .184
16.0	17.0	.704 +/- .124

TABLE 5-6. (Continued)

F 2/3

ET BIN EDGES (GEV)		FRACTION OF EVENTS WITH P(CALR) > .7
.0	.5	.384 +/- .074
.5	1.0	.278 +/- .035
1.0	1.5	.241 +/- .028
1.5	2.0	.156 +/- .019
2.0	2.5	.121 +/- .015
2.5	3.0	.095 +/- .012
3.0	3.5	.095 +/- .015
3.5	4.0	.092 +/- .019
4.0	4.5	.057 +/- .012
4.5	5.0	.033 +/- .008
5.0	5.5	.109 +/- .052
5.5	6.0	.110 +/- .048
6.0	6.5	.029 +/- .018
6.5	7.0	.058 +/- .014
7.0	7.5	.084 +/- .023
7.5	8.0	.113 +/- .031
8.0	8.5	.151 +/- .045
8.5	9.0	.125 +/- .060
9.0	9.5	.172 +/- .037
9.5	10.0	.238 +/- .061
10.0	10.5	.212 +/- .080
10.5	11.0	.493 +/- .110
11.0	11.5	.520 +/- .195
12.0	12.5	.878 +/- .063
12.5	13.5	.754 +/- .184
14.5	16.5	.686 +/- .191

TABLE 5-6. (Continued)

M 1/2

ET BIN EDGES (GEV)		FRACTION OF EVENTS WITH P(CALR) > .7
.0	.5	.326 +/- .063
.5	1.0	.239 +/- .024
1.0	1.5	.164 +/- .020
1.5	2.0	.141 +/- .017
2.0	2.5	.107 +/- .013
2.5	3.0	.094 +/- .014
3.0	3.5	.105 +/- .019
3.5	4.0	.082 +/- .021
4.0	4.5	.078 +/- .020
4.5	5.0	.075 +/- .030
5.0	5.5	.135 +/- .074
6.0	6.5	.076 +/- .019
6.5	7.0	.088 +/- .032
7.0	7.5	.161 +/- .032
7.5	8.0	.260 +/- .118
8.0	8.5	.266 +/- .040
8.5	9.0	.332 +/- .078
9.0	9.5	.298 +/- .060
9.5	10.0	.264 +/- .080
10.0	10.5	.426 +/- .131
10.5	11.0	.643 +/- .121
11.0	11.5	.497 +/- .174
11.5	12.0	.620 +/- .176
12.0	12.5	.832 +/- .093
12.5	13.0	.878 +/- .079
13.5	14.0	.764 +/- .207

TABLE 5-7. Mean (Global) E_t^C/E^C and E_t/E for LPS Monte Carlo high transverse energy events.

	Global	A-global	B 2/3	F 2/3	M 1/2
E_t^C Threshold (GeV)	16.0	16.5	13.5	11.5	11.5
Mean E_t^C/E^C (10^{-3})	63.0±2.5	60.5±4.2	71.3±1.4	56.5±1.2	57.3±3.2
Mean E_t/E (10^{-3})	59.4±3.1	56.7±1.6	60.3±4.2	51.3±3.2	54.7±1.2

TABLE 5-8. Mean (Global) E_t^C/E^C and E_t/E for QCD/brem Monte Carlo high transverse energy events.

	Global	A-global	B 2/3	F 2/3	M 1/2
E_t^C Threshold (GeV)	16.0	16.5	13.5	11.5	11.5
Mean E_t^C/E^C (10^{-3})	66.5±1.1	69.3±2.2	71.0±1.4	56.1±1.6	64.2±0.9
Mean E_t/E (10^{-3})	63.0±1.1	66.2±2.1	67.6±1.3	52.8±1.7	61.3±0.9

TABLE 5-9. Mean calorimeter planarity versus calorimeter transverse energy for hydrogen data and five apertures.

GLOBAL

ET BIN EDGES (GEV)		MEAN PLANARITY
.0	.5	.532+/- .008
.5	1.0	.699+/- .004
1.0	1.5	.640+/- .004
1.5	2.0	.590+/- .004
2.0	2.5	.558+/- .004
2.5	3.0	.535+/- .004
3.0	3.5	.507+/- .004
3.5	4.0	.495+/- .005
4.0	4.5	.485+/- .005
4.5	5.0	.470+/- .006
5.0	5.5	.461+/- .006
5.5	6.0	.449+/- .007
6.0	6.5	.445+/- .008
6.5	7.0	.434+/- .009
7.0	7.5	.440+/- .009
7.5	8.0	.455+/- .011
8.0	8.5	.431+/- .011
8.5	9.0	.412+/- .013
9.0	9.5	.438+/- .017
9.5	10.0	.425+/- .018
10.0	10.5	.407+/- .017
10.5	11.0	.412+/- .020
11.0	11.5	.406+/- .009
11.5	12.0	.399+/- .011
12.0	12.5	.411+/- .013
12.5	13.0	.415+/- .016
13.0	13.5	.410+/- .008
13.5	14.0	.419+/- .010
14.0	14.5	.420+/- .011
14.5	15.0	.414+/- .015
15.0	15.5	.410+/- .008
15.5	16.0	.399+/- .008
16.0	16.5	.410+/- .009
16.5	17.0	.403+/- .011
17.0	17.5	.400+/- .013
17.5	18.0	.397+/- .015
18.0	18.5	.430+/- .016
18.5	19.0	.419+/- .019
19.0	19.5	.385+/- .025
19.5	20.5	.430+/- .029
20.5	21.5	.505+/- .041
21.5	23.5	.327+/- .048

TABLE 5-9. (Continued)

A-GLOBAL

ET BIN EDGES (GEV)		MEAN PLANARITY
.0	.5	.565+/- .006
.5	1.0	.673+/- .004
1.0	1.5	.618+/- .004
1.5	2.0	.573+/- .004
2.0	2.5	.543+/- .004
2.5	3.0	.517+/- .004
3.0	3.5	.498+/- .004
3.5	4.0	.490+/- .005
4.0	4.5	.473+/- .006
4.5	5.0	.456+/- .006
5.0	5.5	.456+/- .007
5.5	6.0	.440+/- .008
6.0	6.5	.438+/- .009
6.5	7.0	.436+/- .011
7.0	7.5	.439+/- .013
7.5	8.0	.448+/- .013
8.0	8.5	.429+/- .015
8.5	9.0	.426+/- .019
9.0	9.5	.458+/- .021
9.5	10.0	.402+/- .027
10.0	10.5	.379+/- .029
10.5	11.0	.412+/- .030
11.0	11.5	.447+/- .045
11.5	12.0	.409+/- .016
12.0	12.5	.411+/- .021
12.5	13.0	.433+/- .028
13.0	13.5	.387+/- .037
13.5	14.0	.420+/- .017
14.0	14.5	.427+/- .020
14.5	15.0	.443+/- .025
15.0	15.5	.375+/- .027
15.5	16.0	.409+/- .021
16.0	16.5	.378+/- .021
16.5	17.0	.420+/- .022
17.0	17.5	.464+/- .029
17.5	18.0	.412+/- .028
18.0	18.5	.408+/- .038
18.5	19.0	.480+/- .050
19.0	20.0	.467+/- .038
20.0	21.0	.414+/- .086

TABLE 5-9. (Continued)

B 2/3

ET BIN EDGES (GEV)		MEAN PLANARITY
.0	.5	.612+/- .004
.5	1.0	.607+/- .003
1.0	1.5	.560+/- .003
1.5	2.0	.529+/- .003
2.0	2.5	.506+/- .004
2.5	3.0	.492+/- .005
3.0	3.5	.469+/- .005
3.5	4.0	.459+/- .007
4.0	4.5	.456+/- .008
4.5	5.0	.454+/- .010
5.0	5.5	.465+/- .012
5.5	6.0	.446+/- .014
6.0	6.5	.442+/- .019
6.5	7.0	.438+/- .018
7.0	7.5	.423+/- .021
7.5	8.0	.453+/- .040
8.0	8.5	.361+/- .041
8.5	9.0	.379+/- .055
9.0	9.5	.412+/- .047
9.5	10.0	.440+/- .025
10.0	10.5	.411+/- .023
10.5	11.0	.539+/- .040
11.0	11.5	.381+/- .021
11.5	12.0	.432+/- .033
12.0	12.5	.468+/- .035
12.5	13.0	.454+/- .037
13.0	13.5	.420+/- .025
13.5	14.0	.482+/- .031
14.0	14.5	.462+/- .031
14.5	15.0	.468+/- .049
15.0	16.0	.416+/- .033
16.0	17.0	.497+/- .049
17.0	19.0	.491+/- .056

TABLE 5-9. (Continued)

F 2/3

ET BIN EDGES (GEV)		MEAN PLANARITY
.0	.5	.627+/- .003
.5	1.0	.593+/- .003
1.0	1.5	.542+/- .003
1.5	2.0	.506+/- .003
2.0	2.5	.492+/- .004
2.5	3.0	.479+/- .005
3.0	3.5	.450+/- .006
3.5	4.0	.444+/- .008
4.0	4.5	.439+/- .009
4.5	5.0	.442+/- .012
5.0	5.5	.433+/- .015
5.5	6.0	.455+/- .018
6.0	6.5	.448+/- .023
6.5	7.0	.426+/- .033
7.0	7.5	.456+/- .052
7.5	8.0	.399+/- .055
8.0	8.5	.467+/- .039
8.5	9.0	.428+/- .036
9.0	9.5	.368+/- .071
9.5	10.0	.507+/- .024
10.0	10.5	.501+/- .032
10.5	11.0	.461+/- .060
11.0	11.5	.487+/- .033
11.5	12.5	.484+/- .035
12.5	13.5	.578+/- .048
13.5	15.5	.817+/- .045

TABLE 5-9. (Continued)

M 1/2

ET BIN EDGES (GEV)		MEAN PLANARITY
.0	.5	.622+/- .003
.5	1.0	.575+/- .003
1.0	1.5	.534+/- .003
1.5	2.0	.500+/- .003
2.0	2.5	.473+/- .004
2.5	3.0	.473+/- .005
3.0	3.5	.458+/- .007
3.5	4.0	.442+/- .009
4.0	4.5	.452+/- .011
4.5	5.0	.428+/- .016
5.0	5.5	.442+/- .021
5.5	6.0	.464+/- .024
6.0	6.5	.442+/- .033
6.5	7.0	.406+/- .036
7.0	7.5	.488+/- .101
7.5	8.0	.472+/- .075
8.0	8.5	.421+/- .034
8.5	9.0	.476+/- .051
9.0	9.5	.574+/- .091
9.5	10.0	.454+/- .041
10.0	10.5	.523+/- .056
10.5	11.0	.482+/- .061
11.0	11.5	.524+/- .067
11.5	12.5	.445+/- .033
12.5	13.5	.629+/- .074
13.5	15.5	.543+/- .094

TABLE 5-10. Fraction of events with high calorimeter planarity (> 0.7) versus calorimeter transverse energy for hydrogen data and five apertures.

GLOBAL

ET BIN EDGES (GEV)		FRACTION OF EVENTS WITH P(CALR) > .7
.0	.5	.508 +/- .010
.5	1.0	.572 +/- .009
1.0	1.5	.461 +/- .008
1.5	2.0	.369 +/- .008
2.0	2.5	.310 +/- .008
2.5	3.0	.265 +/- .008
3.0	3.5	.223 +/- .008
3.5	4.0	.201 +/- .009
4.0	4.5	.178 +/- .009
4.5	5.0	.163 +/- .010
5.0	5.5	.159 +/- .011
5.5	6.0	.123 +/- .012
6.0	6.5	.103 +/- .012
6.5	7.0	.104 +/- .014
7.0	7.5	.141 +/- .016
7.5	8.0	.143 +/- .018
8.0	8.5	.083 +/- .017
8.5	9.0	.091 +/- .020
9.0	9.5	.085 +/- .026
9.5	10.0	.100 +/- .028
10.0	10.5	.099 +/- .025
10.5	11.0	.057 +/- .028
11.0	11.5	.071 +/- .012
11.5	12.0	.084 +/- .017
12.0	12.5	.077 +/- .018
12.5	13.0	.082 +/- .024
13.0	13.5	.073 +/- .011
13.5	14.0	.102 +/- .016
14.0	14.5	.063 +/- .016
14.5	15.0	.101 +/- .023
15.0	15.5	.085 +/- .012
15.5	16.0	.065 +/- .011
16.0	16.5	.084 +/- .013
16.5	17.0	.082 +/- .017
17.0	17.5	.079 +/- .018
17.5	18.0	.090 +/- .024
18.0	18.5	.103 +/- .025
18.5	19.0	.074 +/- .027
19.0	19.5	.065 +/- .031
19.5	20.5	.129 +/- .045
20.5	21.5	.160 +/- .083

TABLE 5-10. (Continued)

A-GLOBAL

ET BIN EDGES (GEV)		FRACTION OF EVENTS WITH P(CALR) > .7
.0	.5	.521 +/- .009
.5	1.0	.522 +/- .008
1.0	1.5	.421 +/- .008
1.5	2.0	.335 +/- .007
2.0	2.5	.289 +/- .008
2.5	3.0	.235 +/- .008
3.0	3.5	.200 +/- .008
3.5	4.0	.194 +/- .009
4.0	4.5	.173 +/- .010
4.5	5.0	.150 +/- .011
5.0	5.5	.133 +/- .012
5.5	6.0	.115 +/- .013
6.0	6.5	.098 +/- .014
6.5	7.0	.101 +/- .017
7.0	7.5	.113 +/- .020
7.5	8.0	.117 +/- .022
8.0	8.5	.122 +/- .025
8.5	9.0	.096 +/- .030
9.0	9.5	.112 +/- .035
9.5	10.0	.036 +/- .035
10.0	10.5	.049 +/- .047
10.5	11.0	.080 +/- .044
11.0	11.5	.143 +/- .092
11.5	12.0	.061 +/- .021
12.0	12.5	.078 +/- .030
12.5	13.0	.075 +/- .042
13.5	14.0	.088 +/- .024
14.0	14.5	.097 +/- .031
14.5	15.0	.159 +/- .048
15.5	16.0	.110 +/- .033
16.0	16.5	.079 +/- .031
16.5	17.0	.113 +/- .037
17.0	17.5	.133 +/- .055
17.5	18.0	.078 +/- .043
18.0	18.5	.083 +/- .078
18.5	19.0	.143 +/- .092
19.0	20.0	.125 +/- .067

TABLE 5-10. (Continued)

B 2/3

ET BIN EDGES (GEV)		FRACTION OF EVENTS WITH P(CALR) > .7
.0	.5	.514 +/- .007
.5	1.0	.394 +/- .006
1.0	1.5	.317 +/- .006
1.5	2.0	.257 +/- .007
2.0	2.5	.230 +/- .007
2.5	3.0	.190 +/- .008
3.0	3.5	.159 +/- .009
3.5	4.0	.165 +/- .012
4.0	4.5	.149 +/- .013
4.5	5.0	.124 +/- .016
5.0	5.5	.159 +/- .021
5.5	6.0	.086 +/- .021
6.0	6.5	.108 +/- .029
6.5	7.0	.099 +/- .030
7.0	7.5	.099 +/- .035
7.5	8.0	.172 +/- .077
9.5	10.0	.120 +/- .040
10.0	10.5	.049 +/- .034
10.5	11.0	.188 +/- .075
11.0	11.5	.044 +/- .025
11.5	12.0	.149 +/- .056
12.0	12.5	.147 +/- .067
12.5	13.0	.087 +/- .081
13.0	13.5	.093 +/- .044
13.5	14.0	.204 +/- .057
14.0	14.5	.121 +/- .065
14.5	15.0	.167 +/- .105
15.0	16.0	.075 +/- .050
16.0	17.0	.125 +/- .114

TABLE 5-10. (Continued)

F 2/3

ET BIN EDGES (GEV)		FRACTION OF EVENTS WITH P(CALR) > .7
.0	.5	.522 +/- .006
.5	1.0	.375 +/- .006
1.0	1.5	.279 +/- .006
1.5	2.0	.222 +/- .006
2.0	2.5	.193 +/- .007
2.5	3.0	.175 +/- .009
3.0	3.5	.136 +/- .010
3.5	4.0	.122 +/- .012
4.0	4.5	.097 +/- .014
4.5	5.0	.134 +/- .020
5.0	5.5	.103 +/- .024
5.5	6.0	.143 +/- .034
6.0	6.5	.117 +/- .039
6.5	7.0	.149 +/- .056
7.0	7.5	.111 +/- .102
7.5	8.0	.111 +/- .102
8.5	9.0	.108 +/- .058
9.5	10.0	.167 +/- .050
10.0	10.5	.182 +/- .073
10.5	11.0	.154 +/- .137
11.0	11.5	.139 +/- .064
11.5	12.5	.205 +/- .064
12.5	13.5	.367 +/- .092
13.5	15.5	.778 +/- .187

TABLE 5-10. (Continued)

M 1/2

ET BIN EDGES (GEV)		FRACTION OF EVENTS WITH P(CALR) > .7
.0	.5	.498 +/- .005
.5	1.0	.339 +/- .006
1.0	1.5	.264 +/- .006
1.5	2.0	.217 +/- .007
2.0	2.5	.171 +/- .008
2.5	3.0	.154 +/- .009
3.0	3.5	.158 +/- .012
3.5	4.0	.117 +/- .014
4.0	4.5	.117 +/- .018
4.5	5.0	.119 +/- .026
5.0	5.5	.109 +/- .032
5.5	6.0	.152 +/- .042
6.0	6.5	.119 +/- .055
6.5	7.0	.071 +/- .068
7.0	7.5	.286 +/- .228
8.0	8.5	.125 +/- .067
8.5	9.0	.182 +/- .093
9.0	9.5	.222 +/- .187
9.5	10.0	.154 +/- .080
10.0	10.5	.267 +/- .129
11.0	11.5	.333 +/- .134
11.5	12.5	.132 +/- .061
12.5	13.5	.433 +/- .166
13.5	15.5	.333 +/- .186

TABLE 5-11. Mean (Global) E_t^C/E^C for hydrogen target data high transverse energy events.

	Global	A-global	B 2/3	F 2/3	M 1/2
E_t^C Threshold (GeV)	16.0	16.5	13.5	11.5	11.5
Mean E_t^C/E^C (10^{-3})	62.6±0.2	66.3±0.4	72.4±0.5	57.0±0.6	63.3±0.7

TABLE 5-12. Vertex position data for F 2/3 and B 2/3 events, hydrogen target data -- Global trigger.

	Number of events	$\bar{x}$ (mm)	σ_x (mm)	$\bar{y}$ (mm)	σ_y (mm)
Run group G0					
F 2/3 $E_t^C < 12.5$ GeV	212	-5.7±0.4	5.3±0.3	4.1±0.3	4.9±0.2
B 2/3 $E_t^C < 13.8$ GeV	459	-6.1±0.2	5.3±0.2	3.9±0.2	5.1±0.2
F 2/3 $E_t^C > 12.5$ GeV	2	...	...	...	...
B 2/3 $E_t^C > 13.8$ GeV	10	-2.4±2.0	6.2±1.4	3.4±1.7	5.5±1.2
Run group GA					
F 2/3 $E_t^C < 12.5$ GeV	42	-7.9±0.4	2.8±0.3	3.1±0.6	3.8±0.4
B 2/3 $E_t^C < 13.8$ GeV	56	-7.7±0.4	3.1±0.3	4.3±0.8	5.8±0.5
F 2/3 $E_t^C > 12.5$ GeV	13	-6.9±0.7	2.7±0.5	2.4±0.9	3.1±0.6
B 2/3 $E_t^C > 13.8$ GeV	51	-7.8±0.6	4.0±0.4	5.3±0.8	5.8±0.6
Run group GB					
F 2/3 $E_t^C < 12.5$ GeV	26	-7.5±0.8	4.2±0.6	1.4±0.7	3.5±0.5
B 2/3 $E_t^C < 13.8$ GeV	20	-7.0±1.3	5.8±0.9	1.9±1.2	5.5±0.9
F 2/3 $E_t^C > 12.5$ GeV	7	...	...	...	...
B 2/3 $E_t^C > 13.8$ GeV	41	-6.3±0.7	4.5±0.5	2.2±1.0	6.6±0.7

TABLE 5-13. Vertex position data for F 2/3 and B 2/3 events, hydrogen target data -- Interacting Beam trigger.

	Number of events	$\bar{x}$ (mm)	σ_x (mm)	$\bar{y}$ (mm)	σ_y (mm)
Run group IO					
F 2/3 E_t^C < 6.0 GeV	5328	-5.3±0.06	4.5±0.04	3.4±0.06	4.2±0.04
B 2/3 E_t^C < 6.5 GeV	5307	-5.3±0.06	4.5±0.04	3.4±0.06	4.2±0.04
F 2/3 E_t^C > 6.0 GeV	20	-6.3±0.9	3.9±0.6	4.6±0.8	3.8±0.6
B 2/3 E_t^C > 6.5 GeV	41	-5.2±0.8	4.9±0.5	3.5±0.7	4.2±0.5
Run group IA					
F 2/3 E_t^C < 6.0 GeV	5070	-5.9±0.04	3.0±0.03	2.9±0.05	3.8±0.04
B 2/3 E_t^C < 6.5 GeV	5057	-5.9±0.04	3.0±0.03	2.9±0.05	3.7±0.04
F 2/3 E_t^C > 6.0 GeV	15	-7.1±0.7	2.7±0.5	2.8±1.0	3.7±0.7
B 2/3 E_t^C > 6.5 GeV	28	-6.1±0.6	3.4±0.5	4.1±0.9	4.9±0.7
Run group IB					
F 2/3 E_t^C < 6.0 GeV	11565	-7.5±0.04	4.8±0.03	2.9±0.04	4.7±0.03
B 2/3 E_t^C < 6.5 GeV	11551	-7.5±0.04	4.8±0.03	2.9±0.04	4.7±0.03
F 2/3 E_t^C > 6.0 GeV	56	-8.3±0.6	4.7±0.4	2.3±0.7	5.2±0.5
B 2/3 E_t^C > 6.5 GeV	70	-7.1±0.5	4.4±0.4	1.1±0.6	4.9±0.4
Run group IP					
F 2/3 E_t^C < 6.0 GeV	9478	-5.5±0.06	7.7±0.06	4.2±0.05	4.5±0.03
B 2/3 E_t^C < 6.5 GeV	9462	-5.5±0.06	7.7±0.06	4.2±0.05	4.5±0.03
F 2/3 E_t^C > 6.0 GeV	38	-7.9±1.2	7.5±0.9	5.1±0.9	5.6±0.6
B 2/3 E_t^C > 6.5 GeV	54	-4.8±0.8	7.5±0.5	3.6±0.9	6.3±0.5

TABLE 5-14. Vertex position data for F 2/3 and B 2/3 events, nuclear target data -- Global trigger.

	Number of events	$\bar{x}$ (mm)	σ_x (mm)	$\bar{y}$ (mm)	σ_y (mm)
Run group GA -- Aluminum					
F 2/3 E_t^C < 11.5 GeV	15	-7.8±0.6	2.3±0.4	5.8±1.2	4.5±0.8
B 2/3 E_t^C < 15.4 GeV	261	-7.5±0.2	2.8±0.1	4.7±0.3	4.6±0.2
F 2/3 E_t^C > 11.5 GeV	22	-8.0±0.7	3.4±0.5	2.4±0.8	3.6±0.5
B 2/3 E_t^C > 15.4 GeV	44	-7.3±0.4	2.6±0.3	4.1±0.7	4.4±0.5
Run group GA -- Copper					
F 2/3 E_t^C < 11.5 GeV	34	-8.4±0.5	2.7±0.3	4.6±0.7	4.3±0.5
B 2/3 E_t^C < 15.4 GeV	538	-7.6±0.1	2.6±0.1	4.7±0.2	4.5±0.1
F 2/3 E_t^C > 11.5 GeV	52	-8.0±0.5	3.3±0.3	3.4±0.6	4.3±0.4
B 2/3 E_t^C > 15.4 GeV	69	-7.2±0.3	2.2±0.2	4.2±0.5	4.1±0.4

TABLE 5-15. Vertex position data for Global, A-global, and M 1/2 events, hydrogen data -- Global trigger.

	Number of events	$\bar{x}$ (mm)	σ_x (mm)	$\bar{y}$ (mm)	σ_y (mm)
Run group GA					
Global $E_t^C < 18.7$ GeV	1257	-7.2±0.1	3.0±0.1	4.8±0.1	4.9±0.1
A-global $E_t^C < 17.3$ GeV	158	-7.2±0.4	3.5±0.3	4.6±0.4	4.7±0.3
M 1/2 $E_t^C < 11.5$ GeV	11	-7.8±0.8	2.7±0.6	5.2±1.0	3.2±0.7
Global $E_t^C > 18.7$ GeV	49	-8.2±0.6	4.0±0.4	5.2±0.7	5.8±0.5
A-global $E_t^C > 17.3$ GeV	59	-8.0±0.5	3.7±0.3	4.5±0.8	6.0±0.6
M 1/2 $E_t^C > 11.5$ GeV	26	-7.4±0.4	1.8±0.2	2.5±0.9	4.7±0.7

TABLE 5-16. Mean calorimeter planarity versus calorimeter transverse energy for aluminum data and five apertures.

GLOBAL

ET BIN EDGES (GEV)		MEAN PLANARITY
.0	.5	.484+/- .046
.5	1.0	.717+/- .028
1.0	1.5	.651+/- .026
1.5	2.0	.600+/- .028
2.0	2.5	.555+/- .026
2.5	3.0	.495+/- .024
3.0	3.5	.533+/- .027
3.5	4.0	.544+/- .027
4.0	4.5	.497+/- .025
4.5	5.0	.490+/- .028
5.0	5.5	.453+/- .028
5.5	6.0	.492+/- .032
6.0	6.5	.462+/- .030
6.5	7.0	.423+/- .042
7.0	7.5	.366+/- .027
7.5	8.0	.383+/- .028
8.0	8.5	.423+/- .031
8.5	9.0	.407+/- .030
9.0	9.5	.438+/- .048
9.5	10.0	.428+/- .054
10.0	10.5	.349+/- .032
10.5	11.0	.433+/- .034
11.0	11.5	.372+/- .016
11.5	12.0	.387+/- .018
12.0	12.5	.369+/- .018
12.5	13.0	.384+/- .024
13.0	13.5	.385+/- .011
13.5	14.0	.376+/- .011
14.0	14.5	.385+/- .013
14.5	15.0	.325+/- .014
15.0	15.5	.385+/- .009
15.5	16.0	.377+/- .008
16.0	16.5	.384+/- .009
16.5	17.0	.374+/- .011
17.0	17.5	.366+/- .013
17.5	18.0	.385+/- .014
18.0	18.5	.362+/- .011
18.5	19.0	.380+/- .014
19.0	19.5	.388+/- .016
19.5	20.0	.375+/- .020
20.0	20.5	.388+/- .028
20.5	21.0	.382+/- .031
21.0	21.5	.348+/- .032
21.5	22.0	.426+/- .058
22.0	23.0	.470+/- .053

TABLE 5-16. (Continued)

A-GLOBAL

ET BIN EDGES (GEV)		MEAN PLANARITY
.0	.5	.503+/- .041
.5	1.0	.681+/- .027
1.0	1.5	.623+/- .025
1.5	2.0	.567+/- .025
2.0	2.5	.550+/- .024
2.5	3.0	.508+/- .023
3.0	3.5	.545+/- .029
3.5	4.0	.519+/- .023
4.0	4.5	.461+/- .027
4.5	5.0	.478+/- .032
5.0	5.5	.468+/- .029
5.5	6.0	.424+/- .033
6.0	6.5	.413+/- .034
6.5	7.0	.410+/- .038
7.0	7.5	.417+/- .042
7.5	8.0	.431+/- .029
8.0	8.5	.416+/- .034
8.5	9.0	.370+/- .057
9.0	9.5	.509+/- .064
9.5	10.0	.372+/- .059
10.0	10.5	.395+/- .034
10.5	11.0	.378+/- .037
11.0	11.5	.368+/- .020
11.5	12.0	.383+/- .022
12.0	12.5	.356+/- .029
12.5	13.0	.403+/- .030
13.0	13.5	.373+/- .014
13.5	14.0	.362+/- .015
14.0	14.5	.395+/- .017
14.5	15.0	.394+/- .011
15.0	15.5	.383+/- .011
15.5	16.0	.395+/- .012
16.0	16.5	.392+/- .016
16.5	17.0	.413+/- .016
17.0	17.5	.379+/- .020
17.5	18.0	.384+/- .016
18.0	18.5	.366+/- .021
18.5	19.0	.411+/- .027
19.0	19.5	.365+/- .031
19.5	20.5	.378+/- .024
20.5	21.5	.487+/- .040
21.5	23.5	.455+/- .086

TABLE 5-16. (Continued)

B 2/3

ET BIN EDGES (GEV)		MEAN PLANARITY
.0	.5	.582+/- .027
.5	1.0	.599+/- .020
1.0	1.5	.543+/- .023
1.5	2.0	.567+/- .019
2.0	2.5	.487+/- .021
2.5	3.0	.481+/- .023
3.0	3.5	.503+/- .024
3.5	4.0	.468+/- .039
4.0	4.5	.437+/- .030
4.5	5.0	.457+/- .027
5.0	5.5	.414+/- .051
5.5	6.0	.418+/- .038
6.0	6.5	.357+/- .059
6.5	7.0	.485+/- .048
7.0	7.5	.454+/- .032
7.5	8.0	.333+/- .097
8.0	8.5	.358+/- .070
9.0	9.5	.402+/- .117
9.5	10.0	.468+/- .085
10.0	10.5	.425+/- .040
10.5	11.0	.464+/- .038
11.0	11.5	.436+/- .062
11.5	12.0	.377+/- .086
12.0	12.5	.381+/- .028
12.5	13.0	.364+/- .038
13.0	13.5	.419+/- .065
13.5	14.0	.446+/- .023
14.0	14.5	.415+/- .025
14.5	15.0	.384+/- .029
15.0	15.5	.403+/- .033
15.5	16.0	.356+/- .053
16.0	16.5	.471+/- .038
16.5	17.0	.479+/- .042
17.0	17.5	.290+/- .052
17.5	18.5	.428+/- .042
18.5	19.5	.361+/- .068

TABLE 5-16. (Continued)

F 2/3

ET BIN EDGES (GEV)		MEAN PLANARITY
.0	.5	.603+/- .023
.5	1.0	.589+/- .020
1.0	1.5	.508+/- .018
1.5	2.0	.536+/- .020
2.0	2.5	.506+/- .022
2.5	3.0	.476+/- .023
3.0	3.5	.456+/- .024
3.5	4.0	.433+/- .026
4.0	4.5	.399+/- .028
4.5	5.0	.406+/- .031
5.0	5.5	.440+/- .040
5.5	6.0	.451+/- .043
6.0	6.5	.346+/- .061
6.5	7.0	.397+/- .034
7.0	7.5	.441+/- .073
7.5	8.0	.377+/- .029
8.0	8.5	.354+/- .031
8.5	9.0	.326+/- .047
9.0	9.5	.395+/- .025
9.5	10.0	.369+/- .027
10.0	10.5	.419+/- .028
10.5	11.5	.418+/- .022
11.5	12.5	.509+/- .046
12.5	14.5	.304+/- .055

TABLE 5-16. (Continued)

M 1/2

ET BIN EDGES (GEV)		MEAN PLANARITY
.0	.5	.605+/- .022
.5	1.0	.578+/- .017
1.0	1.5	.504+/- .019
1.5	2.0	.495+/- .020
2.0	2.5	.488+/- .020
2.5	3.0	.472+/- .026
3.0	3.5	.480+/- .028
3.5	4.0	.412+/- .029
4.0	4.5	.381+/- .026
4.5	5.0	.456+/- .041
5.0	5.5	.401+/- .052
5.5	6.0	.395+/- .042
6.0	6.5	.344+/- .056
6.5	7.0	.520+/- .046
7.0	7.5	.331+/- .027
7.5	8.0	.412+/- .034
8.0	8.5	.405+/- .019
8.5	9.0	.390+/- .023
9.0	9.5	.364+/- .030
9.5	10.0	.440+/- .023
10.0	10.5	.425+/- .023
10.5	11.0	.485+/- .028
11.0	11.5	.372+/- .040
11.5	12.0	.382+/- .032
12.0	13.0	.444+/- .037
13.0	14.0	.471+/- .080

TABLE 5-17. Mean calorimeter planarity versus calorimeter transverse energy for copper data and five apertures.

GLOBAL

ET BIN EDGES (GEV)		MEAN PLANARITY
.0	.5	.446+/- .066
.5	1.0	.669+/- .083
1.0	1.5	.591+/- .053
1.5	2.0	.513+/- .041
2.0	2.5	.557+/- .039
2.5	3.0	.484+/- .044
3.0	3.5	.469+/- .041
3.5	4.0	.473+/- .050
4.0	4.5	.529+/- .059
4.5	5.0	.463+/- .056
5.0	5.5	.456+/- .064
5.5	6.0	.532+/- .072
6.0	6.5	.387+/- .048
6.5	7.0	.325+/- .088
7.0	7.5	.469+/- .064
7.5	8.0	.350+/- .061
8.0	8.5	.419+/- .058
9.5	10.0	.343+/- .049
15.0	15.5	.370+/- .008
15.5	16.0	.363+/- .007
16.0	16.5	.377+/- .007
16.5	17.0	.364+/- .008
17.0	17.5	.360+/- .009
17.5	18.0	.377+/- .011
18.0	18.5	.355+/- .016
18.5	19.0	.384+/- .017
19.0	19.5	.396+/- .023
19.5	20.5	.361+/- .018
20.5	21.5	.375+/- .043
21.5	23.5	.431+/- .044

TABLE 5-17. (Continued)

A-GLOBAL

ET BIN EDGES (GEV)		MEAN PLANARITY
.0	.5	.473+/- .062
.5	1.0	.613+/- .082
1.0	1.5	.558+/- .041
1.5	2.0	.575+/- .046
2.0	2.5	.474+/- .038
2.5	3.0	.500+/- .034
3.0	3.5	.484+/- .059
3.5	4.0	.497+/- .049
4.0	4.5	.471+/- .042
4.5	5.0	.290+/- .054
5.0	5.5	.419+/- .052
5.5	6.0	.489+/- .062
6.5	7.0	.413+/- .067
7.0	7.5	.393+/- .068
7.5	8.0	.461+/- .050
8.5	9.0	.371+/- .048
14.5	15.0	.366+/- .010
15.0	15.5	.371+/- .009
15.5	16.0	.384+/- .009
16.0	16.5	.360+/- .010
16.5	17.0	.366+/- .013
17.0	17.5	.385+/- .018
17.5	18.0	.396+/- .023
18.0	19.0	.390+/- .018
19.0	20.0	.379+/- .030
20.0	22.0	.408+/- .044

TABLE 5-17. (Continued)

B 2/3

ET BIN EDGES (GEV)		MEAN PLANARITY
.0	.5	.480+/- .049
.5	1.0	.552+/- .047
1.0	1.5	.588+/- .031
1.5	2.0	.454+/- .031
2.0	2.5	.517+/- .041
2.5	3.0	.427+/- .050
3.0	3.5	.429+/- .046
3.5	4.0	.416+/- .052
4.0	4.5	.498+/- .035
4.5	5.0	.394+/- .061
5.0	5.5	.446+/- .078
5.5	6.0	.285+/- .063
6.0	6.5	.350+/- .055
13.5	14.0	.408+/- .019
14.0	14.5	.363+/- .016
14.5	15.5	.393+/- .017
15.5	16.5	.384+/- .029
16.5	18.5	.476+/- .050

F 2/3

ET BIN EDGES (GEV)		MEAN PLANARITY
.0	.5	.535+/- .041
.5	1.0	.521+/- .033
1.0	1.5	.537+/- .035
1.5	2.0	.465+/- .035
2.0	2.5	.443+/- .041
2.5	3.0	.442+/- .041
3.0	3.5	.433+/- .054
3.5	4.0	.347+/- .039
4.0	4.5	.401+/- .050
4.5	5.0	.472+/- .058
5.0	5.5	.442+/- .044
10.0	11.0	.381+/- .015
11.0	12.0	.427+/- .022
12.0	14.0	.447+/- .042

TABLE 5-17. (Continued)

M 1/2

ET BIN EDGES (GEV)		MEAN PLANARITY
.0	.5	.530+/- .040
.5	1.0	.504+/- .029
1.0	1.5	.554+/- .032
1.5	2.0	.458+/- .033
2.0	2.5	.436+/- .052
2.5	3.0	.377+/- .044
3.0	3.5	.472+/- .044
3.5	4.0	.429+/- .032
4.0	4.5	.353+/- .048
4.5	5.0	.470+/- .058
5.0	5.5	.319+/- .055
9.5	10.5	.397+/- .013
10.5	11.5	.387+/- .016
11.5	13.5	.407+/- .025

TABLE 5-18. Mean calorimeter planarity versus calorimeter transverse energy for lead data and five apertures.

GLOBAL

ET BIN EDGES (GEV)		MEAN PLANARITY
.0	.5	.433+/- .057
.5	1.0	.679+/- .037
1.0	1.5	.611+/- .042
1.5	2.0	.592+/- .034
2.0	2.5	.545+/- .039
2.5	3.0	.494+/- .045
3.0	3.5	.526+/- .039
3.5	4.0	.499+/- .035
4.0	4.5	.425+/- .048
4.5	5.0	.456+/- .040
5.0	5.5	.434+/- .036
5.5	6.0	.393+/- .047
6.0	6.5	.437+/- .052
6.5	7.0	.383+/- .055
7.0	7.5	.487+/- .040
7.5	8.0	.465+/- .036
8.0	8.5	.367+/- .045
8.5	9.0	.471+/- .045
9.0	9.5	.407+/- .063
9.5	10.0	.331+/- .052
10.0	10.5	.370+/- .041
10.5	11.0	.425+/- .050
11.0	11.5	.382+/- .016
11.5	12.0	.414+/- .020
12.0	12.5	.432+/- .020
12.5	13.0	.380+/- .024
13.0	13.5	.379+/- .010
13.5	14.0	.386+/- .011
14.0	14.5	.383+/- .013
14.5	15.0	.380+/- .014
15.0	15.5	.370+/- .011
15.5	16.0	.385+/- .011
16.0	16.5	.383+/- .009
16.5	17.0	.358+/- .010
17.0	17.5	.380+/- .009
17.5	18.0	.384+/- .011
18.0	18.5	.380+/- .009
18.5	19.0	.382+/- .012
19.0	19.5	.366+/- .014
19.5	20.0	.395+/- .018
20.0	20.5	.365+/- .020
20.5	21.5	.397+/- .021
21.5	22.5	.366+/- .031
22.5	24.5	.298+/- .069

TABLE 5-18. (Continued)

A-GLOBAL

ET BIN EDGES (GEV)		MEAN PLANARITY
.0	.5	.453+/- .052
.5	1.0	.646+/- .038
1.0	1.5	.631+/- .040
1.5	2.0	.535+/- .032
2.0	2.5	.588+/- .040
2.5	3.0	.517+/- .040
3.0	3.5	.486+/- .036
3.5	4.0	.470+/- .031
4.0	4.5	.390+/- .037
4.5	5.0	.439+/- .048
5.0	5.5	.404+/- .035
5.5	6.0	.488+/- .040
6.0	6.5	.341+/- .050
6.5	7.0	.496+/- .055
7.0	7.5	.347+/- .054
7.5	8.0	.421+/- .044
8.0	8.5	.389+/- .074
8.5	9.0	.465+/- .056
9.0	9.5	.263+/- .049
9.5	10.0	.309+/- .072
10.0	10.5	.417+/- .037
10.5	11.0	.451+/- .047
11.0	11.5	.401+/- .023
11.5	12.0	.389+/- .020
12.0	12.5	.403+/- .028
12.5	13.0	.476+/- .031
13.0	13.5	.391+/- .013
13.5	14.0	.384+/- .015
14.0	14.5	.369+/- .016
14.5	15.0	.384+/- .014
15.0	15.5	.394+/- .013
15.5	16.0	.375+/- .012
16.0	16.5	.385+/- .013
16.5	17.0	.402+/- .013
17.0	17.5	.367+/- .014
17.5	18.0	.378+/- .012
18.0	18.5	.365+/- .014
18.5	19.0	.371+/- .023
19.0	20.0	.387+/- .018
20.0	21.0	.372+/- .029
21.0	23.0	.348+/- .053

TABLE 5-18. (Continued)

B 2/3

ET BIN EDGES (GEV)		MEAN PLANARITY
.0	.5	.521+/- .038
.5	1.0	.601+/- .029
1.0	1.5	.562+/- .035
1.5	2.0	.526+/- .027
2.0	2.5	.494+/- .029
2.5	3.0	.503+/- .035
3.0	3.5	.419+/- .037
3.5	4.0	.409+/- .039
4.0	4.5	.375+/- .039
4.5	5.0	.485+/- .045
5.0	5.5	.394+/- .043
5.5	6.0	.402+/- .086
6.0	6.5	.261+/- .054
6.5	7.0	.552+/- .079
7.0	7.5	.406+/- .083
7.5	8.0	.454+/- .076
8.0	8.5	.328+/- .078
9.5	10.0	.343+/- .058
10.0	10.5	.451+/- .031
10.5	11.0	.402+/- .038
11.0	11.5	.359+/- .047
11.5	12.0	.349+/- .040
12.0	12.5	.386+/- .022
12.5	13.0	.407+/- .028
13.0	13.5	.423+/- .039
13.5	14.0	.342+/- .024
14.0	14.5	.420+/- .022
14.5	15.0	.373+/- .021
15.0	15.5	.388+/- .026
15.5	16.0	.366+/- .030
16.0	16.5	.385+/- .025
16.5	17.5	.385+/- .029
17.5	18.5	.383+/- .031
18.5	20.5	.385+/- .066

TABLE 5-18. (Continued)

F 2/3

ET BIN EDGES (GEV)		MEAN PLANARITY
.0	.5	.551+/- .034
.5	1.0	.535+/- .027
1.0	1.5	.540+/- .029
1.5	2.0	.501+/- .034
2.0	2.5	.510+/- .029
2.5	3.0	.413+/- .031
3.0	3.5	.438+/- .031
3.5	4.0	.438+/- .043
4.0	4.5	.388+/- .053
4.5	5.0	.465+/- .031
5.0	5.5	.339+/- .043
5.5	6.0	.271+/- .046
6.5	7.0	.398+/- .046
7.0	7.5	.371+/- .049
7.5	8.0	.410+/- .033
8.0	8.5	.469+/- .029
8.5	9.0	.392+/- .041
9.0	9.5	.339+/- .025
9.5	10.0	.355+/- .028
10.0	10.5	.369+/- .040
10.5	11.5	.398+/- .024
11.5	12.5	.466+/- .048
12.5	14.5	.513+/- .046

TABLE 5-18. (Continued)

M 1/2

ET BIN EDGES (GEV)		MEAN PLANARITY
.0	.5	.564+/- .030
.5	1.0	.523+/- .025
1.0	1.5	.569+/- .027
1.5	2.0	.501+/- .034
2.0	2.5	.405+/- .032
2.5	3.0	.419+/- .026
3.0	3.5	.436+/- .048
3.5	4.0	.393+/- .048
4.0	4.5	.419+/- .039
4.5	5.0	.399+/- .049
5.0	5.5	.405+/- .051
5.5	6.0	.328+/- .061
6.0	6.5	.400+/- .052
6.5	7.0	.469+/- .043
7.0	7.5	.431+/- .025
7.5	8.0	.347+/- .024
8.0	8.5	.388+/- .017
8.5	9.0	.403+/- .020
9.0	9.5	.403+/- .027
9.5	10.0	.410+/- .027
10.0	10.5	.384+/- .025
10.5	11.0	.373+/- .035
11.0	11.5	.429+/- .029
11.5	12.5	.387+/- .025
12.5	13.5	.412+/- .048
13.5	15.5	.410+/- .054

TABLE 5-19. Fraction of events with high calorimeter planarity (> 0.7) versus calorimeter transverse energy for aluminum data and five apertures.

GLOBAL

ET BIN EDGES (GEV)		FRACTION OF EVENTS WITH P(CALR) > .7
.0	.5	.462 +/- .063
.5	1.0	.588 +/- .070
1.0	1.5	.494 +/- .055
1.5	2.0	.420 +/- .056
2.0	2.5	.294 +/- .050
2.5	3.0	.209 +/- .044
3.0	3.5	.268 +/- .054
3.5	4.0	.241 +/- .058
4.0	4.5	.070 +/- .047
4.5	5.0	.122 +/- .051
5.0	5.5	.143 +/- .050
5.5	6.0	.105 +/- .057
6.0	6.5	.079 +/- .053
6.5	7.0	.115 +/- .075
8.0	8.5	.071 +/- .068
8.5	9.0	.079 +/- .053
9.5	10.0	.118 +/- .107
10.5	11.0	.063 +/- .060
11.0	11.5	.031 +/- .018
11.5	12.0	.041 +/- .023
12.0	12.5	.043 +/- .024
12.5	13.0	.082 +/- .039
13.0	13.5	.060 +/- .015
13.5	14.0	.044 +/- .014
14.0	14.5	.053 +/- .016
14.5	15.0	.015 +/- .015
15.0	15.5	.058 +/- .012
15.5	16.0	.049 +/- .010
16.0	16.5	.036 +/- .010
16.5	17.0	.036 +/- .012
17.0	17.5	.047 +/- .015
17.5	18.0	.049 +/- .018
18.0	18.5	.018 +/- .010
18.5	19.0	.043 +/- .017
19.0	19.5	.065 +/- .026
19.5	20.0	.056 +/- .027
20.0	20.5	.067 +/- .045
20.5	21.0	.053 +/- .051

TABLE 5-19. (Continued)

A-GLOBAL

ET BIN EDGES (GEV)		FRACTION OF EVENTS WITH P(CALR) > .7
.0	.5	.434 +/- .058
.5	1.0	.559 +/- .061
1.0	1.5	.469 +/- .051
1.5	2.0	.356 +/- .047
2.0	2.5	.264 +/- .047
2.5	3.0	.186 +/- .043
3.0	3.5	.274 +/- .058
3.5	4.0	.131 +/- .046
4.0	4.5	.091 +/- .050
4.5	5.0	.160 +/- .055
5.0	5.5	.128 +/- .053
6.0	6.5	.097 +/- .064
7.5	8.0	.083 +/- .056
9.0	9.5	.167 +/- .146
11.0	11.5	.133 +/- .120
11.5	12.0	.076 +/- .036
12.0	12.5	.102 +/- .048
12.5	13.0	.059 +/- .056
13.5	14.0	.039 +/- .019
14.0	14.5	.040 +/- .022
14.5	15.0	.086 +/- .036
15.5	16.0	.030 +/- .017
16.0	16.5	.050 +/- .024
16.5	17.0	.080 +/- .027
17.0	17.5	.060 +/- .029
17.5	18.0	.038 +/- .037
18.5	19.0	.105 +/- .044
19.0	19.5	.071 +/- .048
19.5	20.5	.042 +/- .040

TABLE 5-19. (Continued)

B 2/3

ET BIN EDGES (GEV)		FRACTION OF EVENTS WITH P(CALR) > .7
.0	.5	.486 +/- .043
.5	1.0	.397 +/- .044
1.0	1.5	.349 +/- .042
1.5	2.0	.264 +/- .041
2.0	2.5	.132 +/- .037
2.5	3.0	.123 +/- .038
3.0	3.5	.130 +/- .043
3.5	4.0	.237 +/- .072
4.0	4.5	.102 +/- .048
5.5	6.0	.111 +/- .102
6.5	7.0	.077 +/- .073
9.5	10.0	.071 +/- .048
10.0	10.5	.080 +/- .075
11.0	11.5	.057 +/- .028
11.5	12.0	.063 +/- .035
13.0	13.5	.040 +/- .023
13.5	14.0	.067 +/- .029
14.0	14.5	.085 +/- .040
14.5	15.0	.043 +/- .041
15.0	15.5	.059 +/- .040
15.5	16.0	.081 +/- .054
16.0	16.5	.148 +/- .078
16.5	17.0	.143 +/- .128

F 2/3

ET BIN EDGES (GEV)		FRACTION OF EVENTS WITH P(CALR) > .7
.0	.5	.497 +/- .039
.5	1.0	.399 +/- .039
1.0	1.5	.216 +/- .034
1.5	2.0	.218 +/- .039
2.0	2.5	.149 +/- .040
2.5	3.0	.205 +/- .044
3.0	3.5	.039 +/- .038
3.5	4.0	.123 +/- .047
10.0	10.5	.211 +/- .106
10.5	11.5	.176 +/- .130
11.5	12.5	.209 +/- .128

TABLE 5-19. (Continued)

M 1/2

ET BIN EDGES (GEV)		FRACTION OF EVENTS WITH P(CALR) > .7
.0	.5	.497 +/- .036
.5	1.0	.332 +/- .035
1.0	1.5	.233 +/- .034
1.5	2.0	.190 +/- .036
2.0	2.5	.110 +/- .034
2.5	3.0	.143 +/- .050
3.0	3.5	.121 +/- .046
6.5	7.0	.429 +/- .224
10.5	11.0	.429 +/- .224
11.5	12.0	.167 +/- .146
13.0	14.0	.250 +/- .148

TABLE 5-20. Fraction of events with high calorimeter planarity (> 0.7) versus calorimeter transverse energy for copper data and five apertures.

GLOBAL

ET BIN EDGES (GEV)		FRACTION OF EVENTS WITH P(CALR) > .7
.0	.5	.387 +/- .091
.5	1.0	.583 +/- .157
1.0	1.5	.348 +/- .105
1.5	2.0	.294 +/- .082
2.0	2.5	.308 +/- .096
2.5	3.0	.160 +/- .083
3.5	4.0	.263 +/- .111
4.0	4.5	.154 +/- .137
4.5	5.0	.176 +/- .110
5.0	5.5	.250 +/- .148
5.5	6.0	.222 +/- .187
15.0	15.5	.033 +/- .008
15.5	16.0	.024 +/- .006
16.0	16.5	.046 +/- .008
16.5	17.0	.023 +/- .008
17.0	17.5	.027 +/- .009
17.5	18.0	.023 +/- .011
18.0	18.5	.040 +/- .019
18.5	19.0	.064 +/- .025
19.0	19.5	.066 +/- .036
19.5	20.5	.045 +/- .025
21.5	23.5	.105 +/- .097

TABLE 5-20. (Continued)

A-GLOBAL

ET BIN EDGES (GEV)		FRACTION OF EVENTS WITH P(CALR) > .7
.0	.5	.412 +/- .087
.5	1.0	.462 +/- .150
1.0	1.5	.351 +/- .081
1.5	2.0	.320 +/- .099
2.0	2.5	.200 +/- .079
2.5	3.0	.100 +/- .066
3.0	3.5	.250 +/- .148
3.5	4.0	.261 +/- .099
5.0	5.5	.150 +/- .096
5.5	6.0	.154 +/- .137
15.5	16.0	.052 +/- .018
16.0	16.5	.021 +/- .012
16.5	17.0	.023 +/- .013
17.0	17.5	.065 +/- .026
17.5	18.0	.085 +/- .036
18.0	19.0	.069 +/- .027
19.0	20.0	.054 +/- .052
20.0	22.0	.095 +/- .089

B 2/3

ET BIN EDGES (GEV)		FRACTION OF EVENTS WITH P(CALR) > .7
.0	.5	.354 +/- .071
.5	1.0	.424 +/- .089
1.0	1.5	.267 +/- .068
1.5	2.0	.167 +/- .062
2.0	2.5	.226 +/- .080
3.0	3.5	.190 +/- .097
3.5	4.0	.167 +/- .105
4.0	4.5	.111 +/- .102
13.0	13.5	.051 +/- .018
13.5	14.0	.042 +/- .018
14.0	14.5	.037 +/- .021
14.5	15.5	.043 +/- .021
15.5	16.5	.095 +/- .052
16.5	18.5	.182 +/- .093

TABLE 5-20. (Continued)

F 2/3

ET BIN EDGES (GEV)		FRACTION OF EVENTS WITH P(CALR) > .7
.0	.5	.410 +/- .064
.5	1.0	.277 +/- .067
1.0	1.5	.244 +/- .070
1.5	2.0	.158 +/- .064
2.0	2.5	.156 +/- .071
2.5	3.0	.107 +/- .070
3.0	3.5	.125 +/- .114
11.0	12.0	.075 +/- .037
12.0	14.0	.130 +/- .084

M 1/2

ET BIN EDGES (GEV)		FRACTION OF EVENTS WITH P(CALR) > .7
.0	.5	.415 +/- .062
.5	1.0	.179 +/- .054
1.0	1.5	.273 +/- .070
1.5	2.0	.159 +/- .059
2.0	2.5	.250 +/- .095
2.5	3.0	.087 +/- .081
3.0	3.5	.105 +/- .097
11.5	13.5	.063 +/- .035

TABLE 5-21. Fraction of events with high calorimeter planarity (> 0.7) versus calorimeter transverse energy for lead data and five apertures.

GLOBAL

ET BIN EDGES (GEV)		FRACTION OF EVENTS WITH P(CALR) > .7
.0	.5	.533 +/- .076
.5	1.0	.533 +/- .094
1.0	1.5	.381 +/- .077
1.5	2.0	.298 +/- .069
2.0	2.5	.325 +/- .077
2.5	3.0	.143 +/- .092
3.0	3.5	.167 +/- .075
3.5	4.0	.226 +/- .080
4.5	5.0	.095 +/- .089
5.5	6.0	.100 +/- .093
6.5	7.0	.133 +/- .120
7.0	7.5	.143 +/- .075
7.5	8.0	.107 +/- .070
9.0	9.5	.182 +/- .158
10.0	10.5	.095 +/- .089
10.5	11.0	.150 +/- .096
11.0	11.5	.018 +/- .018
11.5	12.0	.094 +/- .031
12.0	12.5	.117 +/- .035
12.5	13.0	.037 +/- .036
13.0	13.5	.044 +/- .012
13.5	14.0	.055 +/- .013
14.0	14.5	.060 +/- .016
14.5	15.0	.045 +/- .018
15.0	15.5	.040 +/- .013
15.5	16.0	.052 +/- .013
16.0	16.5	.048 +/- .011
16.5	17.0	.033 +/- .011
17.0	17.5	.034 +/- .011
17.5	18.0	.041 +/- .014
18.0	18.5	.029 +/- .009
18.5	19.0	.068 +/- .018
19.0	19.5	.025 +/- .014
19.5	20.0	.084 +/- .027
20.0	20.5	.030 +/- .029
20.5	21.5	.042 +/- .029

TABLE 5-21. (Continued)

A-GLOBAL

ET BIN EDGES (GEV)		FRACTION OF EVENTS WITH P(CALR) > .7
.0	.5	.500 +/- .072
.5	1.0	.500 +/- .086
1.0	1.5	.409 +/- .076
1.5	2.0	.226 +/- .060
2.0	2.5	.378 +/- .082
2.5	3.0	.200 +/- .079
3.0	3.5	.103 +/- .068
3.5	4.0	.107 +/- .070
4.5	5.0	.174 +/- .090
5.5	6.0	.118 +/- .107
6.5	7.0	.214 +/- .130
8.5	9.0	.250 +/- .122
11.5	12.0	.026 +/- .026
12.0	12.5	.039 +/- .038
12.5	13.0	.192 +/- .057
13.0	13.5	.094 +/- .062
13.5	14.0	.064 +/- .021
14.0	14.5	.050 +/- .022
14.5	15.0	.055 +/- .024
15.0	15.5	.106 +/- .050
15.5	16.0	.064 +/- .027
16.0	16.5	.040 +/- .019
16.5	17.0	.061 +/- .022
17.0	17.5	.036 +/- .025
17.5	18.0	.031 +/- .022
18.0	18.5	.045 +/- .031
18.5	19.0	.050 +/- .028
19.0	20.0	.062 +/- .027

TABLE 5-21. (Continued)

B 2/3

ET BIN EDGES (GEV)		FRACTION OF EVENTS WITH P(CALR) > .7
.0	.5	.506 +/- .056
.5	1.0	.367 +/- .063
1.0	1.5	.310 +/- .062
1.5	2.0	.160 +/- .055
2.0	2.5	.114 +/- .053
2.5	3.0	.214 +/- .084
3.0	3.5	.097 +/- .064
3.5	4.0	.074 +/- .070
4.5	5.0	.238 +/- .102
7.5	8.0	.222 +/- .187
9.5	10.0	.040 +/- .039
10.0	10.5	.143 +/- .059
10.5	11.0	.091 +/- .060
11.0	11.5	.033 +/- .019
11.5	12.0	.080 +/- .029
12.0	12.5	.085 +/- .033
12.5	13.0	.064 +/- .043
13.0	13.5	.057 +/- .027
13.5	14.0	.034 +/- .019
14.0	14.5	.071 +/- .034
15.0	15.5	.044 +/- .025
15.5	16.0	.063 +/- .030
16.0	16.5	.043 +/- .041
16.5	17.5	.098 +/- .053

F 2/3

ET BIN EDGES (GEV)		FRACTION OF EVENTS WITH P(CALR) > .7
.0	.5	.468 +/- .052
.5	1.0	.277 +/- .050
1.0	1.5	.266 +/- .057
1.5	2.0	.235 +/- .062
2.0	2.5	.190 +/- .064
3.0	3.5	.091 +/- .060
3.5	4.0	.125 +/- .081
8.5	9.0	.158 +/- .100
9.5	10.0	.054 +/- .052
10.5	11.5	.037 +/- .037
11.5	12.5	.327 +/- .111
12.5	14.5	.174 +/- .090

TABLE 5-21. (Continued)

M 1/2

ET BIN EDGES (GEV)		FRACTION OF EVENTS WITH P(CALR) > .7
.0	.5	.459 +/- .048
.5	1.0	.241 +/- .047
1.0	1.5	.279 +/- .056
1.5	2.0	.231 +/- .071
2.0	2.5	.071 +/- .048
2.5	3.0	.098 +/- .046
3.0	3.5	.150 +/- .096
3.5	4.0	.111 +/- .102
7.0	7.5	.500 +/- .354
8.0	8.5	.182 +/- .093
9.5	10.0	.056 +/- .053
11.0	11.5	.105 +/- .097
11.5	12.5	.115 +/- .075
12.5	13.5	.133 +/- .099

TABLE 5-22. Mean (Global) E_t^C/E^C for nuclear target data high transverse energy events.

	Global	A-global	B 2/3	F 2/3	M 1/2
E_t^C Threshold (GeV)	16.0	16.5	13.5	11.5	11.5
Mean E_t^C/E^C (10^{-3})					
Aluminum	67.6±0.2	70.9±0.3	75.8±0.4	61.1±1.1	68.6±0.7
Copper	67.6±0.2	70.5±0.3	75.1±0.3	59.6±0.7	68.9±0.7
Lead	68.9±0.2	71.5±0.3	75.8±0.3	61.8±0.9	68.3±0.8

References for Chapter V

1. G. Hanson *et al.*, Phys. Rev. Lett. **35**, 1609 (1975).
2. E. Farhi, Phys. Rev. Lett. **39**, 1587 (1977).
3. C. DeMarzo *et al.*, Phys. Lett. **112B**, 173 (1982).
4. F. Lopez, Ph.D. dissertation, University of Illinois at Chicago, 1983 (unpublished).
5. S. Brandt and H. D. Dahmen, Z. Phys. **C1**, 61 (1979).
6. T. Åkesson *et al.*, Phys. Lett. **118B**, 185 (1982).
7. B. C. Brown *et al.*, Phys. Rev. D **29**, 1895 (1984).
8. B. Brown *et al.*, Phys. Rev. Lett. **49**, 711 (1982).

CHAPTER VI

DISCUSSION AND CONCLUSIONS

In this chapter I present a summary of my findings. Comparisons to theory and to results from other experiments are made, and I present a simple phenomenological model that reflects some of the qualitative features of the nuclear target cross section data.

6.1. Proton-proton summary

I have studied cross sections and event structure as functions of the transverse energy (E_t) measured in each of five full-azimuth apertures of a large segmented calorimeter; these apertures, in order of decreasing geometric acceptance, are labelled Global, A-global, B 2/3, F 2/3, and M 1/2. The B 2/3 and F 2/3 apertures cover regions of acceptance which are nearly symmetric with respect to reflection in the transverse plane in the proton-proton center of mass.

The transverse energy spectra from our proton-proton data are generally in disagreement with the predictions of two models of high transverse energy production: an isotropic, limited-p_t model (LPS) and a hard-scattering model based on quantum chromodynamics incorporating noncolinear gluon bremsstrahlung (QCD/brem). In the Global and A-global apertures at transverse energies larger than 10 GeV the experimental data lie an order of magnitude or more above the prediction of either of the models (which in fact give surprisingly similar predictions for the cross sections in much of their area of overlap). Agreement is better in the smaller apertures, with the experimental data above the QCD/brem model predictions by about a factor of 5 out to the largest values of transverse energy in M 1/2. The LPS model does slightly worse at moderate transverse energies; it becomes increasingly difficult to get events at higher transverse energy from the LPS model, because to do so it is necessary to generate enormous multiplicities (charged particle multiplicities greater than about 40).

However, the spectra presented in Chapter IV have not been corrected for a background apparently present in the experiment but not simulated in the Monte Carlos. Evidence for this background comes from a comparison of events with high transverse energy in the B 2/3 aperture ("B 2/3 events") and events with high transverse energy in the F 2/3 aperture ("F 2/3 events"), and includes: an enhancement of the cross section for high E_t in the B 2/3 aperture as compared to that for F 2/3; differences in the event structure of F 2/3 and B 2/3 events; and differences in the vertex positions for F 2/3 and B 2/3 events. Of events with very high transverse energy in the B 2/3 aperture I have estimated 70% to 90% are due to the background. Vertex position studies suggest a smaller but still significant fraction of the events with high transverse energy in the Global, A-global, and M 1/2 apertures are also attributable to background. This background has low planarity (I have estimated 5% has planarity > 0.7) and is asymmetric with respect to reflection in the x-y plane in the nominal proton-proton center of mass. It does not seem to significantly affect the F 2/3 data.

A plausible model is that the background consists of events with two (or more) scatters, the first giving rise to a moderate-p_t (about 6 GeV) particle which then initiates a moderate-E_t collison. An artificial boost of about 3 GeV would suffice to explain the features seen.

Event structure has been studied using the planarity measure, which quantifies the extent to which the final state particles are confined to a plane containing the direction of the incoming particle. For back-to-back, narrow jets planarity is large (near 1), whereas for isotropic, large-multiplicity production mechanisms the planarity of the final state is small (near 0). While the LPS and QCD/brem models give similar results for the cross sections, they differ completely in event structure. For LPS events mean planarity drops monotonically with transverse energy in all apertures, as does the fraction of events that are planar; for QCD/brem events both quantities go through minima at moderate values of transverse energy before climbing to very high values at high E_t. In contrast with both models, both planarity and the fraction of events which are planar stay nearly constant with Global or A-global transverse energy in the proton-proton data. A slight rise in planar structure is present as E_t in the M 1/2 aperture increases and cannot be ruled out for high transverse energy in B 2/3, but as a function of E_t in the F 2/3 aperture, both mean planarity and the size of the high-planarity component grow nearly as fast as in the QCD/brem model's predictions. This forward-backward asymmetry is again attributable to the asymmetric background, and I conclude that planar structure would be clearly visible as well in events with high transverse energy in B 2/3 and M 1/2 if the background were removed.

It should be emphasized that the increase in planarity observed for F 2/3 events is not a consequence of energy-momentum conservation; a full azimuth transverse energy trigger with limited pseudorapidity width does not "cut on the answer" by having an inherent bias in favor of planar events. If it did, an increase in planarity would be seen in the LPS model. The correlation between high planarity and high E_t in the F 2/3 aperture is of dynamical origin. These planar events are very similar to the jet events generated by the QCD/brem model.

6.2. Proton-nucleus summary

The cross sections for production of high E_t^C in each of the five apertures I have studied grow with nucleon number A faster than A. The cross sections (excluding those from proton-proton collisions) may be parametrized as proportional to A^{α}, with α increasing to values of about 1.35 as transverse energy in any of the five apertures except F 2/3 increases. For $E_t^C > 8.5$ GeV in the F 2/3 aperture, α is much smaller; in fact, the data are consistent with $\alpha = 1.0$, though the values measured are systematically greater than 1.0 and the errors could accomodate $\alpha = 1.2$ almost as well.

There is reason to believe the asymmetric background seen in hydrogen target events makes no significant contribution to the nuclear target events. Nevertheless, no strong evidence is seen for any emerging planar structure for nuclear target events in any aperture, although a slight rise in planarity for high transverse energy in F 2/3 is not ruled out.

6.3. Comparison with other experiments

First results from an experiment with a full-azimuth transverse energy trigger, with pseudorapidity width $\Delta\eta = 1.55$, came from the NA5 collaboration.[1] They used 300 GeV/c pion and proton beams and reported no predominant jet structure at high transverse energy.

This surprising result was confirmed for proton beams at 400 GeV/c by E557[2] and another Fermilab experiment, E609;[3] the latter used a full-azimuth trigger with $30° < \theta^* < 120°$. E557 reported also on event structure in events selected with several restricted-azimuth triggers;[2,4,5] for pp collisions with high transverse energy in such apertures, evidence of jet structure was found. E609 has reported large planarity for events selected by requiring high transverse energy in any two calorimeter towers. E557 studied a similar trigger and obtained similar results; however, a planarity increase as a function of transverse energy was also observed in the LPS model,[5] whose production mechanism is isotropic. It therefore appears that this is not an unbiased trigger. Like NA5, E609 has published only data from hydrogen target events.

Data at higher energies come from experiments at the CERN Intersecting Storage Rings and SPS collider. The AFS collaboration has reported evidence of jets in proton-proton collisions at energies of 45 GeV and 63 GeV in the center of mass using a limited-azimuth transverse energy trigger,[6] matching closely the expectations from the "ISAJET" Monte Carlo model as a function of beam energy. The UA1[7] and UA2[8] collaborations used proton-antiproton collisions at a center of mass energy of 540 GeV. The former used an online trigger on high transverse energy in a full-azimuth, $\Delta\eta = 6.0$ aperture for their early data, but found jet stucture predominating only after applying a requirement of high E_t^C in a full-azimuth, $\Delta\eta = 3.0$ aperture during analysis. Later data were taken with a $\Delta\phi = \pi$, $\Delta\eta = 0.75$ E_t^C trigger. UA2 used a $\Delta\phi = 300°$, $\Delta\eta = 2.0$ transverse energy trigger. Both experiments found copious jet production with these requirements.

Fermilab experiment E260 studied the nucleon number dependence of E_t^C production in a limited-$\Delta\phi$ aperture.[9] Their values of the parameter "α" are not directly comparable to ours, however, because theirs were based on a comparison of aluminum and hydrogen data. The cross sections for hydrogen in fact fall below the A^α parametrization, so the values of "α" thereby obtained are much higher than those computed from comparison of heavy targets. Our data indicate that the effect, claimed in Ref. 9, that α for high-E_t^C production is much larger than the α for high-p_t single particle production may be real, but is certainly less strong than the aluminum-hydrogen comparison suggests.

6.4. Comparison with theory

As noted above, neither the LPS model nor the QCD/brem model agrees with the observed cross sections or event structure in all apertures, though the presence of a background complicates the comparison. Note that there are many tunable parameters in the QCD/brem model; perhaps better agreement could be forced. However, we have used only the parameter values suggested by the authors, who tuned them to the NA5 data.

Akesson and Bengtsson[10] discussed high-E_t production in pp and $p\bar{p}$ collisions using a simple phenomenological model with two components: a soft, high-multiplicity part and a hard constituent scattering part. They predicted that the latter will begin to dominate at a crossover transverse energy $E_t = 12\ \Delta\eta\ \Delta\phi/2\pi$. For our Global and A-global apertures this crossover is at about 18 and 16 GeV, respectively. This is near the end of our statistics, but the data do not seem consistent with a significant increase in planarity at these values. For the B 2/3 aperture our data go well beyond the crossover point, $E_t = 10$ GeV, with no sign of a planarity rise. However, there is a planarity rise starting at about 12 GeV in the F 2/3 aperture; this compares favorably with the crossover transverse energy computed from the above formula, 11 GeV. The corresponding planar structure in B 2/3 appears to be masked by the background. For the M 1/2 aperture the predicted crossover is at 9 GeV; there appears to be an increase in the high-planarity component at this point, although the errors are large.

The explanation of the fact that cross sections for high-p_t single particle production increase with A faster than A which has found the most favor is that it is due to multiple scattering of a beam parton from partons in two or more target nucleons. The observation[9] that this effect is stronger for high-E_t production requires one to invoke an additional mechanism. Multiple jets, caused by scattering of more than one beam parton from separate target partons, in combination with multiple scattering, have been used as the basis of an explanation for the high-E_t data.[11,12]

A consequence of such theories is that α should increase at fixed transverse energy as the aperture acceptance $\Delta\omega$ increases. Treleani and Wilk[12] compute this effect for restricted-$\Delta\phi$ calorimeters. In contrast, our data show that for the M 1/2 aperture ($\Delta\eta = 0.73$) α reaches a value of 1.3 at $E_t^C \geq 8$ GeV, while for the Global aperture ($\Delta\eta = 1.49$) the maximum value of α, 1.4, is only slightly larger and occurs at a much larger transverse energy, $E_t^C \geq 17$ GeV.

If either multiple scattering or collective effects within the nucleus are important, they should lead to an enhancement in the rate of production of transverse energy in the backward hemisphere as compared to the forward hemisphere rate. This is confirmed by a comparison of our B 2/3 and F 2/3 cross sections, as well as by measurements of the ratio of calorimeter transverse energy to calorimeter energy. Also, with these mechanisms, one expects the anomalous nuclear enhancement to be smaller in the forward hemisphere, and in fact for the F 2/3 aperture the value of α is consistent with 1.0.

6.5.- A dependence as low-p_t physics?

Explanations of the anomalous nuclear enhancement for high-p_t and high-E_t events which rely on heretofore unobserved collective effects in the nucleus have not met with much success; the idea that values of α in excess of 1.0 can be explained in terms of multiple hard scattering seems to have gained favor. Yet perhaps the effect is even more mundane, in the sense that it can be seen as the natural outcome of an extrapolation of known physics.

At high transverse energy, the behavior of the nuclear target spectra is nearly exponential, $d\sigma/dE_t^C \propto \exp(-\beta E_t^C)$. Considering for now only the Global aperture data, we have

$\beta = 0.906 \pm 0.012\ \mathrm{GeV}^{-1}$ for hydrogen

$\beta = 0.655 \pm 0.012\ \mathrm{GeV}^{-1}$ for aluminum

$\beta = 0.709 \pm 0.012\ \mathrm{GeV}^{-1}$ for copper

$\beta = 0.616 \pm 0.009\ \mathrm{GeV}^{-1}$ for lead.

These fits are shown along with the data points for 13 GeV < E_t^C < 21 GeV in Fig. 6-1.

Let $R_{A1/A2}$ be the normalized ratio of cross sections,

$$R_{A1/A2} = \frac{(1\ /\ \sigma_{abs}^{A1})(d\sigma^{A1}/dE_t^C)}{(1\ /\ \sigma_{abs}^{A2})(d\sigma^{A2}/dE_t)}\ , \tag{6-1}$$

where σ_{abs}^{Ai} is the absorption cross section for element i, from the data of Ref. 13: σ_{abs}^{H} = 32.5 mb, σ_{abs}^{Al} = 415 mb, σ_{abs}^{Cu} = 769 mb, and σ_{abs}^{Pb} = 1752 mb. Using the above fits to the cross sections, $R_{Al/H}$, $R_{Cu/Al}$, and $R_{Pb/Al}$ are exponentials in E_t^C (Fig. 6-2). $R_{Al/H}$ is much larger than $R_{Cu/Al}$ and $R_{Pb/Al}$, and varies much more rapidly.

We would like to see how well we can predict the behavior in Fig. 6-1 using only information obtained from low-p_t proton-nucleus data and high-E_t proton-proton data.

For large center of mass energy squared, s, the charged particle multiplicity is described by the scaling behavior predicted by Koba, Nielsen, and Olesen (KNO scaling), namely

$$\frac{1}{\sigma_{abs}}\frac{d\sigma}{dn_{ch}} = \frac{1}{\langle n_{ch}\rangle}\ \psi\left(\frac{n_{ch}}{\langle n_{ch}\rangle}\right) \tag{6-2}$$

where $d\sigma/dn_{ch}$ is the partial cross section for production of n_{ch} charged particles, $\langle n_{ch} \rangle$ is the average charged particle multiplicity, and $\psi(n_{ch}/\langle n_{ch} \rangle)$ is a function which does not depend directly on energy. I will assume that a similar scaling behavior takes place for total multiplicities in the central region -- i.e., within the Global aperture. Thus the total central multiplicity, n has scaling properties described by a function $\psi(z)$, where $z \equiv n/\langle n \rangle$. Furthermore, I will assume that $\psi(z)$ is the same for pp and pA collisions. KNO scaling is observed for charged particles in the central region,[14] and it is known that for total charged particle multiplicities the same $\psi(z)$ works roughly for pp and pA interactions,[15,16] (though according to Ref. 17 this universality is not exact) so these assumptions seem a reasonable extrapolation from known behavior.

The UA1 collaboration has measured $d\sigma/dn_{ch}$ in the region defined by $|\eta| < 1.3$, out to $n_{ch} = 27$.[15] Parametrizing their results in terms of the KNO variable $z_{ch} \equiv n_{ch}/\langle n_{ch} \rangle$, one finds $\psi(z_{ch}) \propto \exp(-\gamma z_{ch})$ for $z_{ch} > 1.0$, with $\gamma = 1.9$. (UA1 reported a value of $\langle n_{ch} \rangle$ equal to 9.4; therefore their data go out to about $z_{ch} = 3$.) Our Global aperture covers a smaller region, $\Delta\eta = 1.54$; a smaller value of γ may be appropriate for our experiment.

Mean charged particle multiplicities in the central region for pp, pAr, and pXe collisions can be determined from rapidity distributions given in Ref. 16; these data are consistent with a dependence on A parametrized by $\langle n_{ch} \rangle \propto A^{0.14\pm0.02}$. Using this parametrization, one can obtain mean charged multiplicities for pAl, pCu, and pPb. With the assumption that the mean total multiplicity $\langle n \rangle$ is given by $1.5\langle n_{ch} \rangle$, one obtains the following mean total central multiplicities for our nuclear targets:

pp	$\langle n \rangle$ =	4.00
pAl		6.38
pCu		7.19
pPb		8.50

We can use these numbers along with the KNO parametrization from the UA1 data to compute ratios of cross sections for a given multiplicity.

Now one would like to go from cross sections as functions of n to cross sections as functions of transverse energy. Let $B(E_t^C;n)$ be the probability distribution of E_t^C as a function of n. I will assume this to be independent of A -- an assumption for which there is in fact some evidence in the E557 data (Ref. 18). Then

$$\frac{1}{\sigma^A_{abs}} \frac{d\sigma^A}{dE^t_C} = \sum_n \frac{1}{\sigma^A_{abs}} \frac{d\sigma^A}{dn} B(E_t^C;n\ )$$

$$\propto \sum_n \frac{1}{\langle n \rangle_A} \exp(-\gamma n/\langle n \rangle_A)\ B(E_t^C;n)$$

$$\approx \frac{1}{\langle n \rangle_A} \exp(-\gamma \bar{n}/\langle n \rangle_A)\ B(E_t^C;\bar{n}) \tag{6-3}$$

where $\bar{n} = \bar{n}(E_t^C)$ is the mean multiplicity as a function of transverse energy. Now, because $B(E_t^C;n)$ is independent of A, the factor $B(E_t^C;\bar{n})$ drops out of the expression for $R_{A1/A2}$:

$$R_{A1/A2} = \frac{\langle n \rangle_2}{\langle n \rangle_1} \exp\left[-\gamma \bar{n}\left(\frac{1}{\langle n \rangle_1} - \frac{1}{\langle n \rangle_2}\right)\right] . \tag{6-4}$$

All the A dependence here is in the $\langle n \rangle$'s, which were computed above from low-E_t proton-nucleus data, and all the E_t^C dependence is in $\bar{n}$ (E_t^C). Ref. 5 reports measurements of the mean number of hadrons $\langle n_{had} \rangle$ as a function of transverse energy as determined from the E557 high-E_t proton-proton data, using the calorimeter module responses to reconstruct tracks. A reasonable estimate of $\bar{n}$ might be $\bar{n} = 1.5\langle n_{had} \rangle$. The results are:

E_t^C (GeV)	$\langle n_{had} \rangle$	$\bar{n}$ (est.)
14.	15.6	23.4
17.	17.8	26.7
20.	20.5	30.8

Using these, along with the value $\gamma = 1.9$, leads to the predictions of $R_{Al/H}$, $R_{Cu/Al}$, and $R_{Pb/Al}$ plotted for these three values of E_t^C in Fig. 6-3. The lines are the observed ratios, copied from Fig. 6-2. Some of the qualitative features of the observed behavior are reproduced. Since $\bar{n}$ is approximately linear in E_t^C, the exponential behavior is predicted. $R_{Al/H}$ is much larger than $R_{Cu/Al}$ and $R_{Pb/Al}$, and it varies much more rapidly. All three predictions are too high, generally by factors of 2 or 3.

As noted earlier, the value $\gamma = 1.9$ is probably too large for the E557 Global aperture. One can use $R_{Al/H}$ to compute a value for γ and then try to predict $R_{Cu/Al}$ and $R_{Pb/Al}$. The $R_{Al/H}$ data in combination with Eq. 6-4 give

E_t^C	$\gamma\bar{n}$
14.	36.
17.	44.
20.	52.

(In combination with the earlier estimates of $\bar{n}$, these results imply $\gamma = 1.6 \pm 0.1$). Figure 6-4 shows the results obtained with these numbers as inputs. The normalizations of $R_{Cu/Al}$ and $R_{Pb/Al}$ are improved at the expense of a slight increase in their slopes, which were already too high in Fig. 6-2. (In fact, there is no way to get a prediction of the negative slope of $R_{Cu/Al}$).

Obviously, this model is very sensitive to parameter-tuning: a 15% change in γ results in a factor of 2 to 3 change in $R_{Al/H}$. The values of α in the parametrization $d\sigma/dE_t^C = kA^{\alpha}$ may be computed from the values of $R_{A1/A2}$. With $\gamma = 1.6$, for $R_{Cu/Al}$ the corresponding values of α range from 1.4 at $E_t^C = 14$ GeV to 1.7 at 20 GeV; for $R_{Pb/Al}$ one obtains values of α ranging from 1.1 to 1.5 for the same E_t^C values. With $\gamma = 1.9$, one obtains values of α which are about 10% larger.

We therefore see that the "anomalous" nuclear enhancement is not necessarily indicative of new physics, but that a qualitative prediction of ANE can be made using only low-E_t nuclear target data and high-E_t hydrogen target data. The phenomenological model I have presented here is fraught with assumptions, and it is unstable under changes in the parameters. Still, its partial qualitative success suggests that the high-transverse energy proton-nucleus results may be just an extrapolation of previously known physics. I have not attempted to compute predictions for the other apertures, since the answers are so critically dependent on the value chosen for γ.

A more sophisticated approach to this type of analysis was taken by Brody et al.,[19] who attempted to explain the E557 nuclear cross sections in the Global aperture in terms of multiple low-p_t scatters. For two specific models of particle production, the nuclear target cross sections could be predicted from the pp cross sections for low A or low E_t^C. However, the quantitative predictions at high A and high E_t^C do not match the observations. No predictions from these models for smaller apertures are available.

6.6. Conclusions

While the cross sections we observe for proton-proton collisions in which large amounts of transverse energy are deposited in any of five full-azimuth apertures neither agree accurately with the QCD/brem predictions nor show any signs of the onset of new physics -- such as a change from exponential to power-law behavior similar to that seen in high-p_t single particle production -- events selected by a large-E_t requirement in a limited-$\Delta\eta$, full-azimuth aperture have predominantly a back-to-back jet structure similar to that predicted by a hard-scattering model. Events with high transverse energy in larger apertures are predominantly non-jetlike.

For proton-nucleus events with high transverse energy in the region $-0.18 < \eta^* < 0.70$ (F 2/3 aperture) the A-dependence of the cross section is $A^{1.07\pm0.09}$. For high transverse energy in any of the other four apertures studied the cross section increases with A faster than A.

While this effect has been explained in terms of multiple hard scattering within the nucleus, qualitatively similar behavior can be predicted for the Global aperture from low-E_t proton-nucleus data and high-E_t proton-proton data. No indications of jetlike structure for these events are seen.

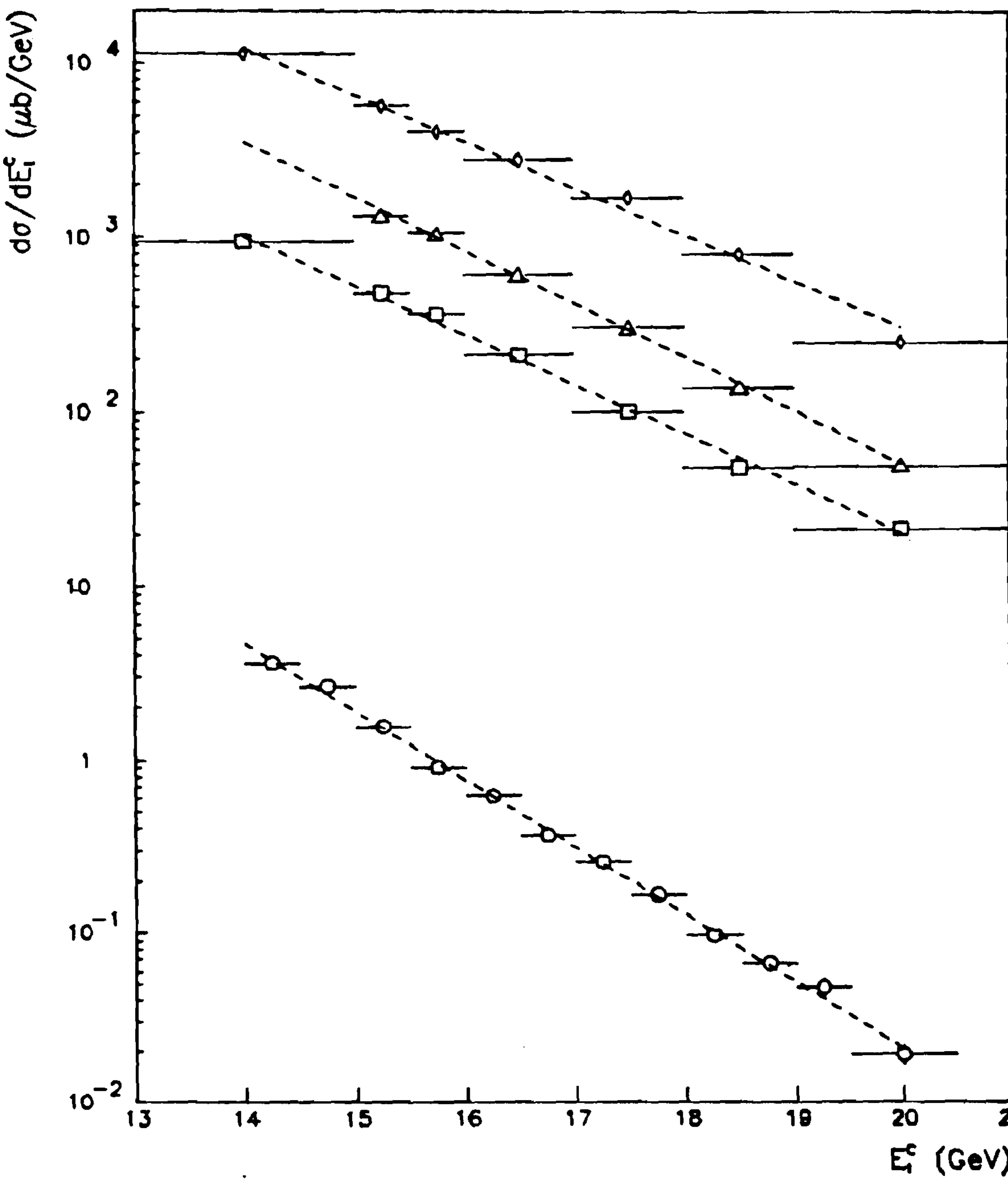

FIG. 6-1. Global $d\sigma/dE_t^C$ as a function of E_t^C for four targets, with fits to exponentials (dashed lines). Circles: Hydrogen. Squares: Aluminum. Triangles: Copper. Diamonds: Lead.

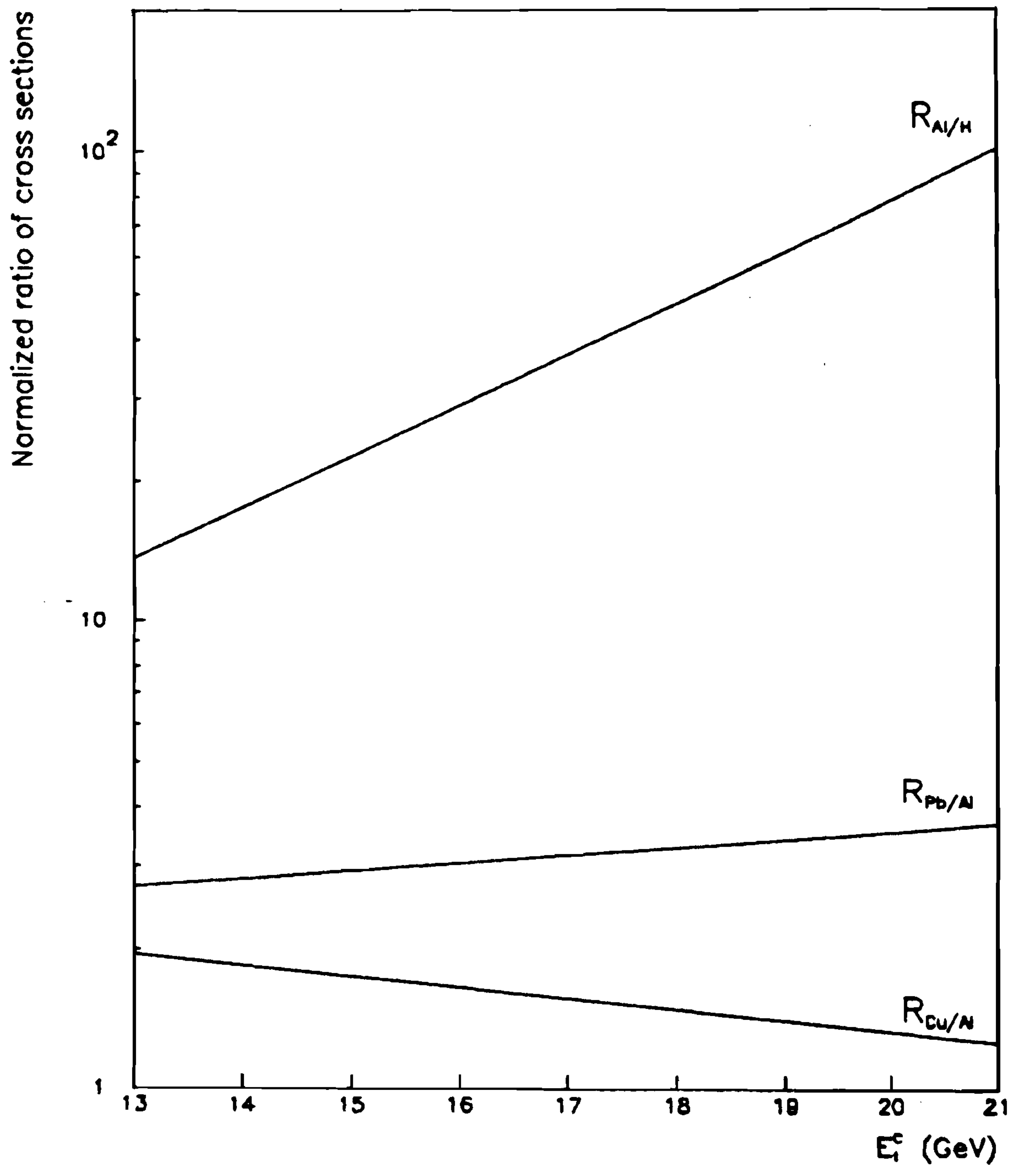

FIG. 6-2. Normalized cross section ratios for three pairs of targets (Al/H, Cu/Al, and Pb/Al), as computed from exponential fits.

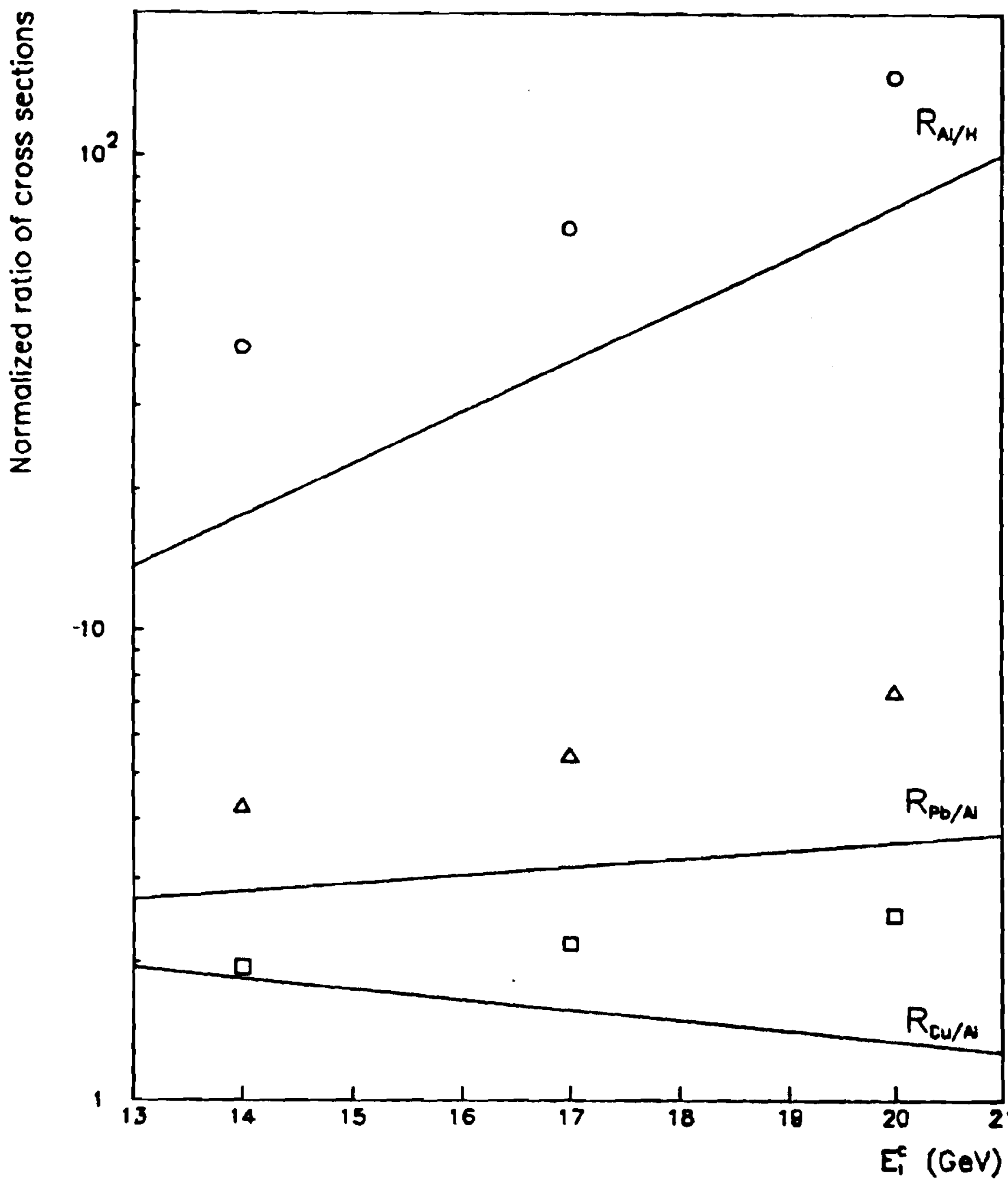

FIG. 6-3. Predicted normalized cross section ratios $R_{Al/H}$ (circles), $R_{Cu/Al}$ (squares), and $R_{Pb/Al}$ (triangles), computed using $\gamma = 1.9$, and the observed values (lines).

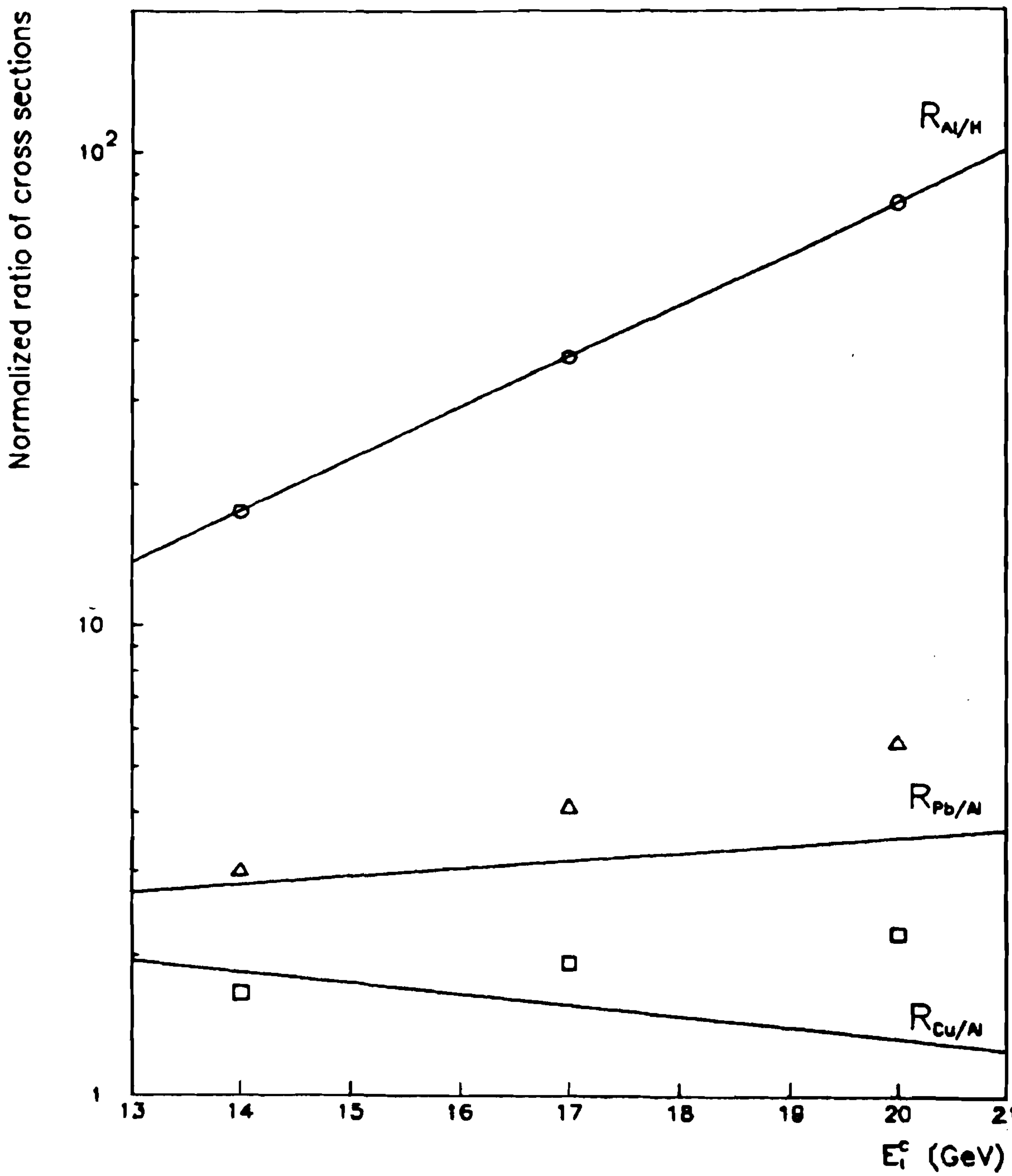

FIG. 6-4. Predicted normalized cross section ratios $R_{Cu/Al}$ (squares) and $R_{Pb/Al}$ (triangles), computed using $R_{Al/H}$ (circles) as input, and the observed values (lines).

References for Chapter VI

1. C. DeMarzo et al., Phys. Lett. 112B, 173 (1982); Nucl. Phys. B211, 375 (1983).
2. B. Brown et al., Phys. Rev. Lett. 49, 711 (1982).
3. W. Selove, J. Phys. Colloq. 43, C3/131 (1982); M. W. Arenton et al., Phys. Rev. D 31, 984 (1985).
4. B. Brown et al., Phys. Rev. Lett. 50, 11 (1983).
5. B. C. Brown et al., Phys. Rev. D 29, 1895 (1984).
6. T. Akesson et al., Phys. Lett. 118B, 185 (1982); 118B, 193 (1982); 123B, 133 (1983).
7. G. Arnison et al., Phys. Lett. 123B, 115 (1983); 132B, 214 (1983).
8. M. Banner et al., Phys. Lett. 118B, 203 (1982).
9. C. Bromberg et al., Phys. Rev. Lett. 42, 1202.
10. T. Akesson and H.-U. Bengtsson, Phys. Lett. 120B, 233 (1983).
11. F. Takagi, Phys. Rev. Lett. 43, 1296 (1979); V. V. Zmushko, Sov. J. Nucl. Phys. 32, 231 (1980).
12. D. Treleani and G. Wilk, Nuovo Cimento 60A, 201 (1980).
13. A. S. Carroll et al., Phys. Lett. 80B, 319 (1979).
14. A. Kernan, in Workshop on Proton-Antiproton Collider Physics, Madison, Wisconsin (AIP Conference Proceedings 85), edited by V. Barger, D. Cline, and F. Halzen (AIP, New York, 1982), p. 325.
15. L. Voyvodic, in Fermilab preprint Conf-82/29-THY/EXP, 1982 (unpublished).
16. C. DeMarzo et al., Phys. Rev. D 26, 1019 (1982).

17. E. R. Nakamura, M. Murayama, and A. Nakamura, Phy. Rev. D 27, 1457 (1983).

18. A. Zieminski et al., Bull. Am. Phys. Soc. 27, 18 (1982).

19. H. Brody, S. Frankel, W. Frati, and I. Otterlund, Phys. Rev. D 28, 2334 (1983).

APPENDIX A

APPARATUS AND DATA ACQUISITION

An overview of the apparatus used for experiment E557 was presented in Chapter II. In this appendix I give some technical details about the beam line and the Multiparticle Spectrometer (MPS) not covered in the earlier description.

A.1. M6W Beam Line

Between the spring of 1977, when the M6W beam line was described in a report by E. Malamud[1], and the spring 1981 run of E557, the only major change in M6W was the replacement of conventional dipole magnets in the second bend string by superconducting magnets, enabling transport of protons with momenta up to 400 GeV/c. This section gives a short description of the beam line as of Spring, 1981.

The primary beam for the Meson Laboratory was protons with 400 GeV/c momentum extracted from the Fermilab main ring, in a spill about one second in duration and a cycle time of ten to fifteen seconds. The fine structure of the primary beam consisted of buckets about one nanosecond long at intervals of 18.8 ns. Primary protons were directed onto a beryllium target, 8.00 inches long by 0.04 inches square, producing secondary particles which were the source for the M6 beam.

This production target was located about 1850 feet upstream of the MPS.

For E557 data taking, the M6W magnets were tuned for transport of 400 GeV/c diffractive protons with an intensity at the MPS of 5×10^5 to 1×10^6 protons per spill. At these intensities fewer than 2% of the buckets were populated and fewer than 0.04% contained more than one particle. For calibration, the beam line was tuned for lower energy (20 to 100 GeV/c) negative beams consisting mostly of pions and electrons. The layout of M6W is shown schematically in Fig. A-1, and the beam profiles are shown in Fig. A-2.

Cherenkov counter C_0, 60 feet in length, was located between the second and third foci. When used to tag electrons in the 20 GeV/c momentum beam used for voltage setting and calibration (see Appendix B), it was filled with helium at about 11.8 PSIA pressure, just under the threshold for pions at 20 GeV/c momentum. Cherenkov light was directed with a focusing mirror onto an RCA 31000M phototube, whose signal was brought to the MPS for use in the calibration trigger. During the data-taking stage of the experiment the counter was pumped down to vacuum.

A.2. Multiparticle spectrometer

The MPS as it existed in 1977 is described in Ref. 2. Here I discuss mainly those parts of the MPS relevant to this analysis which have been added or modified since 1977. Figure 2-1 shows the layout of the MPS for the Spring 1981 running period.

A.2.1. Target station and beam chambers

The target and nearby apparatus are shown in Fig. A-3. Plastic scintillation counters SA, SB, and SC (shown in Fig. 2-1) formed a beam-defining telescope. SA and SB were each 1 5/8" by 1 3/16" and 1/16" thick while SC was 6" square and 1/4" thick and had a 1 5/8" diameter hole.

The incoming particle was tracked by eight proportional wire chambers (PWCs), the BA and BB stations. These are described in the first part of Table A-1. All of these beam chambers were small, with 32 or 64 wires each for a total of 486 signal wires.

A.2.2. The dE/dx and 1×1 counters

Plastic scintillation counter "dE/dx", located just downstream of the nuclear targets, was 8" by 6" by 1/16" in size (x, y, and z) and was viewed by two phototubes. "1×1," another plastic scintillation counter, was 1" by 1" by 1/4" in size (x, y, z) and situated 8.4 meters downstream of the magnet face. It was mounted on a transport mechanism with which we could remotely position the counter vertically and horizontally so that non-interacting beam particles, after being bent through the spectrometer magnet, would strike 1×1. The positions of both of these counters are shown in Fig. 2-1.

A.2.3. Charged particle spectrometer

Downstream of the target were twenty-four proportional wire chamber planes, described in Table A-1. Eleven planes were upstream of the spectrometer magnet (stations A, B', and B). Station C was located in the magnet aperture, and station D was situated just downstream of the magnet.

At the downstream limit of the charged particle spectrometer were twenty-four spark chamber planes, described in Table A-2. The E station contained four modules and the F station four more, each module consisting of three planes measuring x, y, and slant coordinates, respectively. Each plane had two magnetostrictive readout wands, one on each side, for a total of forty-eight; signals were read out by pickups and preamps on the end of each wand. A maximum of fifteen sparks per wand per event could be read out, and in events with multiplicities close to or exceeding thirty some sparks were missed. To alleviate this problem, a set of four PWC planes (one measuring in x, one in y, and two slant) was situated amid the spark chambers and covering the central region; this was the F' station. The 30 ms dead time required by the spark chambers to recover between firings was a limiting factor in our data-taking rate.

The superconducting analysis magnet was a "48D48" dipole, 122 cm long in the z direction, whose upstream face was 1.200 m from the downstream end of the hydrogen target flask. To increase the acceptance of the spectrometer, the pole pieces described in Ref. 2 were removed.

Two multicell Cherenkov counters, C_A and C_B were located, respectively, in the aperture of and downstream of the spectrometer magnet. They were not used in this analysis.

A.2.4. Calorimeter System

The calorimeter was E557's major addition to the MPS and is described in detail in Ref. 3.

Each module in the electromagnetic (EM) section was a sandwich of 1/2" thick scintillator (fifteen pieces) alternating with 1/4" sheets of lead (fourteen pieces). Similarly, each front hadron (FH) module was a sandwich of forty pieces of 1/2" scintillator and forty sheets of 1/2" steel; the back hadron (BH) modules each had twenty-two pieces of 1/2" scintillator and twenty-two pieces of 1" steel (Fig. 2-4).

The scintillator used was an acrylic, doped with napthalene (3% by weight), polyphenylene oxide (PPO, 1%), and phenyl-oxazolyl-phenyl-oxazolyl-phenyl (POPOP, 0.025%). All the pieces of scintillator in each module were optically coupled at one edge to a single wave-shifter bar doped with BBQ, which absorbed the blue light generated in the scintillator and re-emitted it isotropically as green light.[4] A large fraction of the light was then able to propagate by total internal reflection down the wave bar and into an RCA 6342A photomultiplier tube via an acrylic light pipe. It was necessary to tailor a combination of black tape, aluminum foil, and white paint on the faces and edges of the scintillator sheets to get a uniform response.

Table A-3 lists some of the properties of the calorimeter system, and a plot of the resolution is shown in Fig. A-4. The hadron resolution was measured at the MPS in Spring, 1981, just prior to data taking. The electron resolution data come from tests using a tagged electron beam in the Fermilab Tagged Photon Laboratory.

The EM/FH unit was mounted on a transporter which moved in the x and y directions, allowing one to center any of the modules (except those in the top row) on the z axis. This feature was used only during calibration; during data taking the central hole was centered on the beam. A similar transporter carried the BH unit independently. Both transporters could be operated remotely, either by switches from outside the beam enclosure or by a CAMAC switching unit which permitted the calorimeters to be moved under computer control. The LeCroy HV4032 high voltage power supplies for the calorimeter phototubes could also be controlled either manually or through CAMAC.

A system for monitoring the performace of the calorimeter consisted of fiber optic cables connecting each waveshifter bar to a laser which could be pulsed between beam spills. This was intended to provide a controlled light source with which the photomultiplier tube outputs could be studied.

A.3. Data Acquisition

The data collected by the MPS equipment were read by a Digital Equipment Corporation PDP-11/45 computer running MULTI[5], a Fermilab-developed online data collection and analysis program, under the DEC RT11 operating system. In addition, the PDP-11 was able to control several of the devices used in the experiment; the examples of the calorimeter transporters and high voltage supplies have already been mentioned.

The PWC signals were loaded into a single shift register system whenever an interaction in the target region was detected (as indicated by the presence of the **INTBM** logic signal discussed below), unless an earlier trigger was still being processed. The shift register was clocked serially through a controller, which converted the data into one pair of numbers for each "cluster"; a cluster was a set of adjacent wires in which a signal was present, bounded by wires with no signal. The first number of the pair was the address of the first wire in the cluster, and the second was the number of wires constituting the cluster minus one. These data were read by the PDP-11 via direct memory access (DMA) if the event was found to satisfy the trigger requirement currently in effect; the system was then freed to load a new event.

The signals from the spark chamber wands mentioned earlier were digitized by time-to-digital converters and read by the PDP-11 using DMA.

The outputs from the phototubes in the calorimeter and the Cerenkov counters were digitized in analog-to-digital converters (ADC's); the PDP-11 read these data through CAMAC. Other phototube signals (e.g., from C_0, dE/dX, and 1×1) which were discriminated and used in the trigger logic were stored as "tagbits" by the computer, which again read these data via CAMAC. Other tagbits were generated by various signals in the trigger electronics, including bits indicating which of the active trigger requirements was satisfied by the event. Many of the logic signals also were scaled, using both visual and CAMAC scalers. The visual scalers were written down at the end of each run as a check on the CAMAC scalers. Table A-4 lists the various tagbits and scalers used. (The tagbits and scalers relating to triggers not used for this analysis have been omitted).

The data were collected by the PDP-11 computer and were written to magnetic tape at a density of 6250 bpi according to the "IDTYPE" format discussed in Ref. 6. In addition, MULTI was capable of sampling the data and doing a crude level of analysis, e.g., pulse height histograms or scatterplots, or ratios of scalers.

A.4. Trigger logic

The logic for the two main triggers used in this analysis, Global and Interacting Beam, is shown schematically in Fig. A-5.

To detect an interaction we used the counters SA, SB, SC, dE/dx, and 1×1, described above in sections A.2.1 and A.2.2, to make two tests:

one for production of several charged particles just downstream of the target, and one for the removal of a particle from the beam far downstream. A logic signal, "**DEDX**," was generated whenever the summed responses from the two phototubes of dE/dx exceeded a threshold corresponding to passage of two charged particles within 20 ns. The signal from the 1×1 was discriminated at a level below single particle to provide logic signal "**1X1**." The other inputs in Fig. A-5 are as follows: **BMGT** was on when an accelerator spill was in progress; **SA**, **SB**, and **SC** were the outputs of counters SA, SB, and SC discriminated below the single particle level; and **SCRGT** was on during the spark chamber dead time. **MSTRST** was used to reset the data acquisition system after an event had been either read in or rejected.

Several logic signals were generated by conditions indicating a contaminated event using appropriate timing and pulse height discrimination on the beam telescope counters. These conditions were: another particle traversing the telescope within ±130 ns of the pretriggering particle (**EARBM** and **LATBM**); two particles occupying the r.f. bucket where the pretrigger occurred (**DBLBM**); or a second interaction occurring within 200 ns of the first, corresponding to the length of the calorimeter gate (**EARINT** and **LATINT**).

The logic signal indicating a interaction, "**INTBM**," required passage of a beam particle (**BEAM**) together with either **DEDX** or $\overline{\mathbf{1x1}}$. In later analysis we found that **INTBM** was generated by about 90% of all inelastic events.

"**PRETRGLTCH**" prevented the system from loading further PWC data if a second interaction occurred while the first was being processed. In addition, **PRETRGLTCH** stopped the "EFF BEAM" scaler, which counted **BEAM** signals occuring while the apparatus was active.

The analog sum circuits for the calorimeter trigger, used to sum pulse heights from the calorimeter phototubes, provided the summed E_t in various regions of the calorimeter to be discriminated for use in the triggers. A number of transverse energy trigger regions were available, but of these only the sum over all 280 modules, the Global sum, is of interest for this analysis. The Global sum was accumulated for 200 ns in an integrate-and-hold circuit whose output was discriminated and, in coincidence with **STROBE**, formed the Global high E_t trigger.

The other important trigger used in this analysis was Interacting Beam, which required only that an interaction take place in the target region while the apparatus was active (i.e, a **STROBE** signal) without any regard to signals from the calorimeter. (One should not confuse the Interacting Beam trigger with logic signal **INTBM**, which was only one of several requirements in the Interacting Beam trigger).

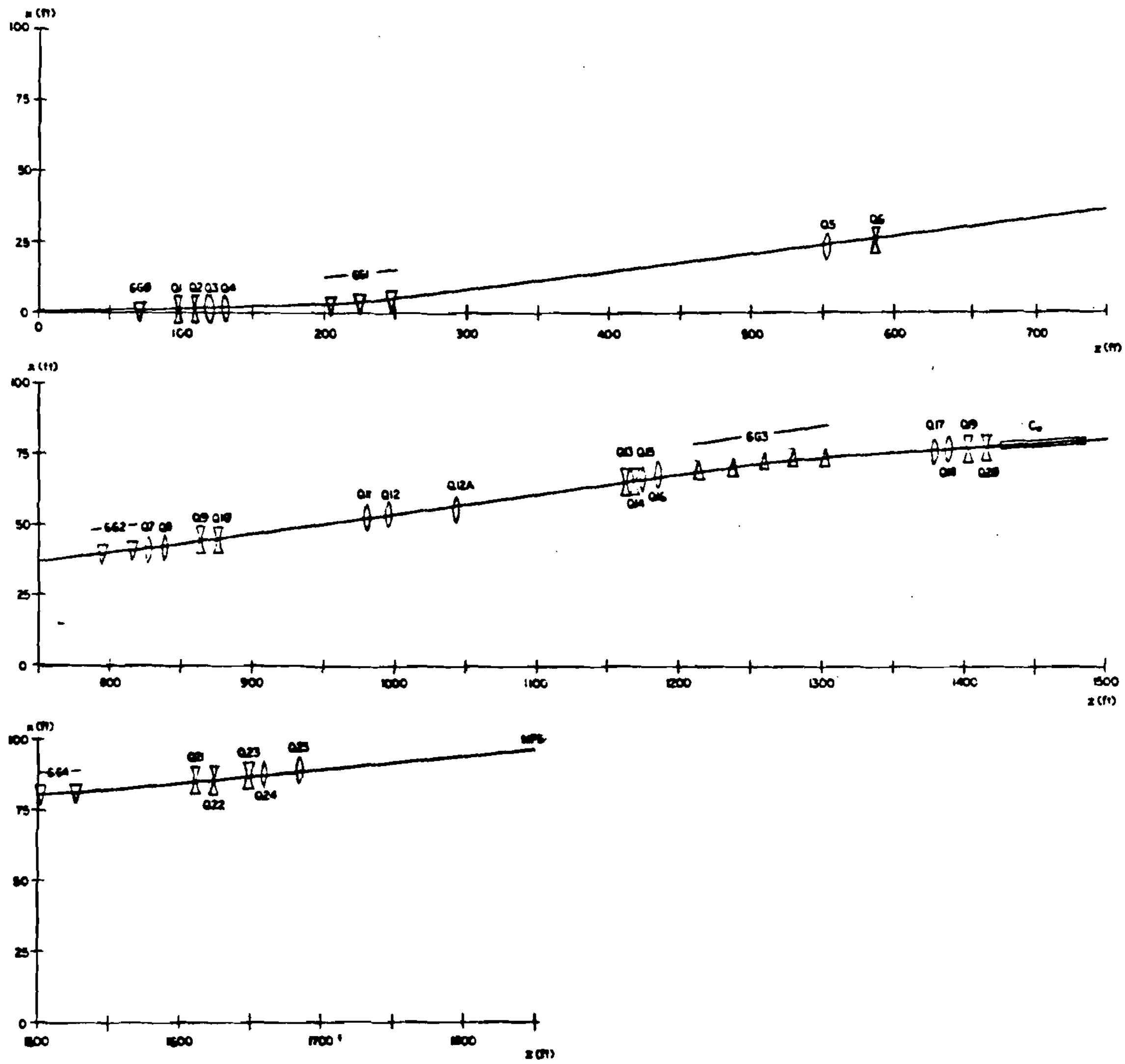

FIG. A-1. M6W optics. Lens shapes represent quadrupole magnets; prism shapes are dipole magnets. C_0, at 1450 feet, is a Cherenkov counter.

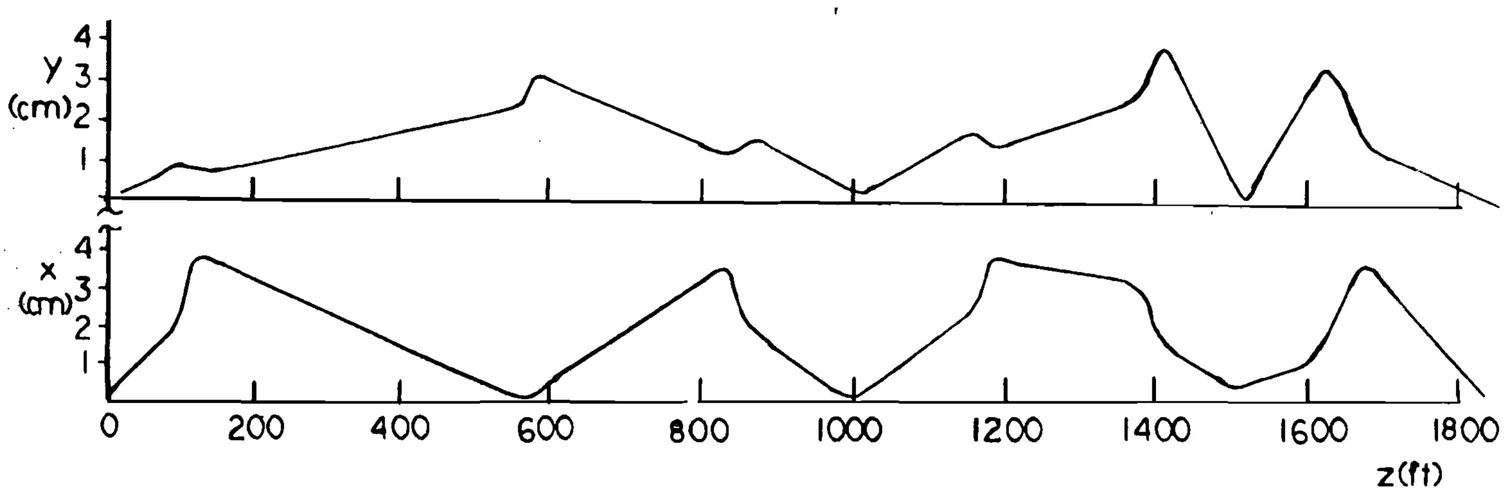

FIG. A-2. M6W beam profiles. Lines show computed widths of 400 GeV proton beam in the x and y directions as a function of distance along the beam line. Note the foci at around 400', 1000', 1530', and 1850' (the MPS).

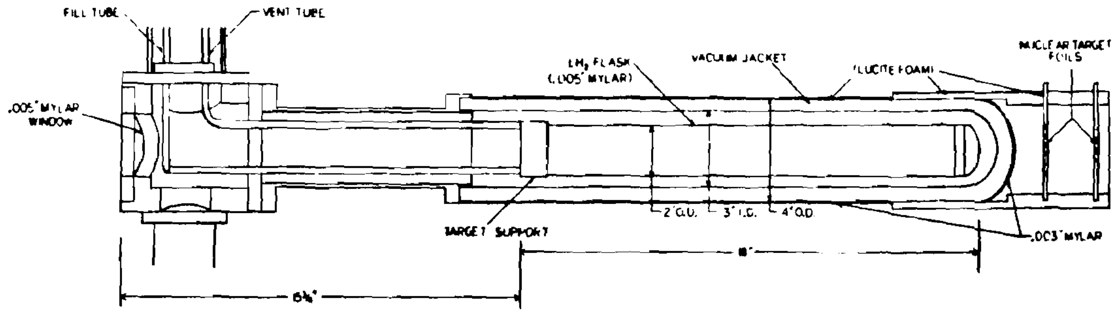

FIG. A-3. E557 target station, showing hydrogen target assembly and holder for nuclear target foils.

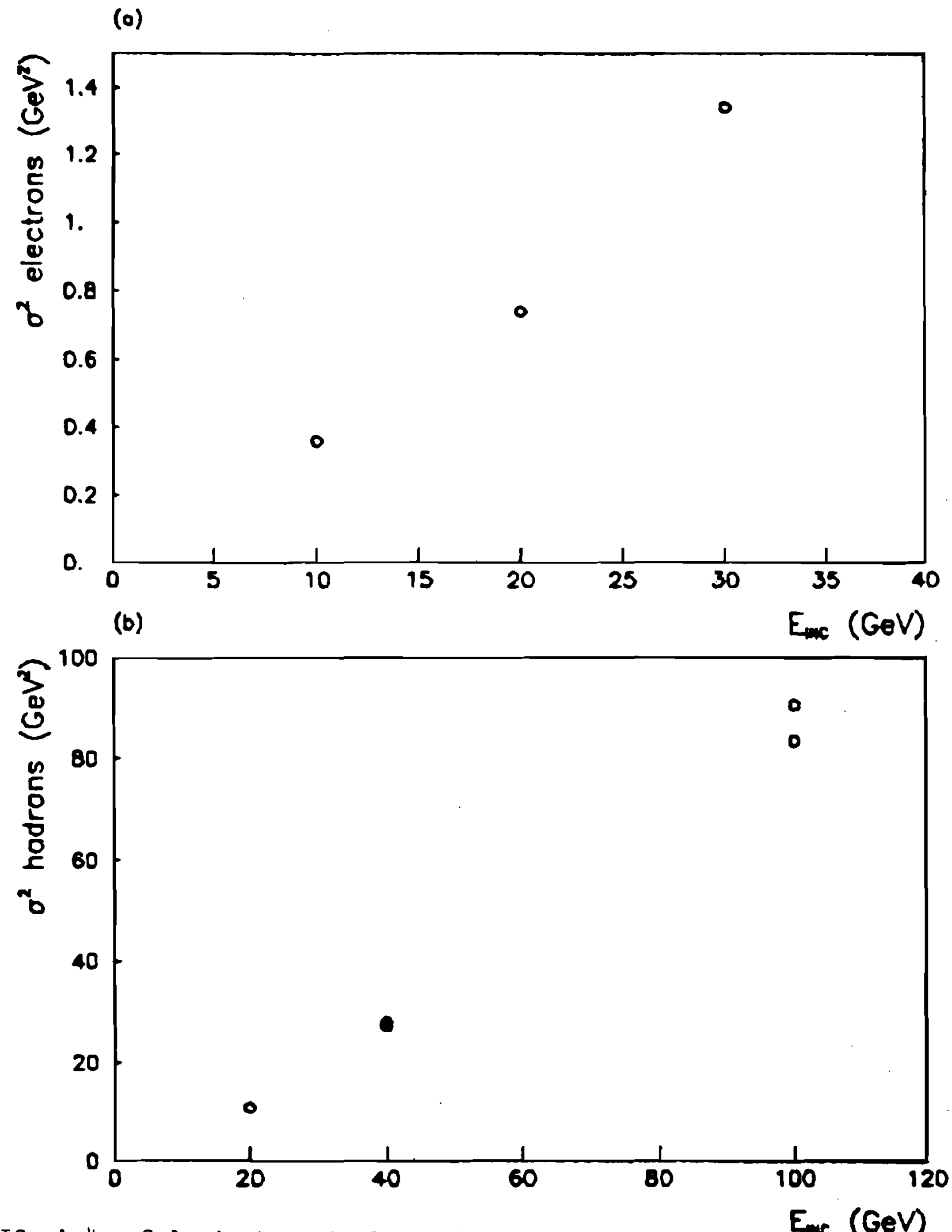

FIG. A-4. Calorimeter single-particle resolution as a function of incident energy for (a) electrons and (b) hadrons. Double points represent measurements for two different modules.

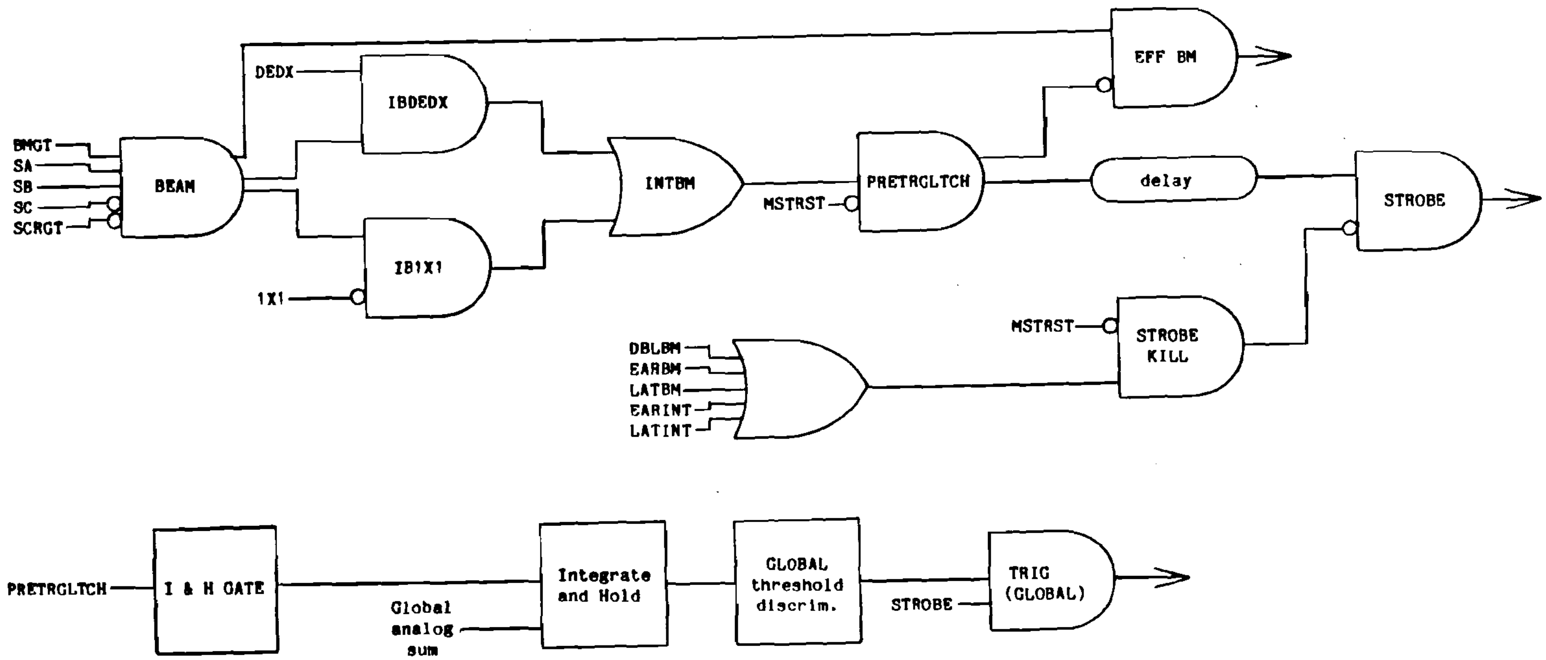

FIG. A-5. E557 trigger logic diagram (simplified). Trigger signals **STROBE** (Interacting Beam) and **TRIG** (Global) are defined, as well as several other signals which are recorded by the scalers and tagbits (table A-4).

TABLE A-1. Proportional Wire Chambers.

PWC Group Label	Gas[a]	Plane Label	No. of Anode Wires	Anode Wire Spacing (mm)	z position (From magnet, meters)	Angle (°)
			Beam defining chambers			
BA	Ar-CO_2	BAY1	64	2.00	-28.450	270.
		BAX1	64	2.00	-28.225	0.
		BAU	64	2.00	-25.923	315.
		BAX2	64	2.00	-21.191	0.
		BAY2	64	2.00	-21.168	270.
BB	Magic	BBX	32	0.98	-3.528	0.
		BBY	32	0.98	-3.518	90.
		BBU	32	0.98	-2.523	225.
			Spectrometer chambers			
A	Magic	AX1	256	0.98	-0.885	0.
		AX2	256	0.98	-0.880	0.
		AY1	256	0.98	-0.874	90.
		AY2	256	0.98	-0.869	90.
		AU	256	0.98	-0.819	45.
		AV	256	0.98	-0.813	135.
B'	Ar-CO_2	BX'2	384	1.95	-0.626	180.
		BX'3	384	1.95	-0.477	180.
B	Ar-CO_2	BX	512	1.95	-0.331	0.
		BY	320	1.95	-0.254	90.
		BU	512	1.95	-0.84	26.6

TABLE A-1. (Continued)

PWC Group Label	Gas[a]	Plane Label	No. of Anode Wires	Anode Wire Spacing (mm)	z position (From magnet, meters)	Angle (°)
C	Ar-CO_2	CX	512	1.95	0.616	0.
		CY	320	1.95	0.696	90.
D	Ar-CO_2	DX	992	1.95	3.022	180.
		DU	864	1.95	3.145	195.
		DY	256	4.62	3.285	270.
		DV	864	1.95	3.424	165.
		DX'	992	1.95	3.546	180.
F'	Ar-CO_2	F'X	320	1.95	6.866	0.
		F'U	320	1.95	6.950	135.
		F'Y	320	1.95	7.194	90.
		F'V	320	1.95	7.260	45.

[a] Gas mixtures were: Ar-CO_2 = 80% argon, 20% carbon dioxide.
Magic = 20% isobutane, 4% methylal, 0.5% Freon 13B1, remainder argon.

TABLE A-2. Spark Chambers.

Group Label	Size (x × y, meters)	Plane Label	Anode Wire Spacing (mm)	z position (From magnet, meters)	Angle (°)
E	2.6 × 1.4	E1X	0.794	6.09	0.0
		E1U	0.794	6.09	-5.4
		E1Y	0.794	6.12	90.0
		E2X	0.794	6.21	0.0
		E2U	0.794	6.21	5.4
		E2Y	0.794	6.24	90.0
		E3X	0.794	6.34	0.0
		E3U	0.794	6.34	-5.4
		E3Y	0.794	6.37	90.0
		E4Y	0.794	6.47	90.0
		E4X	0.794	6.50	0.0
		E4U	0.794	6.50	5.4
F	3.8 × 1.9	F1X	0.794	6.59	0.0
		F1U	0.794	6.59	5.4
		F1Y	0.794	6.62	90.0
		F2X	0.794	6.76	0.0
		F2U	0.794	6.76	5.4
		F2Y	0.794	6.80	90.0
		F3X	0.794	7.04	0.0
		F3U	0.794	7.04	-5.4
		F3Y	0.794	7.08	90.0
		F4X	0.794	7.34	0.0
		F4U	0.794	7.34	5.4
		F4Y	0.794	7.37	90.0

TABLE A-3. Calorimeter.

	EM	FH	BH
Size in x (m)	3.1	3.1	3.6
y	2.3	2.3	2.5
z	0.31	1.08	1.00
Distance from magnet face to front (m)	7.93	8.24	9.91
Absorber:			
Material	Lead	Steel	Steel
Thickness (in.)	0.25	0.5	1.0
Number of pieces	14	40	22
Scintillator:			
Material	Acrylic	Acrylic	Acrylic
Thickness (in.)	0.5	0.5	0.5
Number of pieces	15	40	22
Number of modules	126	126	28
Total thickness in:			
radiation lengths	16.	30.	33.
absorption lengths	0.8	3.8	3.7

TABLE A-4. Tagbits and scalers.

Number	Name	Description
		Tagbits
46	GLB RAW MED	Global sum over medium threshold
49	INT BEAM	Interaction detected
59	GLB DIV MED	Global trigger, medium threshold
67	CO	Signal in Cherenkov counter CO
81	IB DEDX	Interaction detected by DE/DX
82	IB $\overline{1\times1}$	Interaction detected by 1×1
		Scalers
1	BEAM	Beam particles detected
2	EFF BEAM	Beam particles detected while live
3	INT BEAM	Interactions detected
4	PRETRIG	Pretriggers
5	TRIGOR	Triggers
6	TRIG	Triggers while live
7	STROBE	Pretriggers not vetoed
8	EFF INT BEAM	Interactions detected while live
9	SA·SB	Pulse in SA and SB
10	2XSA	2 particles in SA
11	2XSB	2 particles in SB
12	2X KILL	Double beam vetoes
14	EARLY KILL	Early beam vetoes
15	LATE KILL	Late beam vetoes
16	EARLY INT KILL	Early interaction vetoes
17	LATE INT KILL	Late interaction vetoes
27	GLOBAL MED	Global triggers, medium threshold

References for Appendix A

1. E. Malamud, "The M6 Beam Line", 1977 (unpublished).
2. A. Dzierba, E. Malamud, and D. McLeod, Fermilab MPS workshop, 1977 (unpublished).
3. P. Rapp *et al*., Nucl. Inst. and Meth. 188, 285 (1981).
4. P. Klasen, K. Kleinknecht, and D. Pollmann, Nucl. Inst. Meth. 185, 67 (1981).
5. J. F. Bartlett *et al*., Fermilab Program Library writeup PN97.5, 1979 (unpublished); E. K. Quigg, T. D. Lagerlund, D. J. Ritchie, L. M. Taff, Fermilab Program Library writeup PN106, 1981 (unpublished).
6. A. Dzierba *et al*., E557 memo IND-19-79, 1979 (unpublished).

APPENDIX B

VOLTAGE SETTING AND CALIBRATION DATA RUNS

The E557 calorimeter was designed to provide a high transverse energy trigger by using calorimeter phototube voltages chosen such that each phototube gave a signal approximately proportional to the transverse energy deposited in the corresponding calorimeter module. These voltages had to be determined and set before physics data could be taken. Furthermore, the conversion from phototube pulse height to energy for each module had to be known accurately at the time of off-line analysis in order to use the calorimeter to measure energies. In this appendix I discuss the voltage setting system and the special series of runs that provided data for calibration.

B.1. Voltage setting

Calorimeter phototube voltages were set using the online PDP-11. As described in Appendix A, the LeCroy HV4032 high voltage power supplies for the calorimeter phototubes could be controlled by the PDP-11 computer through its CAMAC interface. The beam used during voltage setting was one of negative particles with 20 GeV/c momentum; it consisted mostly of pions and electrons. The target was empty and the spectrometer magnet was turned off. Cherenkov counter C_0 was used to generate an electron tag signal **CO**, which was required along with **BEAM** in the trigger when calibrating EM modules in order to get a sample enriched in electrons.

Under control of the voltage setting program, the EM/FH calorimeter unit was moved until the first EM module was centered on the beam. The high voltage for that module was set to a specified initial value and the other modules were turned off. The task then was to set the phototube voltage so that the resulting pulse height was approximately proportional to the energy deposited in the corresponding module times the sin of θ, the angle between the center of the module and the beam as measured from the center of the hydrogen target when the calorimeter was in its normal, centered position:

$$P = g\ f\ E_{inc} \sin \theta. \tag{B-1}$$

Here P is the phototube pulse height measured as a number of ADC channels, g is the conversion between number of channels and energy, and E_{inc} is the incident beam energy. f is the "containment fraction," that is, the fraction of the incoming energy which is deposited in the module as opposed to leaking from the module from the sides or the back; it was measured for the various module types in a test beam (see Table B-1). For the Spring 1981 run we used g = 400 channels/GeV.

With the voltage set to some initial guessed value, a sample of events was taken. The program estimated the mode of the pulse height distribution and made a new estimate of the correct value for the voltage. The process of taking data samples and revising the estimated voltage was repeated until the program found a value (within a ±5 volt tolerance) that gave the correct pulse height for that module. The program then moved the calorimeter to bring the next module into the beam to set its voltage. After setting the EM module voltages, the program set the FH modules; finally, the EM/FH calorimeter unit was centered on the beam (which then passed through the calorimeter hole) and the BH module voltages were set in the same fashion. Human intervention was required only when a defective module was encountered (e.g. one in which the optical path from the scintillator to the phototube was broken and no meaningful signals were produced). In addition, the top row of modules in the EM/FH unit could not be brought into a position centered on the beam and we had to assume the proper voltages were the same as those for the bottom row.

B.2. Calibration data

The offline calibration program for determining calorimeter gains and pedestals, discussed in Appendix C, made use of data from a special set of runs. The beam momentum used was 20 GeV/c, directed again into the center of each module. The ADC data were written to magnetic tape. Two such series of calibration runs were made, one after voltage setting and before the first physics data runs, and the other about three weeks later, toward the end of the running period. During the first of these series, Cherenkov counter C_0 was used to tag electrons and the tagbit was written to tape.

To check the linearity of the relationship between average pulse height and deposited energy, which had been demonstrated in test beam measurements[1], a series of runs using beam momenta of 10, 20, 30, and 100 GeV/c directed into each of several modules was also taken (Fig. B-1). The good linearity of the calorimeter was confirmed.

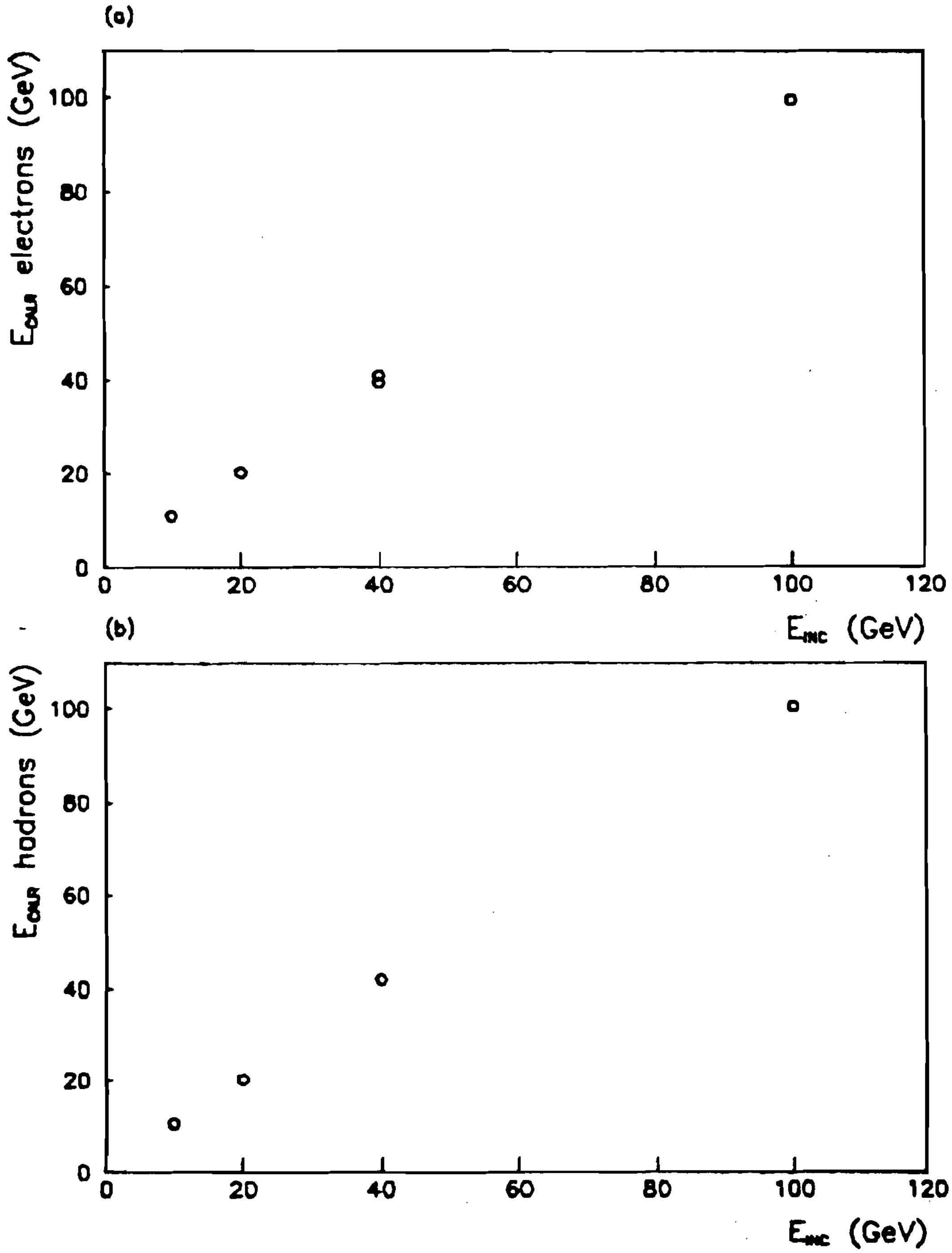

FIG. B-1. Linearity study: Average calorimeter response as a function of incident energy for (a) electrons (b) hadrons. Double points represent measurements for two different modules.

TABLE B-1. Containment Fractions.

		Mean response / beam energy		
Particle	Module size	EM	FH	BH
		E_{inc} = 20 GeV (1981 calibration run)		
Electron	4" × 8"	0.881	0.059	0.0008
	8" × 8"	0.909	0.072	0.0005
	12" × 8"	0.918	0.066	0.0010
Hadron	4" × 8"	0.0294	0.528	0.103
	8" × 8"	0.0258	0.654	0.108
	12" × 8"	0.0240	0.678	0.110
		E_{inc} = 40 GeV (1979 test beam run)		
Electron	4" × 8"	0.75	. .	. .
	8" × 8"	0.81	. .	. .
	12" × 8"	0.84	. .	. .
Hadron	4" × 8"	. .	0.46	. .
	8" × 8"	. .	0.59	. .
	12" × 8"	. .	0.66	. .
	14" × 20"	. .	. .	0.85

References for Appendix B

1. P. Rapp et al., Nucl. Inst. and Meth. 188, 285 (1981).

APPENDIX C

DATA PROCESSING

This appendix describes the processing done to calibrate the calorimeter, determine calorimeter energies, and find the interaction vertex. These tasks were accomplished using the Fermilab CDC Cyber computer system running the TEARS offline analysis program, developed for Fermilab experiments E110 and E260 and considerably modified by the E557 collaboration.[1] In addition, the BLOOD software package, created and used for much of the physics analysis, is described.

C.1. TEARS and MINT

The version of TEARS used for this analysis is written in CDC FORTRAN Extended (a dialect of FORTRAN IV). MINT, another program using many of the data processing routines from TEARS, was used in the later stages of processing. Figure C-1 is a flow diagram for MINT; TEARS is functionally similar, and the name "TEARS" in the following will refer to either TEARS or MINT.

TEARS reads data from an input file whose structure is the "IDTYPE" format described in Ref. 2. This input file could be a raw data tape written by the online computer, a file of Monte Carlo events, or a file written by TEARS as the output of an earlier stage of processing. TEARS can be instructed to copy all, some, or none of the IDTYPE records from the input file to an output file.

The TEARS package includes subroutines, not normally invoked by the TEARS program but callable from any of several user interface routines, for such tasks as vertex finding, track reconstruction, calorimeter analysis, and so forth. In addition, routines are available to write the results of an analysis into new IDTYPE records on the output tape. The principal interface routine, USER, is called after reading in each event. Other user interface routines are called after reading records pertaining to the beginning or end of a run, before processing begins, and after processing the last requested run.

C.2. BLOOD

Much of the physics analysis for this dissertation was done using a simpler software package, developed for this purpose, called BLOOD. Inputs for BLOOD were "Physics Summary Tapes" (PST's) generated by a MINT-based program. The PST's contained calorimeter energies, vertex positions, and other information for each event in a set of runs. A total of nine PST's were used, corresponding to Interacting Beam trigger data from run groups 0, A, B, and P; Global trigger data from run groups 0, A, and B; LPS Monte Carlo data; and QCD/Brem Monte Carlo data. For the latter two PST's, information on the actual particle tracks was also included. The PST format is given in Table C-1.

The BLOOD software package contains three programs, BBOOK, BLOOD, and BPHIST, which are run in sequence: BBOOK sets up control parameters and histograms, BLOOD is the main analysis program, and BPHIST prints and stores the histograms generated by BLOOD. Figure C-2 shows the logic flow for BBOOK, BLOOD, and BPHIST. Conceptually BLOOD is similar to TEARS (intentionally); after some initialization, during which user routine USRINIT is called, the program reads in and unpacks data for each event and calls user routine USER, from which data analysis can be directed. USRTERM is called at the end of processing. Two other user routines, UBOOK and UPHIST, are called by BBOOK and BPHIST, respectively.

C.3. Calibration processing

To permit conversion of calorimeter pulse heights to energies it was necessary to determine accurately the gain and pedestal for each module. The gain is defined as the reciprocal of the slope of the line relating the average pulse height response of the module, $\langle P \rangle$, to the energy deposited, E_{dep}, while the pedestal, P_0, is the intercept:

$$\langle P(E_{dep}) \rangle = \frac{1}{G} E_{dep} + P_0 \ . \qquad \text{(C-1)}$$

The TEARS-based calibration program, which is described in detail elsewhere[3], made use of the series of special runs described in section B.2 to perform a calibration of the calorimeter. The algorithm had two stages. In the first stage, the program computed a pedestal for each module using events where the module was placed far from the beam; the pedestals were stored in a disk file for use in gain calculations.

The program then categorized each event according to the flow diagram in Fig. C-3 as a "muon", "electron", "hadron", "tail", or "ambiguous" event by cuts on the energy seen in the calorimeter modules and, during the first calibration run, the response of Cherenkov counter

C_0. C_0 was not used for the second calibration and the corresponding requirements were suppressed. When calibrating back hadron (BH) modules, E_{sum} was just the response of the BH module and all non-muon, non-tail events were classified as ambiguous events. Table C-2 indicates the fraction of events in each category for the second calibration.

Events classified as muon or tail were not used; ambiguous events were attributed to early-showering hadrons. Average responses for the other three types of events were computed and stored for use in the next stage of calibration. Leakage into other working calorimeter modules was measured using the response of those modules while leakage into defective modules or out of the calorimeter was assumed to be symmetric and therefore equal to leakage into the corresponding working modules.

The second stage of calibration made use of the average responses, leakages, and pedestals determined in the first stage to compute gains separately for electrons in the EM modules and hadrons in the EM, FH and BH modules. (Electrons produced more light at a given energy than did hadrons in the EM modules, resulting in gain values averaging 18% higher for hadrons[4]). If the gains of all modules except the one exposed to the beam were known then the energy leakage E_{leak} could be computed from the pulse heights of the neighboring modules; then, since the beam energy E_{inc}, pulse height P, and pedestal P_0 were known, the gain G could be obtained from

$$\langle E_{inc} - E_{leak} \rangle = G \langle P - P_0 \rangle. \tag{C-2}$$

Of course, at the outset all gains were unknown, so that an initial guess had to be used and the gain-finding procedure iterated. In each iteration all modules in a section (EM, FH, or BH) were adjusted; a new iteration was performed if any module gain had to be corrected by more than 5%. In practice no section required more than five iterations. The BH modules were adjusted first, followed by FH (using hadron events), EM (hadron gains, using ambiguous events), and EM (electron gains, using electron events).

Comparison of results from the two calibration series revealed that the light output of the modules had decreased in the intervening time. These data along with average pulse heights from the Global trigger runs are consistent with a gain drift linear in time and equal to about 10% between the first and second calibrations. The cause of this shift is not known. In our data analysis we adjusted the gains for each run by interpolating between or extrapolating from the two gain measurements to the time of the run being studied. Uncertainties in the time dependence of the gains were among the effects contributing to the quoted uncertainty in our E_t scale.

The laser monitoring system mentioned in Appendix A was intended to permit the gains to be monitored throughout data taking. However, this system performed poorly in the Spring 1981 run, owing to instabilities in both light output and spatial distribution of the light source. Some analysis has been done, but on the whole the laser data seem not to be very useful.[5]

C.4. Pedestal finding and calorimeter energies

Having computed the gains for each module, the remaining difficulty in determining calorimeter energies was that of finding the pedestals.

The ADC pedestals fluctuated from run to run, and indeed within each run from event to event. The primary cause of the pedestal shift appeared to be noise induced by the spark chambers; during the calibration runs, in which the spark chambers were not fired, pedestal drift was not observed. (See also Ref. 6). To determine the average pedestal for each module in a given run, 280 histograms, one for each module, were made of the raw module ADC signals for all events in the run. Even in the high-multiplicity Global trigger events the number of modules over pedestal per event rarely exceeded forty, so the distribution of responses for each module was sharply peaked with a long upward tail. The mode of the distribution was our estimate of the average pedestal for that module and was written to a disk file for use by the later processing programs. A few defective modules were found at this stage by noting that their response distributions were very broad, a characteristic of a noisy channel.

Average pedestals for several modules were plotted as a function of run number and were observed to drift together, that is, at the same time by about the same amount[4,7]. We infer that the pedestals for all modules drifted approximately together. Therefore, a technique similar to that used to find the run-averaged pedestals could be used to estimate the event-by-event drift, in which instead of histogramming each module over all events, a histogram was made for each event over all modules. The histogram entries were ADC pulse heights with the run-averaged pedestals subtracted, so that for events with no pedestal drift the distribution would be peaked at zero with a long upward tail. The actual position of the peak was the estimated pedestal drift for that event and was added to the run-averaged pedestals for each module to arrive at the pedestals for that event. The average event-to-event pedestal shift calculated in this manner was 0.75 channels (about 2 MeV E_t), with an r.m.s. width of about 3.5 channels (9 MeV E_t).

Finally, for each module, the pedestal was subtracted from the pulse height and the result multiplied by the gain to arrive at the energy deposited in the module. Which gain to multiply by, for the EM modules, in principle depended on whether the incoming particle was hadronic or electromagnetic. For this analysis, since I have used no particle identification, it has been assumed that all the energy in the EM modules is due to electromagnetic particles and the energy has been computed with the electromagnetic gains. Since there certainly must be, on the average, some hadron energy in the EM modules, and the electromagnetic gains are smaller than the hadronic gains, I have underestimated the energy in the EM modules. This is one effect which contributed to the need for an E_t correction, as described in Chapter III.

C.5. Vertex finding

The algorithm used to find the vertex for each event was a modification[8] of that used in E110 and E260.[9] It worked in two stages. In the first stage the beam track was found using upstream PWC groups BA1, BA2, and BB. Tracks downstream of the magnet were found in the y-z projection and, for the region upstream of the magnet only, the x-z projection. Only tracks which passed through a fiducial region around the target, 2 m × 6 cm × 6 cm, were accepted. These tracks were ranked according to criteria based on the number of sparks and PWC hits associated with the track, the number of these that were not shared by other tracks, and (as a tiebreaker) the χ^2 of the track fit. Of these the six tracks with the highest rank were used to find the vertex.

In the second pass a fiducial volume was established around the vertex found in the first pass. The tracks which missed this region as well as those that made a large contribution to the χ^2 of the vertex were discarded and the remaining tracks were used to find the final vertex. The estimated vertex finding resolution for Global trigger data was $\sigma_x = \sigma_y = 0.1$ mm, $\sigma_z = 1.5$ mm. The vertex distributions in x, y, and z for a typical Global trigger run are shown in Fig. C-4.

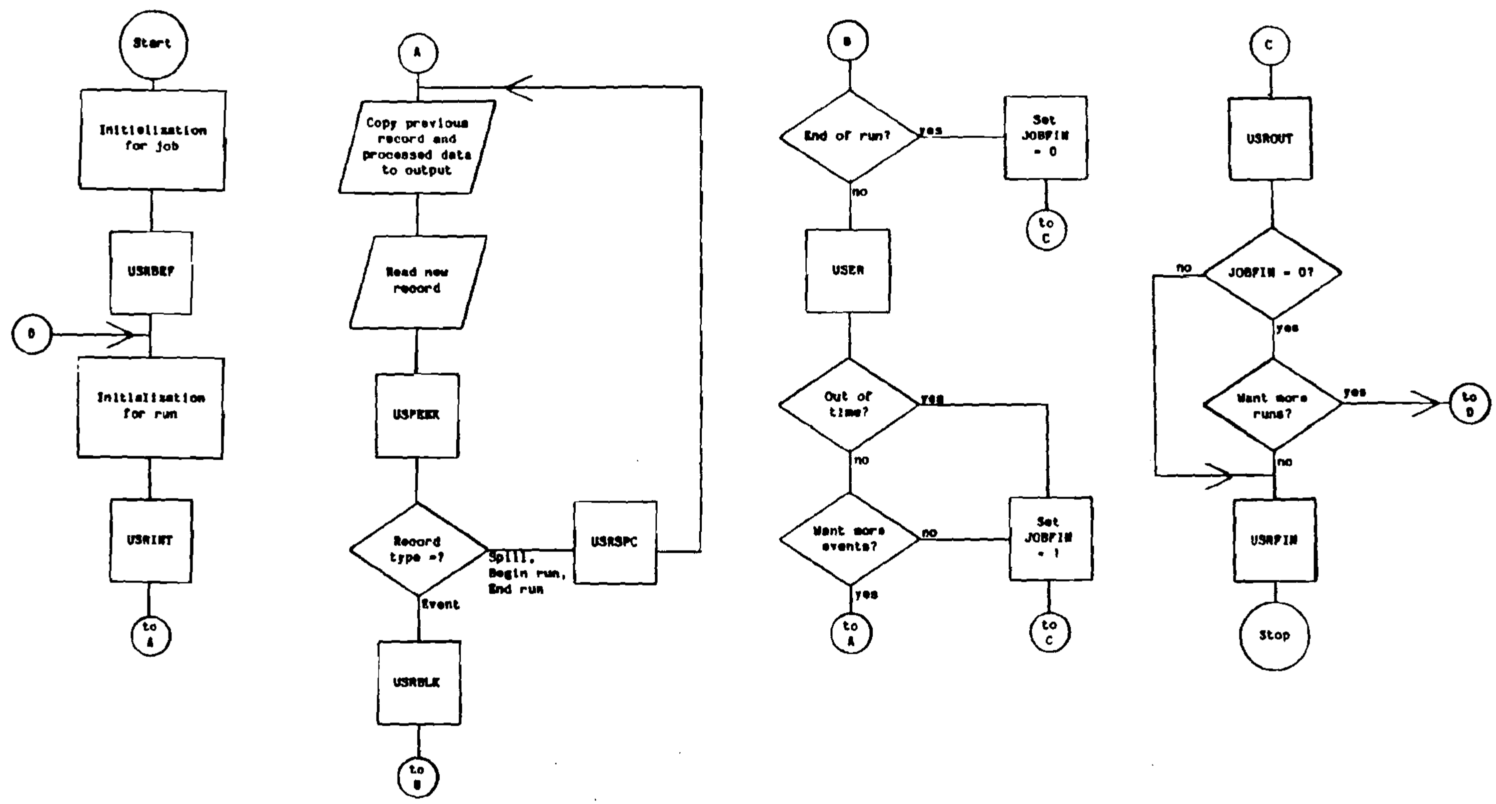

FIG. C-1. TEARS flowchart.

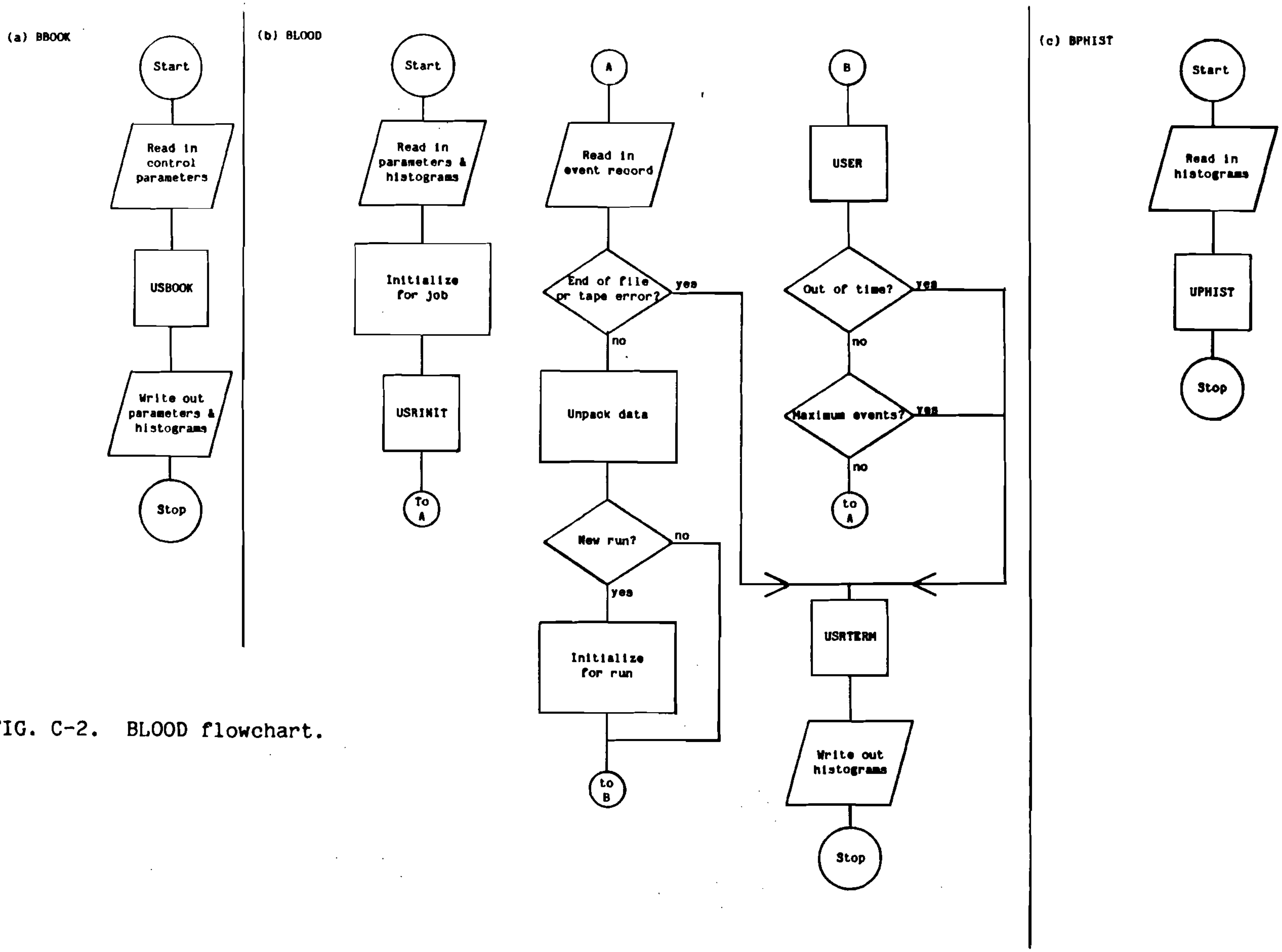

FIG. C-2. BLOOD flowchart.

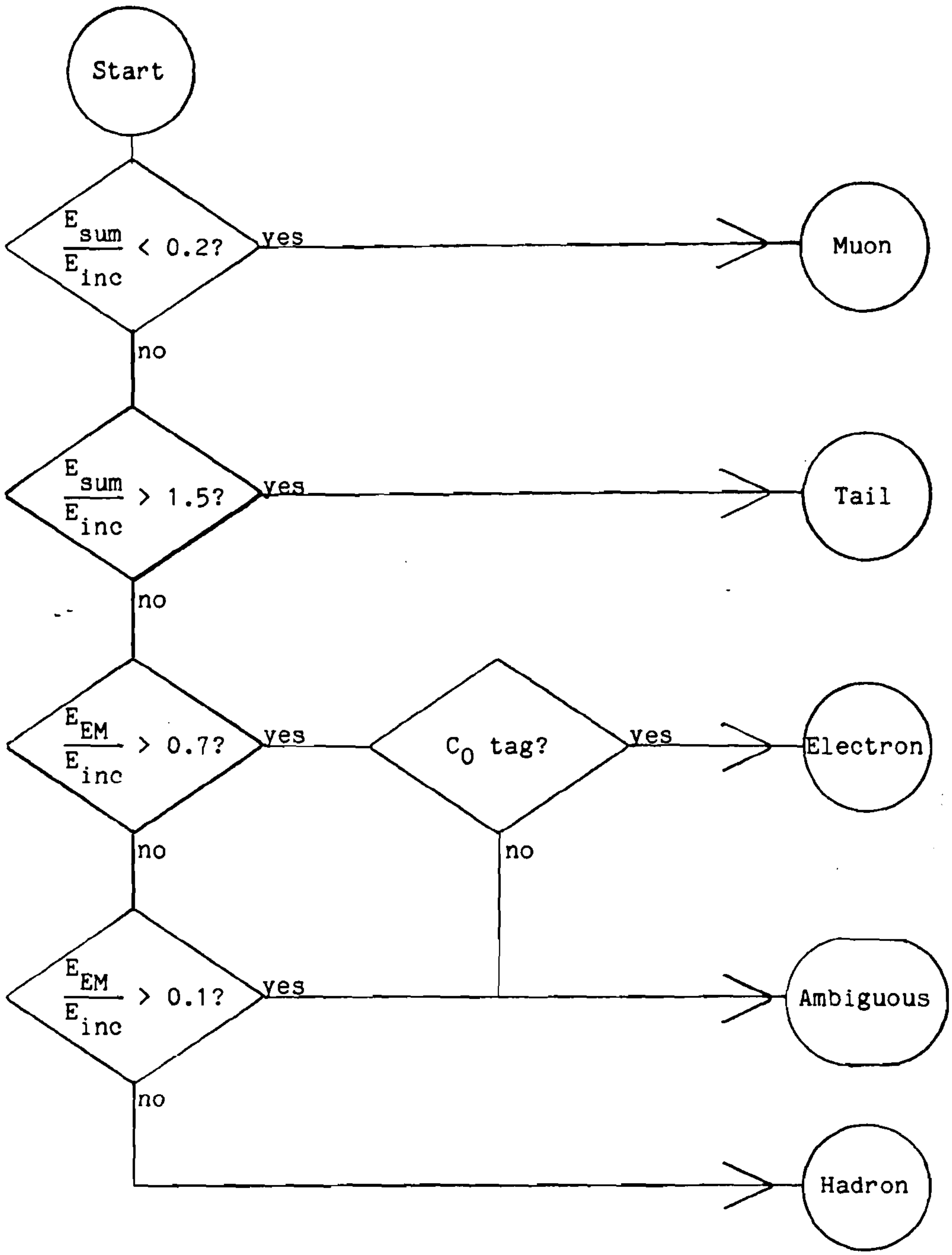

FIG. C-3. Flow diagram for calibration event classification.

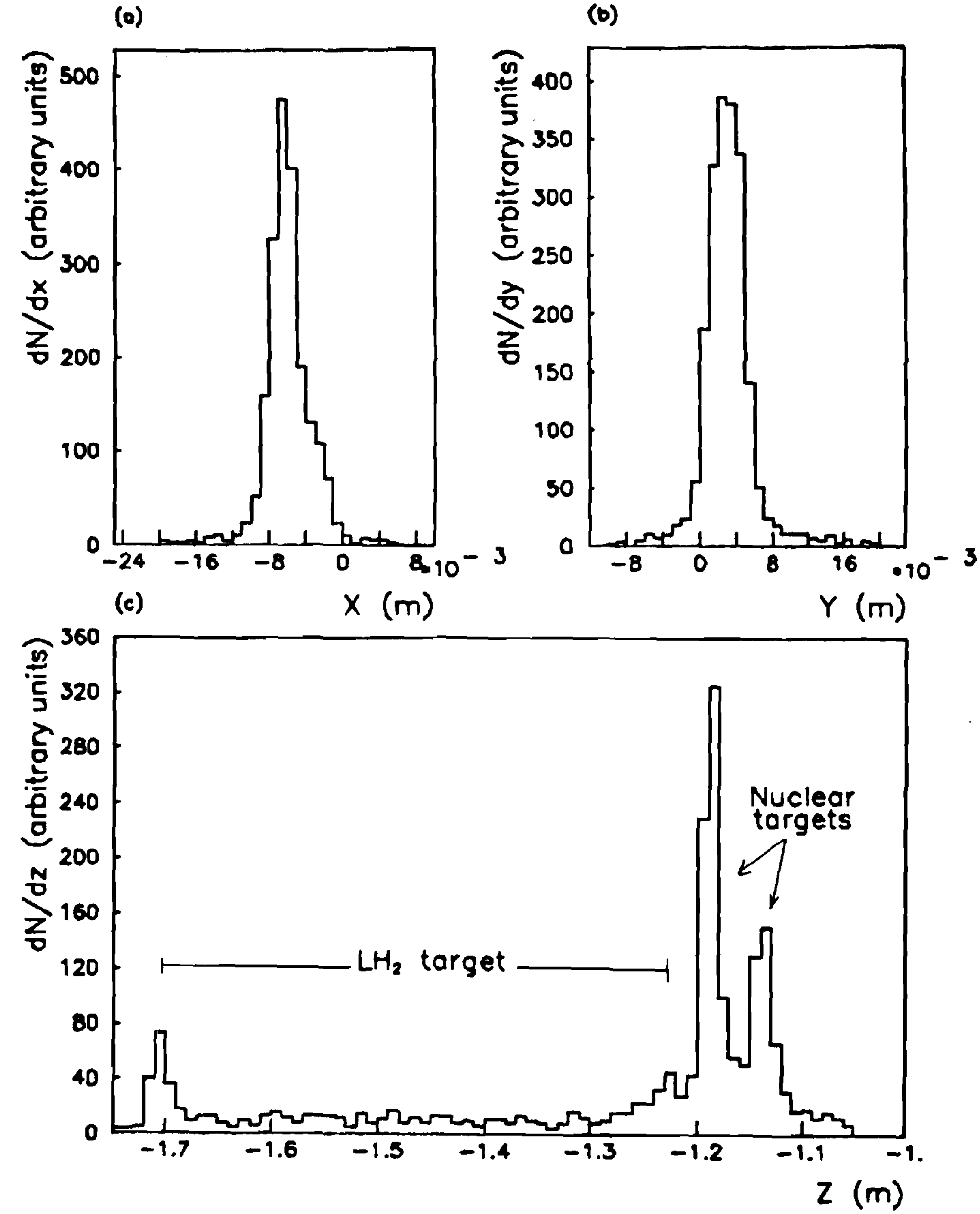

FIG. C-4. Vertex position distributions for run 663. (a) x. (b) y. (c) z.

TABLE C-1. BLOOD PST format.

Unpacked word	Contents	Description
1	NHEAD	Number of words in header (12 or 19).
2	RUNPT/IEVENT	Run number * 100000 + event number.
3 to 5	VTXYZ(3)	x, y, and z of vertex.
6	DVTXYZ3	Error on z of vertex.
7	KTARG/ITHR	Target ID * 100 + threshold flag. Target ID's are: 0 None. 1 Hydrogen. 2 Thin aluminum. 3 Thick aluminum. 4 Thick copper. 5 Lead. 6 Thin copper. Threshold flag is not used.
8	MULT15/MULT30	(Number of modules with $\varepsilon_{ti} > 0.12$ GeV) * 1000 + (Number of modules with $\varepsilon_{ti} > 0.25$ GeV).
9	CALE	Global aperture calorimeter energy.
10	ETCAL	Global aperture calorimeter transverse energy.
11	PLANARI	Calorimeter planarity.
12	PHIPLN	ϕ of calorimeter planarity axis.
	Words 13-19: Monte Carlo PST's only.	
13	RCALE	Global aperture particle energy.
14	RETCAL	Global aperture particle transverse energy.
15	RPLANAR	Particle planarity.
16	RPHIPLN	ϕ of particle planarity axis.

TABLE C-1. (Continued)

Unpacked word	Contents	Description
17	WATE	Event weight.
18	XLUMIN	Luminosity.
19	XTRTCH/XTRTRK	Charged particle multiplicity * 1000 + total multiplicity.
NHEAD to NHEAD + 288	ECAL(288)	Array of module energies, ε_i.
NHEAD + 289 to NHEAD + 294	CPPRC(3,2)	x, y, and z positions of the two calorimeter transporters.
Last 8 × XTRTRK words: Monte Carlo PST's only.		
NHEAD + 295 to NHEAD + 294 × 8 × XTRTRK	TRUTH(800)	Array of particle information. Eight words per particle: Words 1-3 Momentum vector. Word 4 Energy. Words 5-6 x, y at EM calorimeter face. Word 7 Calorimeter module entered (0 if none). Word 8 Module entered if magnet off.

NOTE: On tape, all words except the first NHEAD are packed, three to a CDC 60-bit word.

TABLE C-2. Breakdown of calibration events.

Event Classification	Percentage
Muon	2.5
Tail	1.3
Electron	52.
"Ambiguous"	19.
Hadron	26.

References for Appendix C

1. G. C. Fox, "General TEARS description," E260 memo, 1976 (unpublished); J. Martin, "MINT version 1," E557 memo, 1982 (unpublished).
2. A. Dzierba *et al.*, E557 memo IND-19-79, 1979 (unpublished).
3. P. Devenski, "Calorimeter calibration program user's guide," E557 memo, 1981 (unpublished); "Program for off-line calibration of calorimeter," E557 memo, 1981 (unpublished).
4. P. Devenski, "Pedestals," E557 memo, 1981 (unpublished).
5. S. Teige, "Analysis of E557 calorimeter monitoring data, integrate and hold gains and laser data," E557 memo, 1981 (unpublished).
6. M. Atiya, C. Y. Chi, and W. Sippach, in *Proceedings of the Gas Calorimeter Workshop*, edited by M. Atac (Fermilab, Batavia, Illinois, 1982).
7. P. Devenski and P. Rapp, "2285's: Pedestal jumping and Devenski tracking," E557 memo, 1981 (unpublished).
8. J. Martin, "Descriptions of the subroutines HVERT, OVERT22, GVSEL, and HVOLSEL (vertex-finding routines)," E557 memo, 1980 (unpublished); "The track-finding algorithm," E557 memo, 1981 (unpublished).
9. G. C. Fox, "Vertex determination," E260 memo CIT-25-76, 1976 (unpublished); K. Yung, "Scheme used for vertex determination in our event reconstructions," E260 memo, 1976 (unpublished); C. Bromberg,

G. C. Fox, and K. Yung, "January 1977 vertex algorithm," E557 memo CIT-13-77, 1977 (unpublished).

APPENDIX D

MONTE CARLO SIMULATIONS

In this dissertation I have used two Monte Carlo simulation models to compare to the cross sections and event structure found in our experimental data and to help find corrections for systematic effects which would be difficult to understand analytically. In this appendix I discuss these two simulations.

D.1. Longitudinal Phase Space

The Longitudinal Phase Space (LPS) Monte Carlo is based on a procedure developed by Carey and Drijard[1] for generating events with limited transverse momentum. The generated multiplicity distributions and p_T spectra have been adjusted to agree with bubble chamber data for pp scattering at 400 GeV/c as given in Refs. 2, 3, and 4. The transverse momentum distibution used was

$$f(p_t) = \exp(-4.5\ p_t^{\,2} + m_\pi^2)\ . \tag{D-1}$$

A leading baryon effect is incorporated into the longitudinal momentum distribution.

The charged particle multiplicity, n_{ch}, is distributed according to the KNO fit by P. Slattery,[5]

$$\psi(z=n_{ch}/\langle n_{ch}\rangle) = (3.79z + 33.7z^3 - 6.64z^5 + 0.332z^7)e^{-3.04z} \qquad \text{(D-2)}$$

for multiplicities less than 30 and according to

$$\psi(z) \propto e^{-3.0z} \qquad \text{(D-3)}$$

for higher multiplicities, to match the more recent data; at our energy, $\langle n_{ch}\rangle = 9.0$. Neutral pion multiplicities follow a Poisson distribution, with an average number of π°'s at a given n_{ch}, $\langle n_{\pi^{\circ}}\rangle_{n_{ch}}$, given by:[4]

$$\langle n_{\pi^{\circ}}\rangle_{n_{ch}} = 1.4 + 0.33n_{ch}. \qquad \text{(D-4)}$$

Total multiplicities of up to 70 occur.

No short range correlations are present; there are only long range correlations due to energy and momentum conservation. The lack of short range correlations means the LPS data constitute a standard against which a possible "jet trigger" can be tested: to the extent that an effect is found to be present in the LPS data, that effect cannot be said to be indicative of the presence of jetlike structure.

D.2. QCD/bremsstrahlung

The QCD/bremsstrahlung model was developed by Field, Fox, and Kelly as an improvement of the Feynman-Field model (discussed in Chapter I) in an attempt to explain the non-jetlike structure and large cross section of large-acceptance high E_t triggered events.[6] The major change from the Feynman-Field model was the inclusion of noncollinear gluon bremsstrahlung in the initial and final states. The second Monte Carlo simulation used in this analysis is based on the QCD/brem model. No attempt was made to "tune" its many parameters to fit our data; we used the parameters suggested by the authors which are claimed to give the best agreement with the 300 GeV/c data from NA5.

In this model, the hard scattering process is calculated using quantum chromodynamics (QCD) to leading order. The scattered partons are permitted to radiate off-shell gluons with invariant masses less than those of the parent particles; the remaining energy appears as transverse momentum. The emitted gluons may also radiate. This cascade continues until each particle falls below a mass cutoff. In a similar way the initial state partons are evolved backwards to another cutoff. The events are smeared with an "intrinsic" transverse momentum, k_t.

Hadronization of the partons is handled using the "color string" approach.[7] Gluons are split into $q\bar{q}$ pairs and color singlet clusters are formed. Each cluster then decays according to a phase space method if its invariant mass is under 3 GeV, as back-to-back Feynman-Field type jets (in the cluster CM frame) if its invariant mass is larger than 3 GeV, or as a single hadron if its invariant mass is less than twice the pion mass.

Energy and momentum are not strictly conserved in this model. Due to a divergence of the cross sections at low p_t, a cutoff of $p_t > 1$ GeV is imposed.

It should be noted that the LPS Monte Carlo is not so much a model of the physics responsible for particle distributions as it is simply a phenomenological procedure for generating particles whose distribution matches that seen in low-p_t experimental data. The QCD/brem Monte Carlo, on the other hand, uses QCD as a basis for its simulation of the hard parton-parton scattering and in that sense is a model of a physical theory; however, it uses a phenomenological scheme for fragmentation. Therefore, any comparison of the data to these models -- especially to LPS -- should be seen more as an attempt to improve understanding of the nature of the observed events by comparing their effects in the apparatus to those of simulated events whose nature is "known" than as a test of a physical theory.

D.3. Equipment simulation

The particles generated by both the LPS and QCD/Brem Monte Carlos were processed through a simulation of the E557 apparatus. Interaction vertices were distributed randomly in the fiducial hydrogen target region. The simulation tracked the paths of the final state particles, taking into account geometric acceptances of our apparatus and the field of the spectrometer magnet. For each particle that survived to strike the calorimeter a shower was generated, using the parametrization given in Ref. 8 for the longitudinal development and a Gaussian lateral development. The parameters of this model were adjusted for agreement with our calibration data. The energies of the particles were smeared to correspond to our calorimeter's energy resolution and shower starting points were selected using an exponential distribution, but no other fluctuations in the shower development were modelled. The energy for each module was then computed as the sum over all showers of the energy left in that module by the shower.

The results of the Monte Carlo were written to tape in the same format as was used for the processed experimental data, extended to also include direct information about the final state particles, for use by the analysis programs. The vertex position, which in an experimental data tape would be the result of the vertex finding algorithm, was the actual value generated in the Monte Carlo.

References for Appendix D

1. D. C. Carey and D. Drijard, J. Comput. Phys. 28, 327 (1978).
2. C. Bromberg et al., Phys. Rev. Lett. 31, 1563 (1973).
3. W. S. Toothacker, Univ. of Michigan Report UMBC 77-77 (unpublished); S. Dado et al., Phys. Rev. D 20, 1589 (1979).
4. R. D. Kass et al., Phys. Rev. D 20, 605 (1979).
5. P. Slattery, Phys. Rev. D 7, 2073 (1973).
6. G. C. Fox and R. L. Kelly, in Workshop on Proton-Antiproton Collider Physics, Madison, Wisconsin (AIP Conference Proceedings 85), edited by V. Barger, D. Cline, and F. Halzen (AIP, New York, 1982), p. 435; R. D. Field, G. C. Fox, and R. L. Kelly, Phys. Lett. 119B, 439 (1982).
7. R. D. Field and S. Wolfram, Nucl. Phys. B213, 65 (1983).
8. M. Della-Negra, LAPP preprint EXP-07, 1980 (unpublished).

APPENDIX E

STATISTICS

In this appendix I discuss the statistics of weighted events, and I obtain formulas which were used extensively in the data analysis for this dissertation.

E.1. Moments

Consider a set of random variables x_i where i is in the range (1,2,3,...N). Associated with each x_i is a weight, w_i. As an example, the x_i's might be values for each of N Monte Carlo generated events of some parameter of the event (e.g. energy); the weights are generated by the Monte Carlo to correct for the differences between the particle distribution generated by the Monte Carlo and the real-world distribution being simulated -- the parent distribution.

I will make the simplifying assumption that a single parent distribution is associated with all the x_i's, so, for example, the expectation value of x_i is independent of i; if $\langle u \rangle$ denotes the expectation value of some quantity u, then

$$\langle x_i \rangle = \mu \ . \tag{E-1}$$

Denote by α_n the n'th absolute moment:

$$\alpha_n = \langle x_i^n \rangle \tag{E-2}$$

and let m_n be the n'th central moment:

$$m_n = \langle (x_i-\mu)^n \rangle \ . \qquad \text{(E-3)}$$

The first several m_n's in terms of μ and the α_n's are

$$\begin{aligned} m_0 &= 1 \\ m_1 &= 0 \\ m_2 &= \alpha_2 - \mu^2 \\ m_3 &= \alpha_3 - 3\mu\alpha_2 + 2\mu^3 \\ m_4 &= \alpha_4 - 4\mu\alpha_3 + 6\mu^2\alpha_2 - 3\mu^4 \end{aligned} \qquad \text{(E-4)}$$

Inverting,

$$\begin{aligned} \alpha_2 &= m_2 + \mu^2 \\ \alpha_3 &= m_3 + 3\mu m_2 + \mu^3 \\ \alpha_4 &= m_4 + 4\mu m_3 + 6\mu^2 m_2 + \mu^4 \ . \end{aligned} \qquad \text{(E-5)}$$

The standard deviation (σ), the skewness (γ_1), and the kurtosis (γ_2), are related to m_2, m_3, and m_4 by (Ref. 1):

$$\sigma = \sqrt{m_2} \qquad \text{(E-6)}$$

$$\gamma_1 = \frac{m_3}{\sigma^3} \qquad \text{(E-7)}$$

$$\gamma_2 = \frac{m_4}{\sigma^4} - 3 \ . \qquad \text{(E-8)}$$

E.2. Estimates of μ and m_2

We wish to estimate the central moments and the mean of the parent distribution using the available information -- the sample data. The sample mean is

$$M = \frac{\sum_i w_i x_i}{\sum_i w_i} \qquad \text{(E-9)}$$

and its expected value is

$$\langle M \rangle = (\sum_i w_i)^{-1} \sum_i w_i \langle x_i \rangle = (\sum_i w_i)^{-1} \sum_i w_i \mu = \mu \ . \qquad \text{(E-10)}$$

M is our estimate of μ.

The sample variance is

$$V = \frac{\sum_i w_i(x_i - M)^2}{\sum_i w_i} \quad . \tag{E-11}$$

Its expected value is

$$\begin{aligned} \langle V\rangle &= (\sum_i w_i)^{-1} \sum_i w_i \langle x_i^2 - 2Mx_i + M^2\rangle \\ &= [(\sum_i w_i)^{-1} \sum_i w_i \langle x_i^2\rangle] - \langle M^2\rangle \quad . \end{aligned} \tag{E-12}$$

The first term is just α_2 and the second is

$$\begin{aligned} \langle M^2\rangle &= (\sum_i w_i)^{-2} \langle \sum_{ij} w_i w_j x_i x_j\rangle \\ &= (\sum_i w_i)^{-2} \langle \sum_i w_i^2 x_i^2 + \sum_{ij} w_i w_j x_i x_j (1-\delta_{ij})\rangle \quad . \end{aligned} \tag{E-13}$$

In the second sum, the terms with i=j are zero due to the $(1-\delta_{ij})$ factor, and for $i \neq j$, $\langle x_i x_j\rangle = \mu^2$; therefore $x_i x_j$ can be replaced by μ^2 in all terms in the second sum. Defining $R_n = \Sigma_i (w_i)^n / (\Sigma_i w_i)^n$, the result is

$$\langle M^2\rangle = \alpha_2 R_2 + \mu^2(1-R_2) \tag{E-14}$$

so

$$\begin{aligned} \langle V\rangle &= (\alpha_2 - \mu^2)(1-R_2) \\ &= m_2(1-R_2) \quad . \end{aligned} \tag{E-15}$$

Therefore an unbiased estimate of m_2 is

$$v = \frac{V}{1-R_2} = \frac{(\sum_i w_i)^2}{(\sum_i w_i)^2 - \sum_i w_i^2} V \quad . \tag{E-16}$$

In the case of unweighted data, $w_i = 1$ for all i and

$$v = \frac{N}{N-1} V \ , \tag{E-17}$$

the well-known formula for estimating the parent variance from the sample variance.

E.3. Estimates of variances of M and v

In order to do statistics involving M and v -- for example, to do fits to the mean and variance of E_t^C as functions of E_t in Chapter III -- it is necessary to estimate the variances of these quantities. The variance of M is

$$\begin{aligned} \mathrm{Var}(M) &= \langle M^2 \rangle - \langle M \rangle^2 \\ &= (\alpha_2 - \mu^2) R_2 = m_2 R_2 \ . \end{aligned} \tag{E-18}$$

So an estimate of Var(M) is

$$\begin{aligned} \sigma_M^2 = vR_2 &= \frac{\sum_i w_i^2}{(\sum_i w_i)^2 - \sum_i w_i^2} V \\ &= \frac{V}{N-1} \text{ in the unweighted case.} \end{aligned} \tag{E-19}$$

The variance of v is obtained in essentially the same way. The only new computation is that of $\langle V^2 \rangle$, which is equal to

$$(\sum_i w_i)^{-2} \langle \sum_{ij} w_i w_j (x_i^2 x_j^2 - 2x_i^2 M + M^4) \rangle \ . \tag{E-20}$$

This comes out to

$$\begin{aligned} \langle V^2 \rangle &= m_2^2 + (m_4 - 3m_2^2)R_2 + 3m_2^2 R_2 - 2(m_4 - m_2^2)R_3 + (m_4 - 3m_2^2)R_4 \\ &= m_2^2 (1 + \gamma_2 R_2 + 3R_2^2 - 2(\gamma_2 + 2)R_3 + \gamma_2 R_4) \ , \end{aligned} \tag{E-21}$$

using $m_4=(\gamma_2+3)m_2^2$.

If the parent distribution is assumed to be one that has zero kurtosis (e.g. a Gaussian) then

$$\langle V^2\rangle = m_2^2(1 + 3R_2^2 - 4R_3) \ . \tag{E-22}$$

So, in this case, $(1 + 3R_2^2 - 4R_3)^{-1}V^2$ is an unbiased estimate of m_2^2, and

$$\mathrm{Var}(v) = \left(\frac{1}{1-R_2}\right)^2(\langle V^2\rangle - \langle V\rangle^2)$$

$$= \left(\frac{1}{1-R_2}\right)^2(2R_2 + 2R_2^2 - 4R_3)m_2^2 \ . \tag{E-23}$$

Therefore an unbiased estimate of Var(v) is

$$\sigma_v^2 = 2v^2\left(\frac{R_2+R_2^2-2R_3}{1+3R_2^2-4R_3}\right) \ . \tag{E-24}$$

The case where $\gamma_2 \neq 0$ is much more complicated; it will not be discussed here, nor was it used in the analysis presented herein.

References for Appendix E

1. H. Cramér, Mathematical Methods of Statistics, (Princeton University, Princeton, 1946).

ERRATA

Figure 5-10(a) had its axes mislabelled and should be replaced by the version shown below.

Also note that the four pages consisting of the Curriculum Vitae and Approval Sheet were bound incorrectly; their order should be reversed, and they should occur before the Abstract as the first four pages.

(a)